BOSTON UNIVERSITY

GRADUATE SCHOOL OF ARTS AND SCIENCES

Dissertation

EVIDENCE FOR NEUTRINO MASS FROM OBSERVATIONS OF ATMOSPHERIC NEUTRINOS WITH SUPER–KAMIOKANDE

by

MARK D. MESSIER

B.S., Massachusetts Institute of Technology, 1993
M.A., Boston University, 1999

Submitted in partial fulfillment of the

requirements for the degree of

Doctor of Philosophy

1999

Acknowledgments

I would like to thank all the people whose support and advice have contributed to my education and advancement in physics. Special thanks to James Stone, my advisor, who introduced me to Super–Kamiokande, Larry Sulak and Ed Kearns who provided much advice and guidance. Thanks also to my thesis committee, Steven Ahlen, Kenneth Lane, John Butler and William Skocpol for their questions, comments and insights. I would also like to extend my gratitude to those with whom I have worked most closely at Boston University, K. Scholberg, A. Habig, C. Walter, M. Earl, C. Orth and C. Okada for their expertise, advice, and friendship. Thanks also to D. Sondak for his help getting me up and running on the O2000 cluster.

Super–Kamiokande benefits from the excellent leadership of its spokesmen, Yoji Totsuka, James Stone and Henry Sobel who have all been a great source of advice and encouragement.

I would like to thank T. Kajita and E. Kearns whose leadership of the atmospheric neutrino and proton decay analysis group has made these results possible and K. Kaneyuki for all his close work with me. The analysis presented in dissertation depends on the hard work of many people who deserve special mention: Y. Itow, M. Shiozawa, J. Kameda, M. Etoh, K. Okumura, K. Ishihara, S. Kasuga, C. McGrew, B. Viren, C. Mauger, D. Casper, J. Learned, D. Kielczewska, and W. Gajewski. My research has been supported by a grant from the U.S. Department of Energy.

Finally I wish to express my deep gratitude to those closest to me. My parents, John and Anne, have been a constant source of love and support. My wife Ann has gracefully put up with all my travel and long hours with love, understanding, and patience. Completion of this work would not have been possible with out her support. This dissertation is dedicated to the memory of my sister Jeanne whose spirit continues to guide me.

EVIDENCE FOR NEUTRINO MASS FROM OBSERVATIONS OF ATMOSPHERIC NEUTRINOS WITH SUPER–KAMIOKANDE

MARK D. MESSIER

Boston University Graduate School of Arts and Sciences, 1999

Major Professor: James L. Stone, Professor of Physics

ABSTRACT

This dissertation presents an analysis of atmospheric neutrino data from a 736-day (45.3 kiloton-year) exposure of the Super–Kamiokande detector. Super–Kamiokande is a 50 kiloton water Cherenkov detector located in Gifu Prefecture, Japan. The detector began taking data on April 1, 1996 and has recorded roughly 6000 atmospheric neutrino interactions. The data provide evidence for neutrino oscillations and hence evidence for non-zero neutrino mass.

The atmospheric neutrino data exhibit a significant deficit of muon neutrino interactions which varies with zenith angle. This deficit is inconsistent with expectations based on calculations of the atmospheric neutrino flux and cannot be explained by any combination of known systematic uncertainties. Neutrino oscillations of $\nu_\mu \leftrightarrow \nu_\tau$ with nearly maximal mixing and $1 < \Delta m^2 < 8 \times 10^{-3}$ eV^2 provide a consistent explanation of the observed muon neutrino deficit. Oscillations of ν_μ to a non-interacting sterile neutrino also fit the data well with a smaller region of allowed oscillation parameters. In addition to two-flavor oscillation hypotheses, several three-flavor neutrino mixing schemes are examined. The data are found to be consistent with a range of three-flavor mixing hypotheses that have the general features of large $\nu_\mu - \nu_\tau$ mixing, $\Delta m^2_{12} < \Delta m^2_{23}$ and $10^{-3} < \Delta m^2_{23} < 10^{-2}$ eV^2.

Contents

Acknowledgments ii

Abstract iii

Table of Contents iii

List of Figures vii

List of Tables xviii

1 Introduction 1

1.1 History of the Neutrino 1

1.2 Mass of the Neutrino 5

1.3 Atmospheric Neutrinos 7

2 Phenomenology of Neutrino Oscillations 10

2.1 Neutrino Oscillation in Vacuum 10

2.2 Neutrino Oscillations in Matter 14

2.2.1 Results For Two Flavors 16

2.2.2 Results For Three Active Flavors 19

3 Experimental Searches for Neutrino Oscillations 23

3.1 Solar Neutrino Experiments 23
3.2 Reactor Experiments 25
3.3 Accelerator Experiments 27
3.4 Atmospheric Neutrino Experiments 29
3.5 Summary of Neutrino Oscillation Searches 33

4 The Super–Kamiokande detector 36

4.1 Physical Description 36
4.1.1 Water Cherenkov Radiation 36
4.1.2 Super–Kamiokande Water Tank 37
4.1.3 Water Purification System 40
4.2 Inner Detector 41
4.2.1 20-inch Photomultiplier 41
4.2.2 Front End Electronics and Data Acquisition 42
4.3 Outer Detector 43
4.3.1 Outer Detector Photomultipliers 43
4.3.2 Front End Electronics and Data Acquisition 45
4.4 Calibration 49
4.4.1 Relative Gain Calibration 49
4.4.2 Absolute Gain Calibration 50
4.4.3 Timing Calibration 51
4.4.4 Water Transparency 52

5 Atmospheric Neutrinos in Super–Kamiokande 59

5.1 Fully-Contained Event Selection 59
5.1.1 First Reduction 62
5.1.2 Second Reduction 63

5.1.3 Third Reduction 63
5.1.4 Fourth Reduction: The "Flashscan" Algorithm 65
5.1.5 Scanning 72
5.2 Partially-Contained Event Selection 73
5.2.1 First Reduction 73
5.2.2 Second Reduction 74
5.2.3 Third Reduction 75
5.2.4 Fourth Reduction 75
5.2.5 Fifth Reduction 75
5.2.6 Scanning 76
5.3 Event Reconstruction 76
5.3.1 Fully-Contained Event Reconstruction 76
5.3.2 Partially-Contained Event Reconstruction 92

6 Prediction of Atmospheric Neutrino Event Rates 95
6.1 Atmospheric Neutrino Flux 95
6.1.1 Primary Cosmic Ray Flux 96
6.1.2 Interactions of Cosmic Ray Nuclei with Air 99
6.1.3 Interaction of Secondary Particles in Air 100
6.2 Neutrino Cross Sections 102
6.2.1 Elastic scattering 103
6.2.2 Single Pion Modes 106
6.2.3 Multi-pion Production 108
6.3 Detector Simulation 112

7 Event Summaries 113
7.1 Estimates of Sample Composition 113

7.2 Vertex and Momentum Distributions 115
7.3 Double Ratio Results and Zenith Angle Distributions 119

8 Neutrino Oscillation Analysis **125**

8.1 Simulation of Neutrino Oscillations 125
8.1.1 Atmospheric Neutrino Production Heights 125
8.1.2 Neutrino Propagation Through the Earth 131
8.1.3 Flux Weights for Neutrino Oscillations 133
8.1.4 Estimates of ν_τ Appearance 135
8.2 Statistical Method of Neutrino Oscillation Fits 136
8.2.1 Definition of χ^2 136
8.2.2 Test of Statistical Treatment 145
8.2.3 Treatment of the Physical Boundary 147
8.3 Results for Two-Flavor Neutrino Oscillations 152
8.3.1 $\nu_\mu \leftrightarrow \nu_\tau$ 153
8.3.2 $\nu_\mu \leftrightarrow \nu_{sterile}$ 160
8.3.3 $\nu_\mu \leftrightarrow \nu_e$ 161
8.4 Estimating L/E_ν 162
8.5 Alternate Hypotheses 169
8.6 Results for Three-Flavor Neutrino Oscillations 172
8.6.1 Three-fold Maximal Mixing 174
8.6.2 Bi-maximal Mixing 176
8.6.3 Democratic Mixing 178

9 Conclusions **181**

Bibliography **182**

List of Figures

1.1 A diagram of an atmospheric neutrino experiment. 8

2.1 Feynman diagrams for forward scattering in matter. All non-sterile neutrino flavors experience interactions shown in (a), but only electron neutrinos experience those shown in (b). 14

2.2 The neutrino mixing angle for various matter densities is plotted as a function of the ratio of the neutrino energy to vacuum mass-squared difference for $\nu_\mu \leftrightarrow \nu_e$ oscillations. 18

2.3 The effective mass-squared differences for two neutrinos for various matter densities and neutrino energies. 19

2.4 Oscillation probabilities as a function of energy for neutrinos crossing a 1000 km thick slab of matter with a density of 3 g/cm^3 under the assumption of three-fold maximal mixing and $\Delta m^2_{12} = 2 \times 10^{-5}$ eV^2 and $\Delta m^2_{23} = 5 \times 10^{-3}$eV^2. Dotted curves show the oscillation probabilities for zero matter density. 21

2.5 Oscillation probabilities for neutrinos crossing a 1000 km thick slab of matter with a density of 10 g/cm^3 under the assumption of three-fold maximal mixing and $\Delta m^2_{12} = 2 \times 10^{-5}$ eV^2 and $\Delta m^2_{23} = 5 \times 10^{-3}$eV^2. Dotted curves show the oscillation probabilities for zero matter density. 22

3.1 The solar neutrino spectrum with experimental thresholds. [53] . . . 24

3.2 The solar neutrino peak as measured by Super–Kamiokande [62]. The best-fit requires 47% suppression of the expected flux as calculated in Ref. [54] 26

3.3 Summary of atmospheric neutrino R measurements [41, 40, 47, 43, 42, 80]. In each case the inner error is statistical and the outer error includes the estimated systematic uncertainties. 30

3.4 The $(\mu/e)_{DATA}/(\mu/e)_{MC}$ as a function of cosine zenith angle for the Kamiokande sub-GeV and multi-GeV samples. Dashed curve for sub-GeV is the expectation for best-fit oscillations to the combined sub-GeV and multi-GeV samples, the dot-dashed curve is for best-fit to the sub-GeV sample alone. In the right panel, the dashed curve is the best-fit oscillation expectation for $\nu_\mu \leftrightarrow \nu_e$ oscillations and the dotted curve is for best fit $\nu_\mu \leftrightarrow \nu_\tau$ ($\sin^2 2\theta = 1$, $\Delta m^2 = 0.01$ eV^2) oscillations [44]. 31

3.5 Rates of neutrino-induced upward-going muons in Super–Kamio-kande [85]. Solid curve is the predicted flux with the best-fit -10% normalization factor applied. The dashed curve is the best-fit expectation for $\nu_\mu \rightarrow \nu_x$ oscillations with $\Delta m^2 = 3.5 \times 10^{-3}$ eV^2 and $\sin^2 2\theta = 1$ with a $+8\%$ normalization to the total flux applied. 32

3.6 Allowed and excluded regions of parameter space for $\nu_\mu \leftrightarrow \nu_e$ neutrino oscillations. In each case, the excluded regions lie to the right of the curves. References are given in the text. 34

3.7 Allowed and excluded regions of parameter space for $\nu_\mu \leftrightarrow \nu_\tau$ neutrino oscillations. In each case, the excluded regions lie to the right of the curves. References are given in the text. 35

4.1 An illustration of Cherenkov radiation. 38
4.2 A schematic drawing of the Super–Kamiokande detector 39
4.3 The reflectivity of Tyvek used in the outer-detector. Top curve shows measured value and the lower curves show the estimated values for the different faces of the Super–Kamiokande tank. 39
4.4 The water purification system. 40
4.5 Schematic drawing of the 20-inch PMT's used in Super–Kamiokande. 41
4.6 20-inch PMT quantum efficiency as a function of wavelength. 41
4.7 Block diagram for in inner detector DAQ system. 44
4.8 Block diagram for a single QTC channel. 45
4.9 OD trigger rate and OD/ID trigger coincidence rate as a function of OD trigger threshold. 46
4.10 Setup used for QTC testing. 46
4.11 Top: The measured TDC vs. ADC (converted to pC) values for a single QTC daughercard. The bottom shows the fit residuals to a straight line fit. 47
4.12 Outer detector data acquisition system [91]. 48
4.13 The Xe relative gain calibration system. 49
4.14 The spread in relative gains for the inner detector PMT's 50
4.15 The relative photo-sensitive area and a function of incident angle. . . 51
4.16 The Nickel calibration source. 52
4.17 A typical single-photoelectron peak for a 20 inch PMT. 53
4.18 Laser system used for relative timing calibration. 53
4.19 The timing-pulse height distribution (TQ-map) for a typical 20 inch PMT. 54
4.20 The setup for measuring water transparency. 55

4.21 Measurement of the water transparency at 420 nm. 55
4.22 The attenuation coefficient $(1/L(\lambda))$ as measured in Super–Kamiokande. Solid lines show the attenuation coefficients used in Monte Carlo simulations of Cherenkov light in the Super–Kamiokande detector. 56
4.23 The water transparency measured using cosmic ray muons. 57
4.24 The water transparency as measured with cosmic ray muons as a function of time during the 736-day analysis period. 58

5.1 A typical pair of fully-contained events, the top is $\mu-$like and the bottom is $e-$like. Note that in both cases the outer-detector (shown at top right) has no cluster of hit PMT's. The distribution of PMT hit times is shown in the histogram. The peak in the $\mu-$like event near $t = 1600$ ns is from an electron produced by the decay of the muon. 60
5.2 A typical partially contained event. Note the cluster of outer-detector PMT hits shown at the upper right. 61
5.3 A typical pair of flasher events. These events occurred within 20 minutes of each other. 67
5.4 Correlation for pairs of atmospheric neutrino Monte Carlo and flasher events. 68
5.5 Cut to determine if two events are "matches". 69
5.6 Distributions of maximum correlation versus the number of events matched for 10-years of atmospheric neutrino Monte Carlo and 414-days of tagged flasher events. Events to the right of the solid line are removed from the sample. 70

5.7 Comparison of automated flasher cuts with human scanners. 93% of the events labeled flashers or noise by human scan are removed automatically. 70
5.8 A-fit vertex distributions for sub-GeV, multi-GeV, $e-$like and $\mu-$like events. 79
5.9 A-fit angular distributions for sub-GeV, multi-GeV, $e-$like and $\mu-$like events. 80
5.10 Hough transform for a 2-ring event. 81
5.11 Single-ring identification probability for charged-current quasi-elastic events and the single-ring, quasi-elastic, event fraction as functions of momentum. 83
5.12 Single-ring identification probability for charged-current quasi-elastic events and the quasi-elastic event fraction as functions of momentum. 84
5.13 The difference in Monte Carlo vertex position and fitted vertex position as measured along the particle track direction for MS-fit and A-fit. The gains in vertex resolution by MS-fit come mostly from improved vertex resolution along the the particle track direction. 89
5.14 Final vertex resolutions for sub-GeV, multi-GeV, $e-$like, and $\mu-$like events following MS-fit. 90
5.15 The direction resolution of MS-fit for sub-GeV, multi-GeV, $e-$like and $\mu-$like events. 91
5.16 The relation between the total corrected p.e. and momentum for electrons and muons. 92
5.17 Absolute energy scale determination from several sources. 93
5.18 Momentum resolution as a function of energy for electrons and muons [92]. 93

6.1 Observed fluxes of H (top), He (middle) and CNO (bottom). Lines are for parameterizations for solar average (solid), solar minimum (dotted) and solar maximum (dashed) [96]. 96
6.2 The average number of Sun spots per day for each year since 1970 [105]. 97
6.3 The cutoff rigidity in GeV for the Super–Kamiokande site following the calculation of Ref. [96]. In the figure, $\Theta = 0°$ corresponds to particles arriving from directly over head, and $\Theta = 180°$ those from directly below. The azimuthal angles $(0°, 90°, 180°, 270°)$ are south, east, north and west. 98
6.4 Comparison of the estimated μ^- flux with experimental data [96]. . . 100
6.5 The $(\nu_\mu + \bar{\nu}_\mu)/(\nu_e + \bar{\nu}_e)$, $\nu_\mu/\bar{\nu}_\mu$ and $\nu_e/\bar{\nu}_e$ ratios as functions of neutrino energy for calculations by Honda [96], BGS [97], BN [102], and LK [103].101
6.6 The estimated neutrino flux verse zenith angle for the Honda [96] (solid line) and Bartol [97] (dashed line) calculations. 101
6.7 Total neutrino cross section weighted by $E_\nu^{-1.7}$ to approximate $dN/d(\ln E_\nu)$ where N is proportional to the number of interactions. 103
6.8 Total anti-neutrino cross section weighted by $E_\nu^{-1.7}$ to approximate $dN/d(\ln E_\nu)$ where N is proportional to the number of interactions. . 104
6.9 Distribution of Fermi momentum for nucleons in ^{1}6O. 105
6.10 Quasi-elastic and elastic scattering neutrino cross-sections for free and bound nuclei. 106
6.11 Neutrino single pion cross sections. 107
6.12 Anti-neutrino single pion cross sections. 108
6.13 Cross sections for coherent single pion production. 109
6.14 The fraction of pions that no not interact, are absorbed, scatter inelastically, or undergo charge-exchange as a function of pion momentum.109

6.15 Multiple pion production cross sections. 110

7.1 Distribution of the number of rings found for data and Monte Carlo. . 114

7.2 The particle identification parameter used to separate $e-$like and $\mu-$like events. The Monte Carlo is shown separately for charged-current, and neutral-current events. 116

7.3 Vertex distributions for the FC sub-GeV and multi-GeV samples. . . 117

7.4 Vertex distributions for the PC sample. 118

7.5 Momentum distributions for the single-ring sub-GeV e-like and μ-like samples. 118

7.6 Momentum distributions for the multi-GeV e-like, μ-like, and Partially Contained samples. 119

7.7 The observed R values versus distance to nearest detector wall. . . . 121

7.8 Atmospheric neutrino event rates as a function of zenith angle cosine for the sub-GeV and multi-GeV+PC event samples. 122

7.9 The $(U-D)/(U+D)$ zenith angle asymmetry is plotted versus momentum for $e-$like and $\mu-$like events. The expectations for no oscillations is shown in the hatched region. The solid-line shows the expectation for $\nu_\mu \leftrightarrow \nu_\tau$ oscillations using the best-fit parameter found in Sec. 8.3.1.123

8.1 The fraction of neutrinos that come from the decays of pions and kaons as a function of neutrino energy. 126

8.2 The average production height for neutrinos from π/K decays and from muon decays for various neutrino energy ranges. The error bars indicate the rms. spread about the mean. The plot ranges from the horizon $\cos\Theta = 0$ to vertically downward-going neutrinos $\cos\Theta = 1$. 129

8.3 The distribution of neutrino production heights for E_ν=1, 5, and 20 GeV for neutrinos from overhead ($\cos\Theta = 1$) and near the horizon ($\cos\Theta = 0.05$). 130
8.4 Density of the Earth as a function of radius. 131
8.5 Comparison of the ν_μ survival probability for the cases $\nu_\mu \leftrightarrow \nu_e$ and vacuum oscillations for neutrinos propagating through the Earth. . . 133
8.6 Comparison of the ν_μ survival probability for the cases $\nu_\mu \leftrightarrow \nu_{sterile}$ and vacuum oscillations for neutrinos propagating through the Earth. 134
8.7 Estimated energy spectrum and zenith angle distribution of ν_τ's that interact in Super–Kamiokande assuming $\nu_\mu \leftrightarrow \nu_\tau$ oscillations with $\sin^2 2\theta = 1.0$ and $\Delta m^2 = 3.5 \times 10^{-3}$ eV^2. 136
8.8 The average angle between the neutrino and the reconstructed lepton directions as a function of the reconstructed lepton momentum. Results for ν_μ and ν_e have been combined as there is no significant difference for the two flavors. 137
8.9 Estimates of the number of neutrinos produced in the rock over the Super–Kamiokande detector. 143
8.10 Distributions of χ^2 obtained from simulations of measurements of oscillation parameters using atmospheric neutrinos. χ^2_{true} is evaluated at the input values of the oscillation parameters; χ^2_{min} is evaluated at the value of the oscillation parameters that minimize χ^2. Each distribution is compared to the expected behavior (solid line); $\chi^2(DoF = 69)$ for χ^2_{true} and $\chi^2(DoF = 67)$ for χ^2_{min}. 146

8.11 Distributions of the difference $\chi^2_{true} - \chi^2_{min}$ which is used to assign confidence levels to oscillation parameters. The expected behavior is shown by the solid line. The χ^2 differences corresponding to the 90% CL and 99%CL intervals are shown in the hatched regions. 146

8.12 The distribution of χ^2 minima for 10,000 simulated measurements of $\sin^2 2\theta$ and Δm^2 using 736 days of atmospheric neutrinos. 148

8.13 The difference between the input and estimated values of the sub-GeV and multi-GeV $\mu-$like/$e-$like ratios expressed in terms of the size of their expected errors. 149

8.14 The χ^2 differences corresponding to the 68%, 90%, and 99% confidence intervals for a bounded physical region. $\Delta\chi^2$ is the difference between the value of χ^2_{min} and the value of χ^2 on the physical boundary; it is taken positive if χ^2_{min} occurs inside the physical region and negative if outside the physical region. 151

8.15 Allowed oscillation parameters for $\nu_\mu \leftrightarrow \nu_\tau$ oscillations. 154

8.16 Allowed oscillation parameters for $\nu_\mu \leftrightarrow \nu_\tau$ oscillations including the unphysical region $\sin^2 2\theta > 1$. 155

8.17 The confidence intervals for $\nu_\mu \leftrightarrow \nu_\tau$ oscillation parameters estimated using the method of Feldman and Cousins. 156

8.18 Best fit residuals for fits to $\nu_\mu \leftrightarrow \nu_\tau$ oscillations. 157

8.19 Atmospheric neutrino zenith angle event rates. Hatched region shows expectation for no oscillations with Monte Carlo statistical error, line is the best-fit expectation for $\nu_\mu \leftrightarrow \nu_\tau$ neutrino oscillations and the points are the data. The 7 momentum bins used in the fit have been combined into 4 for the purposes of the figure. 158

8.20 The multi-GeV $e-$like and $\mu-$like zenith angle rates in ten bins. . . . 158

8.21 Estimated Super–Kamiokande allowed regions for the year 2002 (4.5 live-years) and 2006 (8 live-years). 159
8.22 Super–Kamiokande allowed oscillations parameters for $\nu_\mu \leftrightarrow \nu_{sterile}$ oscillations. 161
8.23 Super–Kamiokande atmospheric neutrino zenith angle event rates are plotted with the best-fit expectation for $\nu_\mu \leftrightarrow \nu_{sterile}$ oscillations. The key is same as Fig. 8.19 162
8.24 Super–Kamiokande best-fit probability for oscillations parameters assuming $\nu_\mu \leftrightarrow \nu_e$ oscillations. 163
8.25 Super–Kamiokande atmospheric neutrino zenith angle event rates for the best-fit case of $\nu_\mu \leftrightarrow \nu_e$ oscillations. The key is same as Fig. 8.19. 164
8.26 The average momentum fraction transfered to the final state lepton for single-ring charged-current neutrino interactions as a function of reconstructed lepton momentum. The distributions for e-like and μ-like events are plotted separately with fits to 4^{th} and 5^{th} order polynomials respectively. 165
8.27 The estimated percent resolution of neutrino L/E_ν is plotted as a function of L/E_ν. 166
8.28 The atmospheric neutrino single-ring event rates with $p > 400$ MeV/c versus reconstructed L/E_ν are shown for a 45 kt-yr exposure of the Super-Kamiokande detector. Expected rates in the absence of neutrino oscillations are shown in the hatched regions. The dashed line is the expectation for oscillations of ν_μ to ν_τ with $\Delta m^2 = 3.5 \times 10^{-3}\text{eV}^2$ and $\sin^2 2\theta = 1.0$. 167

8.29 The ratio of data over Monte Carlo is plotted versus L/E_ν. The dashed line shows the expectation for oscillations of ν_μ to ν_τ with $\Delta m^2 = 3.5^{-3}\text{eV}^2$ and $\sin^2 2\theta = 1.0$. The slight dependence of the expected e-like ratio results from a roughly 2% ν_μ charged-current contamination in the e-like sample. 168
8.30 Excluded regions for the muon neutrino decay hypothesis. 169
8.31 Best-fit zenith angle distributions assuming ν_μ decay (solid line). The hatched region show the expectation for no oscillations. 170
8.32 Confidence intervals for neutrino oscillations due to Lorentz non-invariance. 172
8.33 Expected zenith angle fits for best-fit oscillations assuming Lorentz non-invariance (solid line). Hatched region shows expectations for no oscillations. 173
8.34 The allowed oscillation parameters assuming three-fold maximal neutrino mixing. 175
8.35 Best-fit zenith angle rates assuming three-fold maximal mixing. . . . 176
8.36 The allowed oscillation parameters assuming bi-maximal mixing. . . . 177
8.37 Best-fit zenith angle rates assuming bi-maximal mixing. 178
8.38 The allowed oscillation parameters assuming democratic neutrino mixing. 179
8.39 Expected zenith angle distributions for democratic neutrino mixing. . 180

List of Tables

3.1 Summary of solar neutrino flux measurements. The predicted fluxes are based on the solar model calculations in Ref. [54]. 25

3.2 Summary of solutions to the world solar neutrino data [66]. 25

4.1 Specifications of the 20-inch Hamamatsu PMT. 42

5.1 Full-contained data event selection summary. 62

5.2 Summary of the partially-contained event selection steps. 73

6.1 The power law fits used to model the high energy cosmic ray fluxes [96]. 99

7.1 Number of events in each reconstruction class from a 20 year Monte Carlo simulation of atmospheric neutrino interactions in the Super–Kamiokande detector. Charged–current interactions are given separately for ν_e and ν_μ (in parenthesis). 115

7.2 Summary of the sub-GeV, multi-GeV and PC event samples compared with the Monte Carlo prediction. 120

7.3 Summaries of the number of up- and down-going events for the sub-GeV and multi-GeV samples. Note that the asymmetry for the multi-GeV $\mu-$like samples combines the FC and PC samples which have different live-times; the PC events have been scaled to the FC live-time. 124

8.1 Parameters used in the calculation of neutrino production heights. . . 127
8.2 Sources and estimates of uncertainties in the predicted $\mu-$like/$e-$like ratio for the sub-GeV and multi-GeV samples [92]. 140
8.3 Contributions to the uncertainty in the relative normalization of the fully-contained multi-GeV $\mu-$like sample and the partially-contained sample. 141
8.4 Sources and estimates of systematic uncertainties in the prediction of U/D where U is the number of up-going events and D is the number of down-going events for the sub-GeV and multi-Gev $e-$like and $\mu-$like samples. 142
8.5 Summary of two-flavor neutrino oscillation fits. Best-fit points are for $(\sin^2 2\theta, \Delta m^2\ \mathrm{eV}^2)$. 153
8.6 Best fit values of the Monte Carlo input parameters for two-flavor oscillation modes. 154
8.7 Summary of CKM angles for 3-flavor mixing schemes. 174
8.8 Summary of the fit parameters for three-flavor mixing. 174

Chapter 1

Introduction

Neutrinos they are very small
They have no charge and have no mass
And do not interact at all.
...
At night, they enter at Nepal
And pierce the lover and his lass
From underneath the bed - you call
It wonderful: I call it crass.

–John Updike

1.1 History of the Neutrino

Although John Updike preferred the word "crass" in his poetic description of the neutrino, the most common word used in the popular press is "elusive". Perhaps then, it is appropriate that the history of the neutrino begins in 1930 with a proposal by Wolfgang Pauli at a conference he did not attend. The spectrum of β particles emitted from the radioactive decay of nuclei had been known to be continuous since 1914 [1]. This presented a puzzle: energy conservation does not allow a continuous spectrum in a two-body decay. Pauli attempted to solve this problem as well as the discrepancy between the predicted and measured spins of the N and ^{6}Li atoms, by imagining a single particle with spin 1/2 and no charge. Preferring a ball in Zurich

to the conference in Tübingen, Pauli addressed his colleagues at the conference in a letter [2]:

> Dear Radioactive Ladies and Gentlemen:
>
> I beg you to receive graciously the bearer of this letter who will report to you in detail how I have hit on a desperate way to escape from the problems of the "wrong" statistics of the N and ^{6}Li and of the continuous β spectrum in order to save the "even-odd" rule of statistics and the law of conservation of energy. Namely the possibility that electrically neutral particles, which I would like to call neutrons might exist inside nuclei; these would have spin 1/2, would obey the exclusion principle, and would in addition differ from photons through the fact that they would not travel at the speed of light. The mass of the neutron ought to be about the same order of magnitude as the electron mass, and in any case could not be greater than 0.01 proton masses. The continuous β spectrum would then become understandable by assuming that in beta decay a neutron is always emitted along with the electron, in such a way that the sum of the energies of the neutron and electron is a constant.
>
> ...
>
> I admit that my way out may look rather improbable at first since if the neutron existed it would have been seen long ago. But nothing ventured, nothing gained. The gravity of the situation with the continuous β spectrum was illuminated by a remark by my distinguished predecessor in office, Mr. DeBye, who recently said to me in Brussels, "Oh, that's a problem like the new taxes; one had best not think about it at all." So one ought to discuss seriously any way that may lead to salvation. Well, dear radioactive friends, weigh it and pass sentence! Unfortunately, I cannot appear personally in Tübingen, for I cannot get away from Zurich on account of a ball which is held here on the night of December 6-7. With best regards to you and to Mr. Baek,
>
> Your most obedient servant,
> W. Pauli

At the time this letter was written only the proton and electron were known to exist; Pauli's "neutron" is known today as the "neutrino". One of Pauli's "radioactive friends", J. Chadwick would discover what we today call the neutron in 1932 for which he would be awarded the Nobel Prize in 1935 [3]. The neutron weighed more than

the proton and was much too heavy to be the particle Pauli had in mind to rescue energy conservation in beta decay.

The continuous β energy spectrum of nuclear beta decay was explained in 1934 by Enrico Fermi [4]. He took up the idea of Pauli's invisible particle, and proposed a quantitative theory of nuclear beta decay which could explain the continuous β spectrum and predict the decay rate. Fermi proposed that the emission of β particles (electrons) was due to the decay of Chadwick's neutron to a proton, an electron, and Pauli's invisible particle which he dubbed the neutrino (Italian for "little neutral one"):

$$n \rightarrow p + e^- + \bar{\nu}. \tag{1.1}$$

The neutrino could have no electric charge and a mass equal or less than the mass of an electron. In describing the interaction Fermi drew on an analogy with the electromagnetic radiation of photons from atoms. The coupling of the four fermions in Eq. 1.1 required a new constant with units of $1/\text{mass}^2$ which today bears Fermi's name.

The next major steps in neutrino history would come 17 years later. The idea that neutrinos could be directly observed via inverse beta decay, $p + \bar{\nu} \rightarrow n + e^+$, was first put forward by Pontecorvo in 1946 [5]. On sabbatical from the Manhattan project in 1951, Fred Reines formed a collaboration with Clyde Cowan to attempt the direct observation of the neutrino. After considering the idea of using a nuclear blast as the neutrino source, they settled on the more prosaic nuclear reactor at Hanford, Washington. There, the two set out to detect the neutrino via inverse beta decay using the coincidence of scintillation light from the positron with the production of a gamma ray from neutron capture on cadmium several μsec later. The project moved to Savannah River and conclusive results were published in 1956 [6, 7] for which

Reines was awarded the Nobel Prize in 1995.

Following the observation of the neutrino, the next step was taken by Lee and Yang who proposed that spatial parity may be violated in beta decay [8]. It was quickly realized by Salam [9] that parity violation in weak interactions could be explained by a vanishing neutrino mass. Parity violation was demonstrated by measurements of the angular distributions of electrons from the beta decay of polarized ^{60}Co atoms by Wu *et al.* [10]. To explain these measurements, it became natural to introduce a two-component theory of the neutrino in which the neutrino field was either "left-handed" (spin and momentum anti-parallel) or "right-handed" (spin and momentum parallel) and exactly massless [11, 12]. The neutrino field was established to be left-handed by M. Goldhaber *et al.* in 1958 [13]. Following these discoveries, exactly massless neutrinos would be a feature of every theory of the weak interactions to the present day.

The first steps towards unification of the weak force and electromagnetism were taken by Glashow in 1961 [14] and Salam and Ward in 1964 [15]. Other contributions would follow, including estimates of the W and Z masses by S. Weinberg in 1967 [16]. Glashow, Salam and Weinberg would share the Nobel Prize in 1979 for their "contribution to the theory of the unified weak and electromagnetic interaction between elementary particles, including, *inter alia*, the prediction of the weak neutral current."

Other major advances in neutrino physics were:

- Proposal of a muon neutrino by Pontecorvo in 1959 [17] and its observation in 1962 at Brookhaven [18] for which L.M. Lederman, M. Schwartz, and J. Steinberger were awarded the Nobel Prize in 1988.

- Observation of neutrinos from the Sun by Ray Davis starting in 1968 [19].

- Discovery of the τ lepton in 1975 [20] which implied the existence of a third generation of neutrino, ν_τ. For the discovery, M. Perl shared the Nobel Prize in 1995.

- Observation of the weak-neutral current interaction $\bar{\nu}_\mu + e^- \rightarrow \bar{\nu}_\mu + e^-$ at CERN in 1976 [21, 22].

- Observation of the $W^\pm$ and Z^0 bosons at CERN in 1983 [23, 24] for which C. Rubbia and S. Van der Meer shared the Nobel Prize in 1984.

- Observation of neutrinos from the supernova explosion SN1987a by the Kamiokande [25] and IMB [26] water Cherenkov detectors. A total of 19 neutrinos were observed over a time range of $\sim$15 sec. with energies between 7.5 – 40 MeV.

- Precise measurements of the Z^0 decay width provided evidence that there are no more than three light neutrinos [27, 28, 29, 30, 31, 32].

1.2 Mass of the Neutrino

Despite these advances, the question of the mass of the neutrino remained unresolved. In his original work on the subject, Fermi suggested using the end-point of the β spectrum from nuclear beta decay to measure the mass of the neutrino. In the process

$$(Z, A) \rightarrow (Z + 1, A) + e^- + \bar{\nu}_e \tag{1.2}$$

the largest electron energy possible is

$$E_{max} = m_i - m_f - m_\nu \tag{1.3}$$

where m_i is the mass of the initial nucleus and m_f is the mass of the final nucleus. Numerous experiments have been made studying the end point of the β spectrum from Tritium decay. The current upper limits on the electron neutrino are 4.35 eV/c^2 [33] and 7.0 eV/c^2 [34]. Interpretation of these results is complicated by the fact that several experiments measure unphysical (negative) values of the neutrino mass-squared from fits to the spectrum end point.

Limits for the muon neutrino mass come from precise measurements of the muon spectrum from pion decay at rest, $m_{\nu_\mu} < 170$ keV [35]. The tau neutrino mass is limited by studies of tau decay to hadrons ($\tau \to 4(5)\pi + \nu_\tau$); $m_{\nu_\tau} < 18.2$ MeV [36].

Besides direct measurement of the neutrino mass, the rates of nuclear neutrinoless double beta decay,

$$(Z, A) \to (Z + 2, A) + e^+ e^+, \tag{1.4}$$

are sensitive to non-zero neutrino mass. The decay rate is proportional to a weighted average of the heavy Majorana neutrino states $\langle m_\nu \rangle$. Neutrinoless double beta decay is only possible if the neutrino is its own anti-particle, and hence its observation would establish that neutrinos are Majorana fermions. Neutrinoless double-beta decay has not been observed and current limits are $\langle m_\nu \rangle < 0.46$ [37] and $\langle m_\nu \rangle < 1.5$ [38].

A third signature of neutrino mass was proposed by Pontecorvo in 1964 [39]. If the neutrino electroweak eigenstates are a superposition of mass eigenstates, then there is a probability that a neutrino created in an electroweak eigenstate α may be observed in a electroweak state β after traveling a distance L. The "oscillation" probability is given by:

$$P(\nu_\alpha \to \nu_\beta) = \sin^2 2\theta \sin^2 \left(\frac{1.27 \Delta m^2(\mathrm{eV}^2) L(\mathrm{km})}{E(\mathrm{GeV})} \right). \tag{1.5}$$

where E is the neutrino energy and Δm^2 is the difference of the mass eigenvalues squared; $\Delta m^2 = m_2^2 - m_1^2$. While it is not possible to measure the values of the neutrino masses (only their differences) using neutrino oscillations, searches for neutrino oscillations can be made sensitive to mass differences much smaller than the limits from direct mass searches. Neutrino oscillation experiments have been made at accelerators, nuclear reactors, and using natural sources such as neutrinos produced in the atmosphere and in the Sun. The wide range of neutrino flight distances and energies covered by these experiments probe Δm^2 from 100 eV^2 down to 10^{-11} eV^2. The evidence for neutrino mass reported in this dissertation is based on the observation of oscillations of neutrinos produced in the atmosphere by the collision of cosmic rays with air.

1.3 Atmospheric Neutrinos

Atmospheric neutrinos are produced in the upper atmosphere when cosmic rays strike air nuclei. These collisions create mesons (mostly pions) which then decay producing neutrinos:

$$\begin{array}{rcl} A_{cr} + A_{air} \rightarrow & \pi^+ & + \cdots \\ & \hookrightarrow \ \mu^+ & + \ \nu_\mu \\ & \hookrightarrow \ e^+ & + \ \bar{\nu}_\mu \ + \ \nu_e . \end{array} \tag{1.6}$$

Note that while the total rate of neutrino production has large uncertainties ($\sim 20\%$) the simple decay chain yields an expected ratio of $(\nu_\mu + \bar{\nu}_\mu)/(\nu_e + \bar{\nu}_e)$ (hereafter ν_μ/ν_e) of roughly 2 with only 5% uncertainty. Also, due to geometry, the atmospheric neutrino flux is expected to be up-down symmetric at high energies; roughly the same number of neutrinos are expected to arrive from above the horizon as from below.

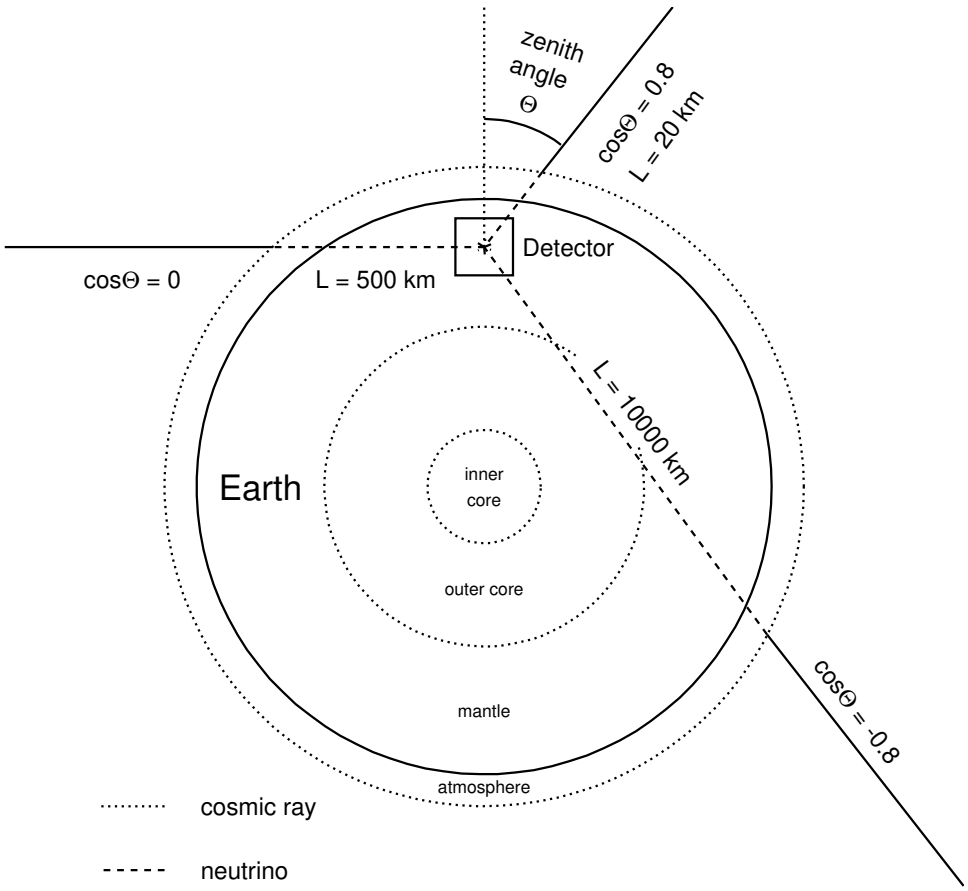

Figure 1.1: A diagram of an atmospheric neutrino experiment.

The flux of atmospheric neutrinos provide an excellent source for neutrino oscillation studies. As shown in Fig. 1.1, a detector located near the surface of the Earth sees neutrinos that travel only ∼20 km when it looks up, while neutrinos that arrive from below the detector travel roughly 10,000 km. This broad range of L coupled with the atmospheric neutrino spectrum, which extends out to 100 GeV (falling like $E^{-2.7}$), make observations of atmospheric neutrinos sensitive to Δm^2 down to 10^{-5} eV^2. The signatures for oscillations of atmospheric neutrinos are:

(1) deviations from the predicted ν_μ/ν_e ratio, and

(2) up-down asymmetries in the neutrino flux.

Indications of (1) were found by the water Cherenkov experiments IMB [40], and Kamiokande [41], although other iron-based experiments were in agreement with expectations [42, 43]. Evidence for (2) was found by the Kamiokande experiment [44]. Observations of both signatures have been made with high-statistics by Super–Kamiokande [45, 46, 47]. The size of the deviations in ν_μ/ν_e and the up-down asymmetry are used to measure $\sin^2 2\theta$ and Δm^2. The data from Super–Kamiokande analyzed in this dissertation are consistent with oscillations of $\nu_\mu \leftrightarrow \nu_\tau$ (or $\nu_{sterile}$) with nearly maximal mixing and $1 \times 10^{-3} < \Delta m^2 < 8 \times 10^{-3}$ eV^2. This evidence for neutrino oscillation implies a non-zero neutrino mass.

Chapter 2

Phenomenology of Neutrino Oscillations

2.1 Neutrino Oscillation in Vacuum

If neutrinos have mass, the basis which diagonalizes the electroweak Hamiltonian ("flavor basis") will in general be a superposition of the mass eigenstates. In the vacuum, this mixing is expressed as:

$$|\nu_\alpha\rangle = \sum_i U_{\alpha i}|\nu_i\rangle \tag{2.1}$$

where the electroweak eigenstates are labeled by Greek indices ($\alpha = e, \mu, \tau, \ldots$) and the mass eigenstates are labeled by Arabic indices ($i = 1, 2, 3, \ldots$). In units where $c = \hbar = 1$, the time evolution of the neutrino state is given by:

$$\frac{d|\nu_i\rangle}{dt} = -i\sum_j H_{ij}|\nu_j\rangle. \tag{2.2}$$

with the solution

$$|\nu_i(t)\rangle = \sum_j e^{-iH_{ij}t}|\nu_j(t=0)\rangle. \tag{2.3}$$

H is given in the mass basis by:

$$H_{ij} = \delta_{ij}(p^2 + m_i^2)^{\frac{1}{2}}. \tag{2.4}$$

In the limit where the neutrino mass is much smaller than its momentum ($m_i \ll p$), H can be approximated by:

$$H_{ij} \simeq \delta_{ij}(p + \frac{m_i^2}{2p}). \tag{2.5}$$

The transition matrix from an electroweak eigenstate α to an electroweak eigenstate β, $A_{\alpha\beta}(t)$, is computed by substituting the form of the Hamiltonian given in Eq. 2.5 into Eq. 2.3 and transforming from the mass eigenbasis to the electroweak eigenbasis:

$$|\nu_\beta\rangle = A_{\alpha\beta}(t)|\nu_\alpha\rangle \tag{2.6}$$

$$A_{\alpha,\beta}(t) = \sum_i U_{\alpha i}U_{i\beta}^\dagger \exp(-i\frac{m_i^2}{2p}t) \tag{2.7}$$

where the common phase ($-ipt$) has been suppressed. The probability that a neutrino produced in an electroweak eigenstate α will be observed in the electroweak eigenstate β after time t is given by the square of the transition matrix A:

$$P(\alpha \to \beta) = |A_{\alpha\beta}|^2. \tag{2.8}$$

While Eqs. 2.7 and 2.8 are exact for an arbitrary number of neutrinos, the solution for two neutrinos has a particularly simple and useful form. For two neutrinos, the

mixing matrix can be written in terms of a single mixing angle θ:

$$U = \begin{pmatrix} \cos\theta & \sin\theta \\ -\sin\theta & \cos\theta \end{pmatrix}. \tag{2.9}$$

Substituting this definition of U into Eq. 2.7 gives:

$$A(\nu_\mu \to \nu_\tau) = \cos\theta \sin\theta [\exp(-i\frac{\Delta m^2}{2p}t) - 1] \tag{2.10}$$

where the common phase $-im_1^2 t/2p$ has been suppressed and $\Delta m^2 \equiv m_2^2 - m_1^2$. The two electroweak eigenstates ν_μ and ν_τ have been chosen for the purposes of illustration. The transition probability is then given by

$$P(\nu_\mu \to \nu_\tau) = \cos^2\theta \sin^2\theta [\exp(-i\frac{\Delta m^2}{2p}t) - 1][\exp(i\frac{\Delta m^2}{2p}t) - 1] \tag{2.11}$$

which following some straight forward manipulations simplifies to

$$P(\nu_\mu \to \nu_\tau) = \sin^2 2\theta \sin^2\left(\frac{1.27\Delta m^2(\mathrm{eV}^2)L(\mathrm{km})}{E(\mathrm{GeV})}\right). \tag{2.12}$$

The time t has been replaced by the propagation distance L and the neutrino momentum has been replaced by its energy E. The factor, $1.27 = 10^3/(4\hbar c)$, results from the conversion from natural units to laboratory units.

Neutrino oscillations can only occur while there is sufficient overlap of the mass-state wave functions. The phase difference between the two wave functions will gradually increase with distance, eventually causing the wave functions to become incoherent and oscillations to cease. For a neutrino source localized to an interval δx, the coherence length is defined as the distance at which the neutrino states are

separated by an amount δx. Assuming that the mass states travel with velocities $v_1 = p_1/E_1$ and $v_2 = p_2/E_2$ this distance is given by [48]:

$$\begin{aligned} L_{coh} &\simeq \frac{\delta x}{(p_1/E_1 - p_2/E_2)}, \\ L_{coh} &= \frac{2E^2\delta x}{\Delta m^2} \end{aligned} \tag{2.13}$$

With $L_{osc} \equiv 4\pi E/\Delta m^2$, the maximum number of observable oscillation cycles is limited to:

$$N = L_{coh}/L_{osc} \simeq 10^{12} E(\text{MeV})\delta\text{x(m)} \tag{2.14}$$

This is typically an extremely large number of oscillations and is only relevant for neutrinos that travel astronomical distances. For example, taking $\Delta m^2 = 0.001$ eV^2 the coherence length for a neutrino source of $E = 10$ MeV localized to within $\delta x =$ 1 km is $L_{coh} \simeq 2\times 10^{20}$ m, roughly the distance to the galactic center. Given this large distance, terrestrial neutrino experiments are unaffected; however, loss of coherence may be important for studies of neutrinos from supernovae.

The vacuum solution for three neutrinos does not have a simple, closed form but can be computed numerically from Eqs. 2.7 and 2.8 once the mixing matrix is specified. The mixing matrix relating the three electroweak eigenstates to the three mass eigenstates can be parameterized in terms of three mixing angles θ_{12}, θ_{13}, and θ_{23}, and a single phase δ_{13} which breaks charge-parity (CP) conservation. A common form advocated by the Particle Data Group is:

$$U = \begin{pmatrix} c_{12}c_{13} & s_{12}c_{13} & s_{13}e^{-i\delta_{13}} \\ -s_{12}c_{23} - c_{12}s_{23}s_{13}e^{i\delta_{13}} & c_{12}c_{23} - s_{12}s_{23}s_{13}e^{i\delta_{13}} & s_{23}c_{13} \\ s_{12}s_{23} - c_{12}c_{23}s_{13}e^{i\delta_{13}} & -c_{12}s_{23} - s_{12}c_{23}s_{13}e^{i\delta_{13}} & c_{23}c_{13} \end{pmatrix} \tag{2.15}$$

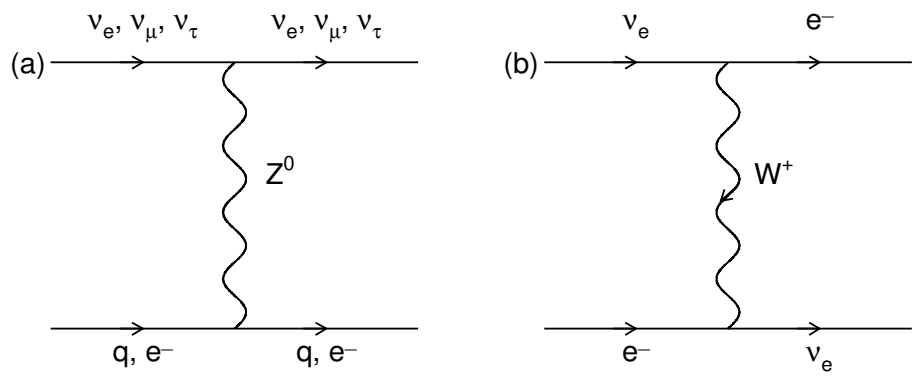

Figure 2.1: Feynman diagrams for forward scattering in matter. All non-sterile neutrino flavors experience interactions shown in (a), but only electron neutrinos experience those shown in (b).

where $c_{ij} = \cos\theta_{ij}$ and $s_{ij} = \sin\theta_{\alpha j}$.

2.2 Neutrino Oscillations in Matter

In matter, neutrino propagation is affected by charged-current and neutral-current forward scattering with electrons and quarks. The effects of matter on neutrino propagation were first treated by Wolfenstein [49] and Mikheyev and Smirnov [50] and hence are commonly referred to as MSW oscillations. The treatment presented here closely follows the formalism presented in Ref. [51] incorporating ideas in Refs. [48, 52]. The sign error in the effective matter Hamiltonian in the early literature on the subject (including Refs. [49, 50, 51]) has been corrected.

As neutrinos propagate through matter there is the possibility of forward scattering off nucleons (quarks) and electrons in matter. Figure 2.1 shows Feynman diagrams for these processes. These interactions are all identical for the three known neutrino flavors (e, μ, and τ) except for the charge-current forward scattering of electron neutrinos with electrons in matter. This interaction contributes to the effective

potential of electron neutrinos in matter:

$$H_{eff} = \pm\sqrt{2}G_F N_e \tag{2.16}$$

where the plus sign is taken for neutrinos and the minus sign is taken for anti-neutrinos, N_e is the electron number density, and G_F is Fermi's constant. In the mass basis, the effective Hamiltonian for a neutrino with energy E, assuming $p \gg m_i$ is:

$$H_{ij} = (m_i^2/2E)\delta_{ij} + \sqrt{2}G_F N_e U_{ie}^{\dagger} U_{ej}. \tag{2.17}$$

If one starts with a set of wave functions ψ_i which are pure mass eigenstates at time $t = 0$ ($\psi_i^{(j)}(t = 0) = \delta_{ij}$) and arranges these in a square matrix:

$$X_{ij} \equiv \psi_j^{(i)}(t), \tag{2.18}$$

then the time evolution of X_{ij} is given by:

$$idX_{ij}/dt = X_{ik}H_{kj}. \tag{2.19}$$

For constant N_e the Hamiltonian is time-independent and the evolution of X_{ij} is given by:

$$X_{ij}(t) = \left[\exp(-iHt)\right]_{ij}. \tag{2.20}$$

The transition matrix A is then given by transforming to the electroweak basis:

$$A(\nu_\alpha \to \nu_\beta) = \sum_{ij} U_{\alpha i} X_{ij} U_{j\beta}^{\dagger}. \tag{2.21}$$

Following Ref. [51], the matrix X can be written using LaGrange's formula:

$$X = \sum_k \left[\prod_{j \neq k} \frac{(2EH - M_j^2 1)}{\delta M_{kj}^2} \right] \exp(-i \frac{M_k^2 L}{2E}), \tag{2.22}$$

where $M_i/2E$ are the eigenvalues of H and $\delta M_{ij}^2 \equiv M_j^2 - M_i^2$.

2.2.1 Results For Two Flavors

Active Neutrinos

Again the solution for two-flavor (labeled by e and α) neutrino oscillation has a simple form. Taking the vacuum mass differences and mixing matrix as in Eq.2.9 the Hamiltonian is given by:

$$H = \begin{pmatrix} \frac{m_1^2}{2E} + \sqrt{2} G_F N_e \cos^2\theta & \sqrt{2} G_F N_e \sin\theta\cos\theta \\ \sqrt{2} G_F N_e \sin\theta\cos\theta & \frac{m_2^2}{2E} + \sqrt{2} G_F N_e \sin^2\theta \end{pmatrix} \tag{2.23}$$

in the mass-eigenbasis. The Hamiltonian in Eq. 2.23 can be diagonalized by choosing eigenvectors of the form

$$\begin{aligned} \nu_1^{'} &= \nu_e \cos\theta_M - \nu_\alpha \sin\theta_M \\ \nu_2^{'} &= \nu_e \sin\theta_M + \nu_\alpha \cos\theta_M \end{aligned} \tag{2.24}$$

with the matter mixing angle θ_M given by:

$$\sin^2 2\theta_M = \frac{\sin^2 2\theta}{[\xi - \cos 2\theta]^2 + \sin^2 2\theta}. \tag{2.25}$$

The difference in the squares of the eigenvalues of H is:

$$\Delta M^2 = \Delta m^2 \left([\xi - \cos 2\theta]^2 + \sin^2 2\theta \right)^{\frac{1}{2}}, \tag{2.26}$$

where

$$\xi = 2\sqrt{2} G_F N_e \frac{E}{\Delta m^2}. \tag{2.27}$$

The solution can then be written in a form similar to that for vacuum oscillations:

$$P(\nu_e \to \nu_e) = 1 - \sin^2 2\theta_M \sin^2 \left(\frac{1.27 \Delta M^2 L}{E} \right). \tag{2.28}$$

At very low matter densities ($\xi \ll 1$) the vacuum solution ($\sin^2 2\theta_M = \sin^2 2\theta, \Delta M^2 = \Delta m^2$) is recovered. At high densities ($\xi \gg 1$) oscillations are suppressed by $1/\xi^2$. Resonant enhancement of the transition probability occurs with $\sin^2 \theta_M = 1$ when $\xi = \cos 2\theta$. In terms of $E/\Delta m^2$ this gives:

$$\frac{E(\text{GeV})}{|\Delta m^2|(\text{eV}^2)} = \frac{6.55 \times 10^3}{\frac{Z}{A} \rho(\text{g/cm}^3)} \cos 2\theta. \tag{2.29}$$

Resonant conversion of neutrinos is only possible if $\Delta m^2 > 0$ and for anti-neutrinos if $\Delta m^2 < 0$. Figure 2.2 shows the dependence of $\sin^2 2\theta_M$ on the ratio $E/|\Delta m^2|$ and Fig. 2.3 plots the transition probabilities as a function of $E/|\Delta m^2|$ for various matter densities.

Sterile Neutrinos

Sterile neutrinos by definition have no weak interactions. In matter, sterile neutrinos do not participate in any of the interactions diagrammed in Fig. 2.1 and hence there is an effective potential difference that separates active and sterile neutrinos in matter.

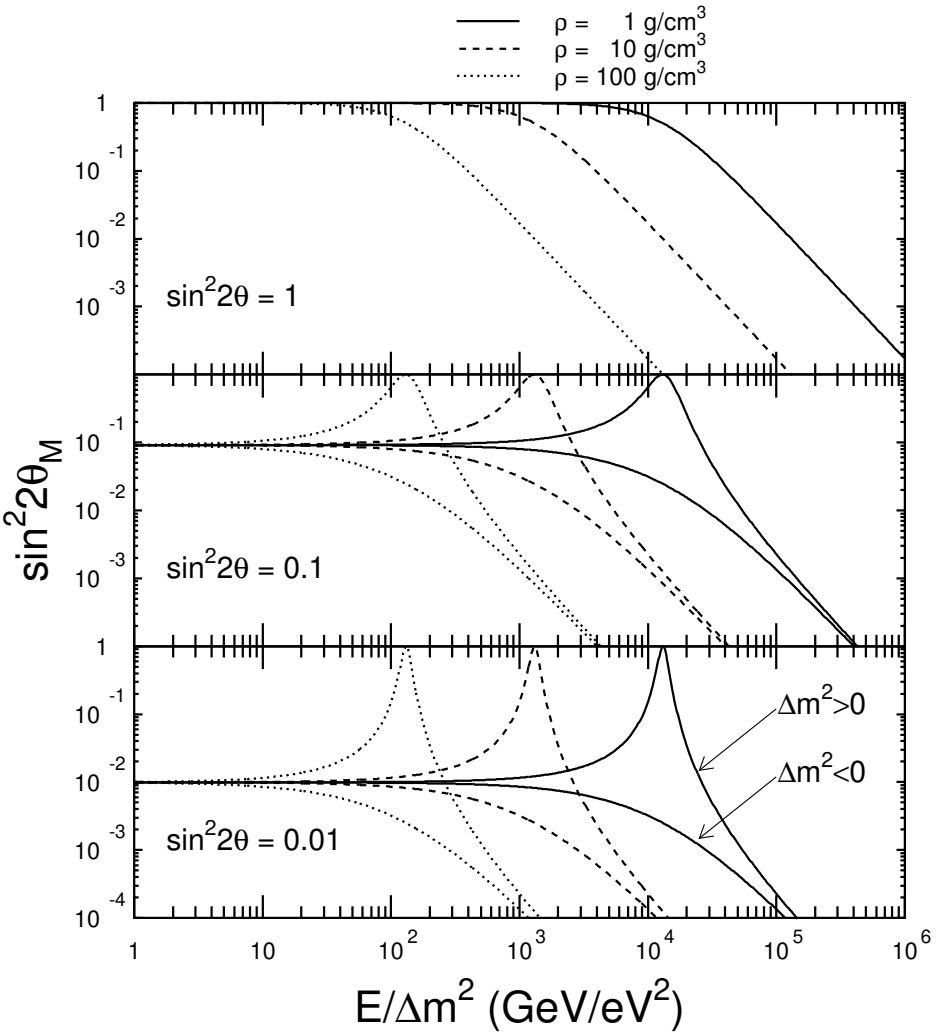

Figure 2.2: The neutrino mixing angle for various matter densities is plotted as a function of the ratio of the neutrino energy to vacuum mass-squared difference for $\nu_\mu \leftrightarrow \nu_e$ oscillations.

Following Ref.[52]

$$H_{eff} = \mp G_F \frac{N_n}{2} = \mp 3.814 \times 10^{-4} \frac{\mathrm{eV}^2}{\mathrm{GeV}} \rho(\mathrm{g\ cm}^{-3})(1 - \frac{Z}{A}), \tag{2.30}$$

where the minus sign is taken for neutrinos, the plus sign is taken for anti-neutrinos, N_n is the neutron density in matter, ρ is the mass density, and $(1-Z/A)$ is the neutron

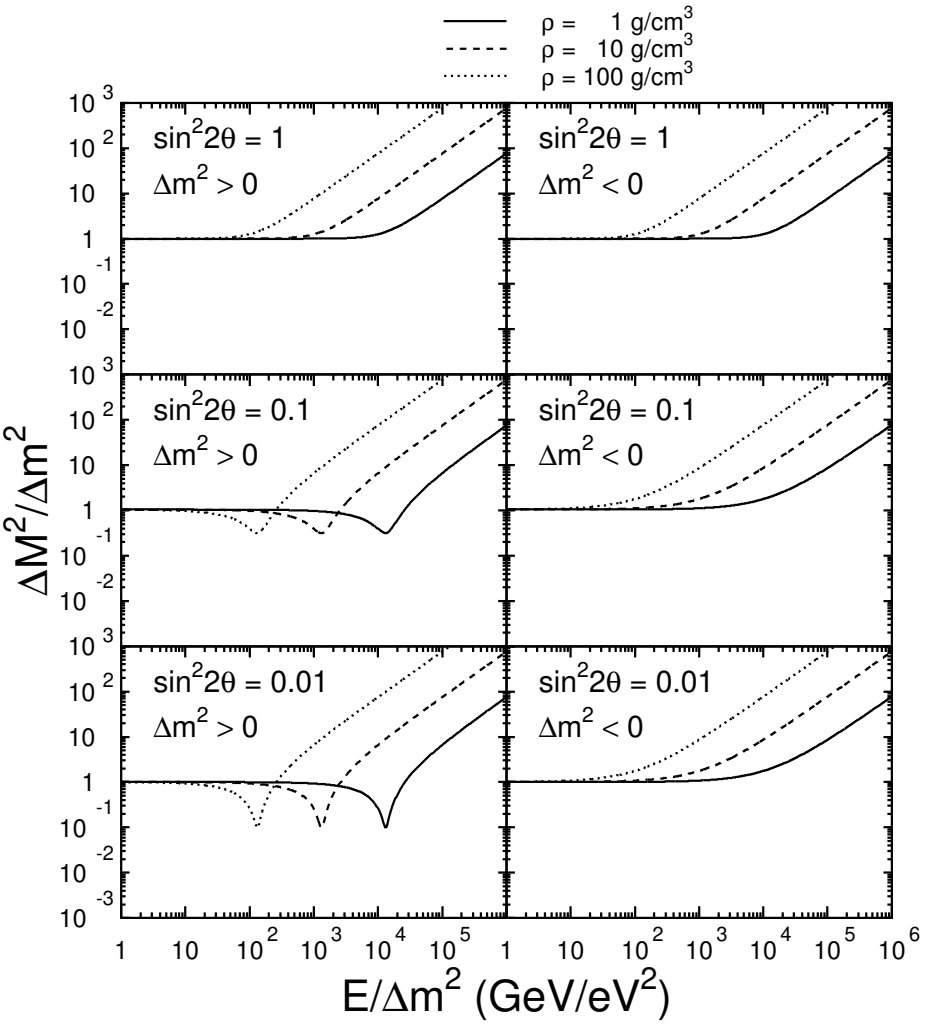

Figure 2.3: The effective mass-squared differences for two neutrinos for various matter densities and neutrino energies.

fraction. The solution follows that for active neutrinos above with the replacement $N_e \to -N_n/2$.

2.2.2 Results For Three Active Flavors

The solution for three-flavor (e, μ, τ) neutrino propagation in matter of constant density has been solved in Ref.[51]. Incorporating the sign correction in more recent

references, the eigenvalues of the three-flavor Hamiltonian are given by:

$$M_i^2 = -\frac{2}{3}(\alpha^2 - 3\beta^2)^{1/2} \cos\left[\frac{1}{3}\arccos(\frac{2\alpha^3 - 9\alpha\beta + 27\gamma}{2(\alpha^2 - 3\beta)^{3/2}})\right] + m_1^2 - \alpha/3, \qquad (2.31)$$

with

$$\begin{aligned}
\alpha &= -2\sqrt{2}EG_F N_e + \Delta m_{12}^2 + \Delta m_{13}^2, & (2.32)\\
\beta &= \Delta m_{12}^2 \Delta m_{13}^2 - 2\sqrt{2}EG_F N_e \times \\
&\quad \left[\Delta m_{12}^2(1 - |U_{e2}|^2) + \Delta m_{13}^2(1 - |U_{e3}|^2)\right], & (2.33)\\
\gamma &= -2\sqrt{2}EG_F N_e \Delta m_{12}^2 \Delta m_{13}^2 |U_{e1}^2|. & (2.34)
\end{aligned}$$

The three values of M_i^2 are provided by the three roots of $\cos(\frac{1}{3}\arccos)$ and the mixing matrix U can be parameterized as in Eq. 2.15. Again the transition amplitudes only depend on the the mass-squared differences $\Delta m_{ij}^2 \equiv m_j^2 - m_i^2$, $M_j^2 - M_i^2$ and $M_j^2 - m_i^2$. In general six parameters ($\theta_{12}, \theta_{23}, \theta_{13}, \delta_{13}, \Delta m_{12}^2$ and Δm_{23}^2) are required to specify the three neutrino oscillation solution. In principle, the expressions for M_i^2 can be substituted in Eqs. 2.21 and 2.22 to obtain the matrix of transition amplitudes A and transition probabilities $P_{\alpha\beta}$, however, the resulting expressions are algebraically opaque. A and $P_{\alpha\beta}$ are easily computed numerically, however. Figures 2.4 and 2.5 demonstrate the results of these calculations for the case of three-fold maximal neutrino mixing ($\theta_{12} = \pi/4, \theta_{23} = \pi/4, \theta_{13} = \arcsin(\sqrt{3}/3), \delta_{13} = \pi/2$) with $\Delta m_{12}^2 = 2 \times 10^{-5}$ eV^2 and $\Delta m_{23}^2 = 5 \times 10^{-3}$ eV^2 for fixed matter densities of 3 and 10 g/cm^3. The figures use a fixed neutrino flight distance of 1000 km. In each case there is a suppression of the ν_e oscillation probability with respect to the vacuum oscillation calculation, with larger densities causing greater suppression.

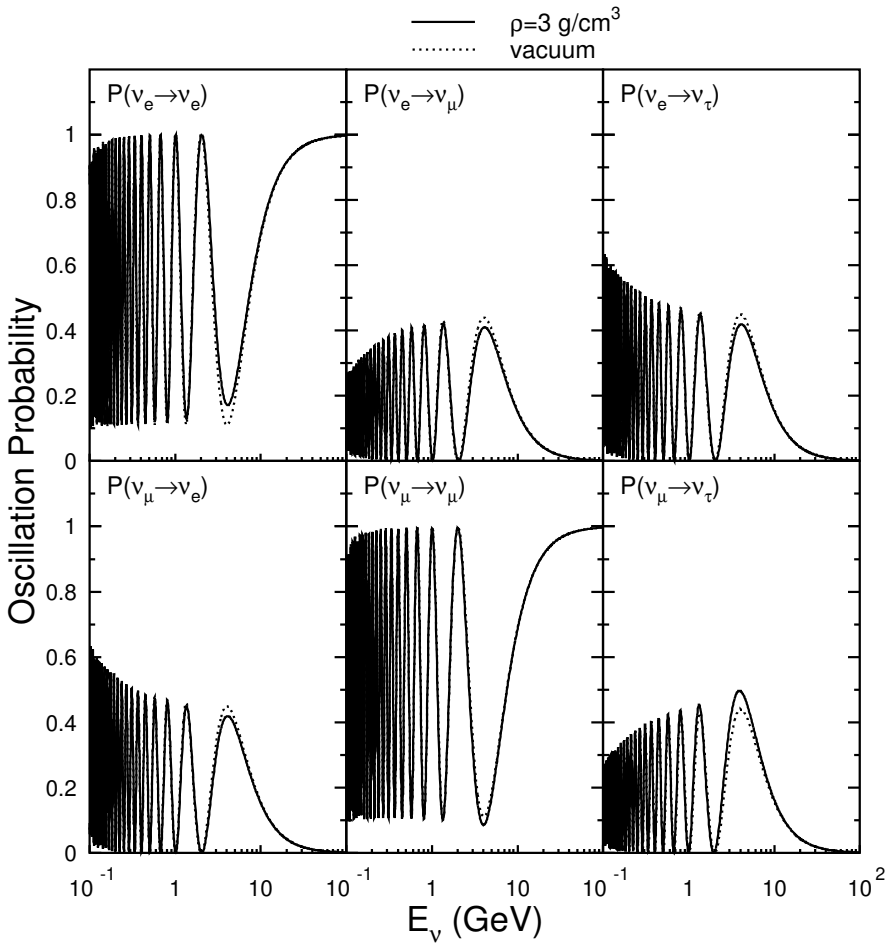

Figure 2.4: Oscillation probabilities as a function of energy for neutrinos crossing a 1000 km thick slab of matter with a density of 3 g/cm^3 under the assumption of three-fold maximal mixing and $\Delta m^2_{12} = 2 \times 10^{-5}$ eV^2 and $\Delta m^2_{23} = 5 \times 10^{-3}$eV^2. Dotted curves show the oscillation probabilities for zero matter density.

Matter effects become important for neutrino oscillation calculations when

$$1.5 \times 10^{-4} \frac{E(\mathrm{GeV}) N_e(\mathrm{mole/cm^3})}{\Delta m^2(\mathrm{eV}^2)} \simeq 1. \tag{2.35}$$

The largest matter density encountered by atmospheric neutrinos is $\sim$12 g/cm^3 ($N_e \simeq$

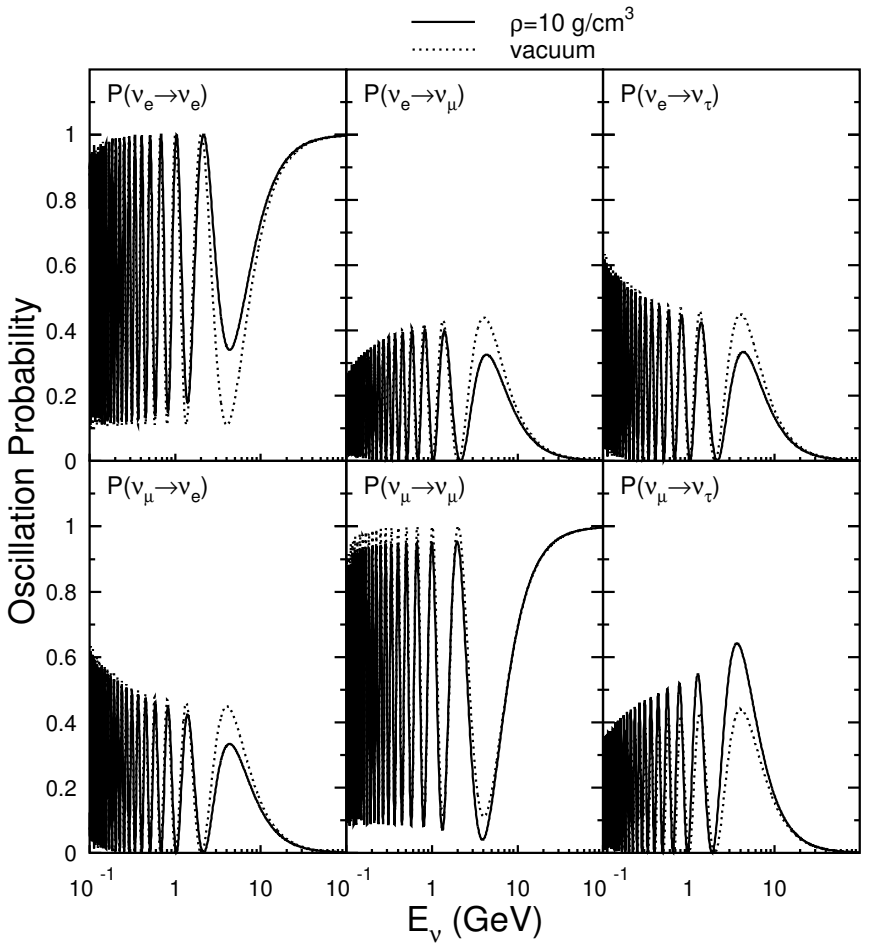

Figure 2.5: Oscillation probabilities for neutrinos crossing a 1000 km thick slab of matter with a density of 10 g/cm^3 under the assumption of three-fold maximal mixing and $\Delta m^2_{12} = 2 \times 10^{-5}$ eV^2 and $\Delta m^2_{23} = 5 \times 10^{-3}$eV^2. Dotted curves show the oscillation probabilities for zero matter density.

6 mole/cm^3). For Δm^2 in the range 10^{-3} eV^2 – 10^{-2} eV^2 matter effects begin to become noticeable at neutrino energies of roughly 1 GeV and are significant at energies above 5 GeV.

Chapter 3

Experimental Searches for Neutrino Oscillations

Several neutrino sources have been used in searches for neutrino oscillations. These include neutrinos from nuclear reactors, accelerators, as well as neutrinos produced naturally in the Sun and atmosphere. In this section, I briefly summarize these searches.

3.1 Solar Neutrino Experiments

The Sun is powered by nuclear fusion and is a tremendous source of neutrinos of keV-MeV energies. The solar neutrino fluxes predicted in Ref. [54] are shown in Fig. 3.1. Solar neutrinos have been observed since 1968 starting with the ground-breaking Homestake experiment [19, 55]. The Homestake experiment observes solar neutrinos via the interaction $\nu_e + {}^{37}\mathrm{Cl} \rightarrow e^- + {}^{37}\mathrm{Ar}$. Following a $\sim$2 month exposure of a large volume of highly purified C_2Cl_4 the Ar is chemically extracted, and the solar neutrino flux is inferred from the number of Ar produced during the exposure time. Later radio-chemical experiments, SAGE [56, 57] and GALLEX [58, 59], used the

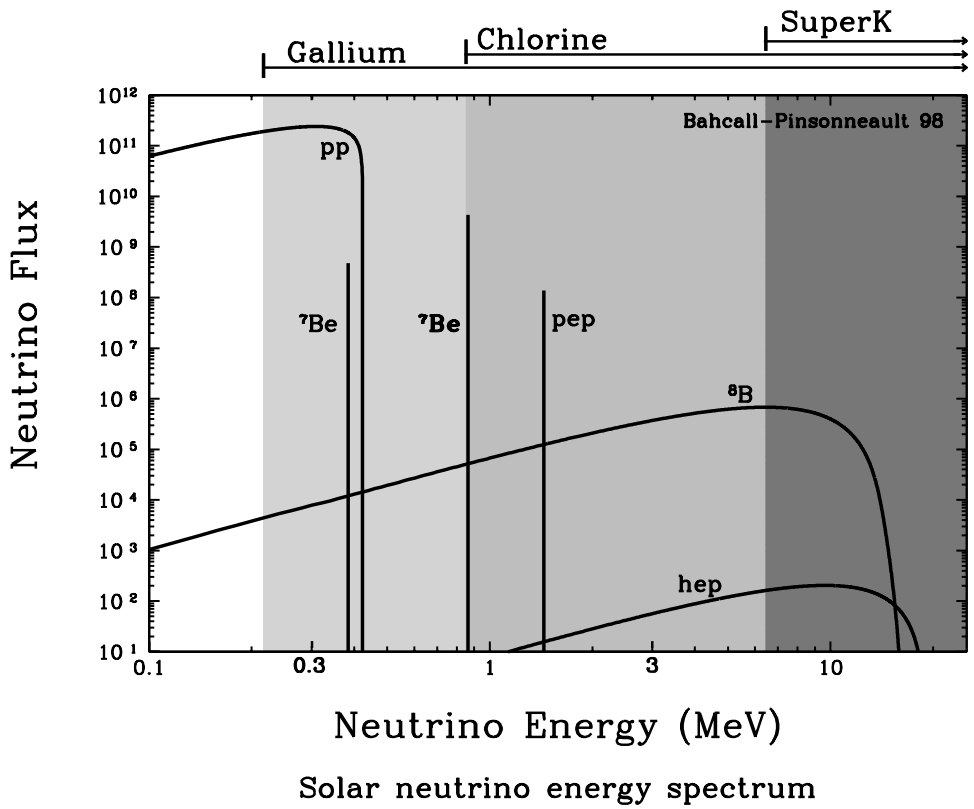

Figure 3.1: The solar neutrino spectrum with experimental thresholds. [53]

interaction $\nu_e + {}^{71}\mathrm{Ga} \rightarrow e^- + {}^{71}\mathrm{Ge}$. Following an exposure of roughly 2 weeks the Ge is extracted and counted. The water Cherenkov experiments Kamiokande [60, 61] and Super-Kamiokande [62, 63] observed solar neutrinos via $\nu_e + e^- \rightarrow \nu_e + e^-$. Because the final state electron direction is correlated with the initial neutrino direction this interaction produces a peak in the direction of the Sun as shown in Fig. 3.2. In this way, the Kamiokande experiment was the first to clearly establish the Sun as the source of the observed neutrinos. Each solar neutrino experiment mentioned observes a significant deficit of solar neutrinos relative to the predicted rates. The observed solar neutrino rates, summarized in Table 3.1, are not consistent with any solar model [64] and the observed deficits of solar neutrinos have been attributed to neutrino oscillations. The world solar neutrino data has been fit to neutrino

Experiment	Threshold (MeV)	Measurement/Prediction
Homestake [55]	0.81	$0.33^{+0.06}_{-0.05}$
GALLEX [59]	0.233	0.60 ± 0.07
SAGE [57]	0.233	0.52 ± 0.07
Kamiokande [61]	~ 7	0.54 ± 0.07
Super-Kamiokande [62]	~ 6.5	$0.47^{+0.07}_{-0.09}$

Table 3.1: Summary of solar neutrino flux measurements. The predicted fluxes are based on the solar model calculations in Ref. [54].

Solution	$\sin^2 2\theta$	Δm^2	C.L.
Small Mixing Angle (SMA)	6×10^{-3}	5×10^{-6}	19%
Large Mixing Angle (LMA)	0.76	2×10^{-5}	4%
Vacuum Oscillations	0.75	8×10^{-11}	3.8%
"LOW" region	0.96	8×10^{-8}	0.7%

Table 3.2: Summary of solutions to the world solar neutrino data [66].

oscillations by several authors (for example Refs. [65, 66]). There are four regions in $\sin^2 2\theta$ - Δm^2 space which can explain the observed solar neutrino deficits. Matter effects in the Sun are crucial to the solutions with $\Delta m^2 \sim 10^{-5}$ eV^2 with significant regeneration of ν_e in the Earth expected for large mixing angle. The solution near $\Delta m^2 \sim 10^{-10}$ eV^2 relies only on vacuum oscillations. These solutions are summarized in Table 3.2.

3.2 Reactor Experiments

At nuclear power reactors, $\bar{\nu}_e$'s are produced in the fission of ^{235}U, ^{238}U, ^{239}P, and ^{241}Pu with a mean energy of $\sim$ 3 MeV. The anti-neutrinos are detected based on the reaction $\bar{\nu}_e + p \rightarrow e^+ + n$. Detectors are typically placed 10's of meters up to 1 km from the reactor core and search for disappearance of $\bar{\nu}_e$ giving a sensitivity to oscillations with Δm^2 down to $\sim 10^{-3}$ eV^2.

The Gösgen [67] experiment measured the $\bar{\nu}_e$ rate in three detectors placed 37.9,

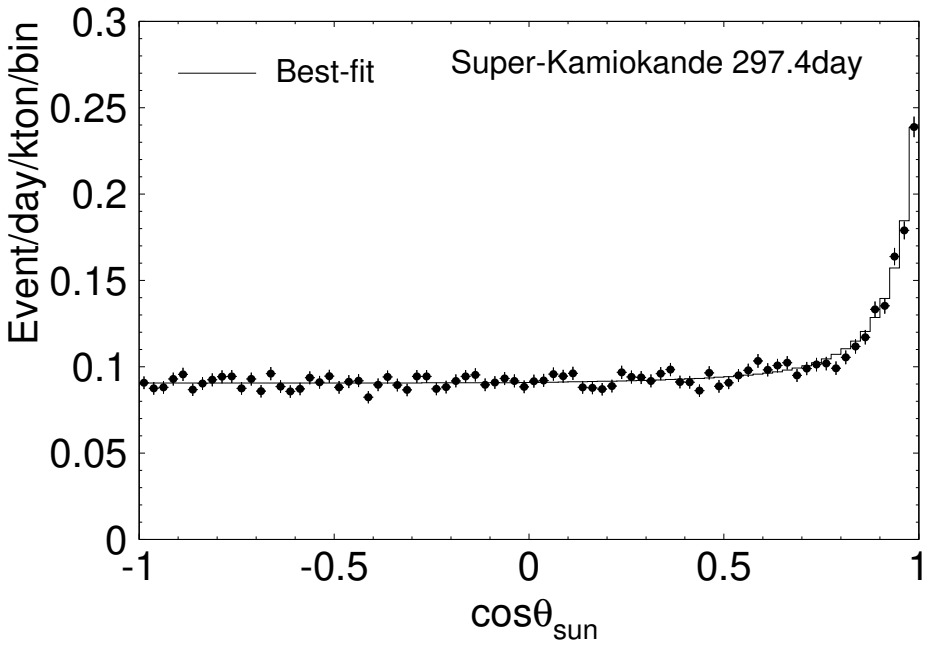

Figure 3.2: The solar neutrino peak as measured by Super–Kamiokande [62]. The best-fit requires 47% suppression of the expected flux as calculated in Ref. [54]

45.9, and 64.7 m from the reactor core. Based on a comparison of the neutrino spectra at each distance, no evidence for oscillations was found, excluding a region of parameter space extending down to 2×10^{-2} eV^2 for $\sin^2 2\theta = 1$ and $\sin^2 2\theta > 0.2$ for $\Delta m^2 > 5$ eV^2. The Bugey [68] experiment also used three detectors, placed at 15, 40 and 95 m from the nuclear core. No evidence for spectral distortions was found in the three detectors, excluding a large range of oscillation parameter space with $\Delta m^2 > 10^{-2}$ eV^2 and $\sin^2 2\theta > 2 \times 10^{-2}$ at 90% confidence level (CL).

The most sensitive reactor neutrino oscillation experiment was carried out by the CHOOZ [69] collaboration. Using a detector placed in a tunnel 1 km from the reactor core, the CHOOZ experiment (completed in 1998) searched for evidence of oscillations by comparing the measured $\bar{\nu}_e$ spectrum with the expected spectrum. No evidence for spectral distortion was found, excluding a region of oscillation parameter

space down to 0.9×10^{-3} eV^2 for $\sin^2 2\theta = 1$ and $\sin^2 2\theta > 0.18$ for large Δm^2.

3.3 Accelerator Experiments

Neutrinos are produced at accelerators from the decay of pions produced from collisions of protons with a target. Proton beam energies are typically $1 - 10$ GeV producing neutrinos of GeV and MeV energies. The dimensions of the experiments are less than 1 km making typical accelerator-based experiments sensitive down to $\Delta m^2 \sim 0.1$ eV^2.

Experiment E-776 at Brookhaven National Lab sought evidence of $\nu_\mu \leftrightarrow \nu_e$ oscillations by searching for ν_e and $\bar{\nu}_e$ appearance 1 km from the neutrino source. The detector used planes of proportional drift tubes interlaced with concrete absorber. No oscillations were found setting the limits $\Delta m^2 < 0.075$ eV^2 for maximal mixing and $\sin^2 2\theta < 0.003$ for large Δm^2 [70].

At Fermilab, the E-531 collaboration sought evidence for oscillations of $\nu_e \leftrightarrow \nu_\tau$ and $\nu_\mu \leftrightarrow \nu_\tau$ using an emulsion spectrometer to search for τ decays. No candidates were found [71, 72, 73].

Several neutrino oscillation searches have been conducted at CERN. These are:

- CDHSW [74], which used two detectors placed 130 m and 885 m from the neutrino source to search for oscillations of ν_μ. No evidence was found excluding the region $0.26 < \Delta m^2 < 90$ eV^2.

- CHARM [75], which searched for $\nu_\mu \leftrightarrow \nu_e$ as well as $\nu_\mu \leftrightarrow \nu_\tau$ oscillations by looking for ν_e appearance and by comparing the relative ν_μ fluxes at two detectors placed at 123 m and 903 m from the neutrino source. Limits are $\Delta m^2 < 0.20$ eV^2 for $\nu_\mu \leftrightarrow \nu_e$, and $\Delta m^2 < 0.29$ eV^2 for $\nu_\mu \leftrightarrow \nu_x$, assuming

maximal mixing in both cases.

- CHORUS [76], which used a hybrid detector primarily consisting of a 770 kg nuclear emulsion target to search for τ appearance. No candidates have been found excluding a large region of parameter space for $\nu_\mu \leftrightarrow \nu_\tau$ oscillations with $\Delta m^2 > 1$ eV^2.

- NOMAD [77], which looked for evidence for the decay $\tau^- \rightarrow e^- \bar{\nu}_e \nu_\tau$ as well as other τ decay modes. The detector consists of a series of drift chambers surrounded by a dipole magnet. No oscillations have been found limiting neutrino oscillations of $\nu_\mu \leftrightarrow \nu_\tau$ to $\sin^2 2\theta < 4.2 \times 10^{-3}$ for large Δm^2 and $\Delta m^2 < 1.5$ eV^2 for large mixing angle.

The Liquid Scintillator Neutrino Detector (LSND) at the Los Alamos Meson Physics Facility has reported evidence for appearance of ν_e and $\bar{\nu}_e$ from pure beams of ν_μ and $\bar{\nu}_\mu$. Using a beam of ν_μ produced through the collisions of protons on a water target LSND has used beams produced both by pion decay in flight (DIF): $\pi^+ \rightarrow \mu^+ + \nu_\mu$, and anti-neutrinos produced by the decay at rest (DAR): $\mu^+ \rightarrow e^+ + \nu_e + \bar{\nu}_\mu$. Electron anti-neutrinos are detected via the interaction $\bar{\nu}_e + p \rightarrow e^+ + n$ in correlation with a 2.2 MeV γ from neutron capture $n + p \rightarrow d + \gamma$. Electron neutrinos are detected via ν_e+C$\rightarrow e^-$+C. The neutrino energies produced from DAR range from 20 to 60 MeV while those produced from DIF range between 60 and 200 MeV; neutrino flight distances are roughly 30 m. The experiment reports an excess of $51^{+18.8}_{-16.9}$ in the DAR beam and 21.9 ± 2.1 in the DIF beam. Taken together with excluded regions obtained by other accelerator experiments, these excesses imply neutrino oscillations with $\Delta m^2 \sim 1$ eV^2 and $\sin^2 2\theta \sim 10^{-2}$ [78].

The evidence for neutrino oscillations reported by LSND has not been confirmed. The Karlsruhe Rutherford Medium Energy Neutrino experiment (KARMEN) also

uses liquid scintillator to search for ν_e appearance from a beam of ν_μ produced by muon decay at rest in a detector located at a distance of 17.7 m from the neutrino source. KARMEN has found no evidence for ν_e appearance above the expected background and excludes a region of oscillation parameter space at the edge of the LSND allowed region [79]. Confirmation of the LSND and KARMEN results will be pursued at Fermilab by the MiniBooNE experiment.

3.4 Atmospheric Neutrino Experiments

Several experiments have undertaken measurements of the flavor content of the atmospheric neutrino fluxes. Atmospheric neutrinos are produced from the decays of pions produced when primary cosmic rays strike the upper atmosphere. The spectrum of these neutrinos peaks at $\sim$ 1 GeV and extends to 100's of GeV. The neutrino flight distances vary from 15 km for neutrinos produced directly above the detector, to 13,000 km for neutrinos produced on the opposite side of the Earth, making measurements of atmospheric neutrinos sensitive to Δm^2 down to 10^{-5} eV^2. While the predicted total flux of atmospheric neutrinos is $\sim$ 20% uncertain, the $(\nu_\mu + \bar{\nu}_\mu)/(\nu_e + \bar{\nu}_e)$ ratio is predicted with only 5% uncertainty. This ratio has been measured by several underground experiments. To help interpret the results and cancel systematic uncertainties, these measurements are compared to expectations based on detailed Monte Carlo simulations. The experiments frequently report a "double ratio" $R \equiv (N_\mu/N_e)_{DATA}/(N_\mu/N_e)_{MC}$ where N_μ is the number of ν_μ induced interactions (referred to as "μ-like" or "tracks") and N_e is the number of ν_e induced interactions (referred to as "e-like" or "showers"). R values obtained by several underground water Cherenkov([40], [41, 44],[45, 46, 47]) and iron-calorimeter detectors ([42, 43, 80]) are summarized in Fig. 3.3. All the high-statistics experiments measure

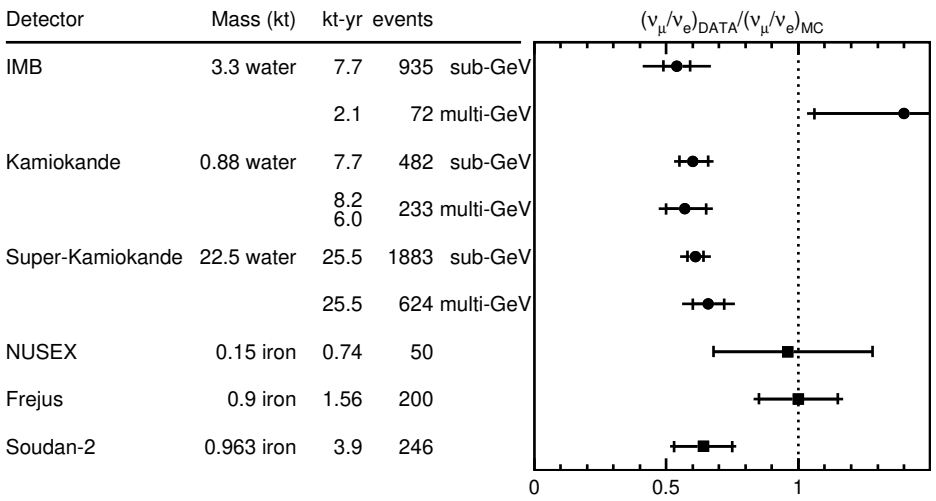

Figure 3.3: Summary of atmospheric neutrino R measurements [41, 40, 47, 43, 42, 80]. In each case the inner error is statistical and the outer error includes the estimated systematic uncertainties.

R values significantly lower than one. Early concerns that the atmospheric neutrino anomaly was only present in the water Cherenkov detectors have been answered by the iron-calorimeter experiment Soudan 2 which also sees an anomaly.

In addition to low values of R, the Kamiokande experiment measured a zenith angle dependence of R in the "multi-GeV" (average parent neutrino energy > 1 GeV) range; no dependence was observed in the "sub-GeV" energy range [44]. The Kamiokande measurements of R versus cosine zenith angle are plotted in Fig. 3.4. Because the neutrino flight distance varies with zenith angle, these measurements suggested that neutrino oscillations could explain the atmospheric neutrino anomaly. The observed zenith angle and momentum distributions of the e- and μ-like events were consistent with both oscillations of $\nu_\mu \leftrightarrow \nu_e$ and $\nu_\mu \leftrightarrow \nu_\tau$ with $\sin^2 2\theta \sim 1$ and

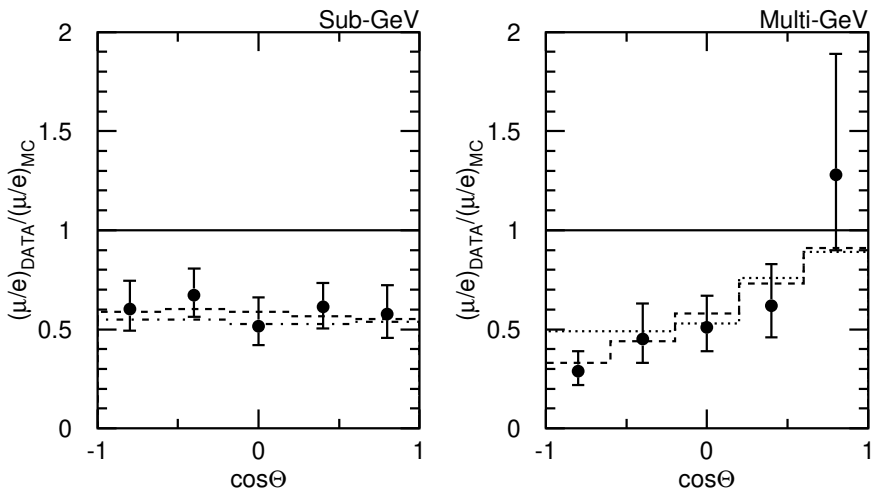

Figure 3.4: The $(\mu/e)_{DATA}/(\mu/e)_{MC}$ as a function of cosine zenith angle for the Kamiokande sub-GeV and multi-GeV samples. Dashed curve for sub-GeV is the expectation for best-fit oscillations to the combined sub-GeV and multi-GeV samples, the dot-dashed curve is for best-fit to the sub-GeV sample alone. In the right panel, the dashed curve is the best-fit oscillation expectation for $\nu_\mu \leftrightarrow \nu_e$ oscillations and the dotted curve is for best fit $\nu_\mu \leftrightarrow \nu_\tau$ ($\sin^2 2\theta = 1$, $\Delta m^2 = 0.01$ eV^2) oscillations [44].

$\Delta m^2 \sim 10^{-2}$ eV^2 and the Kamiokande experiment published the allowed regions in Figs. 3.6 and 3.7.

Measurements of upward-going muons produced by interactions of high energy atmospheric neutrinos with the rock below the detector have been published by the IMB [81], Baksan [82], Kamiokande [83], MACRO [84], and Super-Kamiokande [85] experiments. These measurements are sensitive to ν_μ disappearance due to neutrino oscillations. The IMB measurement of the ratio of stopping muons to through-going muons was consistent with expectations and excluded a region of oscillation parameter space with large mixing and $10^{-3} < \Delta m^2 < 10^{-2}$ eV^2. Re-analysis of the IMB results using revised cross-sections and neutrino fluxes lessen the confidence level at which oscillations can be excluded, but only slightly [86]. Other measurements,

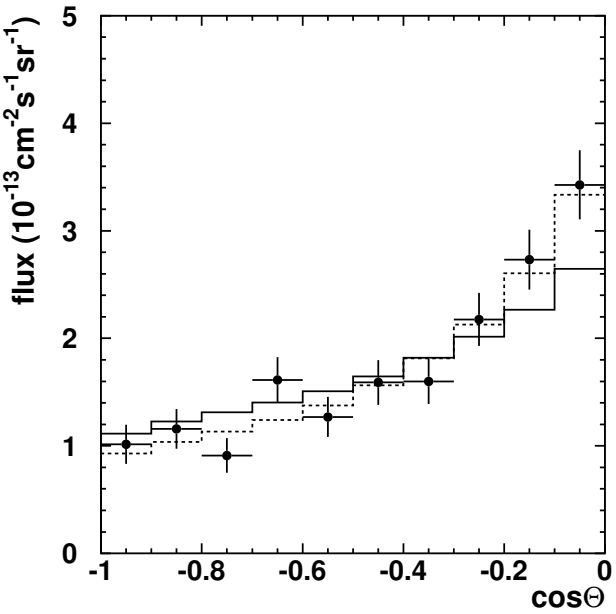

Figure 3.5: Rates of neutrino-induced upward-going muons in Super–Kamiokande [85]. Solid curve is the predicted flux with the best-fit -10% normalization factor applied. The dashed curve is the best-fit expectation for $\nu_\mu \to \nu_x$ oscillations with $\Delta m^2 = 3.5 \times 10^{-3}$ eV^2 and $\sin^2 2\theta = 1$ with a $+8\%$ normalization to the total flux applied.

however, observe a deficit of upward-going muons and a distortion of the zenith angle distributions consistent with neutrino oscillations of ν_μ to ν_x where ν_x is ν_e, ν_μ, or $\nu_{sterile}$ with $\Delta m^2 \sim 10^{-2}$ – 10^{-3} eV^s and maximal mixing. The Super-Kamiokande upward-going muon zenith angle rates, shown in Fig. 3.5, are well fit to neutrino oscillations with $\sin^2 2\theta > 0.4$ and $1 \times 10^{-3} < \Delta m^2 < 5 \times 10^{-3}$ eV^2 [85] in good agreement with the results presented in this dissertation based on the sub-GeV and multi-GeV data samples.

3.5 Summary of Neutrino Oscillation Searches

The results of searches for neutrino oscillations discussed above are summarized in Fig. 3.6 ($\nu_\mu \leftrightarrow \nu_e$, and $\nu_e \leftrightarrow \nu_x$) and Fig. 3.7 ($\nu_\mu \leftrightarrow \nu_\tau$ and $\nu_\mu \leftrightarrow \nu_x$). The three positive signals for neutrino oscillations are from observations of atmospheric neutrinos, solar neutrinos and the DIF and DAR signals from the LSND experiment. The observations of atmospheric neutrinos have been confirmed by several experiments. Solar neutrino deficits are also observed by several experiments using different techniques and with different thresholds. The observations, however, point to several possible solutions. The observation by LSND of ν_e appearance from ν_μ has not been confirmed, but there is currently no other experiment that can exclude the entire LSND allowed region.

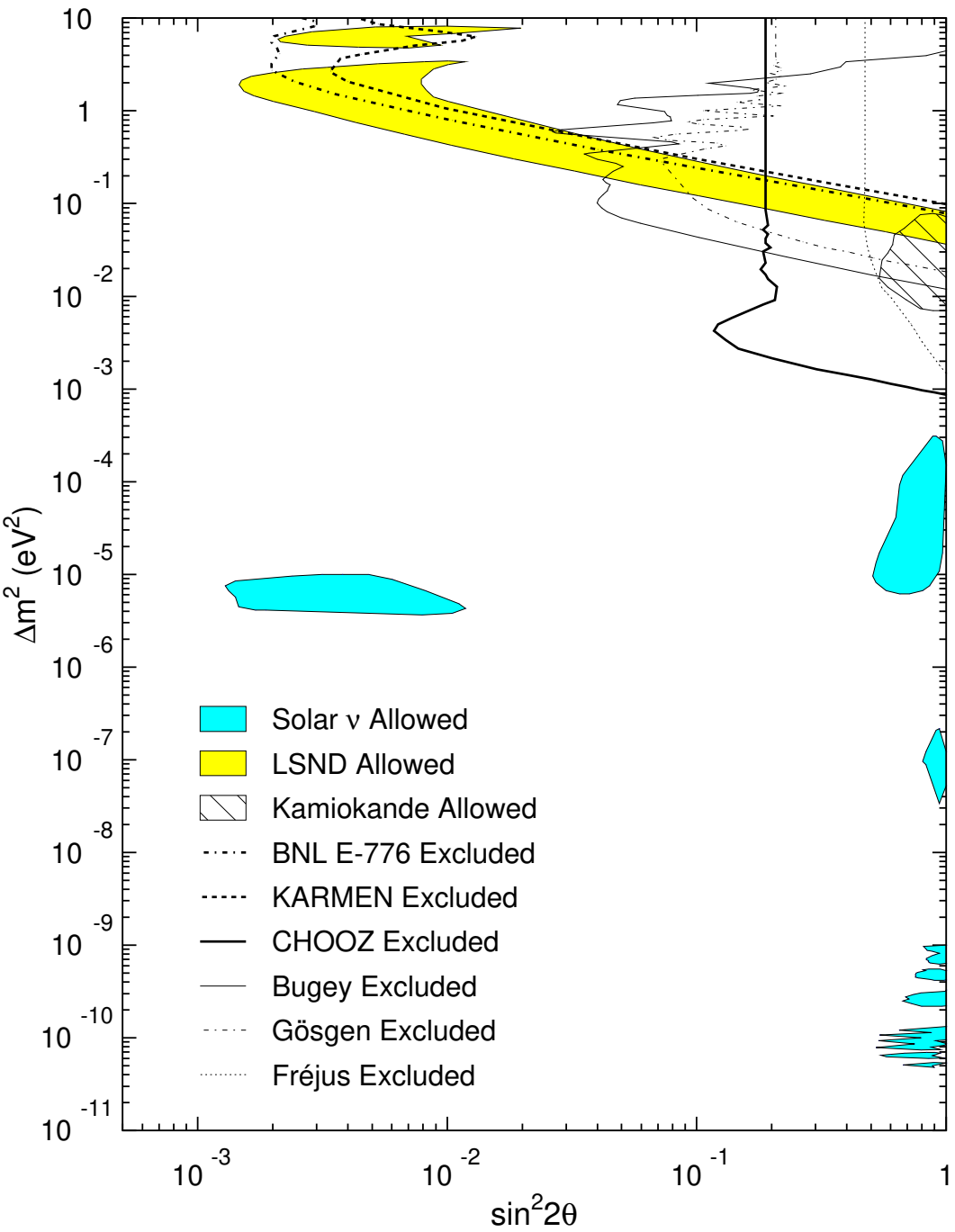

Figure 3.6: Allowed and excluded regions of parameter space for $\nu_\mu \leftrightarrow \nu_e$ neutrino oscillations. In each case, the excluded regions lie to the right of the curves. References are given in the text.

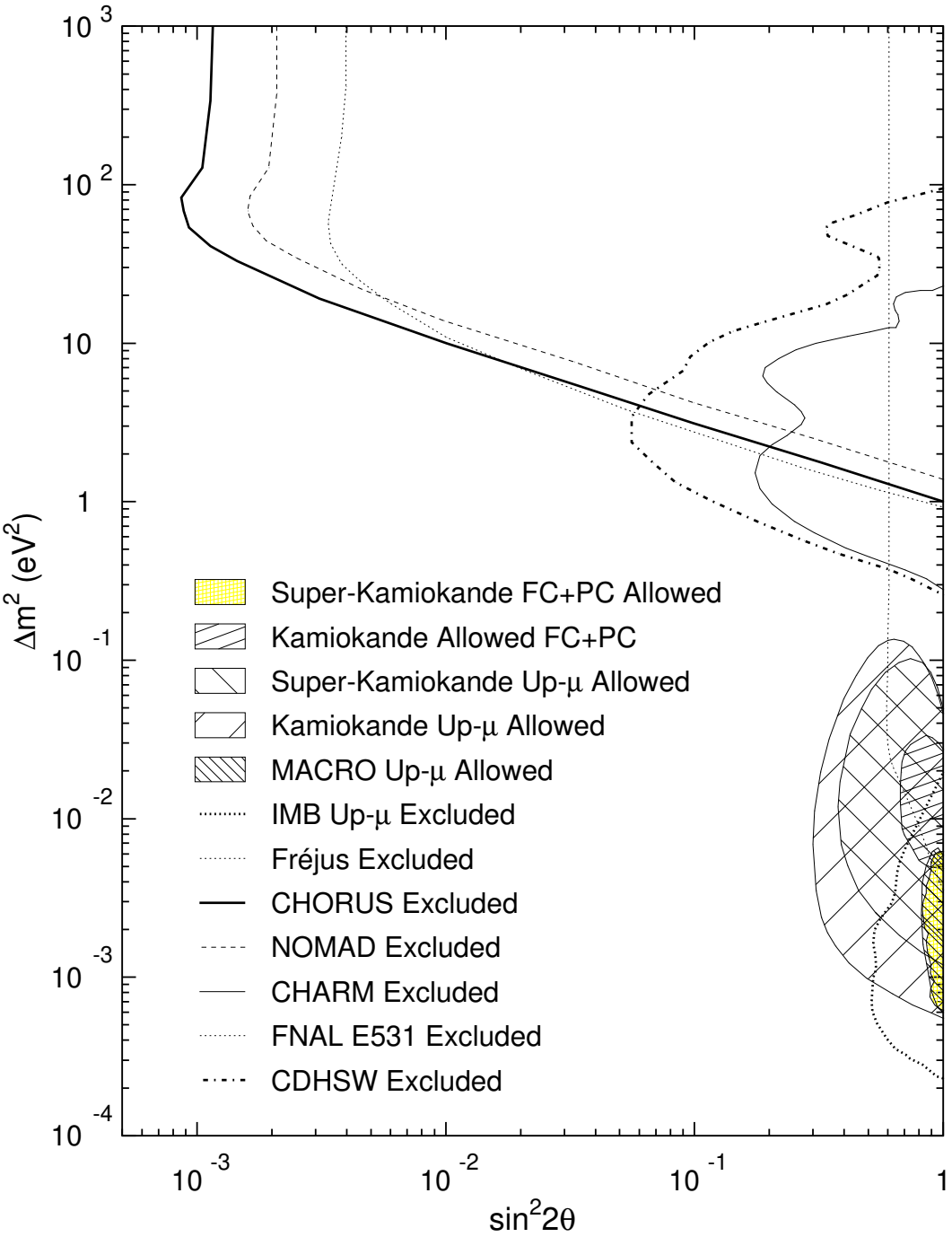

Figure 3.7: Allowed and excluded regions of parameter space for $\nu_\mu \leftrightarrow \nu_\tau$ neutrino oscillations. In each case, the excluded regions lie to the right of the curves. References are given in the text.

Chapter 4

The Super–Kamiokande detector

4.1 Physical Description

The Super–Kamiokande Detector is a 50,000 ton water Cherenkov detector located in Gifu Prefecture, Japan. The detector is located in an active zinc mine and is accessed via a 2000 m long tunnel. The rock over-burden is 1,200 m corresponding to 2,700 equivalent meters of water. This over burden reduces the cosmic ray rate in Super–Kamiokande to ~ 3 Hz.

The detector is operated from a control room located in the mine which is staffed 24 hours a day by one or two physicists who monitor detector performance, data quality, and the detector environment.

4.1.1 Water Cherenkov Radiation

Super–Kamiokande detects relativistic particle through their emission of Cherenkov light. When charged particles pass through a medium with speeds ($\beta \equiv v/c$) faster than light in the medium, $\beta > 1/n$, a shock wave of radiation is created as shown in Fig. 4.1. The radiation, called Cherenkov radiation after its discoverer, forms a wave

front at a critical angle:

$$\theta_C = \arccos \frac{1}{n(\lambda)}. \tag{4.1}$$

The requirement that the particle be traveling faster than the speed of light in the medium leads to a momentum threshold which depends on the mass, m, of the particle:

$$p_{thresh} = \frac{m}{\sqrt{n^2 - 1}}. \tag{4.2}$$

For water the index of refraction varies between n =1.33 at λ = 580 nm and 1.36 at λ = 280 nm giving a typical Cherenkov angle of $\theta_C \simeq 42^\circ$ and a threshold of $p_{thresh} = 1.14m$. The number of Cherenkov photons emitted per unit length per unit wavelength is:

$$\frac{d^2N}{dxd\lambda} = \frac{2\pi\alpha}{\lambda^2}\left(1 - \frac{1}{n^2(\lambda)\beta^2}\right). \tag{4.3}$$

A total of $\sim$ 3400 photons/cm are emitted between λ = 300–550 nm. Over this range, the photomultiplier tube (PMT) detection efficiency averages $\sim$10% giving roughly 340 photons/cm detected, neglecting losses in the water. Particles emitting Cherenkov light form characteristic rings of light on the detector walls. From these rings, the particle's vertex, direction, momentum, and type can be determined.

4.1.2 Super–Kamiokande Water Tank

A schematic drawing of the Super–Kamiokande detector is shown in Fig. 4.2. The water tank for Super–Kamiokande is located in a cavern reinforced with iron rods and 40-50 cm of sprayed concrete. A coat of Mineguard polyurethane was applied to the dome and tunnels to serve as a barrier against radon gas. The water tank is 42 m high and 38 m in diameter. The dome above the tank contains five huts which house

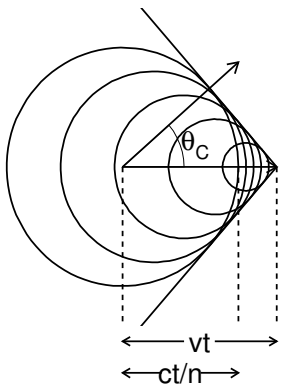

Figure 4.1: An illustration of Cherenkov radiation.

the front end electronics for the inner and outer detectors. At the site the average magnetic field due to the Earth is 450 mG. This is too high for the proper functioning of PMT's and is reduced to 50 mG using 26 Helmholtz coils which surround the tank.

The tank is optically separated into two regions. The inner region contains 32,000 tons of water and is viewed by 11,146 20-inch PMT's custom built for use in Super–Kamiokande. The walls of the inner detector are lined with black polyethylene terephthalate (PET). The outer region is 2.05 m thick along the detector walls and 2.2 m thick on the top and bottom detector surfaces. This region is viewed by 1885 8-inch Hamamatsu R1408 PMT's equipped with wavelength shifter plates. To further enhance light collection the walls are lined with a reflective material called Tyvek. The measured reflectivity of Tyvek is plotted in Fig. 4.3. During construction the reflectivity of the Tyvek was degraded through exposure to dust and fumes and the estimated reflectivity of the Tyvek in the Super–Kamiokande tank is roughly 60% – 85% of the measured values. The outer region is used to veto entering cosmic ray muons and to tag tracks exiting the inner volume. The inner and outer volume are separated by a 55 cm dead region that serves as the PMT support structure.

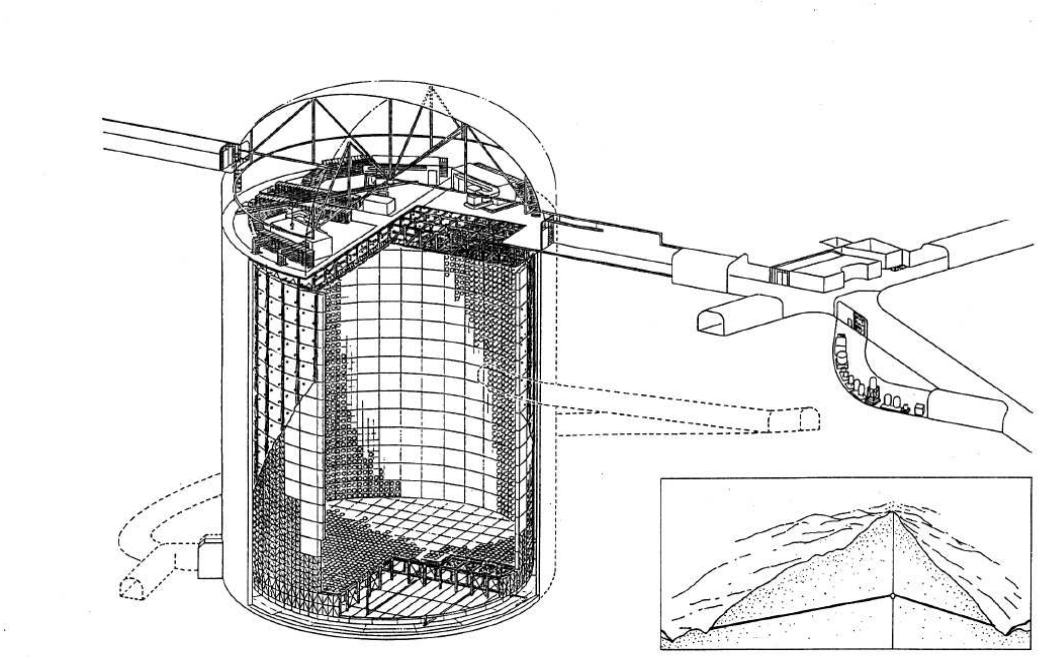

Figure 4.2: A schematic drawing of the Super–Kamiokande detector

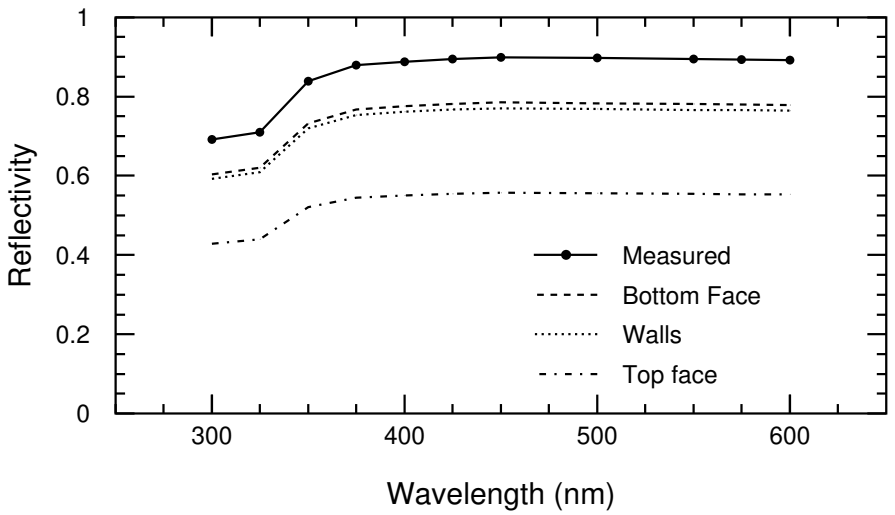

Figure 4.3: The reflectivity of Tyvek used in the outer-detector. Top curve shows measured value and the lower curves show the estimated values for the different faces of the Super–Kamiokande tank.

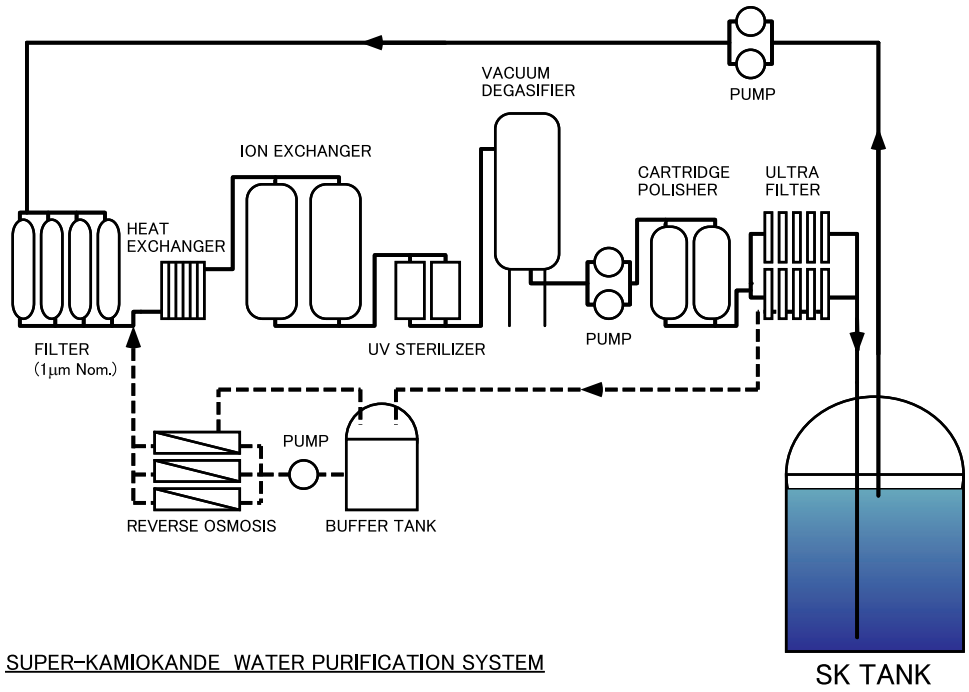

Figure 4.4: The water purification system.

4.1.3 Water Purification System

The water for the Super–Kamiokande experiment is purified in several steps. The system is outlined in Fig. 4.4. Water from the mine is filtered to remove dust and is cooled to 13° C. The water is then passed through an ion-exchanger and sterilized to kill bacteria. Gases such as oxygen and radon are removed and remaining ions are removed using a cartridge polisher. Finally, ultra-filters are used to remove small particles down to sizes of 10 nm. The system purifies water at the rate of 50 m^3/hour. At this rate, is takes just over 40 days to fill the Super–Kamiokande tank. After filling, the water is re-circulated through the system. Current radon levels in the water have been reduced to 1.4 mBq/m^3 [87] and the attenuation length is roughly 100 m at 420 nm.

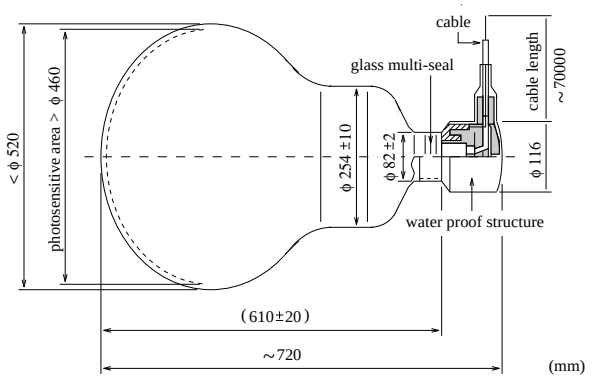

Figure 4.5: Schematic drawing of the 20-inch PMT's used in Super–Kamiokande.

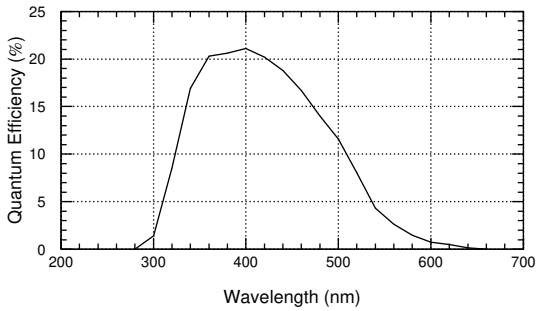

Figure 4.6: 20-inch PMT quantum efficiency as a function of wavelength.

4.2 Inner Detector

4.2.1 20-inch Photomultiplier

The 20-inch photomultipliers (PMT) used in the inner detector (ID) were custom built for use in Super–Kamiokande. A total of 11,146 tubes provide the ID with 40% photocathode coverage. A schematic view of the PMT is shown in Fig. 4.5. Several modifications (detailed in Ref. [88]) to the PMT design were made to improve the PMT energy and timing resolution. Table 4.1 lists the major features of the PMT's. The quantum efficiency of the PMT's peaks at 21% at 400 nm and is plotted in Fig. 4.6.

Photocathode area	50 cm diameter
Photocathode shape	Hemispherical
Window material	4-5 mm Pyrex
Photo-cathode material	Bialkali
Dinodes	11 stage Venetian blind
Pressure tolerance	6 kg/cm^2 water proof
Quantum efficiency	21% at $\lambda = 400$ nm
Gain	10^7 at $\sim$2 kV
Dark current	200 nA
Dark pulse rate	3 kHz
Cathode non-uniformity	<10%
Anode non-uniformity	<40%
Transit time	100 ns
Transit time spread	2.5 ns r.m.s.

Table 4.1: Specifications of the 20-inch Hamamatsu PMT.

4.2.2 Front End Electronics and Data Acquisition

The 11,146 signal cables from the ID PMT's are fed to 48 Tristan-KEK-Online (TKO) crates located in four counting houses ("huts") on the top of the water tank. Each crate contains a GO-NoGo (GONG) module to distribute trigger information, 20 Analog Timing Modules (ATM), and a bus-interface Super-Controller Header (SCH) module. The system is diagrammed in Fig. 4.7. The ATM modules use A/B channel switching so that one channel is active while the other is being digitized. Following a PMT hit, a veto of 900 ns is applied to the channel to reduce hits from after-pulsing. The ATM's operate at a threshold of 0.32 p.e. equivalent. Further details of the ATM modules can be found in Ref. [89]. When a channel triggers, the ATM's produce a square pulse -11 mV in height and 200 ns in width. These pulses are added together to form the "hitsum" which is used for the global trigger. The trigger threshold is equivalent to 29 tubes hits within the 200 ns time window, and is 50% efficient at 4.6 MeV [87]. When a trigger is received, data is transfered from the ATM's to Super Memory Partner (SMP) boards. These are then read out by 8 Sun workstations (2

per counting house) via VME. The data from each workstation is sent to a central online Sun workstation which assembles the data into events. After 70 MB of data has been recorded (roughly 10 minutes), the data is transfered to an off-line computer outside the mine via optical fiber. This machine applies the electronics calibration, saves the data to a magnetic tape library, and farms the data out to the various first level event selection programs for each analysis group.

4.3 Outer Detector

4.3.1 Outer Detector Photomultipliers

The outer detector (OD) uses 1885 8-inch Hamamatsu R1408 PMT's. These PMT's were salvaged from the previous IMB experiment after operation of that experiment ended in 1991. The PMT photocathode is hemispherical in shape and is optically coupled to 60 cm $\times$ 60 cm $\times$ 1.3 cm wavelength shifter plates to enhance light collection [90]. The wave shifter plates are acrylic doped 50:1 with bis-MSB which absorbs light in the blue-green and re-emits in ultra-violet where the PMT sensitivity peaks. The edges of the wavelength shifter plates are coated with reflective aluminized mylar tape. The timing of the PMT's is $\sim$11 ns without the wave shifters and is degraded to roughly 15 ns when the wave shifters are added. This timing resolution is adequate for the OD, and the 60% enhancement in light collection is well worth the penalty in timing resolution.

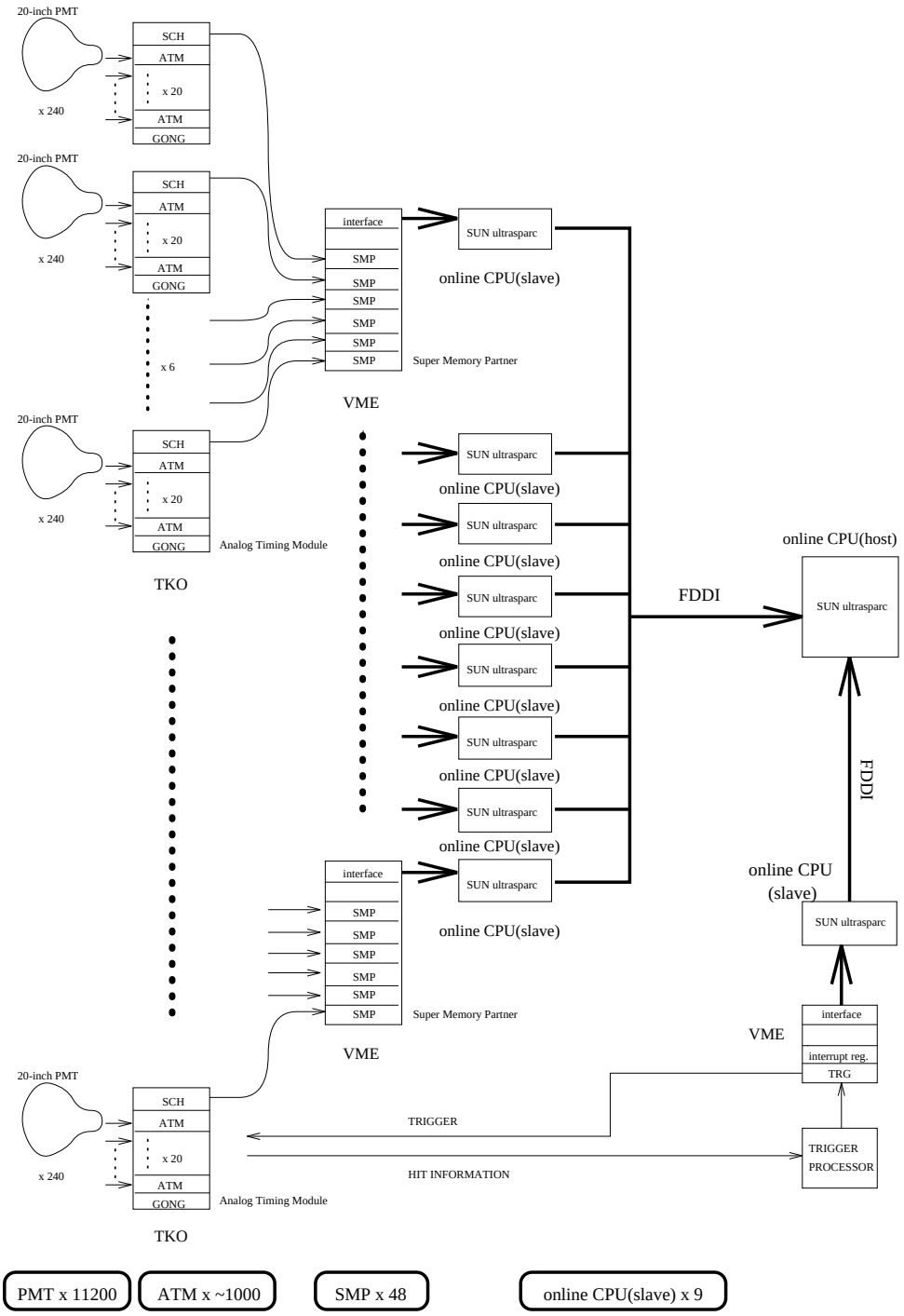

Figure 4.7: Block diagram for in inner detector DAQ system.

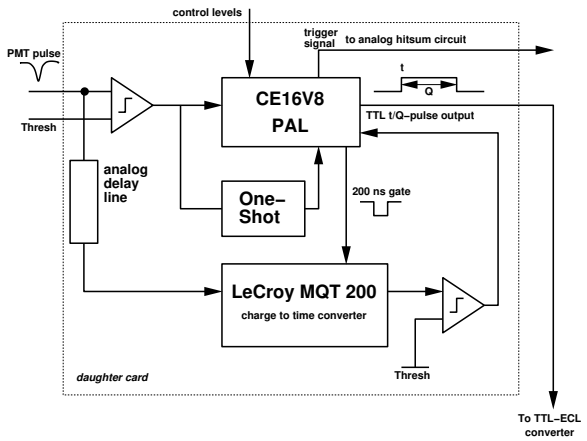

Figure 4.8: Block diagram for a single QTC channel.

4.3.2 Front End Electronics and Data Acquisition

The QTC Module

The front-end electronics for the OD were built at Boston University. The QTC modules (Charge to Time Converters) are custom self-gated ADC's (Analog Digital Converters). The QTC's encode both time and charge information from PMT pulses in a single ECL output which can be read by a standard multi-hit TDC. Time information is encoded in the leading edge of the ECL output and the charge information is encoded in the width. A block diagram of a single channel is shown in Fig. 4.8. The PMT pulse is fed to a LeCroy MQT200 charge-to-time converter. This chip integrates the PMT pulse and outputs a pulse with a length proportional to the PMT charge. The MQT200 is provided an integration gate which is generated by a one-shot fired when the PMT pulse goes over threshold. The gate is 200 ns wide and the PMT pulse is delayed 50 ns to fall inside the integration gate. The output pulse of the MQT200 is discriminated and converted to a TTL pulse using a PAL. The TTL pulse is finally converted to ECL for output.

The QTC's also generate a 20-mV 200-ns square pulse each time a PMT pulse

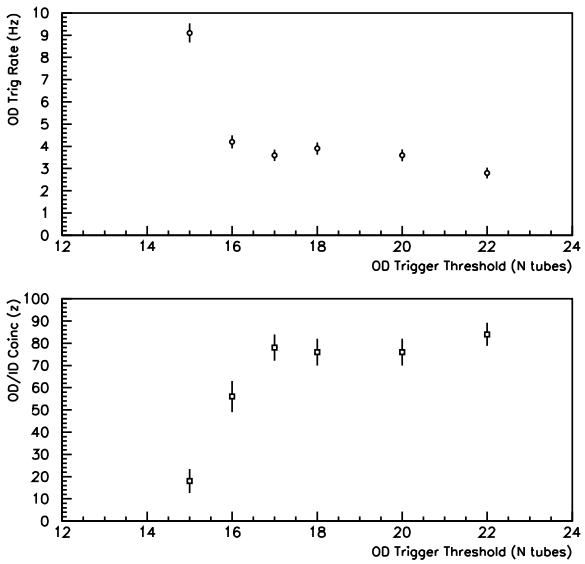

Figure 4.9: OD trigger rate and OD/ID trigger coincidence rate as a function of OD trigger threshold.

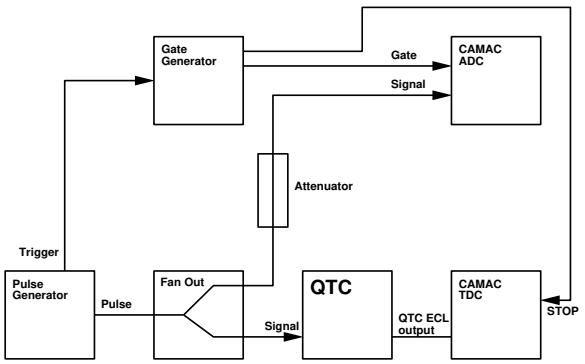

Figure 4.10: Setup used for QTC testing.

goes over threshold. The threshold is set to -25 mV which is approximately 0.25 p.e.. These pulses are summed in each module and are used to form the OD trigger. The trigger is set to a threshold equivalent to 19 OD PMT's firing in a 200 ns coincidence window. The threshold was set by considering the total OD trigger rate as well as the coincidence rate with ID triggers (see Fig. 4.9). When an OD trigger is detected, it is held for 100 ns to see if the ID also triggers. If the ID does not trigger within this interval, the OD will trigger readout of the detector.

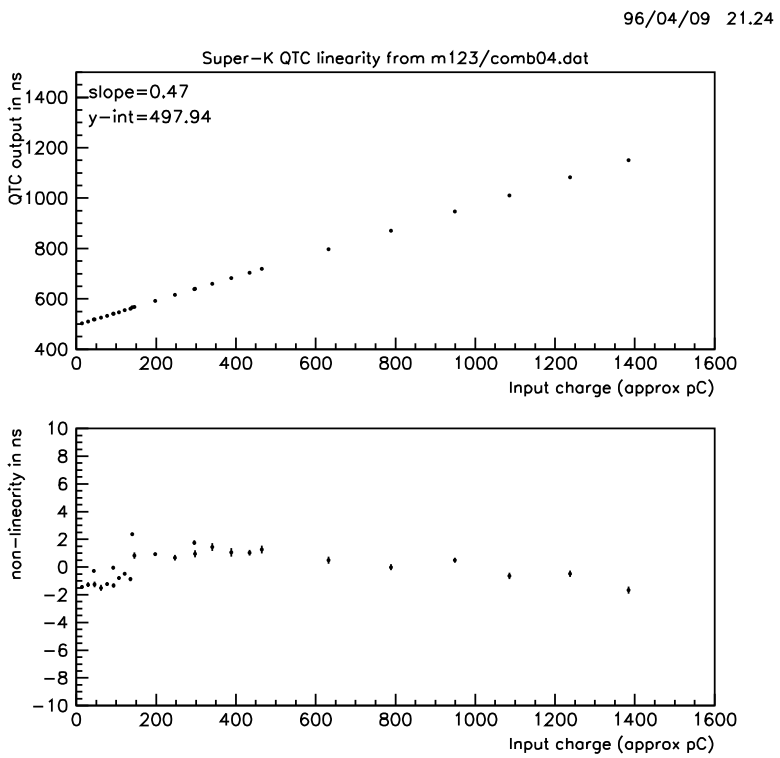

Figure 4.11: Top: The measured TDC vs. ADC (converted to pC) values for a single QTC daughercard. The bottom shows the fit residuals to a straight line fit.

Each QTC channel was tested against a standard ADC using PMT-like test pulses over a range from 0 to 200 photoelectrons. Figure 4.11 shows results for a single channel. Channels were selected to have uniform pedestal values, uniform TDC-ADC slopes, and limited deviations from linearity. The test set up is shown in Fig. 4.10.

Data Acquisition

The OD data acquisition system is diagrammed is Fig. 4.12. The output from the QTC's is read by a LeCroy 1877 Time-to-Digital Converter (TDC). The TDC's reside in 8 FASTBUS crates; 2 per counting house. The TDC's operate in "Common Stop" mode with a buffer of up to 32 μsec and a least count accuracy of 0.5 ns. When a "stop" is received the 16 most recent edges for each channel are digitized and

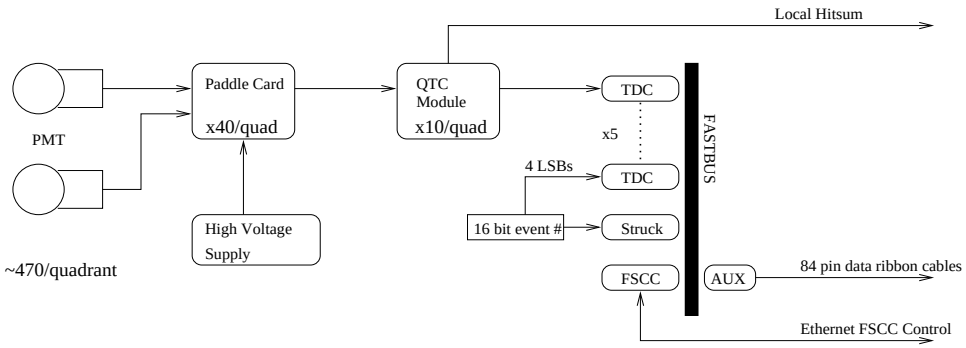

Figure 4.12: Outer detector data acquisition system [91].

stored in memory. Since each PMT hit requires two edges (leading edge gives time, trailing edge gives charge), a total of 8 PMT hits can be recorded in the integration window. The digitization time has been measured to be 1440 ns + 50 ns/edge in Super–Kamiokande [91]. During digitization (typically 2-5 μsec) an "OD-busy" bit is placed in the data stream to mark the limits of the dead time.

The time window for OD data was originally set to be 32 μsec long centered on the trigger time. This long look back period is desirable so that decays from cosmic ray muons can be associated with the cluster of OD hits produced by the entering muon. However, starting in September of 1996 (run 2800) this window was shortened to 16 μsec with the trigger coming 10 μsec into the integration window. Because at most 8 PMT hits can be recorded by the TDC's, this shorter time window reduces the chance that late PMT after-pulses and noise hits would force earlier hits out of the buffer.

The FASTBUS Smart Crate Controller (FSCC) is read out by a Sun workstation via dual-port memory modules attached to a VME crate located in the central counting house. This workstation assembles the OD data and passes it to a central workstation to be integrated with data from the inner-detector.

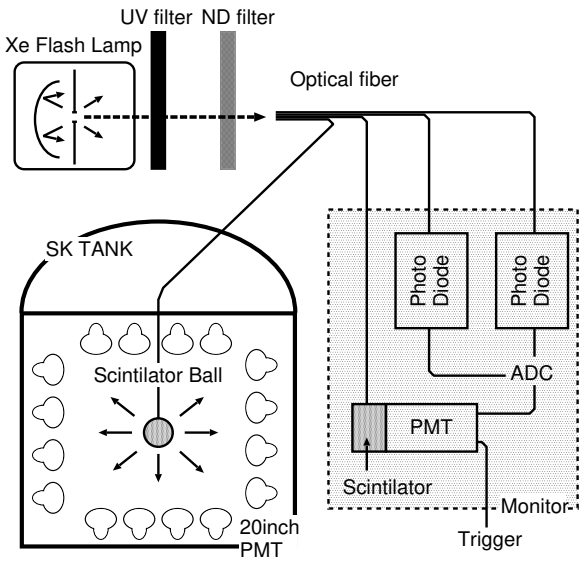

Figure 4.13: The Xe relative gain calibration system.

4.4 Calibration

4.4.1 Relative Gain Calibration

The relative gain of the photomultiplier tubes used in the ID are calibrated using a Xe lamp. The setup is shown in Fig. 4.13. Light from the Xe lamp is passed through an ultra-violet filter. The light is then guided via optical fiber to a scintillator ball which is lowered into the Super–Kamiokande tank. The scintillator is an acrylic ball doped with BBOT scintillator and MgO powder. The BBOT scintillator acts as a wavelength shifter absorbing UV light and re-emitting in blue-green light typical of Cherenkov radiation. The intensity of the UV light is monitored using a 2-inch PMT which is also used to trigger the detector.

The high voltage of each PMT is adjusted so that the "corrected charge" measured by each PMT is the same as all others. The "corrected charge" is the charge measured by each PMT after accounting for PMT acceptance, light attenuation and uniformity of the scintillator ball. The PMT acceptance as a function of incident angle is plotted

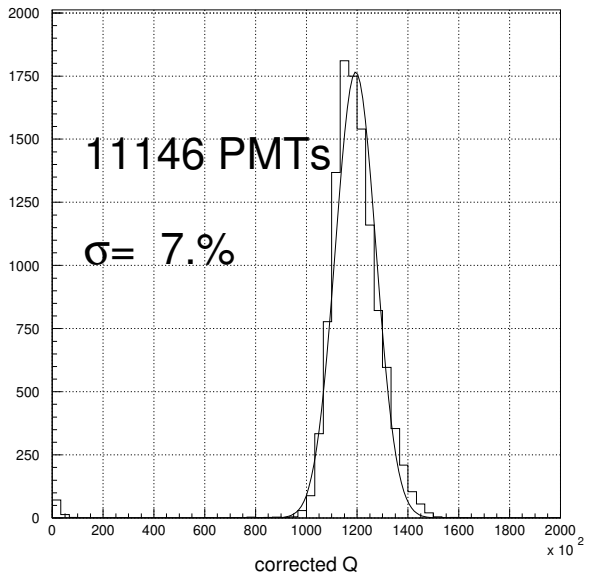

Figure 4.14: The spread in relative gains for the inner detector PMT's

in Fig. 4.15. Measurements are made at several locations through out the detector and for several voltage settings. The spread in the relative gain for the 11,146 ID PMT's is shown in Fig. 4.14. The remaining 7% spread in relative gains is corrected for off-line in software.

4.4.2 Absolute Gain Calibration

The single-photoelectron (s.p.e.) distributions of the ID PMT's are measured to set the absolute gain of each PMT. The absolute gain allows conversion from PMT charge measured in pico-Coulombs (pC) to number of photoelectrons (p.e.). The s.p.e. distribution is measured using photons generated from neutron capture on Ni. The most common interaction is ^{58}Ni + n $\rightarrow ^{59}$Ni + γ(9.0 MeV); lower energy photons are produced through interactions with heavier isotopes of Ni. The calibration source is shown in Fig. 4.16. Neutrons are produced using a ^{252}Cf source which is surrounded by Ni wire. The wire and source are enclosed by a cylindrical plastic case. The

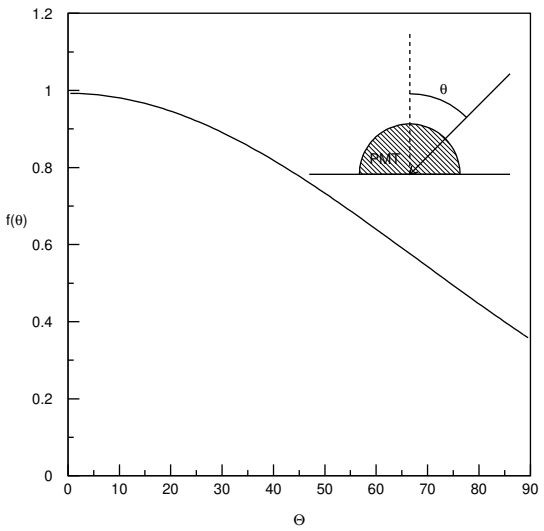

Figure 4.15: The relative photo-sensitive area and a function of incident angle.

number of p.e. detected by each PMT in response to these low energy photons rarely exceeds one, so that the response of each PMT to these events gives the s.p.e. charge distribution. Figure 4.17 shows a typical s.p.e. distribution for an inner detector PMT. The sharp peak near zero pC results from electrons that miss the first dynode. These distributions are made for each PMT and the mean values are used to convert the PMT charge in pC to number of p.e.. On average, 2.055 pC corresponds to 1 p.e..

4.4.3 Timing Calibration

The relative timing of each PMT is measured as a function of PMT charge using the setup diagrammed in Fig. 4.18. An N_2 laser is used to produce a 3 ns burst of light at $\lambda = 337$ nm. This wavelength is increased to 384 nm (which is closer to the peak wavelength of Cherenkov light) using a dye-laser module. The intensity of the light is varied using an optical filter. After the filter, the light is split by two optical fibers

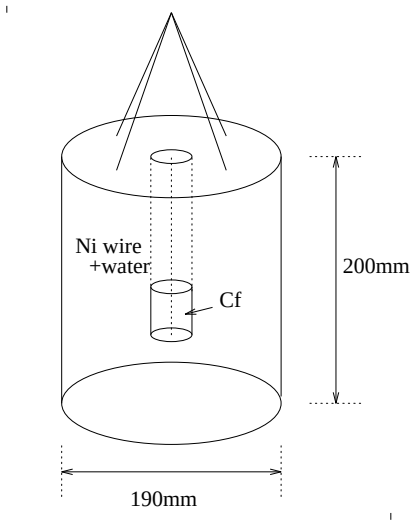

Figure 4.16: The Nickel calibration source.

with one fiber going to a diffuser ball located in the water tank and the second fiber going to a monitor PMT. This PMT is also used to trigger the detector. The diffuser uses a ball of TiO_2 on the end of the optical fiber surrounded by a material called LUDOX which consists of 20 nm glass fragments suspended in a silica gel. Using this system diffuse light can be obtained with only a small spread in the time profile of the pulse. For each event the hit time is recorded as a function of charge for each PMT. From the resulting distributions of time and charge ("TQ-map") the mean time offset as a function of PMT charge is obtained. The width of the distribution gives the timing resolution as a function of PMT charge. A typical "TQ-map" is shown in Fig 4.19. High charge PMT hits are earlier relative to low charge hits and have better time resolution due to the faster rising edge.

4.4.4 Water Transparency

As Cherenkov photons travel through water they are scattered and absorbed resulting in an exponential attenuation of the light intensity as function of the distance

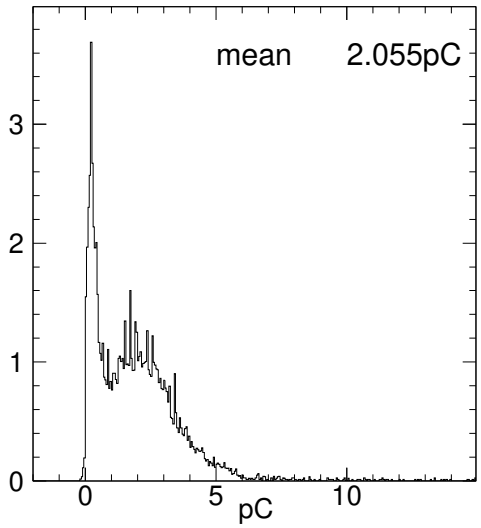

Figure 4.17: A typical single-photoelectron peak for a 20 inch PMT.

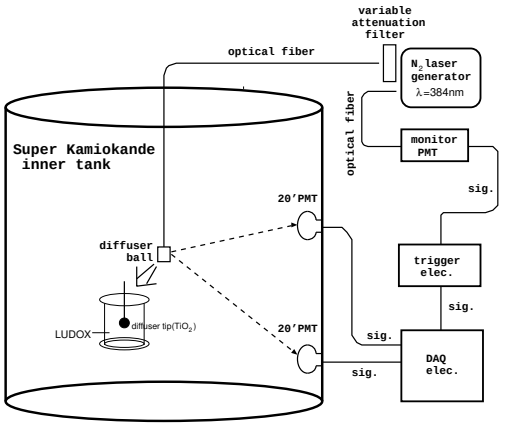

Figure 4.18: Laser system used for relative timing calibration.

from the source to the PMT. The water transparency is the length scale of this attenuation. Water transparency is measured both directly using laser light, and by using Cherenkov light from cosmic ray muons.

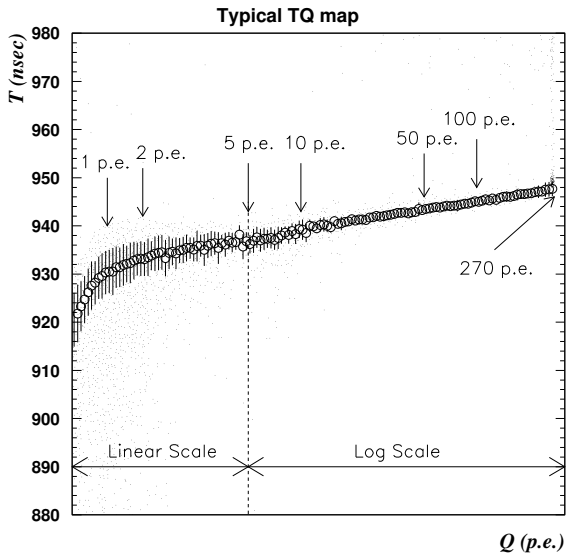

Figure 4.19: The timing-pulse height distribution (TQ-map) for a typical 20 inch PMT.

Measurements using Laser

The setup for measuring the water transparency (Fig. 4.20) is very similar to the setup used for measuring the relative PMT timing offsets. A N_2 laser and dye module are used to produce mono-chromatic light in a range between 337 nm to 600 nm. The light is split with one path going to a 2-inch PMT which is used to monitor the beam intensity and to trigger the detector. The second beam is conducted into the Super–Kamiokande tank via optical fiber. A diffuser ball is placed on the end of the fiber. The light intensity is measured at the top of the tank using a CCD camera for various diffuser ball depths. The water transparency is estimated based on an exponential fit to the light intensity as a function of depth

$$\frac{I_{CCD}}{I_{MonitorPMT}} = A \exp\left(-\frac{l_d}{L(\lambda)}\right). \tag{4.4}$$

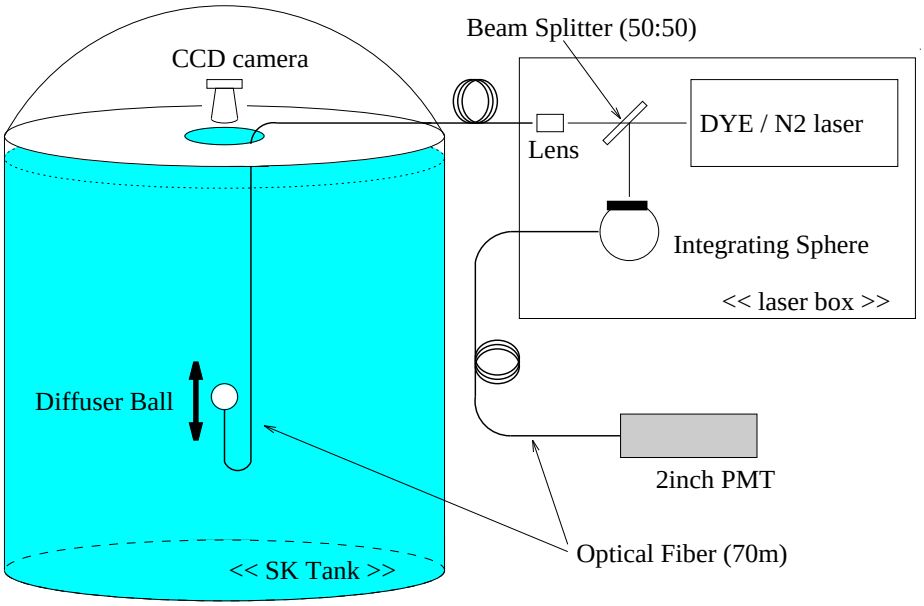

Figure 4.20: The setup for measuring water transparency.

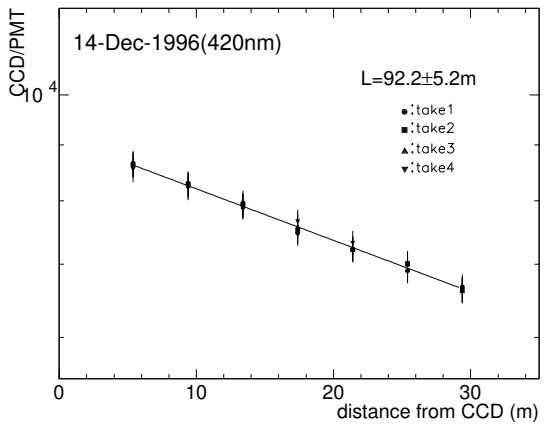

Figure 4.21: Measurement of the water transparency at 420 nm.

Figure 4.21 shows the measured intensity as a function of depth measured at a wavelength of 420 nm. Recent measurements of the water transparency give results of 67.1 m at 337 nm, 103.1 at 400 nm, 34.25 m at 500 nm, and 10.32 m at 580 nm. Figure 4.22 compares these measurements with the attenuation length used in Monte Carlo simulations of Cherenkov light in Super–Kamiokande.

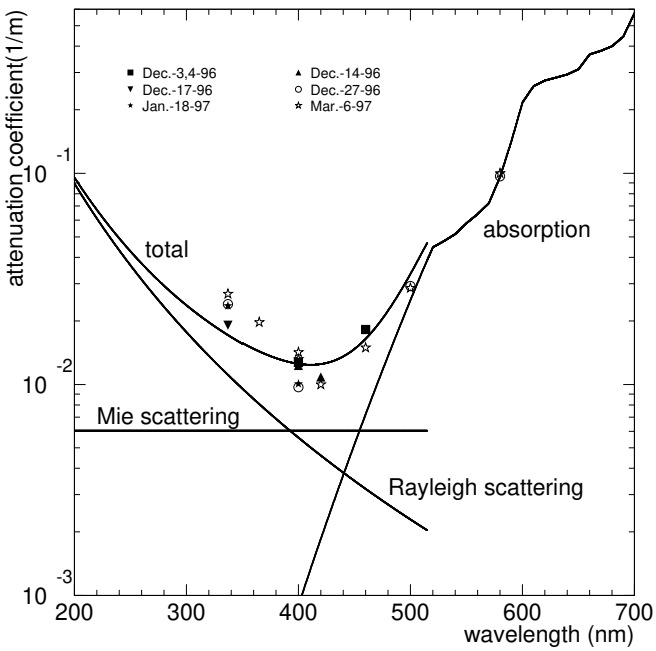

Figure 4.22: The attenuation coefficient $(1/L(\lambda))$ as measured in Super–Kamiokande. Solid lines show the attenuation coefficients used in Monte Carlo simulations of Cherenkov light in the Super–Kamiokande detector.

Measurement using Cosmic Ray Muons

While it is not possible to measure the water transparency for a specific wavelength using natural sources, measurements of water transparency using cosmic ray muons give an effective attenuation length averaged over the Cherenkov spectrum. This natural source allows the water transparency to be monitored constantly without interrupting data taking.

Measurements of the attenuation length using cosmic ray muons use the fact that cosmic ray muons emit a constant number of Cherenkov photons per unit track length. The number of p.e. detected by a PMT can then be expressed as:

$$Q = const. \times \frac{f(\theta)}{l} \exp\left(-\frac{l}{L}\right). \tag{4.5}$$

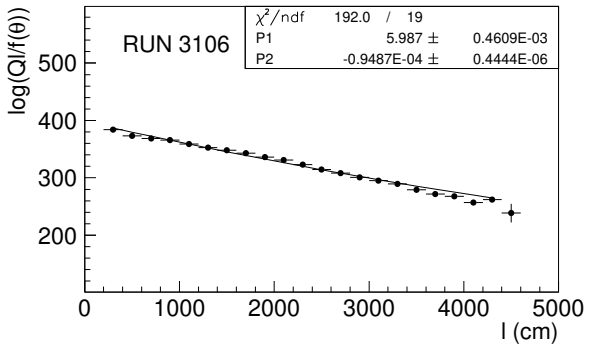

Figure 4.23: The water transparency measured using cosmic ray muons.

Here the PMT charge, Q, is expressed in terms of l, the flight distance for the Cherenkov photon from the muon track to the PMT, $f(\theta)$, the relative PMT acceptance (see Fig. 4.15), and L, the water attenuation length. Note that while the attenuation factor is technically an integral of several exponential factors for various wavelengths, in practice the attenuation is well modeled by a single exponential. Equation 4.5 can be re-written to give:

$$\log\left(\frac{Ql}{f(\theta)}\right) = -\frac{l}{L} + const. \tag{4.6}$$

This quantity is plotted as a function of l in Fig. 4.23 for a typical run. The attenuation length, 105 m, is obtained by fitting a straight line to the resulting distribution. The water attenuation length is calculated for every run and these measurements are used in the estimation of particle momenta. Figure 4.24 shows the variation of water attenuation over the data taking period analyzed in this dissertation. The increases in the water transparency between 200 and 300 days and 700 and 800 days are due to the replacement of ultra-filters in the water purification system.

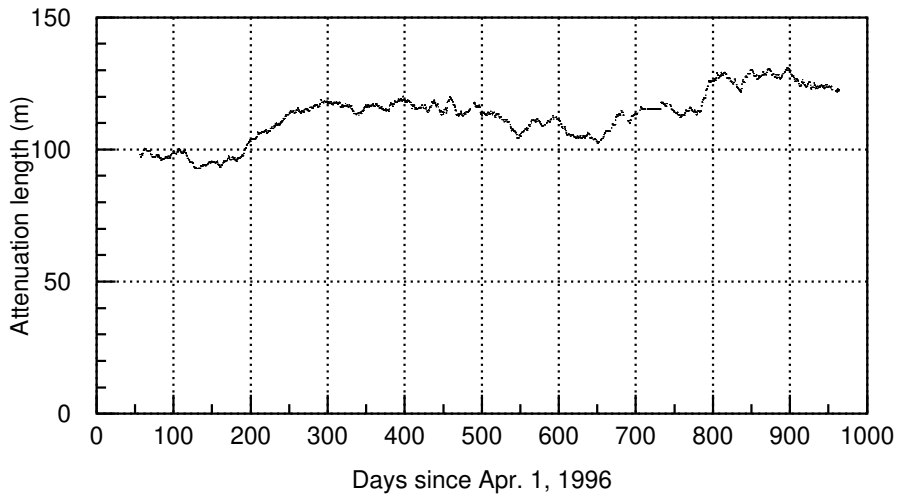

Figure 4.24: The water transparency as measured with cosmic ray muons as a function of time during the 736-day analysis period.

Chapter 5

Atmospheric Neutrinos in Super–Kamiokande

The interactions produced by atmospheric neutrinos produce particles which either stop in the detector or have enough energy to leave the detector. If all the particles produced in the interaction stop inside the detector then the event is called fully-contained (FC); if a particle exits the detector and deposits visible energy in the OD the event is called partially-contained (PC). Figures 5.1 and 5.2 show typical FC and PC events. The main feature which distinguished the two cases is the absence of OD activity for the FC sample and the presence of a cluster of outer detector PMT hits for the PC sample. This chapter outlines the procedures for selecting FC and PC events as well as the procedures used to reconstruct the event vertex, and particle momenta, and directions.

5.1 Fully-Contained Event Selection

Most neutrino interactions produce particles which then stop inside the ID. Because no particles penetrate to the OD these events are easily separated from backgrounds

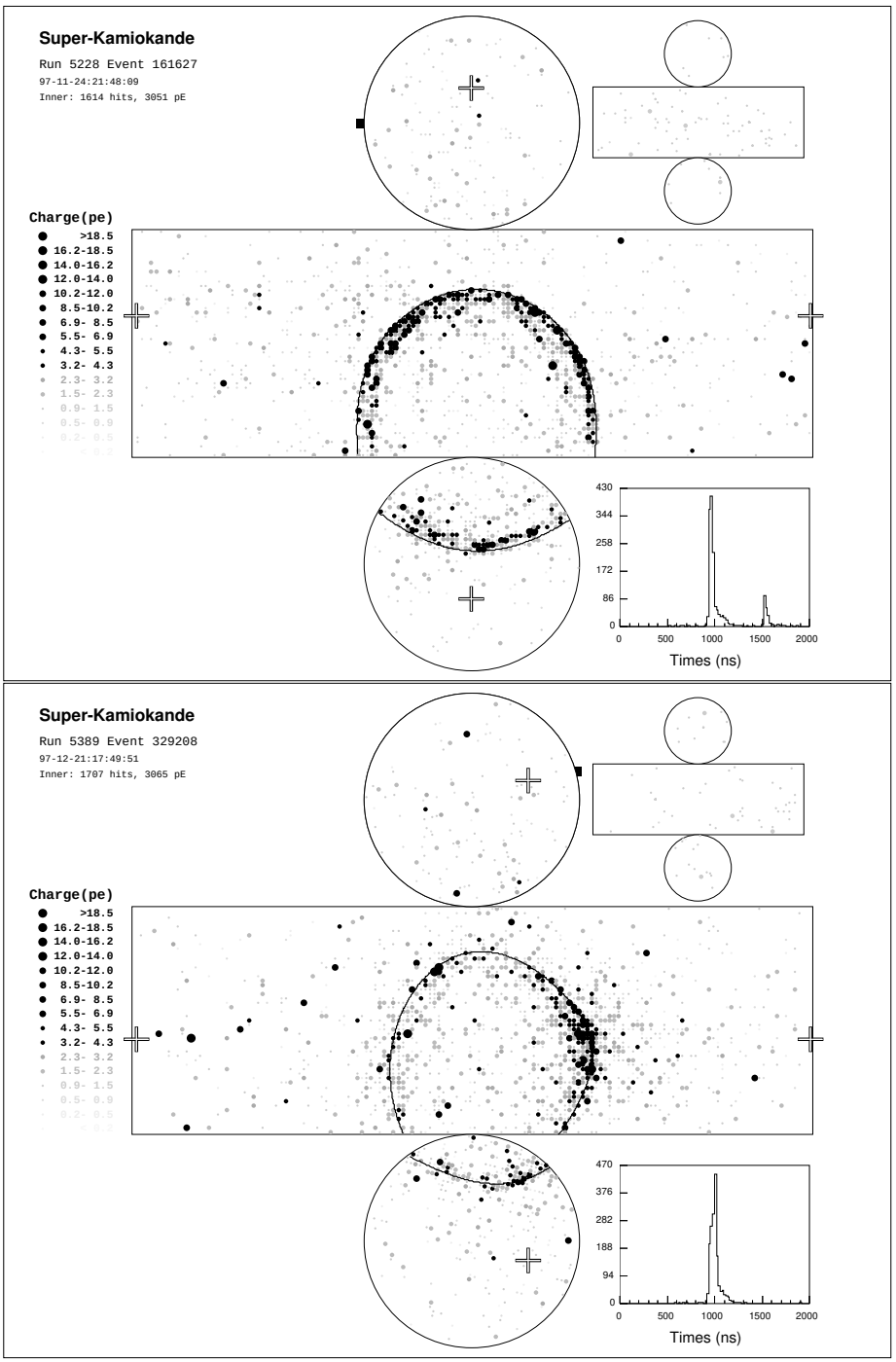

Figure 5.1: A typical pair of fully-contained events, the top is $\mu-$like and the bottom is $e-$like. Note that in both cases the outer-detector (shown at top right) has no cluster of hit PMT's. The distribution of PMT hit times is shown in the histogram. The peak in the $\mu-$like event near $t = 1600$ ns is from an electron produced by the decay of the muon.

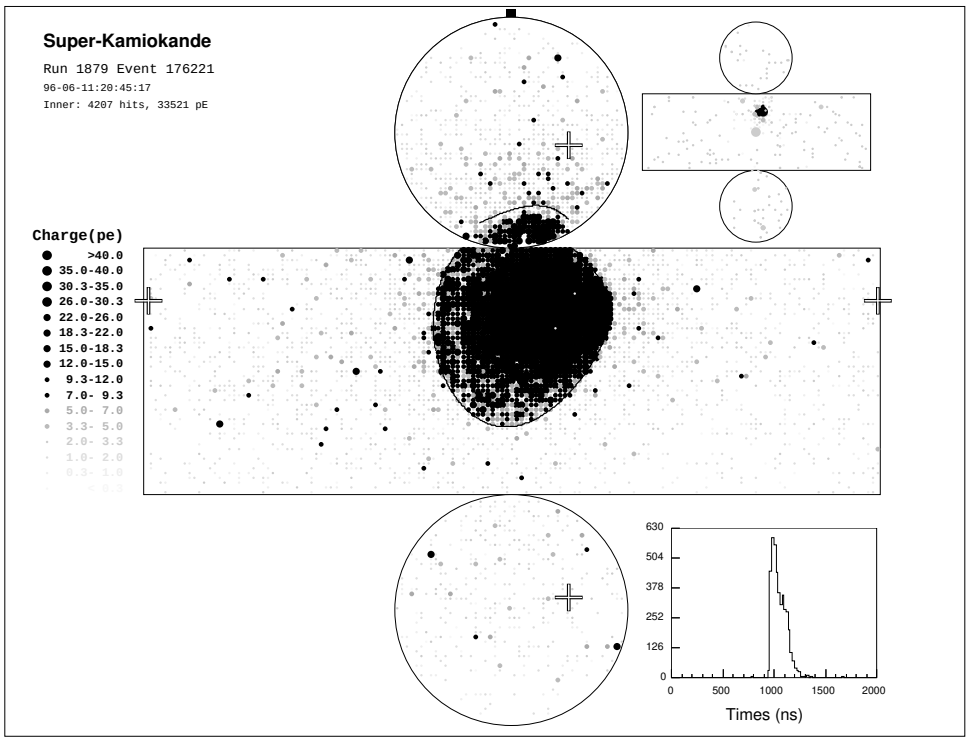

Figure 5.2: A typical partially contained event. Note the cluster of outer-detector PMT hits shown at the upper right.

by requiring little or no activity in the OD. The largest source of background for the FC samples comes from malfunctioning PMT's which spuriously emit light. These events, dubbed "flashers", are removed by a series of cuts and finally by a double human scan. Another source of background is cosmic ray muons which enter the ID through cable bundles. The cables for the PMT's are taken out through the OD in four columns which provide a path for cosmic ray muons to enter the ID without depositing any light in the OD. There are four steps of automated event selection. The output of these steps is then scanned by physicists to remove the remaining background. The steps are summarized in Table 5.1.

Reduction Level	Cuts	Events/day
Raw Data		10^6
1	ID p.e. and OD N_{hit} cuts	3680
2	Tighter OD N_{hit} cut	504
3	Flashing PMT cuts	
	Cosmic ray muon cuts	31.2
4	Repeated flashing PMT cuts	18.5
Scan	Reject remaining flashers	15.1
Final Sample	$E_{vis} > 30$ MeV	
	22.5 k-ton fiducial volume	8.3

Table 5.1: Full-contained data event selection summary.

5.1.1 First Reduction

The objective of the first reduction is to reduce the roughly 20 Giga-bytes of data recorded each day to a manageable size. This is done by applying cuts on time-to-previous event, visible energy and OD activity:

- Time to previous event must be larger than 100 μs. This removes events triggered by the decay of stopped cosmic ray muons.
- The total number of p.e. recorded in a 300 ns time window must be larger than 200. This corresponds to roughly 23 MeV of visible energy, safely removing events below the analysis threshold of 30 MeV.
- The total number of OD PMT hits recorded inside an 800 ns time window must be less than 50.

These cuts are applied to the data as it is collected and reduce the data sample from $\sim 1 \times 10^6$ triggers per day to 3700 events per day.

5.1.2 Second Reduction

The second reduction tightens the cut on OD activity and introduces a cut to remove "flashing" PMT's. The criteria are:

- No OD trigger was recorded or the number of OD PMT hits recorded inside a 800 ns window must be less than 25.
- The ratio of the number of p.e. recorded in any single PMT must be less than half of the total number of p.e. recorded in a 300 ns time window. This cut removes low energy events with a single large noise hit as well as "flashing" PMT's where arcing in a single PMT causes the PMT to record large amounts of charge.

Roughly 500 events per day remain following the second step of data reduction.

5.1.3 Third Reduction

The third reduction targets background from cosmic ray muons and higher energy flashing PMT's.

Events are tested against the hypothesis that they are cosmic ray muons which both entered and exited the ID. PMT's near the entrance and exit point record a large number of p.e. Through-going muons also produce clusters of PMT hits in the OD near the entrance and exit point. To test if an event is a through-going muon, the entry point is assumed to be located at the the earliest hit PMT that has at least two hit neighboring PMT's. The exit point is taken at the center of all saturated PMT hits in the ID. An event is identified as a through-going muon, and removed, if it satisfies each of the following:

- Any single ID PMT recorded more than 230 p.e.

- More than 1000 ID PMT's recorded hits.
- The number of OD hits recorded inside an 800 ns time window within an 8 m radius of the test entry or exit point is more than 9.

At this stage, events are fit under the hypothesis that they are stopping cosmic ray muons. The stop-muon fitter defines the event vertex as the entry point using the same definition as for through-going cosmic ray muons. The fit direction is then selected to maximize the total number of p.e. recorded inside a Cherenkov cone. Events are rejected as stopping-muons if the number of OD hits near the entry point is more than 9 or if the number of OD hits near the entry point is more than 4 and the goodness-of-fit is larger than 0.5.

Occasionally the detector will trigger on a low energy event and a cosmic ray muon will enter the detector during the 2 μs event window. These "accidental hit" events are rejected by requiring fewer than 19 OD PMT hits in a time window from 1300 to 1800 ns (roughly the trigger time plus 400 to 900 ns). Events in this category are also rejected by requiring that the number of p.e. recorded in the ID between 1300 to 1800 ns is less than 5000.

The 11,146 signal cables for the ID PMT's are channeled through twelve locations, eight of which are contained entirely in the OD and four of which travel from the ID through the OD. These four cable bundles create a path for cosmic ray muons to travel into the ID without passing through any of the sensitive volume in the OD. To improve the efficiency to tag these cosmic ray muons, 2 m$\times$2.5 m scintillation counters were installed over the four cable bundles in April of 1997. Events which are fit as stopping muons with entrance within 4 meters of a hit scintillation counter are identified as cosmic ray muons and rejected.

To reject any remaining low energy events a point vertex fit is applied. Using this

vertex, N_{50} is defined as the largest number of hit PMT's inside a sliding residual time window of 50 ns. For low energy events the energy is well estimated by $E = (N_{50}/5)$ MeV. Events which have either 500 or fewer hit ID PMTs and N_{50} less than 50 are rejected. Events which have 500 or fewer hit ID PMT's and are poor fits (goodness-of-fit< 0.5) are also rejected.

Events caused by "flashing" PMT's typically have very erratic PMT hit-time distributions. These events are identified by calculating the minimum number of hit PMT's in a sliding time window from $t = 1200$ ns to $t = 1800$ ns. Event triggers typically occur at $t = 1000$ ns so this range corresponds to 200 ns after the event trigger to 800 ns after the event trigger. The timing distributions of neutrino interactions is typically less than 100 ns so one expects to find only hits from noise hits or possibly decay electrons to occur in this window. Events are rejected as flashers if the minimum number of PMT's found in the time window is more then 14 PMT's, or is more than 9 and the total number of ID hit PMT's is less than 800.

Approximately 30 events per day pass the third stage of the data reduction.

5.1.4 Fourth Reduction: The "Flashscan" Algorithm

Prior to May of 1998 the output of the third stage in the fully-contained data reduction was double-scanned by physicists to remove background events caused by flashing PMT's. To further automate the data reduction procedure and reduce the scanning load I added a fourth stage to the data reduction to remove flasher events.

Many flasher events are easily recognized by human scanners by their repeated patterns. Two events that look almost identical, like those in Fig. 5.3 cannot be due to neutrino interactions and must be due to a malfunctioning PMT. The fourth stage in the fully contained data reduction seeks to automate the process of recognizing

and filtering these repeated patterns.

To facilitate the comparison of events, the ID walls are divided into $N = 1350$ regions roughly 2 m by 2 m. Each region contains roughly 9 PMT's. For each event, a "charge vector" q_i is defined where q_i is the sum of the charges recorded by each PMT in the i^{th} region. Two events A and B are compared by computing the correlation of their charge vectors:

$$r = \frac{1}{N} \sum_{i=1}^{N} \frac{(q_i^A - \langle q^A \rangle)(q_i^B - \langle q^B \rangle)}{\sigma_A \sigma_B} \tag{5.1}$$

with

$$\langle q^{A,B} \rangle \equiv \frac{1}{N} \sum_i q_i^{A,B} \tag{5.2}$$

and

$$\sigma_{A,B} = \frac{1}{N} \left(\sum_{i=1}^{N} (q_i^{A,B})^2 - (\sum_{i=1}^{N} q_i^{A,B})^2 \right). \tag{5.3}$$

Figure 5.4 shows plots of correlation values, r, for all pairs of events from a 10 year atmospheric neutrino Monte Carlo sample and a 414 day data sample of events labeled by a physicist to be caused by flashing PMT's. In the figure, the Monte Carlo has been scaled to the livetime of the data.

For pairs of atmospheric neutrino events, the size of the correlation depends on the number of p.e detected; events with a large number of p.e. tend to be more correlated with other large events. Thus, the cut to label two events a "match" is based on the charge of the events being compared. Figure 5.5 shows the calculated correlation for pairs of atmospheric neutrino Monte Carlo and 414 days of tagged flasher events versus the average of the total charge for the pair of events. Pairs of events whose result falls above the line are called "matches" and pairs of events whose result falls below the line are not called matches. Using this definition of a

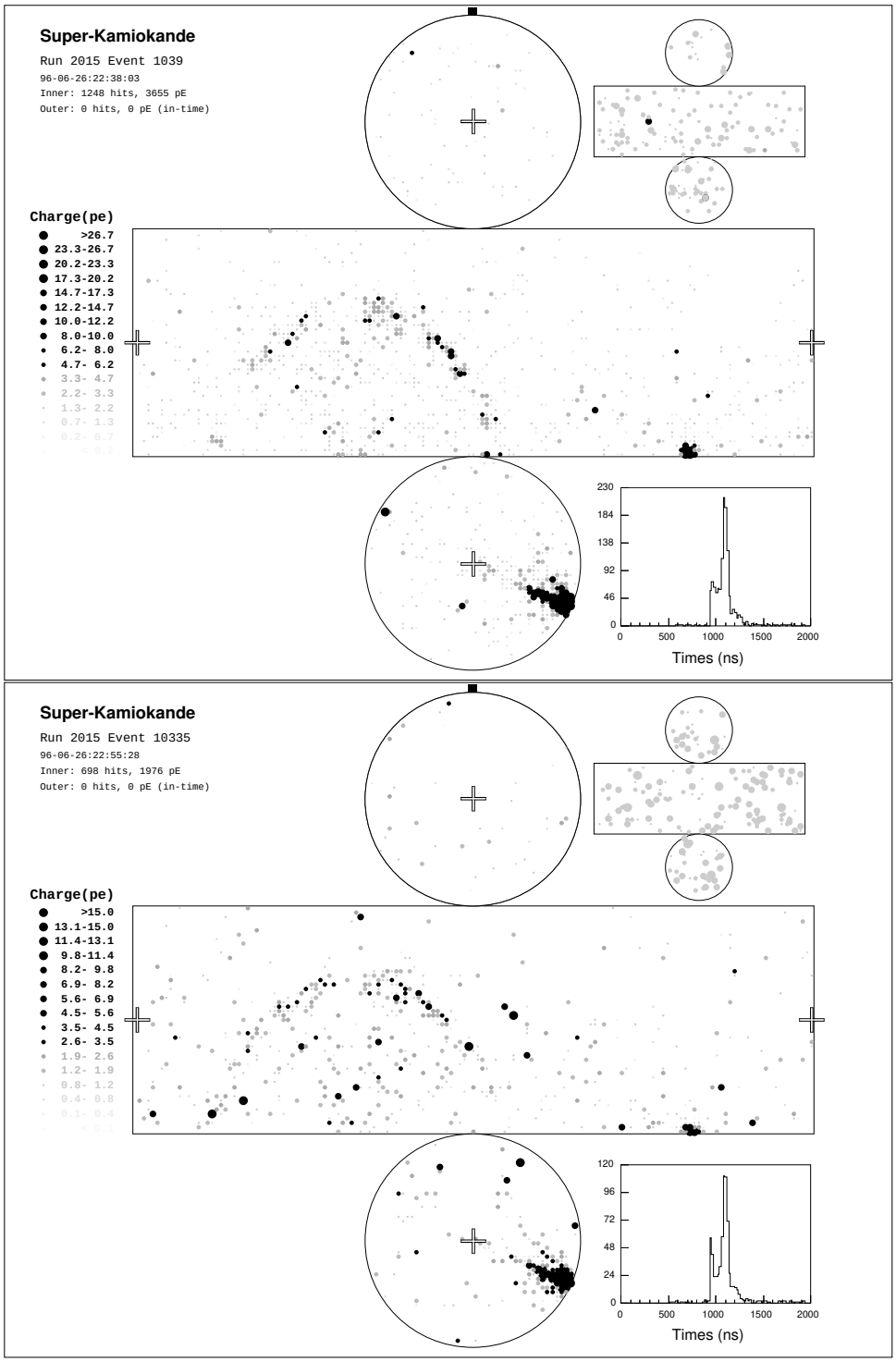

Figure 5.3: A typical pair of flasher events. These events occurred within 20 minutes of each other.

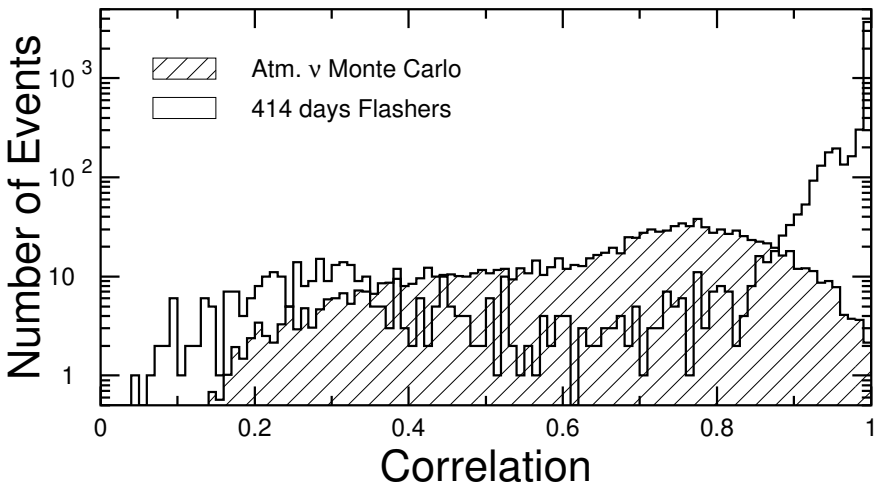

Figure 5.4: Correlation for pairs of atmospheric neutrino Monte Carlo and flasher events.

"match" the algorithm compares all pairs of events in the input file. To keep the execution time of the program from growing as the number of events squared cuts are applied before the correlation is computed. First only events with similar charge are compared. If event A has total charge Q_A and event B has total charge Q_B the correlation is computed if:

$$\frac{(Q^A - Q^B)}{(Q^A + Q^B)^{\frac{1}{2}}} < 5. \tag{5.4}$$

Very high energy events are unlikely to be caused by flashers so an upper limit of 30,000 p.e. is required for the correlation to be computed. For each event the largest correlation value obtained and the total number of matches is recorded. After all pairs of events have been compared the largest correlation value and the total number of matches are used to cut flasher events. The cuts are shown in Fig. 5.6 for neutrino Monte Carlo and tagged flasher events. The cut on the largest correlation decreases as the number of matched events increases; events which match a small number of other events are required to have high maximum correlations. The events flagged by

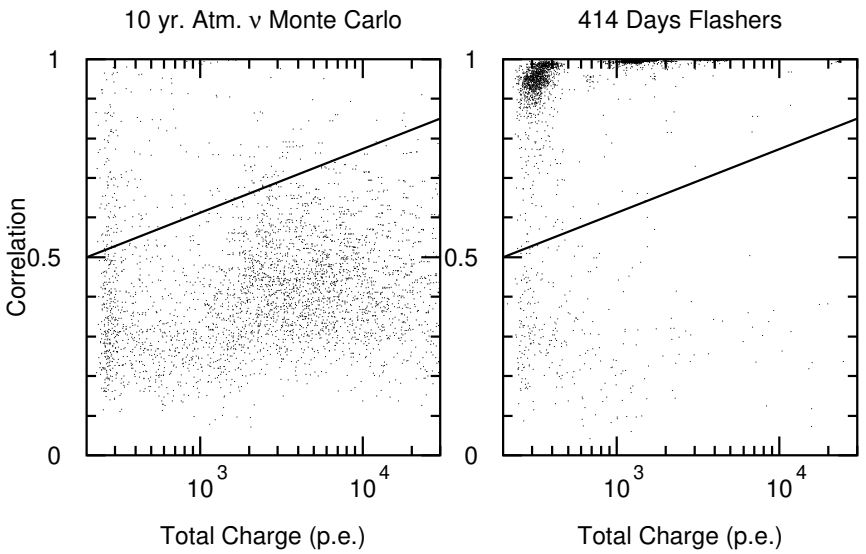

Figure 5.5: Cut to determine if two events are "matches".

this cut are removed in a second pass at the data.

The cuts were tuned using a 10-year atmospheric neutrino Monte Carlo sample and a 414-day scanned sample of partially reduced data. The cuts removed 21 of 75370 Monte Carlo events giving an estimated efficiency for saving neutrino interactions of 99.97%. The program was also tested using 10088 events that were output of the 3$^{\text{rd}}$ reduction stage and scanned by physicist. Of these 10088 events, scanners labeled 3842 neutrinos and 6246 as background. Of the 3842 neutrinos the program removed 20 events. These 20 events were re-scanned and in fact only 2 were neutrinos giving an estimated efficiency to save neutrino events of $3842/3844 = 99.95\%$. Of the 6264 background events, 5141 (82%) were removed automatically. The comparison of human scanners and the "flashscan" program in shown in Fig. 5.7. The program removed 93% of these event labeled flashers or noise by human scanners. While this does not remove enough background to eliminate scanning, the scan load is reduced from 24.4 events per day to 11.9 events per day of which roughly 8.3 events are

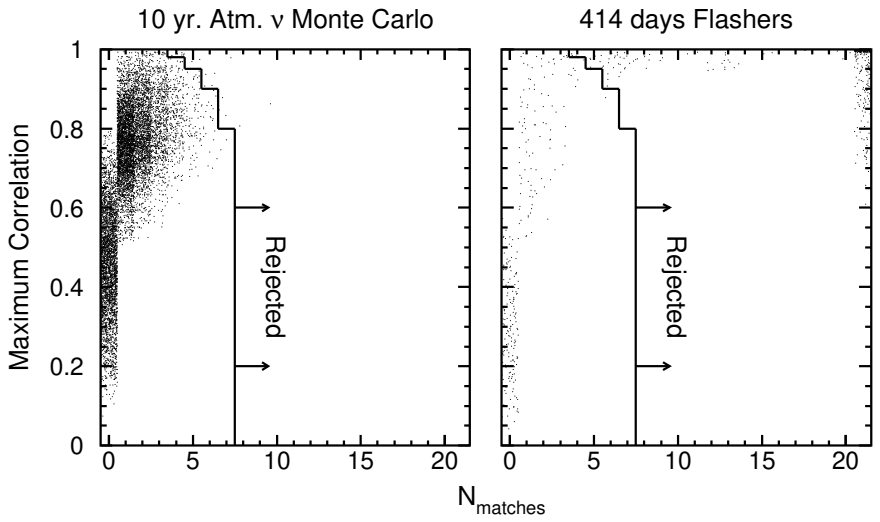

Figure 5.6: Distributions of maximum correlation versus the number of events matched for 10-years of atmospheric neutrino Monte Carlo and 414-days of tagged flasher events. Events to the right of the solid line are removed from the sample.

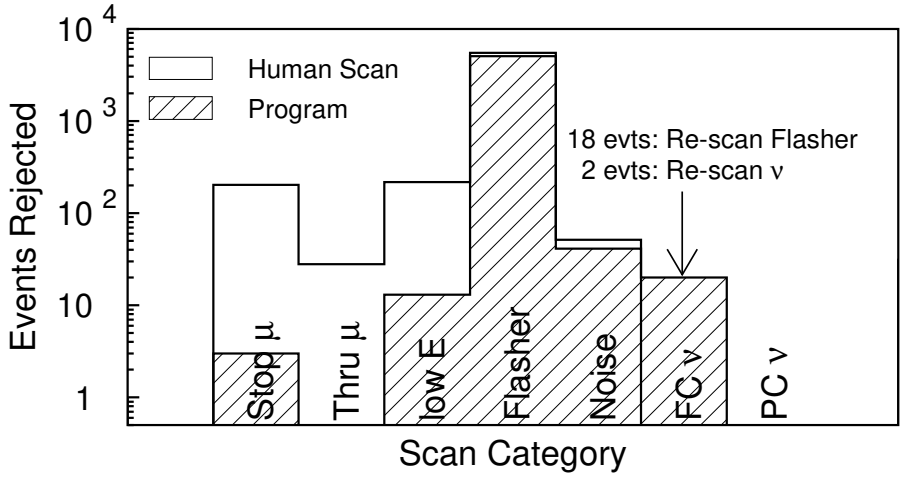

Figure 5.7: Comparison of automated flasher cuts with human scanners. 93% of the events labeled flashers or noise by human scan are removed automatically.

neutrino interactions.

Suggestions for Improvement

Since the implementation of the "flashscan" algorithm several possible improvements have occurred to me that have not been implemented. These are outlined below.

The program currently uses no information about time-correlations. Flasher events typically occur in bursts and are clustered in time. For example, the events in Fig. 5.3 occurred within 20 minutes of each other. One possible way to use time-correlations to help identify flasher events would be to only compute the correlation of events that occur within a certain time interval of each other, or to modify the definition of the "match" parameter:

$$r' = re^{-\frac{\Delta t}{t_0}}, \tag{5.5}$$

where r is defined in Eq. 5.1, Δt is the difference in calendar time between the two events and t_0 would be a time constant of order of days to months. In this way, it would be possible to lower the "match" threshold for events that occur in sequence without mis-labeling neutrino events that happen to resemble one another.

The program could also be used to automatically count the number of flashers in a sub-run (each sub-run contains roughly 10 minutes of data). Sub-runs with excessive flasher activity could be automatically flagged and removed from the data stream.

The efficiency of the program to remove flashers grows as the number of events processed grows; the more opportunities the program has to see a repeated event pattern the more likely it is to be able to flag and remove these events. The program is currently capable of storing up to 10,000 flasher events in memory, which corresponds

roughly to 600-1000 live-days of data. However, because the early reduction processes are run in approximately real time, blocks of data of roughly 100 runs (∼50-90 live-days) are typically processed in a single session lowering the efficiency to remove flashers. A solution to this problem would to move the flasher data base from memory to disk. This change would allow scans of new data to have access to the flasher history from previous runs. This change would also reduce the program size and enable the algorithm to be run as part of earlier reduction steps, prior to other flasher cuts, allowing the program to see more flashing event patterns and increase the efficiency to remove them automatically.

My final suggestion to help move the data reduction towards more complete automation is to reconstruct the output of the automated reduction steps before background events are removed by human hand scan. Well fit vertices and PMT timing residuals are very likely to be powerful tools to separate flasher events from neutrino interactions and studies of reconstructed flasher events are likely to lead to further automated cuts to remove this source of background.

5.1.5 Scanning

The results of the automated steps of the reduction are scanned independently by two physicists to remove remaining background and check data quality. Sub-runs with very large flasher activity or other detector problems are removed from the data stream. Events which are classified differently by the two independent scans are re-scanned by a third physicist who makes the final decision. The final output of the reduction is 15 events per day with less than 0.1% loss of atmospheric neutrino events. The final sample averages 8.3 events/day in the fiducial volume.

Reduction Level	Cuts	Events/day
Raw Data		10^6
1	Time to previous event	
	ID p.e. cut	
	width of OD PMT hit times	
	2 or more OD clusters	1.4×10^4
2	Refined OD clustering	2000
3	Initial vertex/direction fit	
	More than 10 OD hits near entry point	100
4	Distance to detector corner$<$ 1.5 m	
	Long-muon track fit	
	Refined direction and entry point cut	20
5	Precise vertex and direction fit	
	Fewer than 10 hits near exit point in OD	
	ID p.e. cut	2
Scan	Remove final cosmic ray muons	1

Table 5.2: Summary of the partially-contained event selection steps.

5.2 Partially-Contained Event Selection

Unlike events in the FC sample, PC events are expected to have activity in the OD. Thus the separation of PC neutrino interactions from background caused by cosmic ray muons requires a fairly complicated series of cuts. These cuts are applied in five steps and the final sample is selected based on a final double-scan by physicists. The steps are summarized in Table 5.2 [91].

5.2.1 First Reduction

The first stage of the PC reduction seeks to quickly remove low energy events, events triggered by the decay of stopped cosmic ray muons, and through-going comic-ray muons. Through-going cosmic ray muons produce clusters of hits in the OD at both the entrance and exit point. To find these entrance and exit points, a fast clustering algorithm is applied. These clusters of hits can be recognized by both their time and

spatial separation. The cuts made at this level of the reduction are:

- Time to previous event must be larger than 100 μs.
- Total number of p.e. detected in an 800 ns time window must be larger than 1000. This corresponds to $\sim$120 MeV.
- Width of OD PMT times must be less than 240 ns.
- The number OD hit PMT clusters found must be less than 2.

Roughly 14,000 events per day satisfy these requirements.

5.2.2 Second Reduction

In the second step of the reduction a slower, more detailed clustering algorithm is applied to the ID and OD detector hit PMT's. Stopping and through-going cosmic ray muons are removed based the results of this clustering algorithm by requiring:

- Fewer than two clusters found in the OD.
- The single OD cluster must be located entirely on a single face (top, bottom, or wall) of the OD.
- The cluster located in the OD must have a near-by ID cluster. This and the previous requirement remove cosmic ray muons that "clip" the corner of the OD volume.

Following these requirements, 2000 events per day remain.

5.2.3 Third Reduction

At the third step of the PC reduction, a point fit to the PMT hit times is made. Using this vertex, a direction is chosen which maximizes the amount of light inside a cone at the Cherenkov angle. A trial cosmic ray muon entry point is determined by projecting backwards along the fitted direction to the OD. If there are 10 PMT hits in the OD within 8 m of the projected entry point, the event is identified as a cosmic ray muon and rejected. The third step in the PC reduction applies the same flasher cuts as applied in the third stage of the FC reduction. Roughly 100 events per day pass this stage of the reduction.

5.2.4 Fourth Reduction

The fourth stage of the reduction seeks to refine the cuts of the third reduction. The fit direction found in the fourth step is refined by summing the direction vectors from the vertex fitted in the third reduction stage to each PMT, weighting by the PMT charge. A trial entry location is found by projecting backwards along this fit track to the ID wall. If the angle between the direction vector from the fitted vertex to the earliest hit PMT and the charge-weighted direction is less than 37°, the event is rejected. To reject corner-clipping muons, events with vertices closer than 1.5 m to the corner of the ID volume are rejected. At this stage of the reduction a long-track muon fitter is applied. Good fits with tracks longer than 30 m are rejected as cosmic ray muons. Following these cuts, 20 events per day remain.

5.2.5 Fifth Reduction

At the fifth stage of the reduction, a fit is made varying the vertex, direction, track length, and Cherenkov angle to produce a best fit to the ID PMT hit times and

charges. Events with more than 10 hit OD PMT's within a radius of 8 m from the back-extrapolated entrance region are removed. Finally, the number of tubes in the OD cluster where the particle exited must have 10 or more PMT hits. Two events per day pass this final stage.

5.2.6 Scanning

The output of the fully-automated reduction steps is scanned independently by two physicists to remove the remaining stopping and through-going muons from the sample. Events which are classified differently by the first two scans are re-scanned by a third physicist to make the final classification. Following rejection of the remaining cosmic ray background, an average of one PC event is found in Super–Kamiokande per day. Scanning was estimated to be >99% efficient for events in the fiducial volume based on blind scans of Monte Carlo events. The over-all efficiency of the PC reduction is estimated to be ∼88%±5% with inefficiencies entering at each reduction stage at the few percent level [46].

5.3 Event Reconstruction

5.3.1 Fully-Contained Event Reconstruction

The reconstruction of fully-contained events is done in four stages. An initial vertex and direction is found using the PMT timing information, then the number of visible Cherenkov rings are found. Each ring is then assigned a particle type ($e-$like or $\mu-$like). The vertex, direction, and momentum is refined in the final fitting stage. Details of the reconstruction algorithms are also presented in Refs. [92, 93].

Initial Vertex and Direction Fit: "A-fit"

The "auto-fit" (A-fit) algorithm is used to make an initial point-fit to find the event vertex by minimizing the width of the distribution of PMT hit time minus time of flight from the vertex to the PMT. The time residual of the i^{th} PMT is defined as:

$$t_i = t_i^0 - \frac{1}{v(q,l)}\sqrt{(x-x_i)^2 + (y-y_i)^2 + (z-z_i)^2} \tag{5.6}$$

where t_i^0 is the hit time of the i^{th} PMT, $v(q,l)$ is the speed of light in water, (x,y,z) are the coordinates of the trial vertex and (x_i,y_i,z_i) are the coordinates of the i^{th} PMT. Since the speed of light in water is a function of the wavelength, the velocity of light, v, is taken to be a function of the number of p.e. detected, q, (due to the convolution of the Cherenkov spectrum with the PMT acceptance), and the path length l, from the vertex to the PMT. The vertex is found by maximizing the goodness-of-fit defined by:

$$G_p = \frac{1}{N_{PMT}} \sum_i^{N_{PMT}} \exp\left(-\frac{(t_i - \langle t \rangle)^2}{2(f\sigma)^2}\right), \tag{5.7}$$

where N_{PMT} is the number of hit PMT's considered in the fit, t_i is the time the i^{th} PMT fired, $\sigma = 2.5$ ns is the average timing resolution of the PMT's. The scale factor f is taken to be 1.5 and reduces the effects of late, scattered light.

After the vertex has been fit, the track direction and opening angle of the Cherenkov cone (θ_c) are determined by examining the number of p.e. detected as a function of θ, the angle between the track direction and the vector from the vertex to the PMT. The direction and opening angle are found by varying θ_c and the track direction until the quantity:

$$G_d = \frac{\int_0^{\theta_c} q(\theta)d\theta}{\sin\theta_c} \exp\left(-\frac{(\theta_c - \theta_0)^2}{\sigma^2}\right), \tag{5.8}$$

is minimized. Here, θ_0 is the critical Cherenkov angle at $\beta = 1$ and σ is the estimated

rms spread of PMT hits around θ_c.

In the final step, the vertex fit is refined considering the particle track length and scattered Cherenkov light. This is done by defining two goodnesses. For PMT's inside the Cherenkov cone or that were hit at times less that $\langle t \rangle$ the goodness is defined as:

$$G_I = \sum_i^{N_{PMT}} \exp\left(-\frac{(t_i - \langle t \rangle)^2}{2(f\langle\sigma\rangle)^2}\right)/\sigma_i, \tag{5.9}$$

where again $f = 1.5$ and σ_i is the timing resolution of the i^{th} PMT computed as a function of the number of p.e. detected by the PMT. For PMT's outside the Cherenkov cone or PMT's that were hit at times later than $\langle t \rangle$ the goodness is defined as:

$$G_O = \sum_i^{N_{PMT}} \max\left[\exp\left(-\frac{(t_i - \langle t \rangle)^2}{2(f\langle\sigma\rangle)^2}\right), 0.8\exp\left(-\frac{(t_i - \langle t \rangle)^2}{20\text{ ns}}\right)\right]/\sigma_i^2, \tag{5.10}$$

where 20 ns is the mean time difference between direct photons and scattered photons estimated based on Monte Carlo studies. The over-all goodness combines G_I and G_O:

$$G = (G_I + G_O)/\sum_i \frac{1}{\sigma_i^2}. \tag{5.11}$$

The track length is then estimated based on the number of p.e. detected within a 70° cone around the track direction. The residual times are then recalculated assuming the light came from a particle traveling along the track. Using these modified timing residuals, the goodness-of-fit in Eqs. 5.9,5.10 are re-calculated. The procedure is iterated until a final, stable maximum goodness is found.

The vertex resolution and direction resolution of the fitter are plotted in Figs. 5.8 and 5.9 for sub-GeV, multi-GeV, $e-$like and $\mu-$like events.

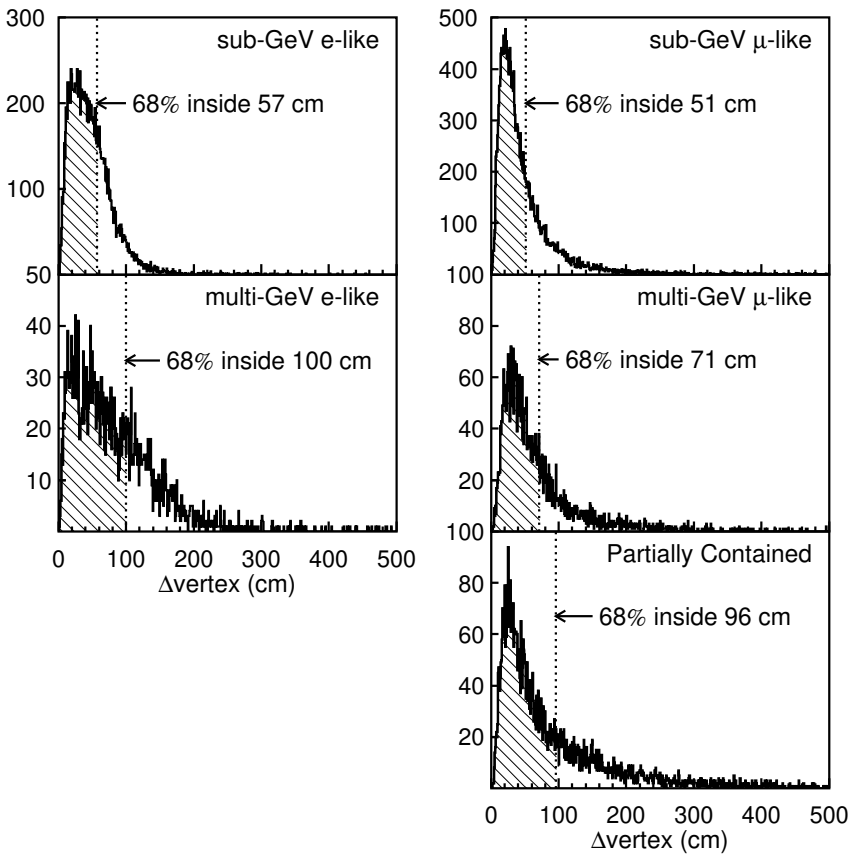

Figure 5.8: A-fit vertex distributions for sub-GeV, multi-GeV, $e-$like and $\mu-$like events.

Ring Counting

After the most energetic Cherenkov ring has been reconstructed, a search is made for other Cherenkov rings in the event. The procedure is done in two basic steps which are iterated until no additional rings are found. The first step is to form the expected charge distribution based on the current number of Cherenkov rings that have been found and compare it to the actual charge distribution in the event. Then, the expected charge distribution is subtracted, and a search is made for addition Cherenkov rings in the event.

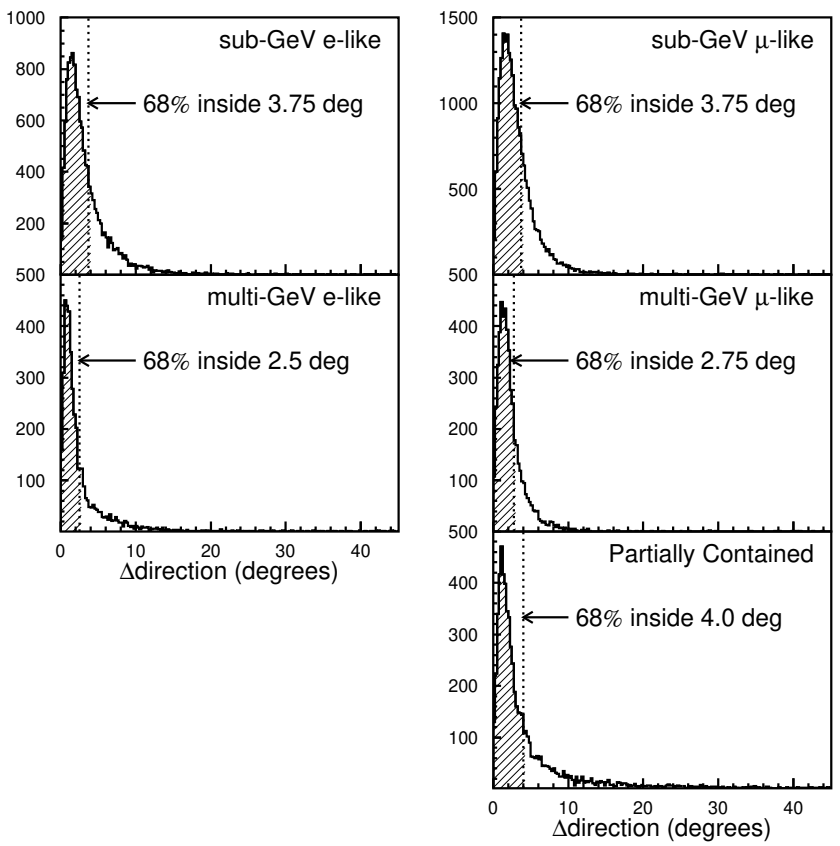

Figure 5.9: A-fit angular distributions for sub-GeV, multi-GeV, $e-$like and $\mu-$like events.

For the first pass, the expected charge distribution is made using the result of the initial vertex, direction, and Cherenkov angle fit described in Sec. 5.3.1. The expected number of p.e. for each PMT is calculated based on an a e-like charge distribution. Using this expected event pattern three maps of the event are made as functions of $\cos\theta$ and ϕ using:

- the difference of the expected charge distribution and the measured charge distribution;
- the difference of the expected charge distribution and the measured charge

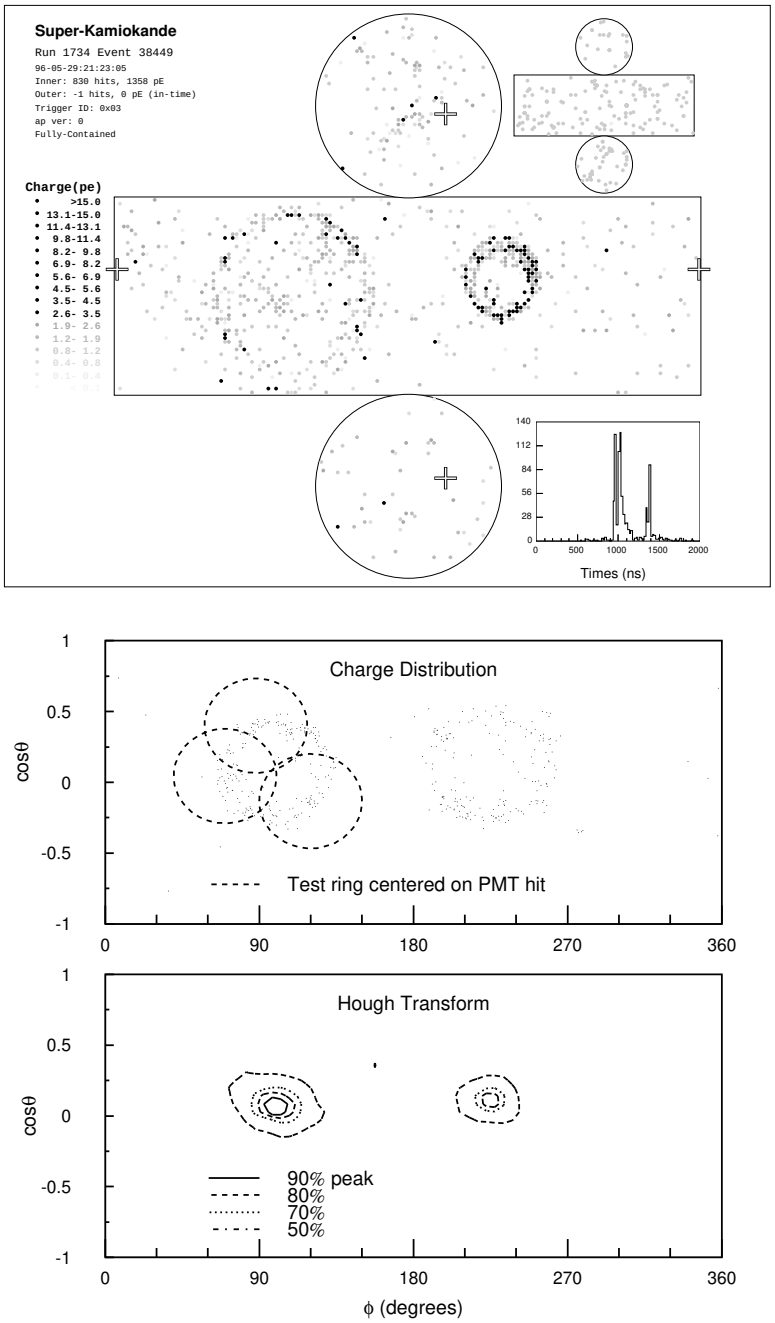

Figure 5.10: Hough transform for a 2-ring event.

distribution divided by the expected error in the charge measurement;

- the charge of PMT's that are not contained in any of the current Cherenkov rings.

To find seed directions for possible additional Cherenkov rings, the Hough transform of each of the three charge maps is computed. The Hough transform is computed by distributing the charge assigned to each PMT in a circle about the PMT at the Cherenkov angle. The distributed charge patterns from PMTs which lie on a Cherenkov ring will constructively interfere in the center of the ring. This transform converts the ring counting problem to a peak finding problem. The process is illustrated in Fig. 5.10. Hough transforms are computed for all angles between 24° and 46° at increments of 2 deg. The three highest peaks from each of the three charge maps (9 total) are retained as possible seed directions for additional Cherenkov rings.

Each of the seed directions is added to the list of Cherenkov rings and a new charge distribution for the events is made. The expected charge distribution is compared to the data charge distribution using a likelihood function. If none of the seeds produce an acceptable fit the search ends; otherwise the seed direction that produces the best fit is added to the list of found Cherenkov rings. The modified charge maps are re-computed and the process iterates.

Figure 5.11 shows the probability that a charged-current quasi-elastic neutrino event will be labeled a single ring event for ν_e and ν_μ induced events. The probability shows little significant momentum dependence. The figure also plots the charged-current quasi-elastic fraction as a function of momentum obtained in the single-ring sample using the ring counting algorithm described. Figure 5.12 shows the probability that a charged-current quasi-elastic neutrino event will be labeled a single ring event for ν_e and ν_μ induced events as a function of the distance of the event

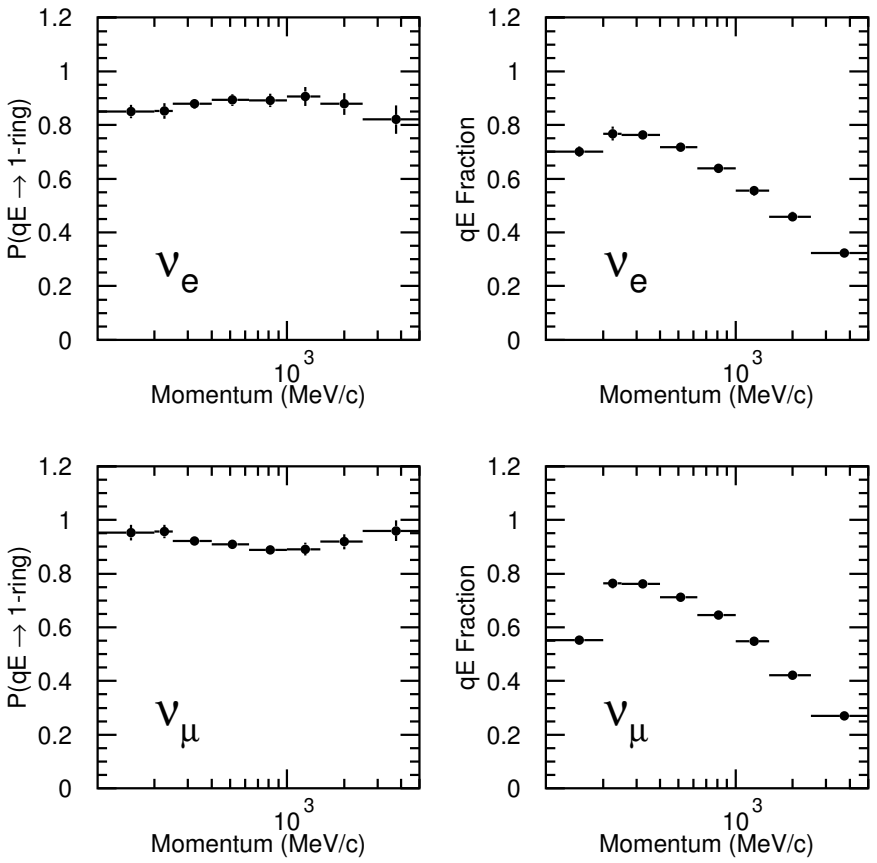

Figure 5.11: Single-ring identification probability for charged-current quasi-elastic events and the single-ring, quasi-elastic, event fraction as functions of momentum.

vertex to the fiducial boundary. There is a slight turn off in the probability as the event vertex approaches the fiducial boundary. The effect is more pronounced for ν_e events than for ν_μ events. The charged-current quasi-elastic fraction of the single ring sample, however, is fairly flat.

Particle Identification

In general, water Cherenkov detectors can distinguish two event classes: electromagnetic showers caused by electrons and gammas, called "e-like", and tracks caused by

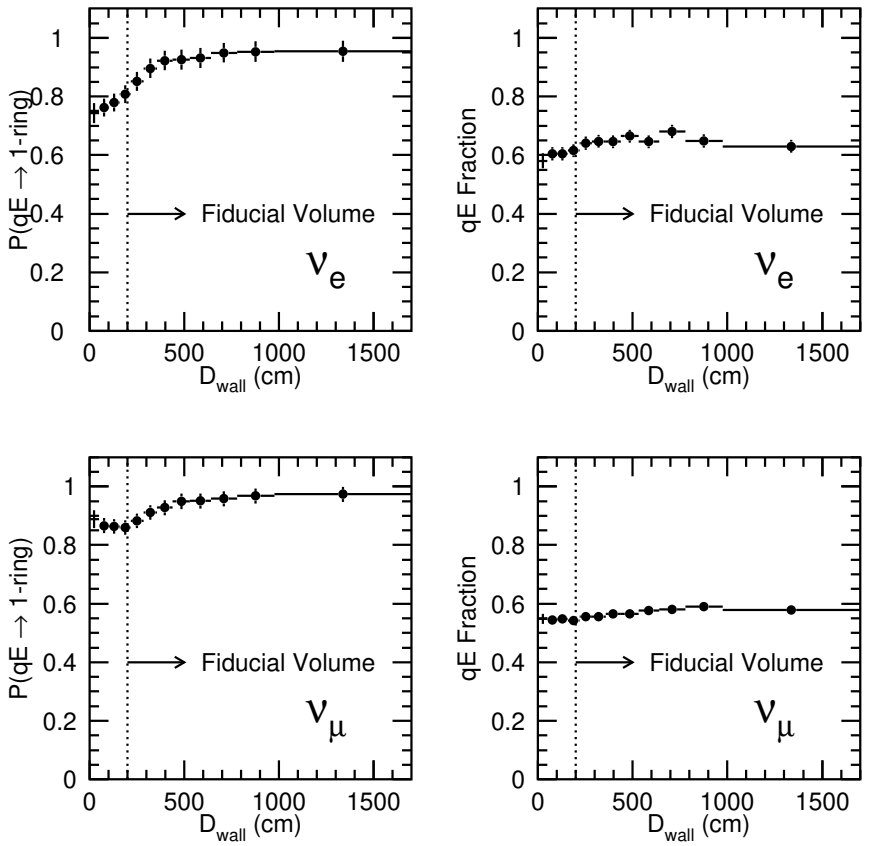

Figure 5.12: Single-ring identification probability for charged-current quasi-elastic events and the quasi-elastic event fraction as functions of momentum.

massive particles such as muons called "μ-like". At low momentum, the two cases can be separated based on the opening angle of the Cherenkov ring.

For e-like events the amount of charge expected in the i^{th} PMT due to direct light is computed as:

$$N_i = \alpha_e N_{MC}(\theta_i, p_e) \left(\frac{16.9 \text{ m}}{l_i}\right)^{1.5} \exp\left(-\frac{l_i}{L}\right) f(\Theta), \tag{5.12}$$

where α_e is an arbitrary normalization factor, $N_{MC}(\theta_i, p_e)$ is the number of p.e.

expected at the polar angle θ_i for an electron of momentum p_e, l_i is the distance from the vertex to the i^{th} PMT, L is the attenuation length of the water, and $f(\Theta_i)$ is the effective solid angle subtended by the i^{th} PMT. The calculation of $N_{MC}(\theta, p_e)$ is estimated by interpolating between results based on a Monte Carlo simulation of the number of p.e. incident on a sphere with radius 16.9 m from electron showers in perfectly clear water for momenta p_e = 100, 300, and 1000 MeV/c. The factor $(16.9\text{ m}/l_i)^{1.5}$ scales this expectation for diffusion using a power law derived from Monte Carlo simulations in water. The exponential factor accounts for losses due to water transparency. The effective PMT photosensitive area, $f(\Theta)$ is based on measurements using 50 cm PMTs shown in Fig. 4.15.

For muons the number of p.e. due to direct light detected at the i_{th} PMT is computed as:

$$N_i = \left[\alpha_\mu \frac{1}{l_i(\sin\theta_i + l_i\frac{d\theta}{dx})}\sin^2\theta_i + N_i^\delta(\theta_i)\right]\exp\left(-\frac{l_i}{L}\right) f\Theta, \tag{5.13}$$

where α_μ is a normalization factor, θ_i is the polar angle to the i_{th} PMT, N_i^δ is the number of p.e. expected from δ-ray production, L is the attenuation length of the water, and $f(\Theta)$ is again the effective photosensitive area of a PMT as seen from angle Θ. The number of p.e. produced by δ-rays is estimated from Monte Carlo simulations. The factor $1/l_i(\sin\theta_i + l_i\frac{d\theta}{dx})$ reflects the change in the expected charge distribution due to the change of the Cherenkov angle as the muon loses energy.

Scattered light is assumed to arrive later than the direct Cherenkov light. The distribution of scattered light in the event is estimated by removing all PMT hits that fall outside a cone 1.5 time larger than the reconstructed Cherenkov cone. A histogram of the timing residuals for the remaining PMT's is made. PMT's hit within a time window starting 30 ns before the peak time and 2σ+5 ns are considered direct

p.e.; PMT's hit later than this time interval are assumed to be from scattered light. The contributions from both scattered light and direct light are added to form the final expected p.e. distribution.

Once the expected number of p.e. in each PMT has been computed the expectation and data can be compared using a maximum likelihood method. The probability P to observe N^{obs} p.e.'s in a PMT given an expectation of N^{exp} p.e.'s is computed in two ways. For PMT's for which fewer than 20 p.e. are expected, the probability is computed based on a table derived from the single-p.e. distribution. For PMT's where the expectation is greater than 20 p.e.'s the probability is assumed Gaussian:

$$P_i = \frac{1}{\sqrt{2\pi}\sigma} \exp\left[-\frac{(N_i^{obs} - N_i^{exp})^2}{2\sigma^2}\right], \tag{5.14}$$

where $\sigma = 1.2^2 N_i^{exp} + (0.1 N_1^{exp})^2$ as before. This probability function is used to calculate the likelihood, $\mathcal{L}$, for PMT's hit by both direct and scattered (late) light with

$$\mathcal{L}_i^{Direct} = P(Nexp, Nobs), \tag{5.15}$$

and

$$\mathcal{L}_i^{Scattered} = P(N_{direct}^{exp}, 0) P(N_{scattered}^{exp}). \tag{5.16}$$

The number of expected p.e.'s for each PMT is computed under the assumption that the particle is e-like or μ-like, and the total likelihood is formed using only PMT's hit within a cone of angular radius 1.5 times larger than the Cherenkov angle:

$$\mathcal{L}(e, \mu) = \prod_i \mathcal{L}_i(e, \mu). \tag{5.17}$$

These likelihoods are converted to χ^2 variables using the relation $\chi^2 = -2 \ln \mathcal{L}$ and

the probability of the fit to the charge pattern is computed as:

$$P^q_{e,\mu} = \exp\left[-\frac{1}{2}(\frac{\chi^2_{e,\mu} - \min(\chi^2_e, \chi^2_\mu)}{\sigma_{\chi^2}})\right] \tag{5.18}$$

The information from the charge pattern is used in combination with information from the Cherenkov angle. At low momenta, massive particles such as muons and pions will have collapsed Cherenkov rings. This information is particularly important at low momenta where few p.e.'s are produced making the e-like and μ-like cases difficult to distinguish based on the charge profiles alone. The e-like - μ-like probability based the opening angle of the Cherenkov ring is:

$$P^\theta_{e,\mu} = \alpha \exp\left(-\frac{1}{2}(\frac{\theta^{exp}_{e,\mu} - \theta^{obs}}{\Delta\theta})^2\right). \tag{5.19}$$

The final probability is combined by computing $P_{e,\mu}$:

$$P_{e,\mu} = P^q_{e,\mu} P^\theta_{e,\mu}. \tag{5.20}$$

A ring is considered e-like if $P_e > P_\mu$ and μ-like if $P_\mu > P_e$. This is implemented by computing a PID parameter given by:

$$\text{PID} = \sqrt{-\log P_\mu} - \sqrt{-\log P_e}, \tag{5.21}$$

which is positive for e-like events and negative for μ-like events.

The performance of the particle identification has been checked in a variety of ways. The distribution of the particle identification parameter is shown in Fig. 7.2 for atmospheric neutrino data and for an atmospheric neutrino Monte Carlo sample. The e-like and μ-like peaks are well separated in both the Monte Carlo and data

samples. Based on the Monte Carlo sample the mis-identification of a ν_e charged-current interaction is $0.5 \pm 0.1\%$. For ν_μ charged-current interactions this probability is $1.0 \pm 0.1\%$. Particle identification has also been applied to stopping cosmic ray muons and electrons from muon decay. The mis-identification probability for cosmic ray muons was estimated to be $0.4 \pm 0.1\%$ and $1.8 \pm 0.5\%$ for decay electrons. Note that the maximum energy of a electron produced from muon decay is 53 MeV, below the sub-GeV sample threshold of 100 MeV. The mis-identification probability decreases as the energy increases. These particle identification techniques have also been tested using a tagged beam of electrons and muons incident on a 1 kilo-ton water Cherenkov detector at KEK [94].

Vertex and Direction Refinement: "MS-fit"

Because the initial vertex and direction fit uses mostly timing information it exhibits a bias between electron and muon events. If the light from long muons tracks is interpreted as coming from a single point, large errors in the estimate of the time-of-flight will be made for photons produced near the end of the muon track. Thus point fits to long muons based on PMT timing "split the difference", fitting the event vertex somewhere in the middle of the muon track. To minimize this bias, a secondary vertex fit ("MS-fit" for muon/shower-fit) is applied which uses the Cherenkov angle and particle ID information.

The refined fitting procedure works in three basic steps. First the direction and vertex positions are varied to maximize the goodness of the fit. Second the vertex position is varied along the track direction to maximize the particle ID likelihood $\mathcal{L}_e$ or $\mathcal{L}_\mu$. These likelihoods are computed as in Eqs. 5.18, 5.19, and 5.20, substituting the fitted Cherenkov angle for the observed Cherenkov angle. In the last step the direction is varied to maximize the particle ID likelihood. These steps are it-

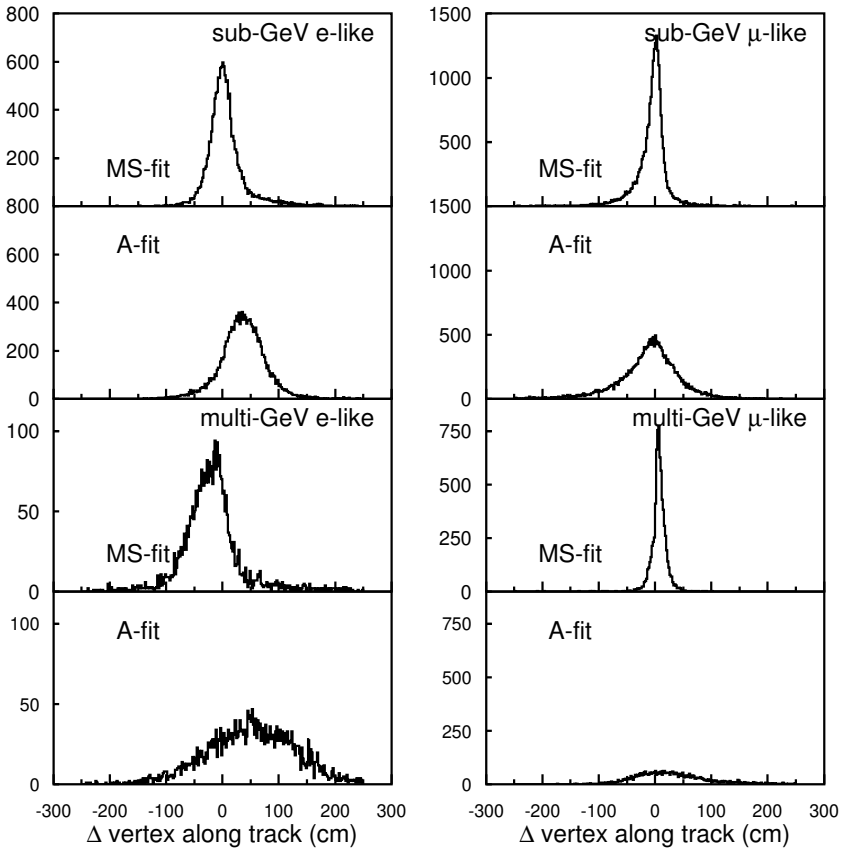

Figure 5.13: The difference in Monte Carlo vertex position and fitted vertex position as measured along the particle track direction for MS-fit and A-fit. The gains in vertex resolution by MS-fit come mostly from improved vertex resolution along the the particle track direction.

erated until the algorithm converges on a fixed vertex and direction. Figure 5.14 shows the difference between the true and reconstructed vertex as measured along the particle direction and perpendicular to the particle track direction before and after the refined vertex fit. The final vertex resolution for MS-fit is shown in Fig. 5.14. Figure 5.15 shows the angular differences between the true particle direction and the reconstructed particle direction based on an atmospheric neutrino Monte Carlo sample.

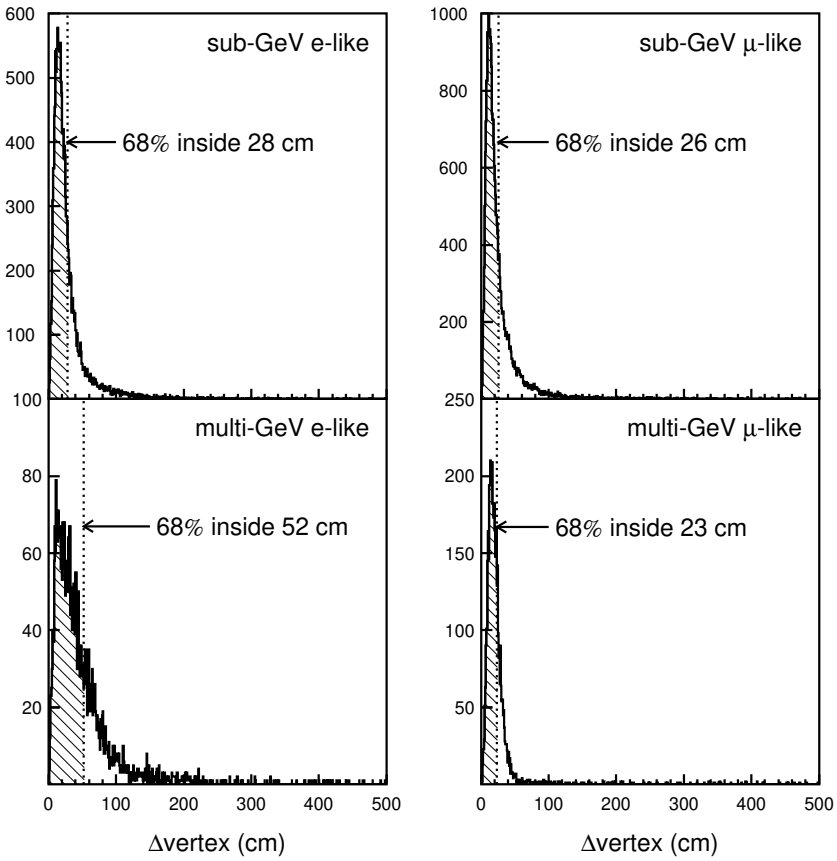

Figure 5.14: Final vertex resolutions for sub-GeV, multi-GeV, $e-$like, and $\mu-$like events following MS-fit.

Momentum Determination

Using the reconstructed vertex, direction, and Cherenkov angle of each ring the momentum is estimated by counting the number of p.e. inside a cone with a 70° opening angle within a residual time window between -50 and 250 ns of the residual time peak. The number of p.e. is corrected for the effective photosensitive region of each PMT as seen from the vertex, and water attenuation and scattering in water. This corrected count of total p.e., R_{tot}, is related to momentum using the results based on a Monte Carlo event sample. Figure 5.16 shows the relation between momentum

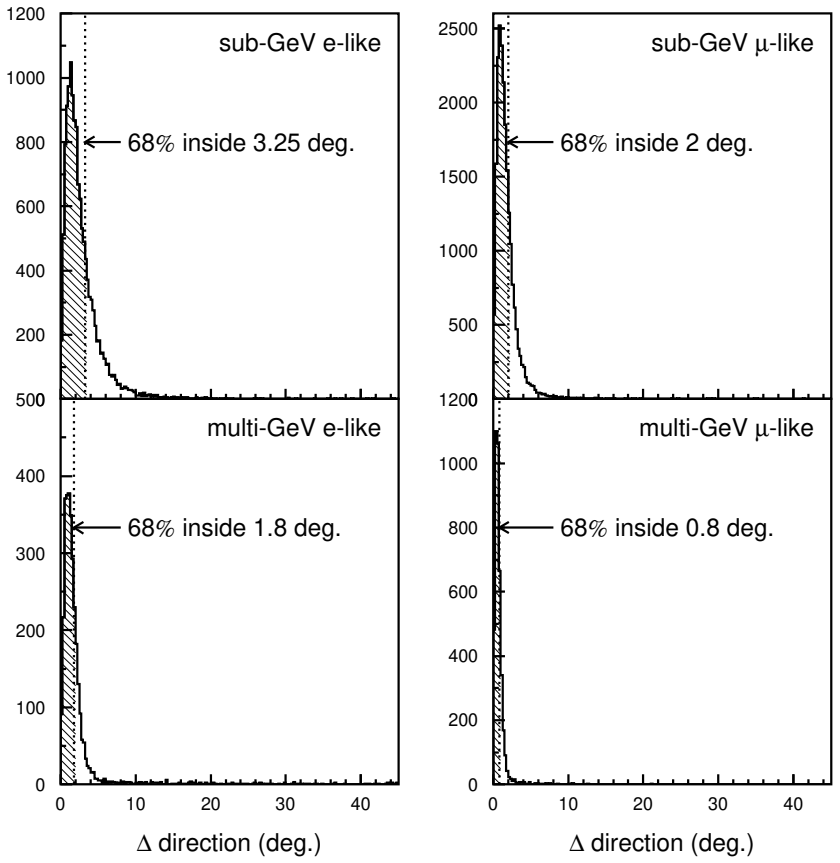

Figure 5.15: The direction resolution of MS-fit for sub-GeV, multi-GeV, $e-$like and $\mu-$like events.

and R_{tot} for electron and muons events. The absolute energy scale of the Monte Carlo is tuned to the data using a variety of sources. At the lowest momentum an electron LINAC [95] is used to inject 16 MeV electrons directly into the detector. At higher energies, the spectrum from Michel electrons and the reconstructed invariant mass of π^0 decays is used. Cosmic ray muons of various energies are also used. At low energies the momentum can be estimated independently using the Cherenkov angle. At higher energies the energy deposited in the detector can be estimated from the path length. The comparisons of these data with the Monte Carlo simulation is

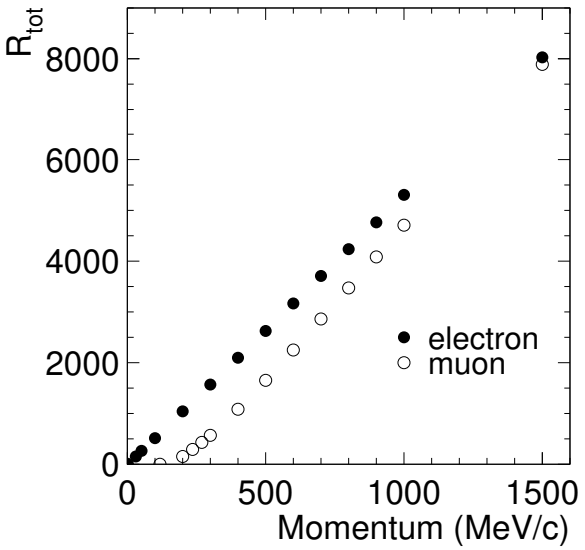

Figure 5.16: The relation between the total corrected p.e. and momentum for electrons and muons.

shown in Fig. 5.17. The Monte Carlo and data agree to within 2.5% over the entire energy range. The momentum resolution for single-ring e-like and μ-like events is shown in Fig 5.18. The resolution is estimated to be:

$$\sigma_e = 0.6 + \frac{2.6}{\sqrt{P_e(\mathrm{GeV}/c)}} \tag{5.22}$$

for electrons, and

$$\sigma_\mu = 1.7 + \frac{0.7}{\sqrt{P_\mu(\mathrm{GeV}/c)}} \tag{5.23}$$

for muons [92].

5.3.2 Partially-Contained Event Reconstruction

The partially-contained sample is naturally a ∼97 % pure sample sample of charged-current muon neutrino interactions. Since the purity is naturally very high, ring counting and particle identification are not needed. Only a vertex and a direction

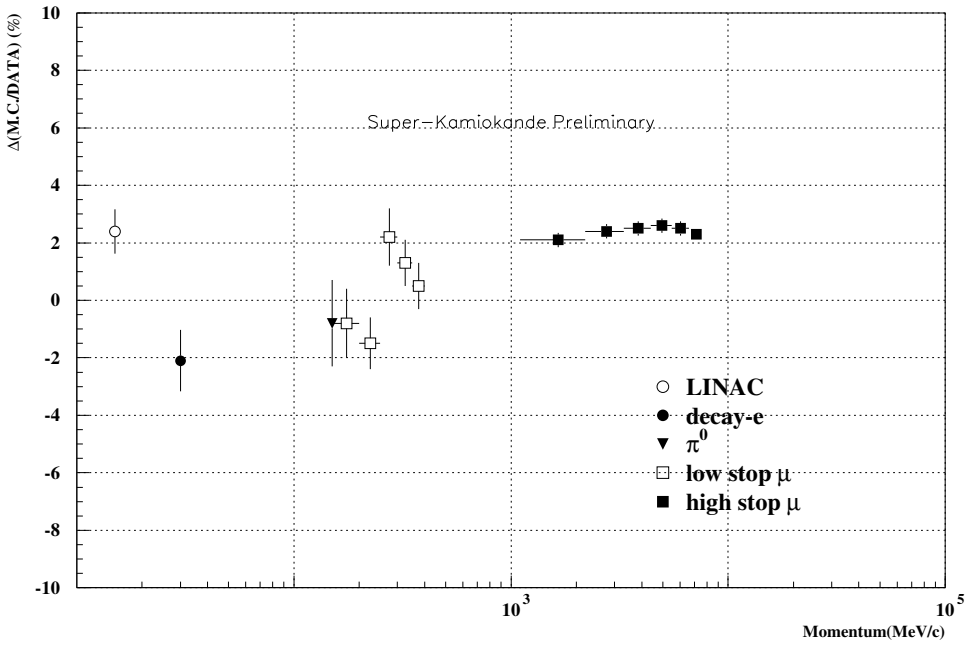

Figure 5.17: Absolute energy scale determination from several sources.

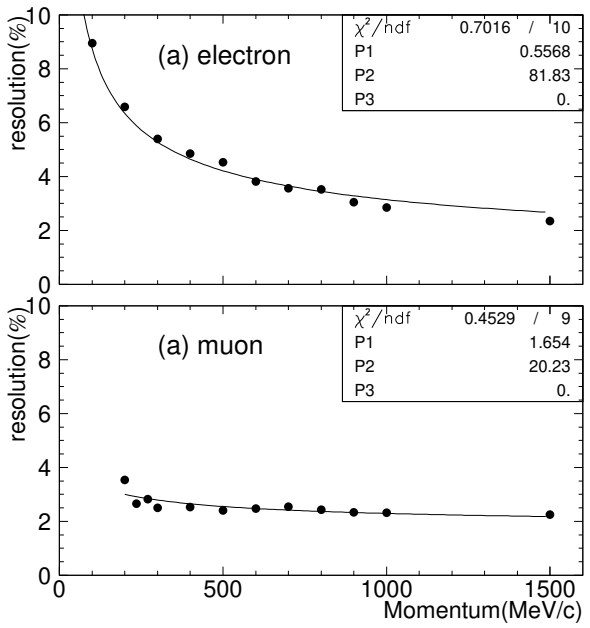

Figure 5.18: Momentum resolution as a function of energy for electrons and muons [92].

are required to perform neutrino oscillation studies with partially-contained events.

The vertex and direction fits for the partially-contained events are obtained from a variation of the A-fit algorithm described in Sec. 5.3.1. No ring counting or particle identification algorithms are run. To ensure that the fitted track is the muon track which left the detector, and not a secondary particle track, a new direction fit is assigned if:

- the number of hit tubes in the OD is 20 or more, and
- there are no saturated ($q > 200$ p.e.) ID PMT's within 2 m of the projected exit point, or
- more than 800 ID PMT's recorded more than 200 p.e.

The first criterion requires the presence of a clear OD cluster. Since PMT's near a muon exit point typically saturate, the second criteria requires the fitted track direction to point toward the muon exit point. The third criteria catches poorly fit direction fits due to the presence of a large number of saturated PMT's. If the first and either the second or third criteria are met, the fitted direction is replaced with a direction vector that points from the fitted vertex to the center of the OD PMT cluster.

Chapter 6

Prediction of Atmospheric Neutrino Event Rates

6.1 Atmospheric Neutrino Flux

Atmospheric neutrino fluxes have been calculated by several authors [96, 97, 98, 99, 100, 101, 102, 103, 104]. Super–Kamiokande uses the flux in Ref. [96] using the calculation in Ref. [97] as a cross-check. This section outlines the flux calculations, summarizing the main results of Ref. [96].

Calculations of the atmospheric neutrino flux require models of

1. the primary cosmic ray flux,

2. the interactions of the cosmic rays in air, and

3. the interactions and decays of the secondary particles in air.

These models are outlined in the sections that follow.

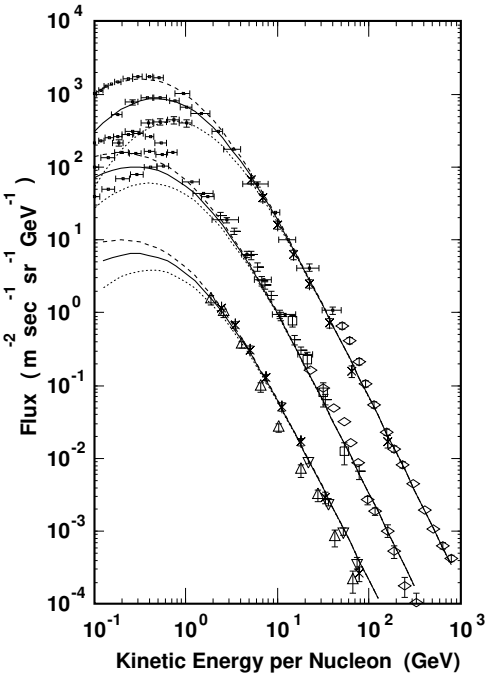

Figure 6.1: Observed fluxes of H (top), He (middle) and CNO (bottom). Lines are for parameterizations for solar average (solid), solar minimum (dotted) and solar maximum (dashed) [96].

6.1.1 Primary Cosmic Ray Flux

Models of the primary cosmic ray flux are computed separately for low energies ($E_{cr} \lesssim 100$ GeV, $E_\nu \lesssim 3$ GeV) and high energies. The primary fluxes of H, He and CNO (Carbon, Nitrogen and Oxygen) have been measured at low energies by a number of experiments. The cosmic ray flux is composed of 95% H, 5% He, and <1% CNO. These account for approximately 80%, 15%, and 5% of the neutrino flux respectively. Figure 6.1 shows the assumed primary cosmic ray flux for solar minimum, average, and maximum compared to experimental measurements

At low energies the effects of the solar wind on the primary cosmic ray flux are important. During periods of high solar activity (solar maximum) the primary flux is lower than during periods of low solar activity (solar minimum). The cosmic ray fluxes are calculated separately for solar minimum, solar average, and solar maximum.

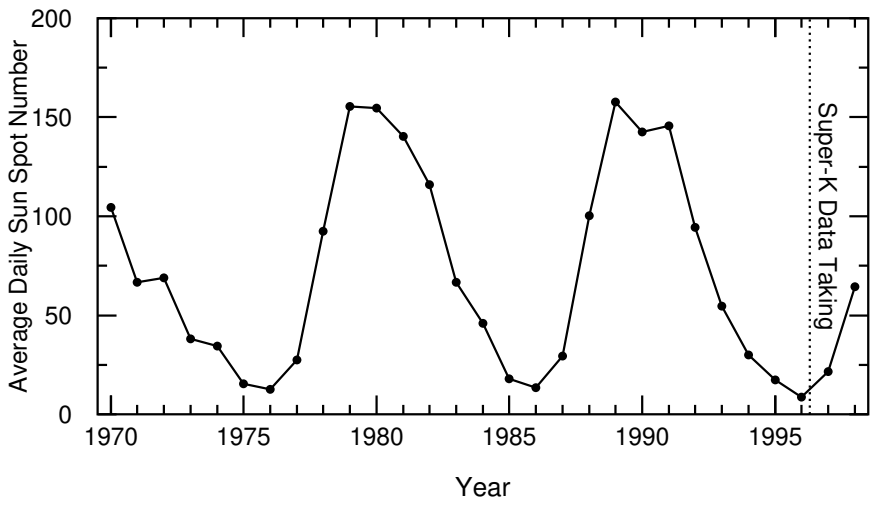

Figure 6.2: The average number of Sun spots per day for each year since 1970 [105].

The solar cycle is traced either through observation of Sun spot numbers or through neutron counters placed atop mountains. The average number of Sun spots for each year is plotted in Fig. 6.2. Solar-minimum occurred in 1996, just as Super–Kamiokande began taking data. We have assumed solar minimum fluxes for the calculation of atmospheric neutrino event rates. The next solar maximum is expected in mid 2001. The difference in the expected sub-GeV event rate for solar minimum is about 2% higher than for solar average.

The effects of the Earth's magnetic field on primary cosmic rays is also important at low energies. A cosmic ray is required to have high rigidity (momentum per unit charge) to penetrate the Earth's magnetic field. The cutoff rigidity is calculated as a function of Θ (zenith angle) and ϕ (azimuthal angle) by propagating antiprotons backwards through the Earth's magnetic field. The Earth field is modeled using expansions calculated in Ref. [106]. The cutoff rigidity is taken to be the minimum antiproton momentum which reaches a radius of 10 Earth radii, where the Earth field

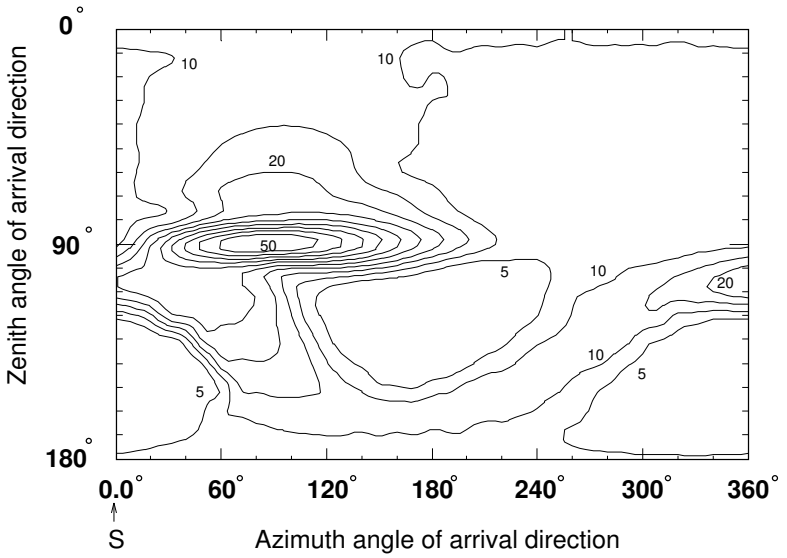

Figure 6.3: The cutoff rigidity in GeV for the Super–Kamiokande site following the calculation of Ref. [96]. In the figure, $\Theta = 0°$ corresponds to particles arriving from directly over head, and $\Theta = 180°$ those from directly below. The azimuthal angles $(0°, 90°, 180°, 270°)$ are south, east, north and west.

and interstellar magnetic fields are of equal size. The cutoff rigidity as a function of Θ and ϕ is plotted in Fig. 6.3 for the Super–Kamiokande site. Note that the cutoff rigidity is much higher for easterly directions than for westerly directions. Thus, a higher cosmic ray flux is expected from the west than from the east. Observation of this east-west effect established that the primary cosmic ray fluxes were primarily positively charged. Recently, the east-west effect was observed for the first time in neutrinos by Super–Kamiokande [107]. This measurement is significant for two reasons. First, it demonstrates that the effects of the Earth's field have been adequately accounted for in the flux calculations. Second it demonstrates the ability to resolve a known angular distortion of the atmospheric neutrino flux using Super–Kamiokande, increasing confidence in the zenith angle measurements that indicate neutrino oscillation.

The cosmic ray fluxes above 100 GeV (which give rise to neutrinos of $\gtrsim 10$ GeV)

	A (m^{-1} sec^{-1} sr^{-1} GeV^{-1})	γ
H	$6.65 \pm 0.13 \times 10^{-2}$	-2.75 ± 0.020
He	$3.28 \pm 0.05 \times 10^{-3}$	-2.64 ± 0.014
CNO	$1.40 \pm 0.07 \times 10^{-4}$	-2.50 ± 0.06
Ne-S	$3.91 \pm 0.03 \times 10^{-5}$	-2.49 ± 0.04
Fe	$1.27 \pm 0.11 \times 10^{-5}$	-2.56 ± 0.04

Table 6.1: The power law fits used to model the high energy cosmic ray fluxes [96].

are fitted to a power law:

$$\mathcal{F}(E) = A \left(\frac{E}{100 \text{ GeV}} \right)^{\gamma}. \tag{6.1}$$

Fit results are given in Table 6.1.

6.1.2 Interactions of Cosmic Ray Nuclei with Air

The interactions of cosmic ray nuclei in air create pions and kaons which then decay producing neutrinos. The decay chain for pions is given in Eq. 1.6. A variety of methods [108, 109, 110, 111] are used to model these interactions over the full energy range. The fraction of K to π is taken to be 7% at 10 GeV, 11% at 100 GeV and 14% at 1000 GeV. The uncertainty in the total cross section is estimated to be 10%. Note that the most probable reaction is

$$p + A_{air} \rightarrow n + \pi^{+} + X \tag{6.2}$$

which leads to a 10-20% excess of ν_e over $\bar{\nu}_e$.

Neutrinos are produced by the decay of pions, kaons, and muons. All decays are assumed to take place along the primary cosmic ray direction. The effects of muon polarization are considered, reducing the ν_e flux by about 10% at $E_\nu = 500$ MeV

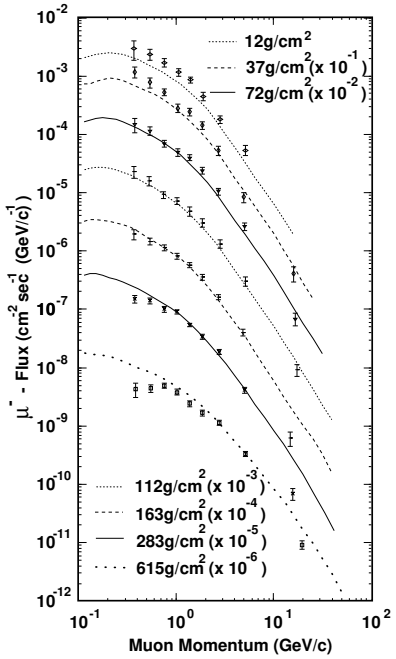

Figure 6.4: Comparison of the estimated μ^- flux with experimental data [96].

and 15% at $E_\nu = 3$ GeV.

6.1.3 Interaction of Secondary Particles in Air

The density and composition of the atmosphere is modeled using a standard table [112], and is used to compute the rates of interaction and decay for pions and kaons. Most mesons with energies below ~10 GeV decay before interacting, but the interaction probability becomes large above 100 GeV. As a cross-check, the calculations are compared with muon flux data at various atmospheric depths. This comparison is shown in Fig. 6.4.

Figure 6.5 shows the $(\nu_\mu + \bar{\nu}_\mu)/(\nu_e + \bar{\nu}_e)$, $\nu_e/\bar{\nu}_e$, and $\nu_\mu/\bar{\nu}_\mu$ ratios for several calculations as a function of energy. Note that all calculations predict a $(\nu_\mu+\bar{\nu}_\mu)/(\nu_e+\bar{\nu}_e)$ ratio of above 2 for energies between 100 MeV and 10 GeV.

The expected zenith angle rates for ν_μ and ν_e and shown in Fig. 6.6. At low

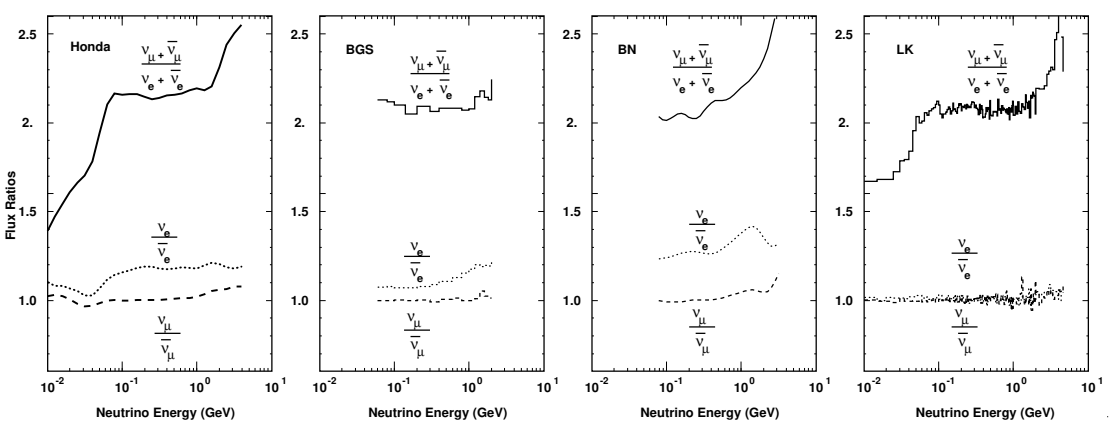

Figure 6.5: The $(\nu_\mu + \bar{\nu}_\mu)/(\nu_e + \bar{\nu}_e)$, $\nu_\mu/\bar{\nu}_\mu$ and $\nu_e/\bar{\nu}_e$ ratios as functions of neutrino energy for calculations by Honda [96], BGS [97], BN [102], and LK [103].

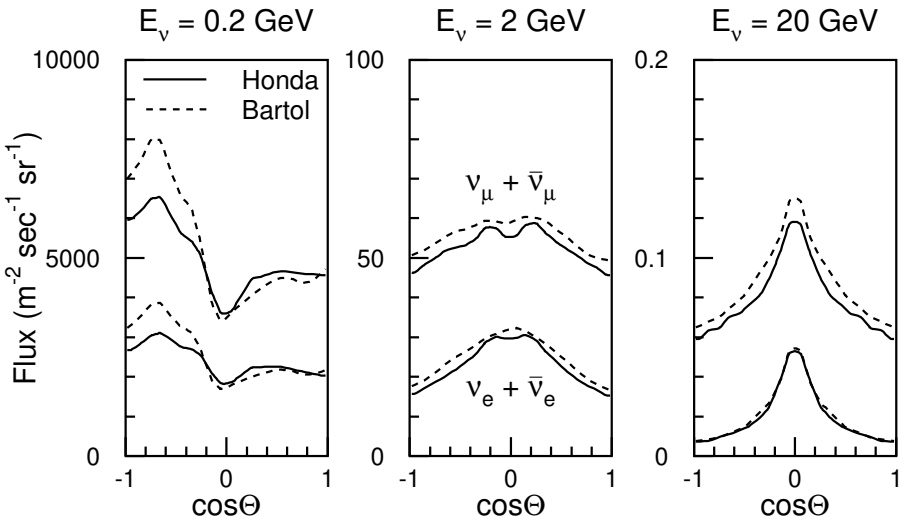

Figure 6.6: The estimated neutrino flux verse zenith angle for the Honda [96] (solid line) and Bartol [97] (dashed line) calculations.

energies the fluxes are asymmetric due to the effects of the Earth's field on the primary cosmic rays; however the fluxes are symmetric at high energies.

6.2 Neutrino Cross Sections

Atmospheric neutrinos are observed through their interactions with nucleons and to a lesser extent orbital electrons. As the ratio of the cross sections for neutrinos on electrons to the cross sections for neutrinos on nucleons is roughly $m_e/m_N \sim 5 \times 10^{-4}$ at neutrino energies of 1 GeV, interactions of neutrinos and electrons can safely be neglected. Several classes of neutrino-nucleon interactions are considered in the prediction of the atmospheric neutrino event rates in Super–Kamiokande. The total cross section is separated into three main classes

$$\sigma_{total} = \sigma_{elastic} + \sigma_{1-\pi} + \sigma_{multi-\pi} \tag{6.3}$$

where the total neutrino-nucleon cross section, σ_{total}, is taken to be the sum of the cross sections for elastic scattering ($\sigma_{elastic}$), single pion production ($\sigma_{1-\pi}$) and deep-inelastic production of multiple pions ($\sigma_{multi-\pi}$). The relative contributions to the total neutrino-nucleon cross sections is shown in Fig. 6.7 for neutrinos and Fig. 6.8 for anti-neutrinos. Based on the atmospheric neutrino fluxes and estimated total neutrino cross-sections, an atmospheric neutrino sample corresponding to a 20-year exposure of the Super–Kamiokande detector was generated.

Below $E_\nu \sim 1$ GeV elastic and quasi-elastic interactions dominate. The contributions to the total cross section for single pion modes peaks near $1 < E_\nu < 3$ GeV. Above $E_\nu = 10$ GeV the neutrino cross sections are dominated by multi-pion production.

The neutrino interaction simulation codes used by Super–Kamiokande were adapted from those used by the Kamiokande experiment [113].

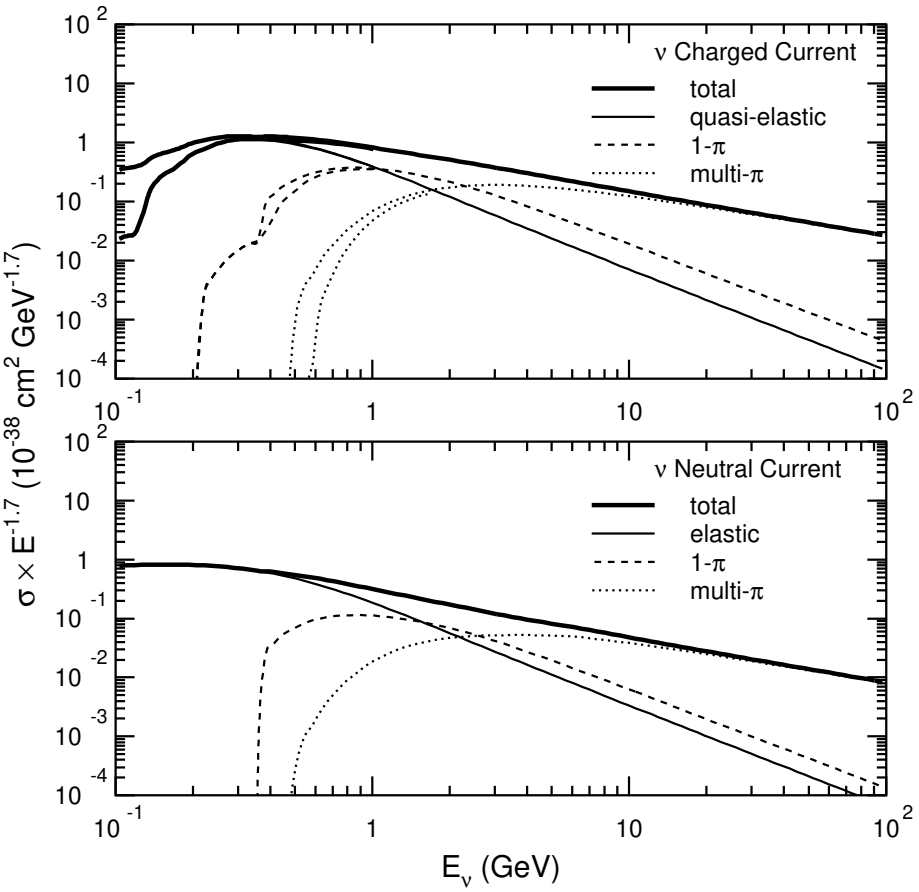

Figure 6.7: Total neutrino cross section weighted by $E_\nu^{-1.7}$ to approximate $dN/d(\ln E_\nu)$ where N is proportional to the number of interactions.

6.2.1 Elastic scattering

The elastic scattering processes on nucleons are charged-current quasi-elastic scattering, $\nu N \to lN'$, and neutral-current elastic scattering, $\nu N \to \nu N$. These processes are calculated according to the standard V-A formulation of weak interactions [114]. Distributions of final state lepton energies and momentum are calculated as a function q^2, the square of the 4-momentum transfer. For interactions on nucleons inside the oxygen nucleus the Fermi momentum of the nucleon is selected randomly from the distribution plotted in Fig. 6.9 which is estimated from results from e^- ^{12}C scat-

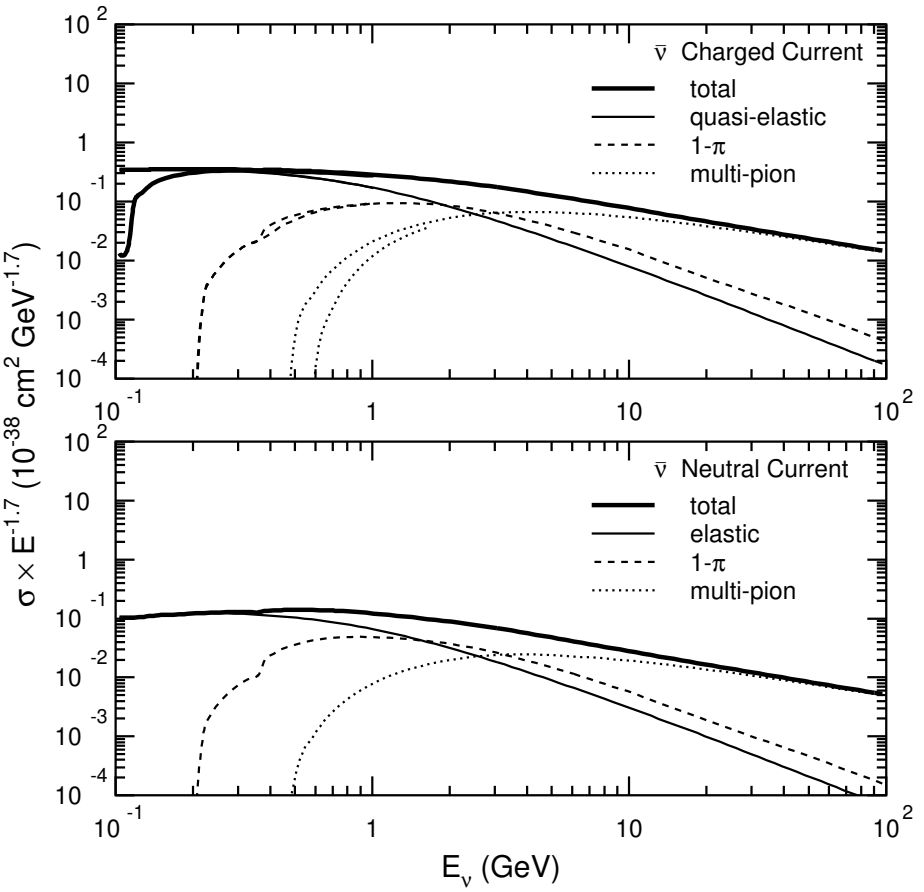

Figure 6.8: Total anti-neutrino cross section weighted by $E_\nu^{-1.7}$ to approximate $dN/d(\ln E_\nu)$ where N is proportional to the number of interactions.

tering experiments [115]. The effects of Pauli blocking are implemented by requiring the recoil nucleon to have a momentum larger than the top of the Fermi surface at 217 MeV/c. If the recoil momentum is less than 217 MeV/c then the interaction is suppressed.

Neutral-current elastic cross sections are derived from the the charged-current cross sections using the following relations:

$$\sigma(\nu p \to \nu p) \quad = \quad 0.153\sigma(\nu n \to e^- p) \tag{6.4}$$

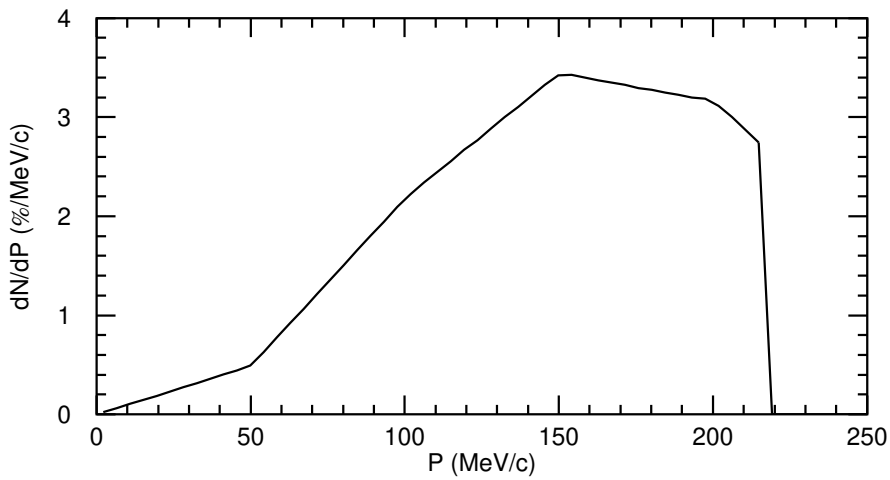

Figure 6.9: Distribution of Fermi momentum for nucleons in $^{1}6$O.

$$\sigma(\bar{\nu}p \to \bar{\nu}p) = 0.218\sigma(\bar{\nu}p \to e^{+}n) \quad (6.5)$$

$$\sigma(\nu n \to \nu n) = 1.5\sigma(\nu p \to \nu p) \quad (6.6)$$

$$\sigma(\bar{\nu}n \to \bar{\nu}n) = 1.0\sigma(\bar{\nu}p \to \bar{\nu}p) \quad (6.7)$$

Neutral-current elastic interactions are only visible when the recoil proton is over threshold or the recoil nucleon interacts in the water to produce pions; hence these interactions are rarely observed. Figure 6.10 shows the charged- and neutral- current quasi-elastic and elastic scattering cross sections for neutrinos on nuclei.

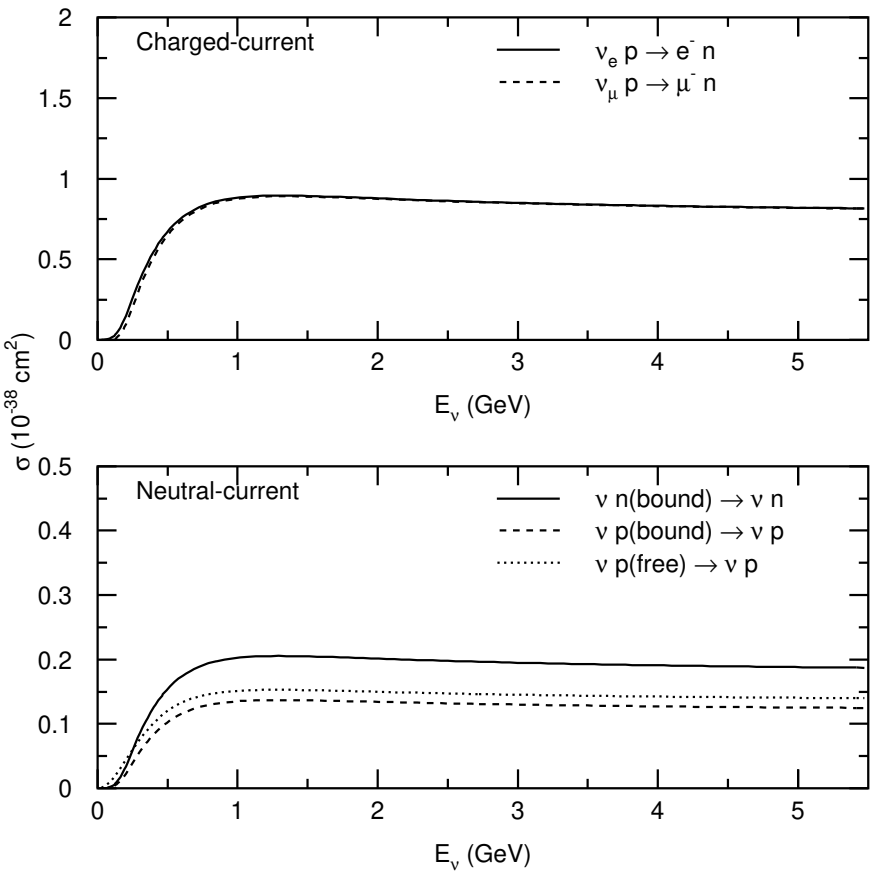

Figure 6.10: Quasi-elastic and elastic scattering neutrino cross-sections for free and bound nuclei.

6.2.2 Single Pion Modes

At intermediate energies $E_\nu \sim 1 - 2$ GeV neutrinos begin to excite resonant states of the nucleons, which decay emitting an single pion

$$\begin{aligned} \nu + N &\rightarrow N^* + (\nu, l) \\ &\hookrightarrow N + \pi \end{aligned} \tag{6.8}$$

The cross sections for these modes are calculated following Rein and Seghal [116]. The strongest resonant state is $N^* = \Delta(1232)$, although 18 other resonant states

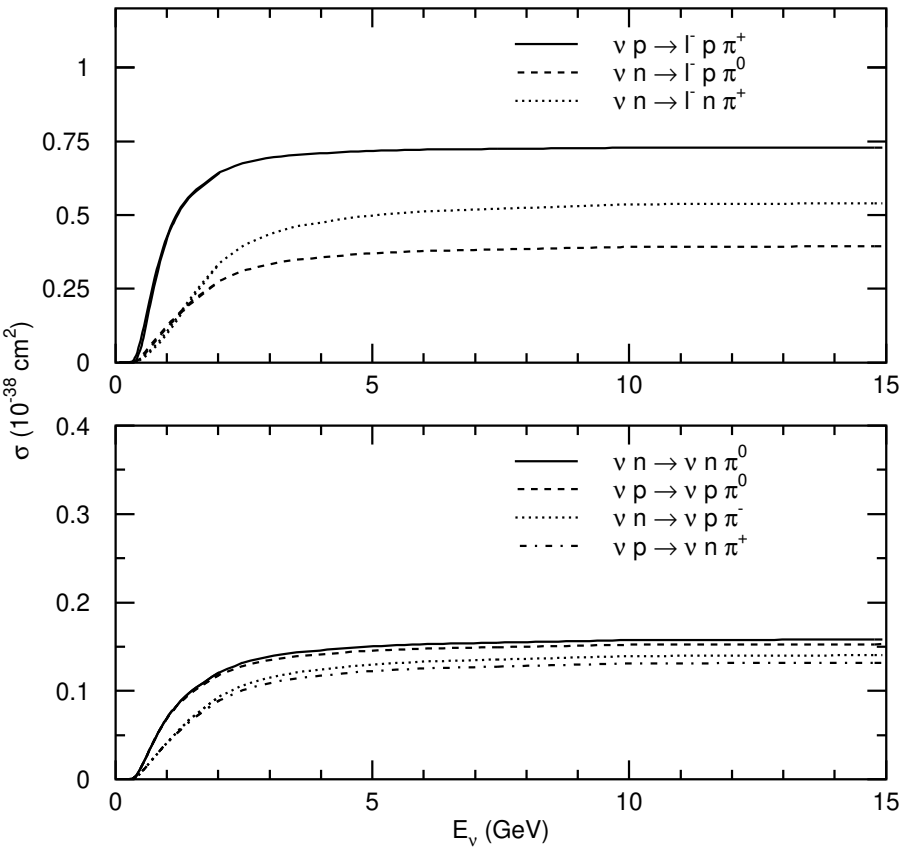

Figure 6.11: Neutrino single pion cross sections.

below 2 GeV, are also considered accounting for interference between resonances. Although pion production dominates, production of other particles (η, and K) is also considered due to their potential contributions to backgrounds for proton decay searches. The angular distribution of the pions from $\Delta(1232)$ are calculated, however decays from other modes are taken to be isotropic.

Single pions are also produced in coherent neutrino interactions with ^{16}O. These cross sections are estimated following Ref [116] and are shown in Fig. 6.13.

The effects of inelastic scattering, charge exchange, and absorption of pions produced in the ^{16}O nucleus are simulated. Figure 6.14 shows the fraction of π^+ produced

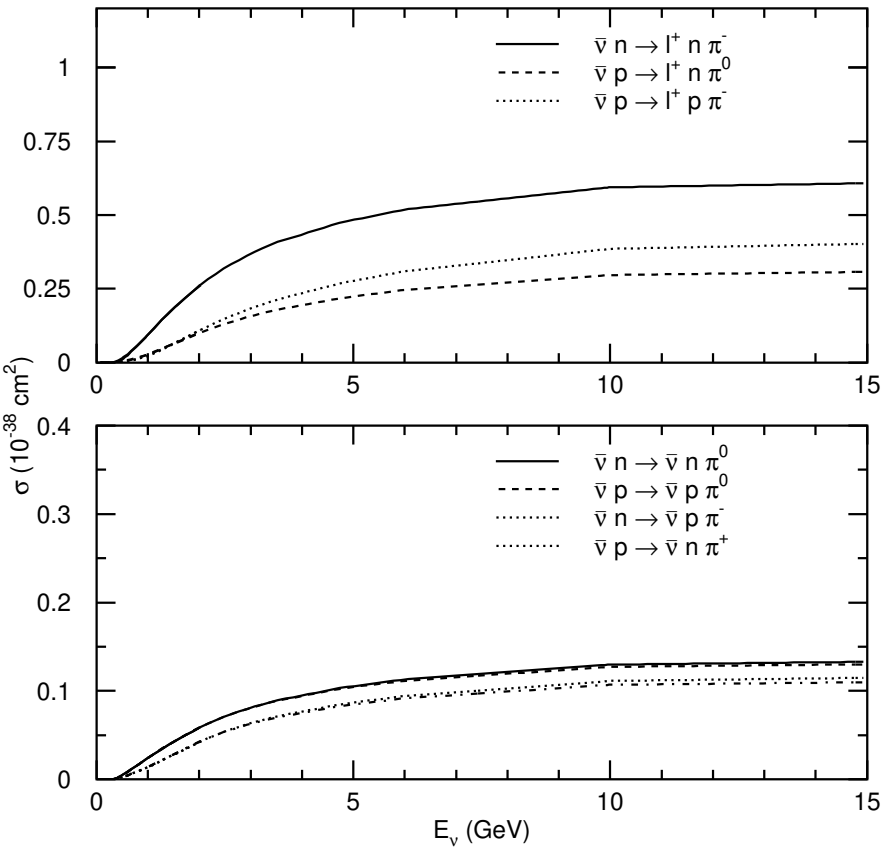

Figure 6.12: Anti-neutrino single pion cross sections.

in the ^{16}O nucleus that do not interact, are absorbed, scatter inelastically, or undergo charge-exchange as a function of the initial pion momentum.

6.2.3 Multi-pion Production

Production of multiple pions is handled in two ways. At low invariant masses ($W <$ 2 GeV) multiple pion production cross sections are calculated according to the model of Rein and Seghal [116]. At high W (above $W > 2$ GeV) the multi-pion cross sections are calculated assuming deep-inelastic scattering using GRV94 parton distribution

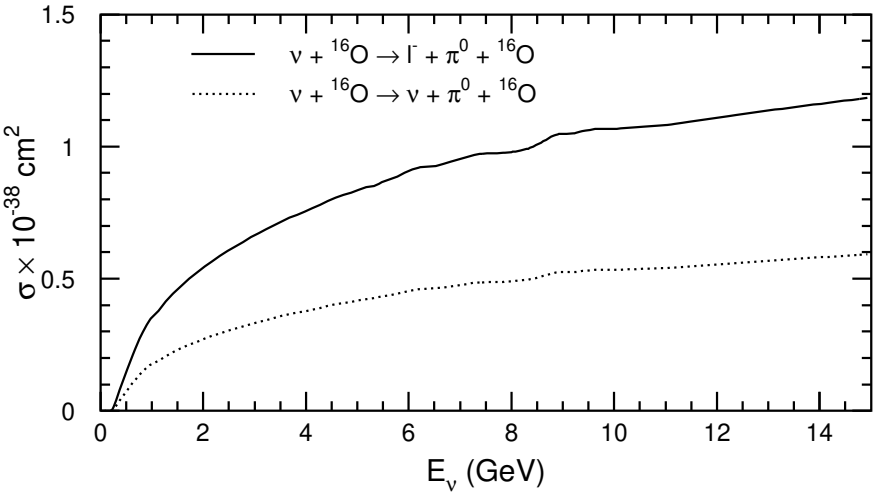

Figure 6.13: Cross sections for coherent single pion production.

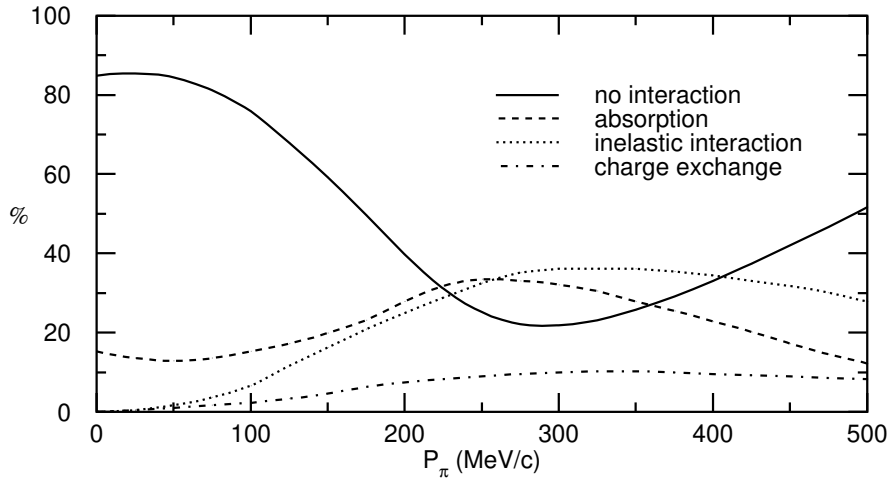

Figure 6.14: The fraction of pions that no not interact, are absorbed, scatter inelastically, or undergo charge-exchange as a function of pion momentum.

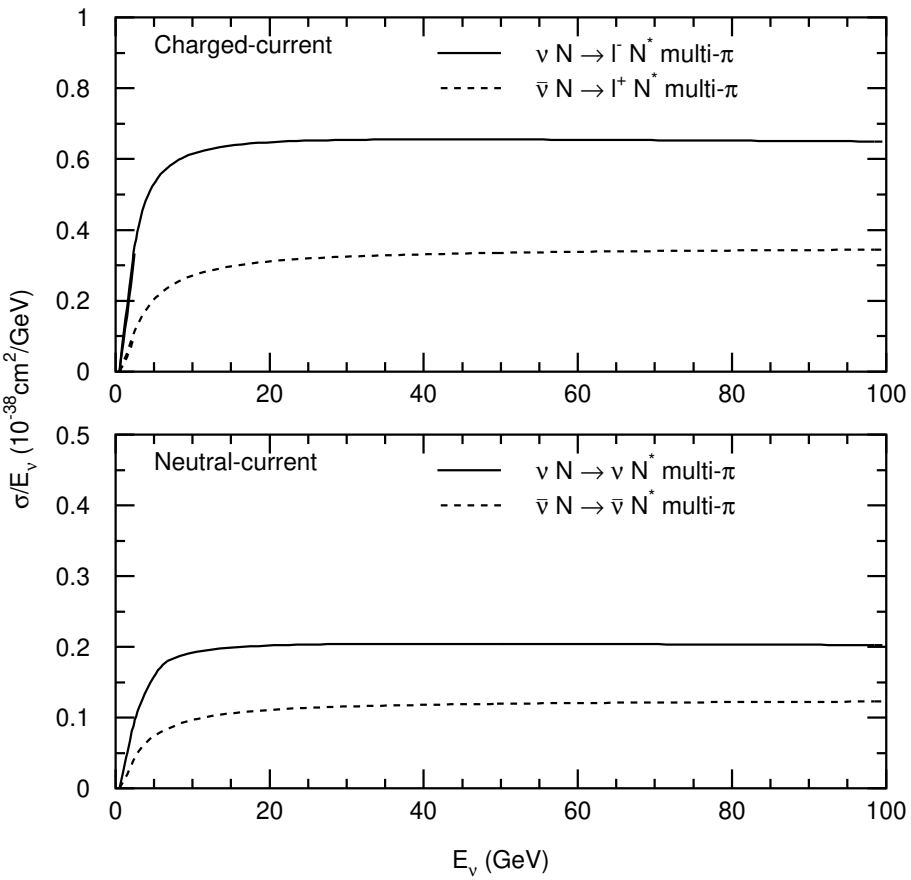

Figure 6.15: Multiple pion production cross sections.

functions [117]. The multi-pion cross sections used to estimate atmospheric neutrino event rates in Super–Kamiokande are shown in Fig. 6.15.

For deep-inelastic scattering the average pion multiplicity $\langle n_\pi \rangle$ is estimated based on a fit to data from Ref. [118] as a function of the invariant mass W:

$$n_\pi = 0.09 + 1.83 \ln W^2. \tag{6.9}$$

The pion forward-backward asymmetry is estimated from Ref. [119]:

$$\frac{\langle n_\pi^{forward} \rangle}{\langle n_\pi^{backward} \rangle} = \frac{0.35 + 0.41 \ln W^2}{0.50 + 0.09 \ln W^2} \tag{6.10}$$

The neutral-current cross section is derived from the charged-current cross sections using the relations:

$$\frac{\sigma(\nu N \to \nu X)}{\sigma(\nu N \to \mu^- X)} = \begin{cases} 0.26 & \text{for } E_\nu < 3 \text{ GeV} \\ (0.26 + 0.4(E_\nu/3 - 1)) & \text{for } 3 < E_\nu < 6 \text{ GeV} \\ 0.30 & \text{for } E_\nu > 6 \text{ GeV} \end{cases} \tag{6.11}$$

and

$$\frac{\sigma(\bar{\nu} N \to \bar{\nu} X)}{\sigma(\bar{\nu} N \to \mu^+ X)} = \begin{cases} 0.39 & \text{for } E_\nu < 3 \text{ GeV} \\ (0.39 - 0.02(E_\nu/3 - 1)) & \text{for } 3 < E_\nu < 6 \text{ GeV} \\ 0.37 & \text{for } E_\nu > 6 \text{ GeV}. \end{cases} \tag{6.12}$$

The estimates are based on data from Ref. [120] for $E_\nu < 3$ GeV, and Ref. [121] for $E_\nu > 3$ GeV.

Again, the effects of pion propagation through the ^{16}O nucleus are simulated.

6.3 Detector Simulation

The particles produced from the neutrino interactions simulated above are passed to a GEANT [122] based detector simulation. Hadronic interactions above 500 MeV are simulated based on the CALOR [123] program; at low energies a special program was developed [113].

Cherenkov photons are generated for each 1 cm step using a Poisson distribution about the mean number of photons at a given wavelength, as calculated using Eq. 4.3. Photons are distributed evenly along the track segment and in azimuth with respect to the track direction. Photons are tracked until they are absorbed or detected. Scattering and absorption in water is computed as a function of wavelength. The cross-section included both scattering off water-molecules (Rayleigh scattering) and off particles in the water (Mie scattering). The cross-sections were tuned to direct measurements of the attenuation length in the Super–Kamiokande tank as a function of wavelength (see Fig. 4.22). Photon reflection and absorption off the black sheet that lines the ID, and the Tyvek reflector in the OD, were measured as a function of wavelength and included in the simulation. Photon detection at the PMT uses the measured PMT quantum efficiency (Fig. 4.6) and estimated PMT reflectivity in water. The PMT response incorporates measured timing and charge resolution. PMT dark noise is also included at rates measured in Super–Kamiokande. During event selection and event reconstruction, dead PMT's are masked using tables computed for each sub-run ($\sim$10 minutes) of real data.

Chapter 7

Event Summaries

The analysis in this thesis uses a total of 736 live-days of FC data and 685 live-days of PC data. A full-detector simulation of atmospheric neutrino events equivalent to 20 live-years has been processed by the same event-selection and event reconstruction steps. The main features of these samples are outlined in this chapter.

7.1 Estimates of Sample Composition

Figure 7.1 compares the distribution of the number of rings found in the FC sample, ($E_{vis} > 30$ MeV, distance to nearest wall larger than 2 m) with the FC Monte Carlo. While the absolute rate of atmospheric neutrino events is 25% uncertain, the shapes are in agreement, indicating that the cross-sections, ring-finding performance and particle tracking are in agreement for data and Monte Carlo.

For the calculation of the atmospheric neutrino ratio and neutrino oscillation analysis, only single-ring events from the FC sample are used. This cut enhances the charged-current quasi-elastic fractions of the sample. These cross-sections are relatively well known and make the association between $\nu_e \rightarrow e-$like and $\nu_\mu \rightarrow \mu-$like straightforward. The FC sample is divided into two parts based on the measured

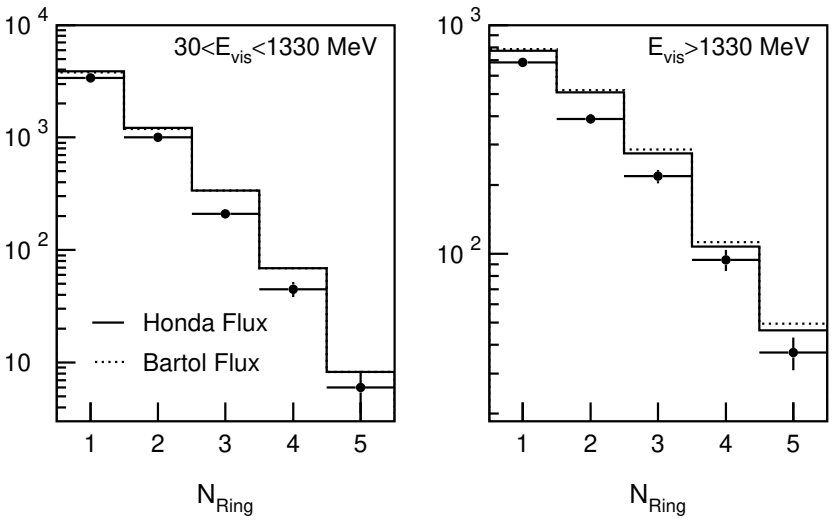

Figure 7.1: Distribution of the number of rings found for data and Monte Carlo.

visible energy, E_{vis}, which is defined to be the energy of an electron shower that would produce the number of p.e. recorded in the event. Historically, the Kamiokande experiment selected events with $E_{vis} < 1.33$ GeV as the region relevant for proton decay searches. The cut is retained for comparison.

The sub-GeV and multi-GeV samples are defined by the following cuts:

- number of Cherenkov rings = 1
- distance to nearest wall > 2 m
- $p_e > 100$ MeV/c, $p_\mu > 200$ MeV/c
- Number of PMT's in largest OD cluster <10
- $E_{vis} < 1.33$ GeV for sub-GeV, $E_{vis} > 1.33$ GeV for multi-GeV.

The estimated compositions of the sub-GeV $e-$like and $\mu-$like samples are summarized in Table 7.1

	CC			NC		
	q. elastic	single-π	multi-π	elastic	single-π	multi-π
sub-GeV						
1-ring e-like	10002 (122)	2623 (157)	356 (148)	27	1118	283
1-ring μ-like	55 (16603)	21 (4398)	5 (502)	125	580	228
2-ring	648 (878)	1310 (2553)	662 (1344)	97	2296	1245
>2-ring	27 (53)	250 (571)	448 (780)	21	276	577
multi-GeV						
1-ring e-like	1237 (27)	882 (39)	349 (38)	0	66	12
1-ring μ-like	3 (2098)	1 (1319)	1 (438)	1	0	0
2-ring	165 (170)	480 (855)	432 (800)	0	14	30
>2-ring	21 (27)	136 (225)	288 (465)	1	14	1245
PC	17 (855)	31 (1155)	20 (898)	0	1	5

Table 7.1: Number of events in each reconstruction class from a 20 year Monte Carlo simulation of atmospheric neutrino interactions in the Super–Kamiokande detector. Charged–current interactions are given separately for ν_e and ν_μ (in parenthesis).

The particle identification parameter that is used to separate $e-$like events from $\mu-$like is plotted in Fig. 7.2. The the $e-$like and $\mu-$like peaks are well separated. Particle identification is estimated to be roughly 98% efficient for both the sub-GeV and multi-GeV samples.

Because PC events must have a highly penetrating muon in the final state, the sample is naturally a very pure sample of ν_μ charged-current events. Thus no single-ring requirement is made and the sample is assumed to be entirely $\mu-$like and are added with the FC, multi-GeV $\mu-$like sample. Table 7.1 summarizes the estimated composition PC sample.

7.2 Vertex and Momentum Distributions

The vertex distributions for data and Monte Carlo are compared for the FC samples in Fig. 7.3 and the partially contained samples in Fig. 7.4. The figures which show radius exclude the region within 2 m of the top and bottom of the tank and the

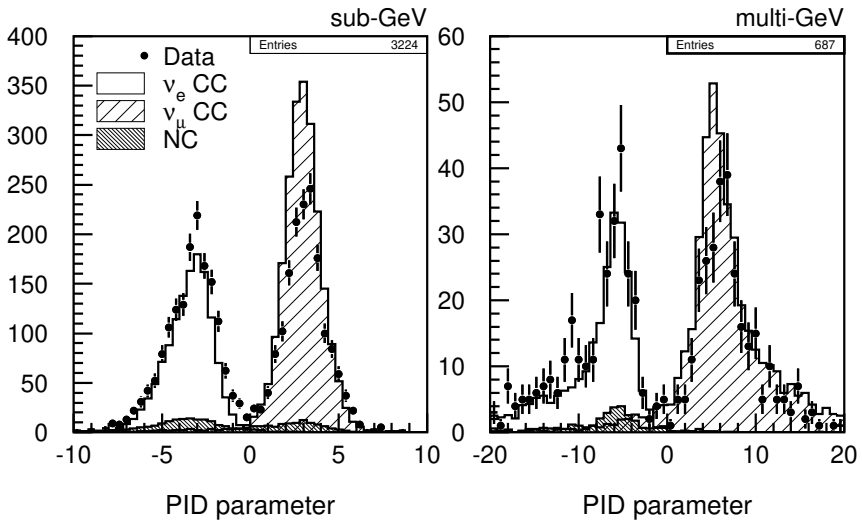

Figure 7.2: The particle identification parameter used to separate $e-$like and $\mu-$like events. The Monte Carlo is shown separately for charged-current, and neutral-current events.

figures which show detector z coordinate exclude events 2 m from the detector barrel. The distributions vary smoothly across the fiducial boundary (shown in each case as a dotted line) and the sub-GeV events exhibit no excess near the detector walls indicating that background from entering neutrons are not present. The FC rates decrease near the detector walls as muons near the wall will exit the detector. The same effect also explains the increase in PC rates near the detector walls.

Figures 7.5 and 7.6 show the momentum distributions of data compared to the Monte Carlo expectation using both Honda and Bartol fluxes. From Fig. 7.5 and 7.6 it is evident that we observe roughly the expected number of $e-$like events but a significant deficit of $\mu-$like events in both high and low energy samples as well as in the PC sample. Figure 7.6 demonstrates the importance of the PC sample. While the multi-GeV $e-$like rates continue out to 100 GeV/c the FC muons rates stop at 10 GeV/c. This is because muons at this energy travel $\sim$ 20 m and leave

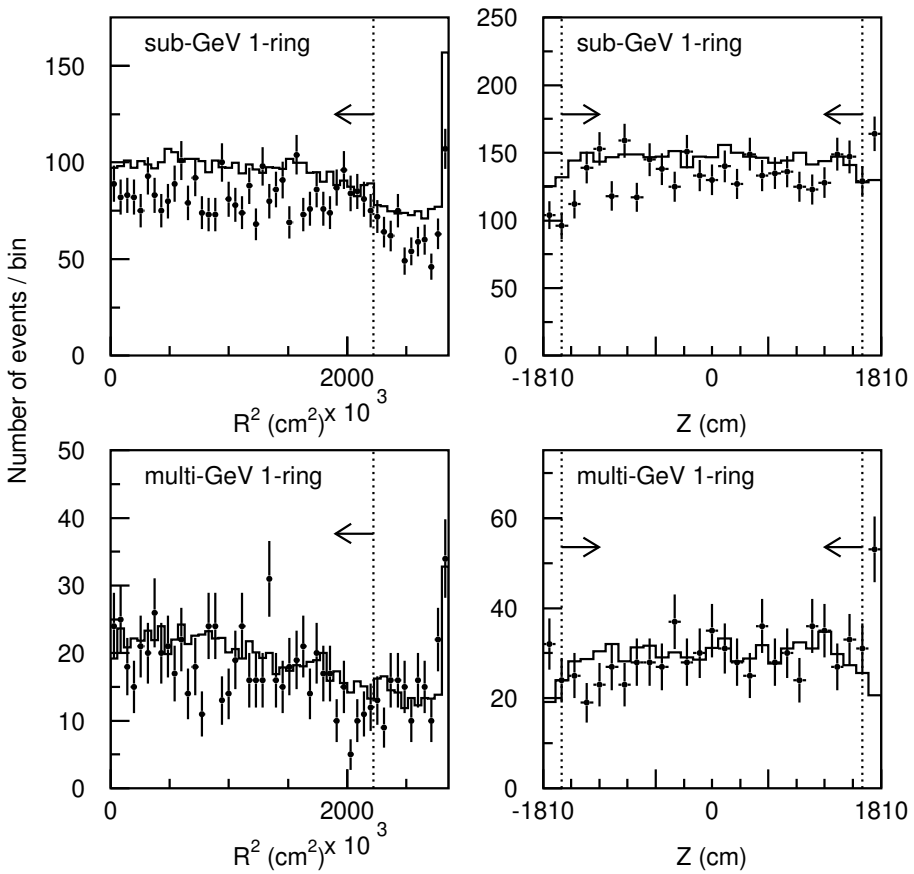

Figure 7.3: Vertex distributions for the FC sub-GeV and multi-GeV samples.

the detector and are recovered in the PC sample. Note that in the PC figure E_{vis} is plotted and not momentum. This is because the muon only deposits a fraction of its energy inside the detector so that only a lower bound on the muon momentum can be reconstructed.

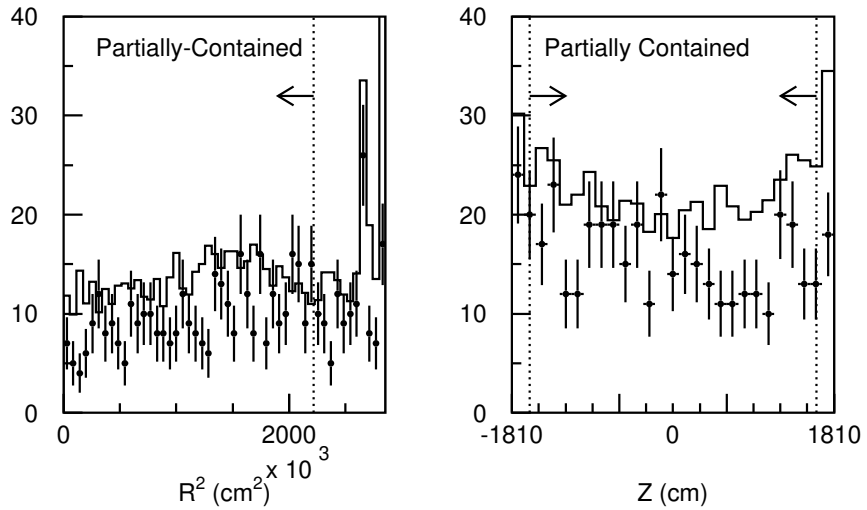

Figure 7.4: Vertex distributions for the PC sample.

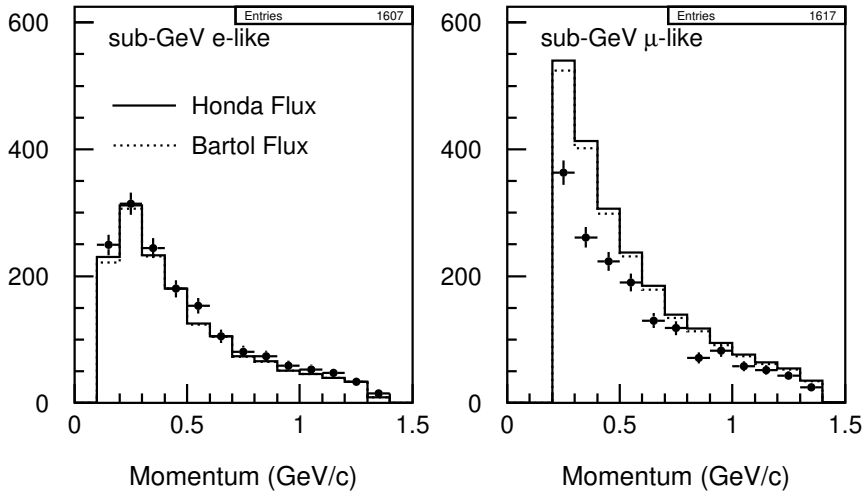

Figure 7.5: Momentum distributions for the single-ring sub-GeV e-like and μ-like samples.

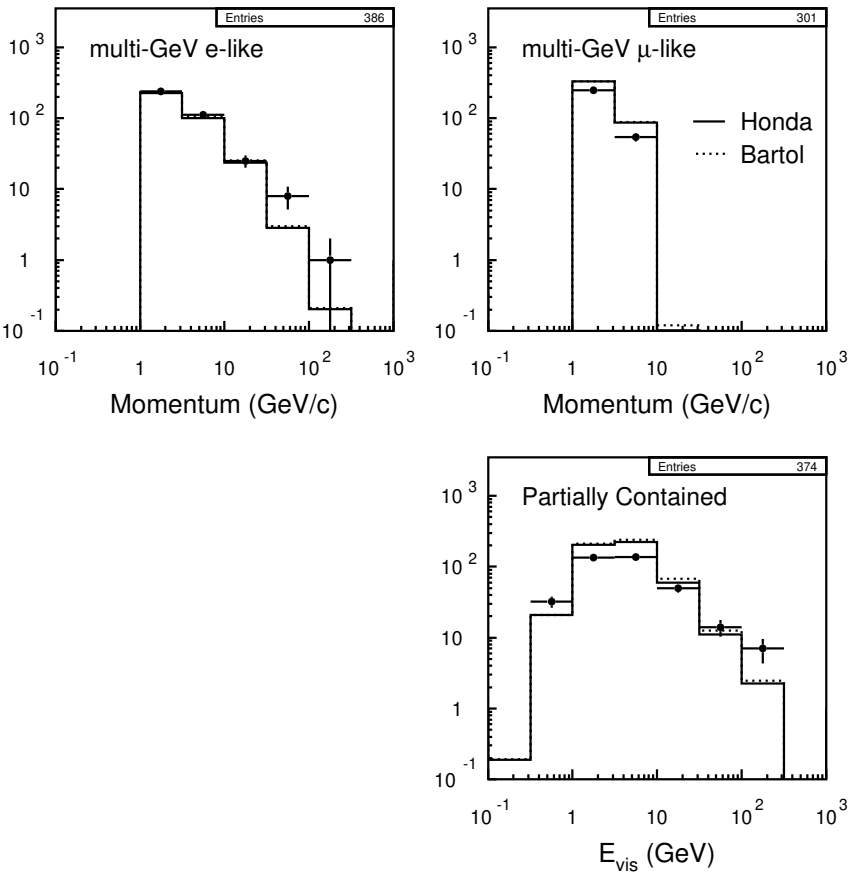

Figure 7.6: Momentum distributions for the multi-GeV e-like, μ-like, and Partially Contained samples.

7.3 Double Ratio Results and Zenith Angle Distributions

The most significant results for the study of neutrino oscillations are the ratios of $\mu-$like and $e-$like events and zenith angle distributions for the sub-GeV and multi-GeV samples. The event rates for the sub-GeV and multi-GeV data and Monte Carlo

	Data	Monte Carlo
sub-GeV		
single-ring	3224	3788.3
e-like	1607	1510.5
μ-like	1617	2277.8
multi-ring	1271	1614.3
total	4495	5402.5
$R =$	$0.67 \pm 0.02\ (stat.) \pm 0.05\ (sys.)$	
multi-GeV		
single-ring	687	773.3
e-like	386	357.4
μ-like	301	415.9
multi-ring	737	925.7
total	1424	1698.9
PC	374	528.7
$R_{FC+PC} =$	$0.66 \pm 0.04\ (stat.) \pm 0.08\ (sys.)$	

Table 7.2: Summary of the sub-GeV, multi-GeV and PC event samples compared with the Monte Carlo prediction.

samples are summarized in Table 7.2. From these event rates, we calculate:

$$R \equiv \frac{(N_\mu/N_e)_{DATA}}{(N_\mu/N_e)_{MC}}$$

$$\mathrm{sub-GeV}: \quad R = 0.67 \pm 0.02 \pm 0.05$$

$$\mathrm{multi-GeV+PC} \quad R = 0.66 \pm 0.04 \pm 0.08.$$

The first uncertainty is statistical, the second is systematic. Estimation of the systematic uncertainties is discussed in Sec. 8.2.1. The probability to have obtained these R values from a fluctuation from $R = 1$ is estimated to be less than 0.001% for the sub-GeV sample and 1% for the multi-GeV sample. Figure 7.7 shows the variation of the R values for the sub-GeV and multi-GeV+PC samples as a function of the distance to the nearest detector wall. The variation of R shows no significant variation throughout the fiducial volume.

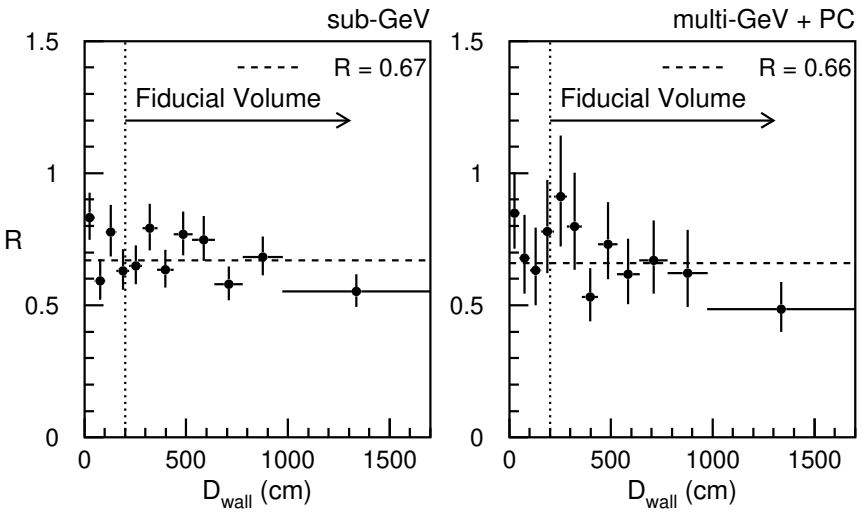

Figure 7.7: The observed R values versus distance to nearest detector wall.

The event-rates are plotted as a function of zenith angle for the sub-GeV and multi-GeV $e-$like and $\mu-$like samples in Fig. 7.8. While the $e-$like distributions match expectations, the $\mu-$like distributions exhibit a significant deviation in both rate and shape. The expected distributions for the $\mu-$like rates is roughly up-down symmetric for both the sub-GeV and multi-GeV samples, however, the data distributions exhibit a significant up-down asymmetry. This asymmetry is quantified by the variable:

$$A = \frac{U - D}{U + D} \tag{7.1}$$

where U is the number of up-going events ($\cos\Theta < -0.2$) and D is the number of down-going events ($\cos\Theta > 0.2$). Figure 7.9 shows the variation of A versus reconstructed lepton momentum. Note that while the $e-$like events match expectation the deviation between the data and expectation for the $\mu-$like grows with increasing momentum. Such behavior cannot be explained by geomagnetic effects as the Earth's magnetic field only effects the neutrino flux below $\sim$3 GeV. Figure 7.9 shows

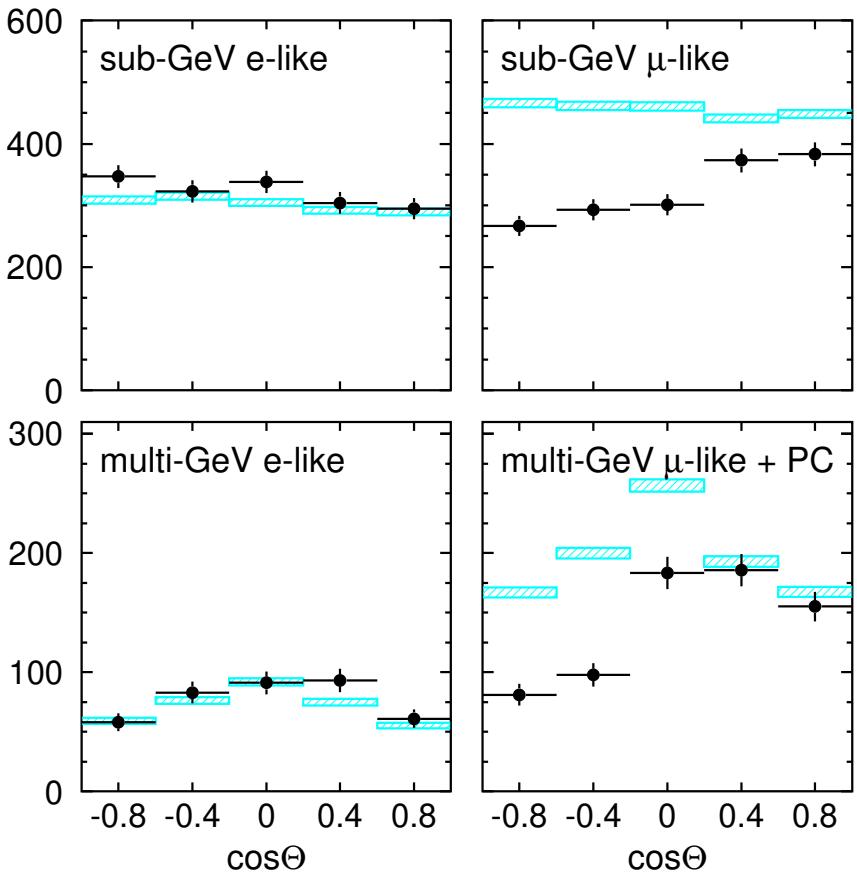

Figure 7.8: Atmospheric neutrino event rates as a function of zenith angle cosine for the sub-GeV and multi-GeV+PC event samples.

the expected behavior A on lepton momentum for $\nu_\mu \leftrightarrow \nu_\tau$ oscillations using the best-fit parameters obtained in Sec. 8.3.1. The expected dependence of A on momentum assuming neutrino oscillations provides a good match to the data. Note that A approaches zero at the lowest momentum even in the case of neutrino oscillations due to the large average scattering angle between the incident neutrino and the final state charged lepton at low energies.

The up-down asymmetry, A, is calculated for three samples in Table 7.3; sub-GeV $p < 400$ MeV/c, sub-GeV $p > 400$ MeV/c and the multi-GeV sample. The up-down

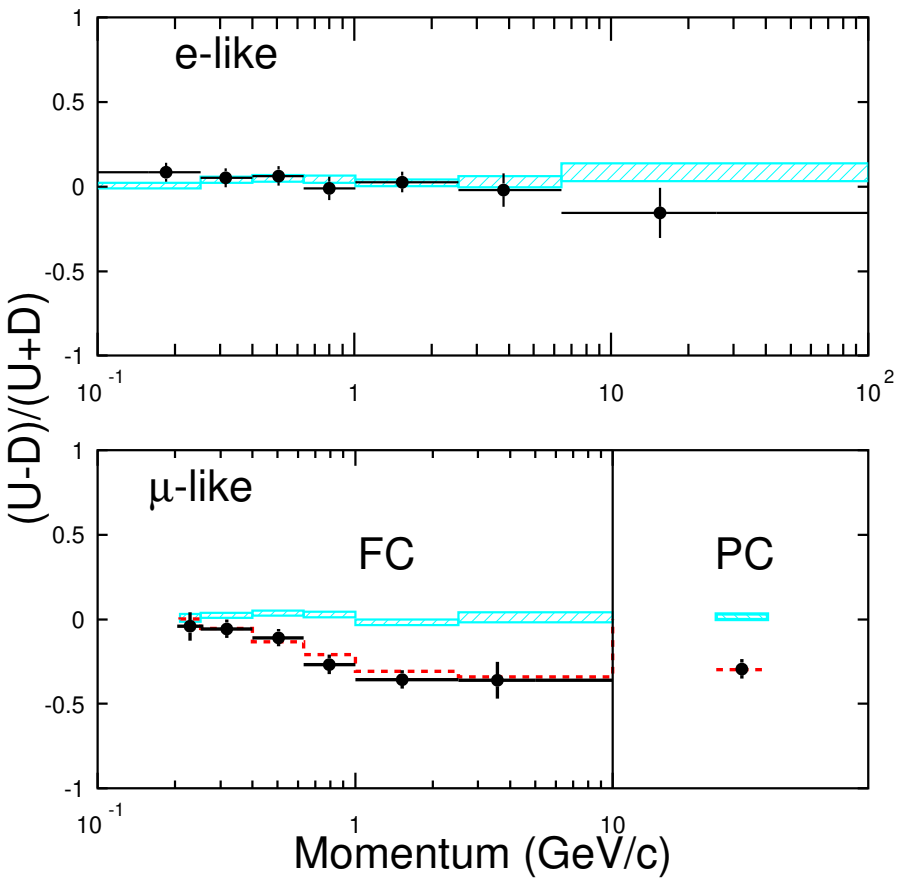

Figure 7.9: The $(U-D)/(U+D)$ zenith angle asymmetry is plotted versus momentum for $e-$like and $\mu-$like events. The expectations for no oscillations is shown in the hatched region. The solid-line shows the expectation for $\nu_\mu \leftrightarrow \nu_\tau$ oscillations using the best-fit parameter found in Sec. 8.3.1.

asymmetry obtained in the multi-GeV sample differs from 0 by more than 7 standard deviations.

	Data			Monte Carlo		
	U	D	A	U	D	A
sub-GeV						
$p < 400$ MeV/c						
$e-$like	345	300	0.07 $\pm$ 0.04	319.1	304.4	0.02 $\pm$ 0.01 $\pm$ 0.02
$\mu-$like	242	260	-0.04 $\pm$ 0.05	387.1	373.0	0.02 $\pm$ 0.01 $\pm$ 0.02
sub-GeV						
$p > 400$ MeV/c						
$e-$like	325	299	0.04 $\pm$ 0.04	304.5	277.6	0.05 $\pm$ 0.01 $\pm$ 0.02
$\mu-$like	318	496	**-0.22 $\pm$ 0.03**	540.5	516.6	**0.02 $\pm$ 0.01 $\pm$ 0.02**
multi-GeV + PC						
$e-$like	141	154	-0.04 $\pm$ 0.06	135.5	130.1	0.02 $\pm$ 0.02 $\pm$ 0.02
$\mu-$like	79	158		161.8	161.6	
PC	93	170	**-0.31 $\pm$ 0.04**	190.8	185.0	**0.01 $\pm$ 0.01 $\pm$ 0.01**

Table 7.3: Summaries of the number of up- and down-going events for the sub-GeV and multi-GeV samples. Note that the asymmetry for the multi-GeV $\mu-$like samples combines the FC and PC samples which have different live-times; the PC events have been scaled to the FC live-time.

Chapter 8

Neutrino Oscillation Analysis

8.1 Simulation of Neutrino Oscillations

Neutrino oscillations are simulated by re-weighting a 20 year equivalent atmospheric neutrino Monte Carlo sample. The simulation includes estimates of neutrino production height distributions, the effects of matter on neutrino propagation through the Earth, the effects of neutrino appearance and disappearance on the neutrino fluxes as well as variations of the event rates due to uncertainties in the inputs to the Monte Carlo calculation.

8.1.1 Atmospheric Neutrino Production Heights

For simulations of neutrino oscillations, the distributions of neutrino production heights are calculated using the analytic approximations in Ref. [124]. The main results of that paper are summarized here.

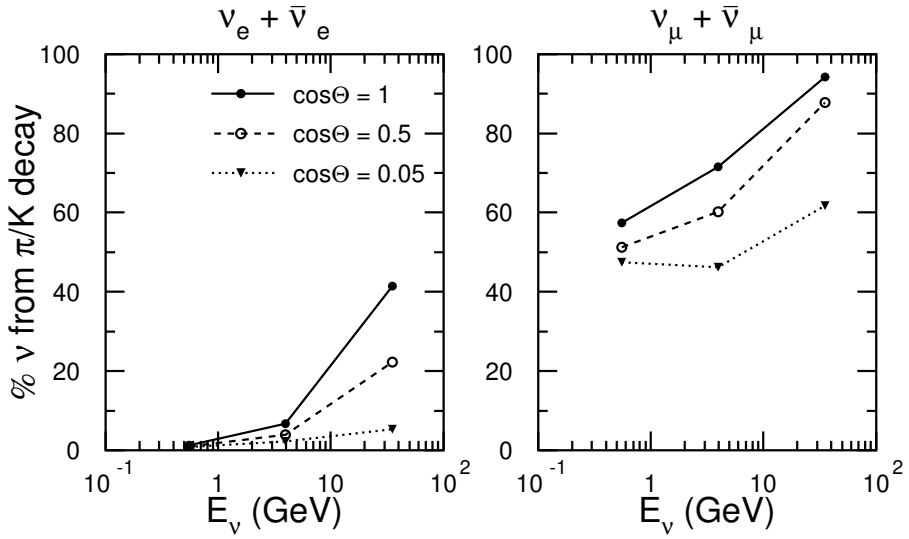

Figure 8.1: The fraction of neutrinos that come from the decays of pions and kaons as a function of neutrino energy.

Calculation of Neutrino Production Heights

The production height is defined to be the distance from the point of neutrino production to the surface of the Earth traveling along the flight path of the neutrino. Above the horizon the total neutrino flight distance is the production height; below the horizon the neutrino flight distance is the sum of the production height and the path length through the Earth ($2R\cos\Theta$), where R is the radius of the Earth and θ is the neutrino zenith angle.

Neutrinos are produced both from the decay of mesons (pions and kaons) produced in the initial interaction of cosmic ray nuclei with air nuclei as well as from the decay of muons which result from the decays of these mesons. The number of neutrinos produced at a production height l per unit length per unit energy at a

γ	Neutrino spectrum power law	1.70
K	$\frac{dN_\nu}{dE_\nu} = KE_\nu^{-(\gamma+1)}$	1.8 cm^{-2}s^{-1}sr^{-1}(GeV)$^\gamma$
λ_N	attenuation length for nucleons	86 g cm^{-2}
Λ_N	interaction length for nucleons	120 g cm^{-2}
X_0	vertical thickness of exponential atmosphere	1030 g cm^{-2}
h_0	scale height for an exponential atmosphere	6.4 km
$Z_{N\pi}$	$\int dx\ x^\gamma dN/dx$ for pions	0.08
$B_K \times Z_{NK}$	$K \to \mu$ branching ratio times $\int dx\ x^\gamma dN/dx$ for kaons	0.0075
r_π	$(m_\mu/m_\pi)^2$	0.5731
r_K	$(m_\mu/m_K)^2$	0.0458
α	dE/dx for muon in air	2 MeV/cm

Table 8.1: Parameters used in the calculation of neutrino production heights.

given zenith angle θ is

$$\frac{dN}{dldE_\nu} = f_{\pi/K}(E_\nu, \cos\Theta)\frac{dN_{\pi/K}}{dldE_\nu} + f_\mu(E_\nu, \cos\Theta)\frac{dN_\mu}{dldE_\nu} \tag{8.1}$$

where $f_{\pi/K}$ is the fraction of neutrinos from decays of pions and kaons and $f_\mu = 1 - f_{\pi/K}$ is the fraction of neutrinos from muon decay. Estimates of $f_{\pi/K}$ based on Monte Carlo simulations are shown in Fig. 8.1.

Because the lifetimes of pions and kaons is short ($c\tau$ = 7.80 m for $\pi^\pm$, 3.71 m for $K^\pm$) the neutrinos from π or K decays are produced essentially at the point where the cosmic ray nuclei strikes the atmosphere. For an exponential atmosphere the number of neutrinos produced at a given distance l per unit energy E_ν can be computed by computing d/dE_ν of the expression for $\frac{dN_{\pi/K}}{dl}$

$$\frac{dN_{\pi/K}}{dl} = \frac{AX_0}{h_0}E_\nu^{-\gamma}\exp\left(-\frac{X}{\Lambda_N}\right)\exp\left(-\frac{l\cos\Theta_{eff}}{h_0}\right) \tag{8.2}$$

where the slant depth X where the pion is produced and decays is given by

$$X = \frac{X_0}{\cos\Theta_{eff}} \exp\left(-\frac{l\cos\Theta_{eff}}{h_0}\right). \tag{8.3}$$

Other parameters in Eq. 8.2 are summarized in Table 8.1. Near the horizon ($\Theta < 70°$) the curvature of the Earth becomes important and is treated by substituting an effective zenith angle θ_{eff}.

Neutrinos from muon decay are treated separately due to the long muon lifetime $c\tau = 659$ m. An approximate expression for differential neutrino production rate from muon decay can be derived by computing d/dE_ν of the following expression for dN_μ/dl

$$\frac{dN_\mu}{dl} = \frac{C_\mu K B}{(\gamma+1)(2E_\nu)^{(\gamma+1)}} \frac{m_\mu c^2}{c\tau} \frac{X}{\lambda_N} \int_0^1 dz\ z^p \exp\left(-\frac{X}{\Lambda_N} z\right) \left[1 + \frac{\alpha X}{2E_\nu}(1-x)\right]^{-(p+\gamma+1)}. \tag{8.4}$$

Here C_μ is obtained from a fit to Monte Carlo simulations and p is given by:

$$p = \frac{h_0}{c\tau\cos\Theta} \frac{m_\mu c^2}{E_\mu + \alpha X}. \tag{8.5}$$

On average, neutrinos from muon decay carry roughly $f = 0.30$ (ν_e) and $f = 0.35$ (ν_μ) of the muon energy. E_μ is taken to be E_ν/f.

The average production height for neutrinos produced from π/K decays and from μ decays are shown in Fig. 8.2 for three neutrino energy ranges as a function of zenith angle. Note that while the production heights from μ decay have a significant energy dependence (due to the lengthening of the muon lifetime in the lab frame) the average production height for neutrinos from π/K decay show no strong dependence on energy. The result of combining the π/K decay production height distributions

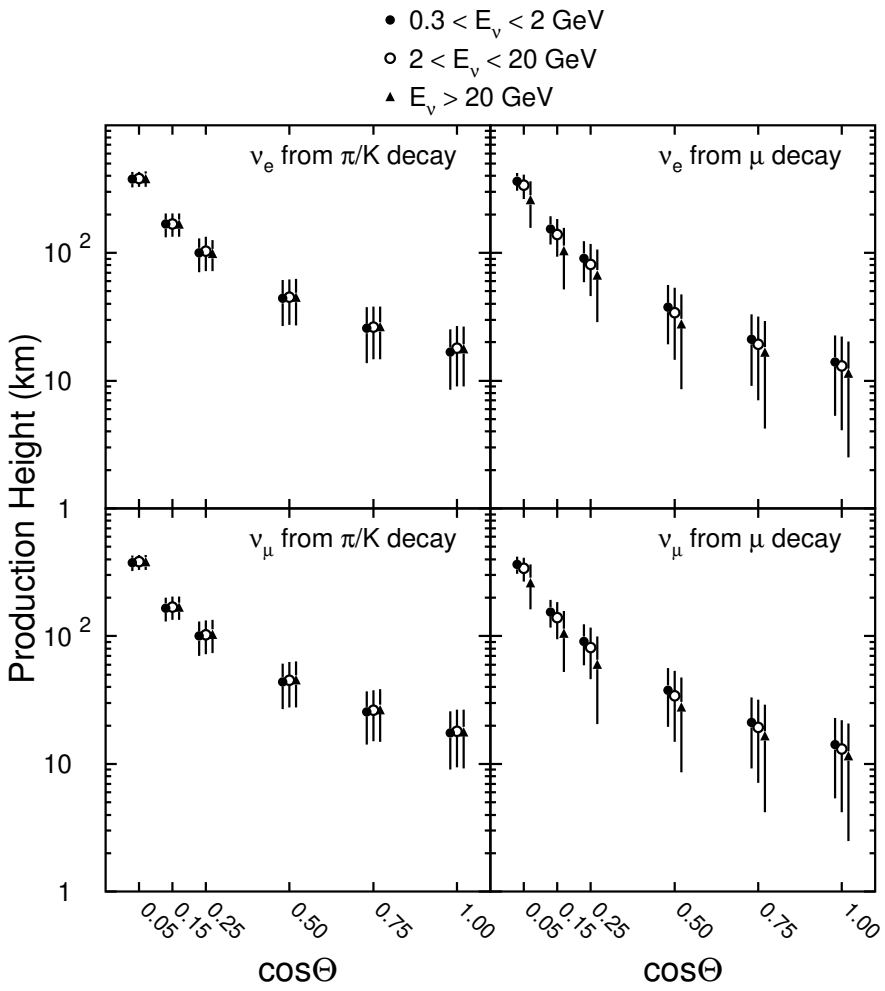

Figure 8.2: The average production height for neutrinos from π/K decays and from muon decays for various neutrino energy ranges. The error bars indicate the rms. spread about the mean. The plot ranges from the horizon $\cos\Theta = 0$ to vertically downward-going neutrinos $\cos\Theta = 1$

and the μ decay production height distributions are shown in Fig. 8.3 for neutrinos produced directly over head and near the horizon.

Estimates of Systematic Uncertainty

Because the neutrino oscillation probability depends on the product of the neutrino flight distance L times the neutrino mass-squared difference Δm^2, errors in esti-

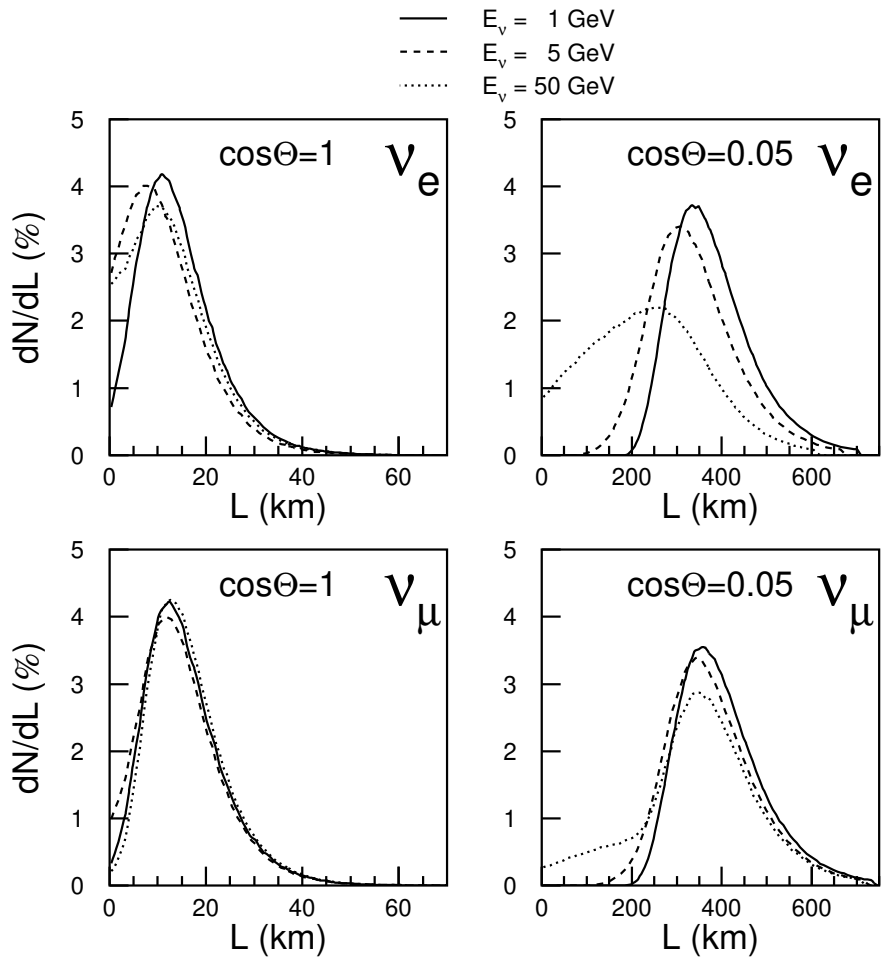

Figure 8.3: The distribution of neutrino production heights for E_ν=1, 5, and 20 GeV for neutrinos from overhead ($\cos\Theta = 1$) and near the horizon ($\cos\Theta = 0.05$).

mating the average neutrino flight distance translate directly to errors in estimates of Δm^2. This uncertainty has been estimated by comparing the present calculation with an independent calculation of the neutrino production heights developed for the Kamiokande experiment. The two calculations agree to within 10%. Similar agreement is found between the Monte Carlo and calculated results reported in Ref. [124] where differences as large as 6% are reported. While the neutrino flight distances for neutrinos produced below the horizon are mostly determined from their path-length

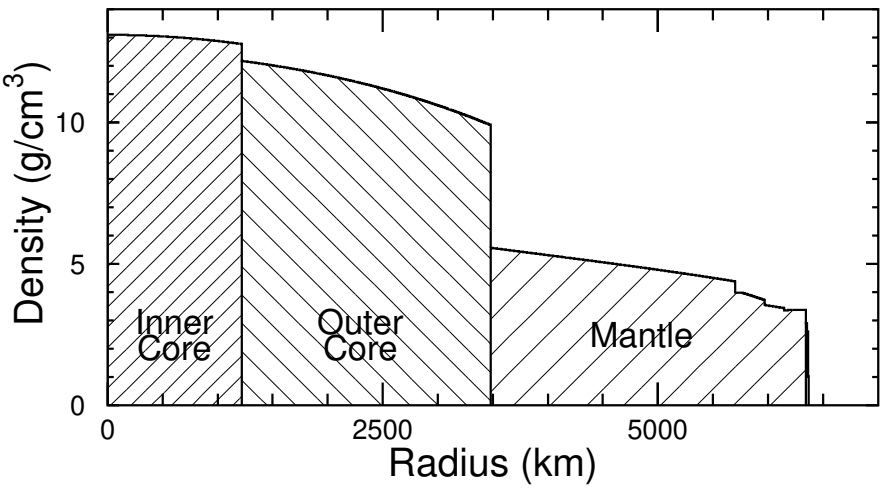

Figure 8.4: Density of the Earth as a function of radius.

through the Earth, the uncertainty in neutrino production heights is conservatively taken to be 10% independent of neutrino zenith angle.

8.1.2 Neutrino Propagation Through the Earth

The effects of matter on the propagation of neutrinos through the Earth become important for neutrino energies of a few GeV for $\Delta m^2 < 10^{-2}$ eV^2. Neutrino propagation through the Earth is treated using the results of Sec. 2.2 for simulations of $\nu_\mu \leftrightarrow \nu_e$, $\nu_\mu \leftrightarrow \nu_{sterile}$ and three-flavor oscillations. Because the effective potentials for ν_μ and ν_τ in matter are identical there are no effects on neutrino propagation due to matter in this mode.

For the calculations, the electron density of the Earth is sampled at 100 segments along the neutrino path. The electron density ρ_e is

$$\rho_e = \frac{Z}{A}\rho_{Earth} \tag{8.6}$$

where the charge-to-mass ration Z/A is taken to be 0.468 in the Earth's core and 0.497 in the mantle and crust[125]. The density of the Earth as a function of radius is taken from Ref. [126] and is shown in Fig. 8.4. Substitution of Earth models (such as [127]) cause negligible differences in the oscillated neutrino fluxes. For simulations involving sterile neutrinos, the neutron density assumes the role of the electron density with the neutron fraction taken to be $(1 - Z/A)$. The electron density of consecutive segments are averaged until the initial segment and the final segment differ by 15% or more. These parameters, 100 initial segments and 15% variation, produce negligible deviations from calculations using higher tolerances and significantly reduce the number of calculations required. For each remaining segment the neutrino transition matrix, A_i, is calculated as a function of the electron density and length of the i^{th} segment. The effects of matter on neutrino propagation are neglected for segments where $1 \times 10^{-4}\rho_e(\text{mole/cm}^3)E(\text{GeV})/\Delta\text{m}^2(\text{eV}^2) < 1$. The final transition matrix A for a neutrino at the detector is the product over the n segments

$$A = A_n A_{n-1} A_{n-2} \cdots A_1. \tag{8.7}$$

The transition probability from flavor α to flavor β is

$$P(\alpha \to \beta) = |A_{\alpha\beta}|^2. \tag{8.8}$$

Figure 8.5 shows the differences between calculations of the ν_μ survival probability for $\nu_\mu \leftrightarrow \nu_e$ oscillations including matter effects in the Earth and without matter effects in the Earth as a function of the cosine of the neutrino zenith angle. The differences are greatest below $\cos\Theta < -0.8$ where neutrinos begin to cross the Earth's core. At high energies and low Δm^2 oscillations are highly suppressed by the matter

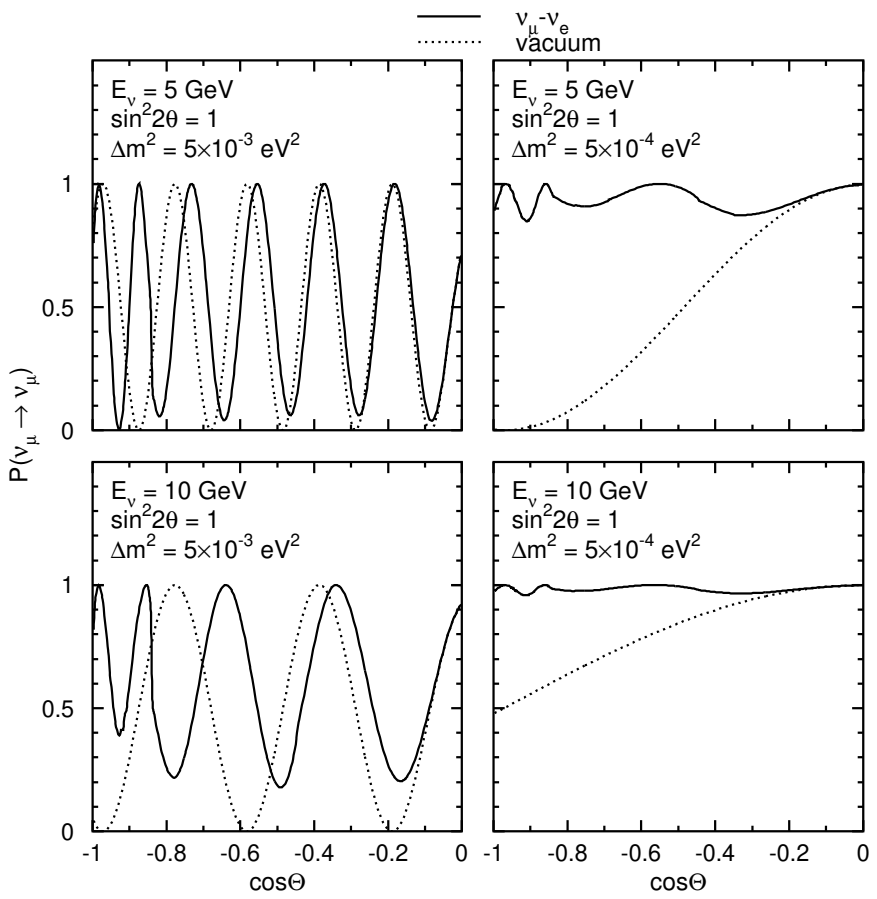

Figure 8.5: Comparison of the ν_μ survival probability for the cases $\nu_\mu \leftrightarrow \nu_e$ and vacuum oscillations for neutrinos propagating through the Earth.

effects. Figure 8.6 shows a similar comparison for oscillations of $\nu_\mu \leftrightarrow \nu_{sterile}$. In general the matter effects for $\nu_\mu \leftrightarrow \nu_{sterile}$ are not as strong as in the case of $\nu_\mu \leftrightarrow \nu_e$ oscillations but are quite significant at high energies and low Δm^2.

8.1.3 Flux Weights for Neutrino Oscillations

The expected atmospheric neutrino event rates for a given set of oscillation parameters $\sin^2 2\theta$ and Δm^2 are computed by re-weighting a large sample (equivalent to a 450 kt-year exposure) on an event-by-event basis for the effects of neutrino oscilla-

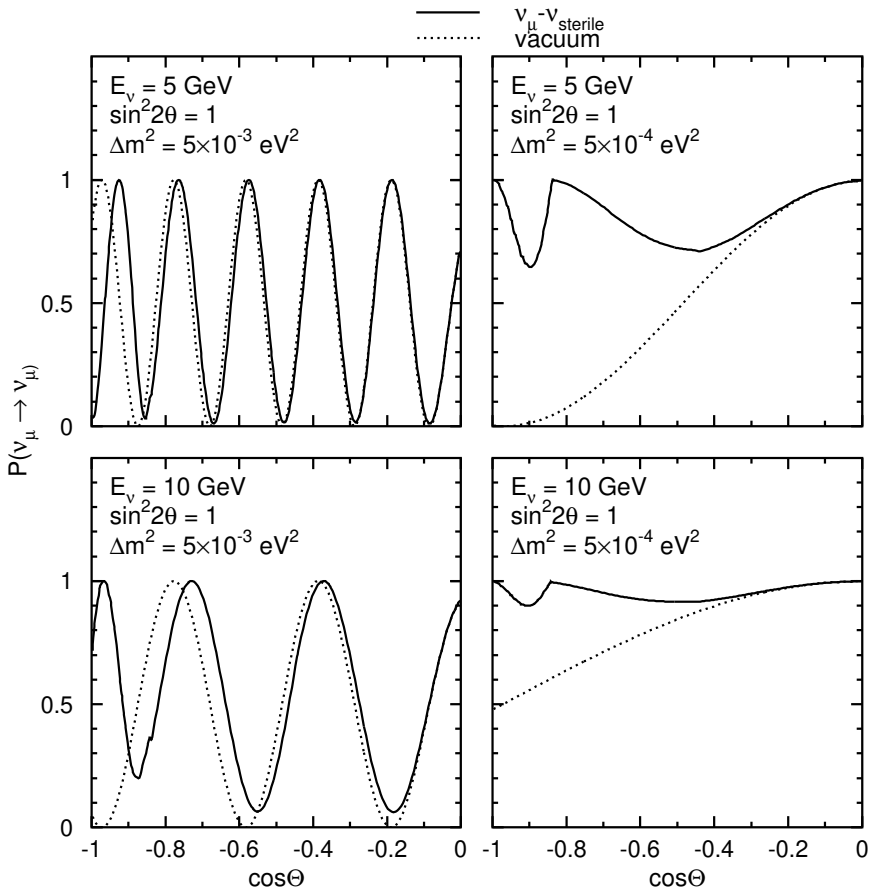

Figure 8.6: Comparison of the ν_μ survival probability for the cases $\nu_\mu \leftrightarrow \nu_{sterile}$ and vacuum oscillations for neutrinos propagating through the Earth.

tions. The oscillated events weights are calculated as:

$$f_\mu = P(\nu_\mu \rightarrow \nu_\mu) + \frac{\mathcal{F}_e(E_\nu, \cos\Theta_\nu)}{\mathcal{F}_\mu(E_\nu, \cos\Theta_\nu)} P(\nu_e \rightarrow \nu_\mu) \tag{8.9}$$

$$f_e = P(\nu_e \rightarrow \nu_e) + \frac{\mathcal{F}_\mu(E_\nu, \cos\Theta_\nu)}{\mathcal{F}_e(E_\nu, \cos\Theta_\nu)} P(\nu_\mu \rightarrow \nu_e). \tag{8.10}$$

$\mathcal{F}_e$ and $\mathcal{F}_\mu$ are the differential neutrino fluxes for ν_e and ν_μ for a given neutrino energy E_ν and zenith angle Θ. The first term in these expressions accounts for the neutrino survival probability; the second term accounts for appearance due to oscillations of

$\nu_e \leftrightarrow \nu_\mu$. These weights are only applied to charge-current neutrino interactions for active-active oscillations. In simulations active-sterile neutrino oscillations, neutral-current interactions are also re-weighted. For simulations of $\nu_\mu \leftrightarrow \nu_\tau$ the expressions simplify as $P(\nu_e \rightarrow \nu_\mu)$ and $P(\nu_\mu \rightarrow \nu_e)$ are zero. In this case the expression for $P(\nu_\mu \rightarrow \nu_\mu)$ is the familiar $1 - \sin^2 2\theta \sin^2(1.27\Delta m^2 L/E)$. For simulations which involve oscillations to ν_e or $\nu_{sterile}$ matter effects on neutrino propagation in the Earth are treated according to Sec. 8.1.2. The possible effects of τ appearance are small due to the high τ production threshold (3.5 GeV) and are neglected (see next section).

8.1.4 Estimates of ν_τ Appearance

The number of charged-current events expected from ν_τ appearance has been estimated for the case of neutrino oscillations of $\nu_\mu \leftrightarrow \nu_\tau$. Assuming oscillations with $\sin^2 2\theta = 1.0$ and $\Delta m^2 = 3.5 \times 10^{-3}$ eV^2 the rate of ν_τ charged-current events is approximated by:

$$N_{\nu_\tau} \simeq \sum_i P^i_{\nu_\mu \rightarrow \nu_\tau} \frac{\sigma_{\nu_\tau,CC}(E^i_\nu)}{\sigma_{\nu_\mu,CC}(E^i_\nu)}, \tag{8.11}$$

where the sum is over charged-current, single-ring $\mu-$like events. This calculation gives approximately 20 events from ν_τ per year in Super–Kamiokande. The number is further reduced by the selection of single rings as only the decays $\tau^- \rightarrow \mu^- \bar{\nu}_\mu \nu_\tau$ (17%) and $\tau^- \rightarrow e^- \bar{\nu}_e \nu_\tau$ (18%) are likely to produce single-ring events. Compared to the single-ring event rate ($\sim$2000/year) τ appearance can safely be neglected. The estimated energy and zenith angle distribution of the ν_τ's that interact in Super–Kamiokande are shown in Fig. 8.7.

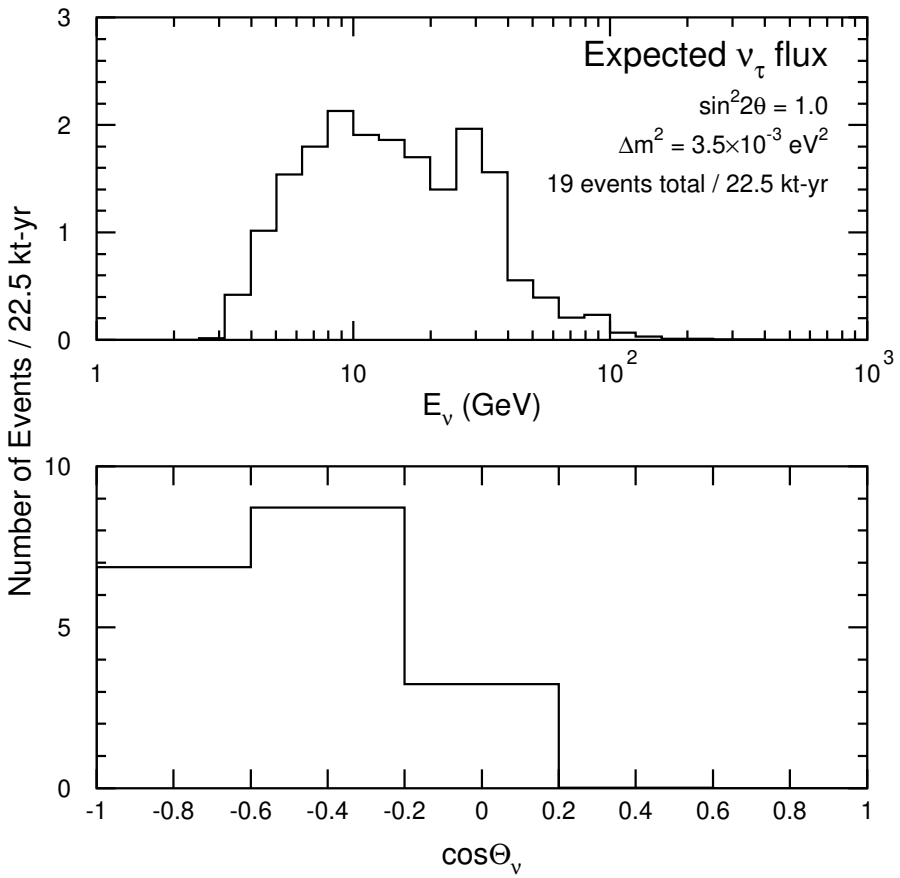

Figure 8.7: Estimated energy spectrum and zenith angle distribution of ν_τ's that interact in Super–Kamiokande assuming $\nu_\mu \leftrightarrow \nu_\tau$ oscillations with $\sin^2 2\theta = 1.0$ and $\Delta m^2 = 3.5 \times 10^{-3}$ eV^2.

8.2 Statistical Method of Neutrino Oscillation Fits

8.2.1 Definition of χ^2

To test neutrino oscillation hypotheses and to estimate neutrino oscillation parameters, we have performed a χ^2 comparison of data and Monte Carlo. The data are binned into 5 equal bins from $\cos\Theta = -1$ to $\cos\Theta = 1$ and 7 momentum bins.

The average angle between the neutrino and the reconstructed lepton is plotted as

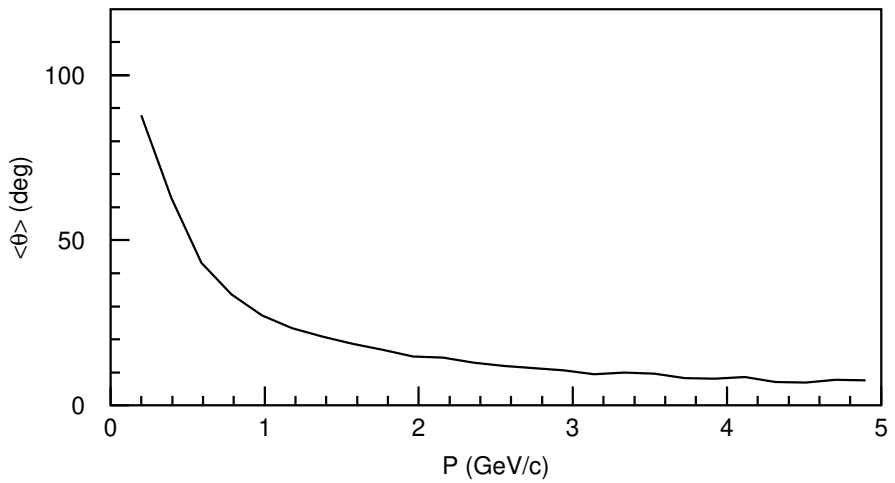

Figure 8.8: The average angle between the neutrino and the reconstructed lepton directions as a function of the reconstructed lepton momentum. Results for ν_μ and ν_e have been combined as there is no significant difference for the two flavors.

a function of reconstructed lepton momentum in Fig. 8.8. Using 5 bins in $\cos\Theta$, the smallest bin spans 23°. The average angle between the neutrino and the reconstructed lepton is 23° at $p_l = 1.2$ GeV/c.

Momentum bins are distributed according to:

$$\begin{aligned}
\text{sub} - \text{GeV } e\text{−like}(\mu\text{−like}) \qquad & p = 100(200), 10^{2.4}, 10^{2.6}, 10^{2.8}, 10^{3.0} \text{ MeV}/c, \\
& E_{vis} < 1330 \text{ MeV} \\
\text{multi} - \text{GeV } e\text{−like} \qquad & p < 10^{3.4} \text{ MeV}/c, p > 10^{3.4} \text{ MeV}/c \\
\text{multi} - \text{GeV } \mu\text{−like} \qquad & \text{fully} - \text{contained}, \text{partially} - \text{contained}
\end{aligned}$$

A total of 70 bins are used:

$$(e\text{−like}, \mu\text{−like}) \times 5 \cos\Theta \times 7 \text{ momentum} = 70. \tag{8.12}$$

With this choice of bins, the number of events per bin ranges between 22 to 111 with an average of roughly 60 events per bin.

In general, χ^2 is defined as:

$$\chi^2 = \Delta^T V^{-1} \Delta, \tag{8.13}$$

where Δ is a vector of differences between data and expectations and V is the error matrix. Following Refs. [44, 67, 128] we have assumed a diagonal error matrix. The quality of this approximation is assessed in Sec.8.2.2. Using this approximation χ^2 is given by:

$$\chi^2 = \sum_{i=1}^{N_{bins}} \frac{\left(N^i_{DATA} - N^i_{MC}(\sin^2 2\theta, \Delta m^2, \vec{\epsilon}\,)\right)}{\sigma_i^2} + \sum_j \frac{\epsilon_j^2}{\sigma_j^2}, \tag{8.14}$$

where N^i_{DATA} is the number of events in the i^{th} bin, N^i_{MC} is the expected number of events in the i^{th} bin for a given set of parameters $\sin^2 2\theta, \Delta m^2, \vec{\epsilon}$ computed as a weighted sum:

$$N^i_{MC} = \sum_{\text{Monte Carlo events}} w(\sin^2 2\theta, \Delta m^2, \vec{\epsilon}\,). \tag{8.15}$$

The errors σ_i include data and Monte Carlo statistics,

$$\sigma_i^2 = \sum w + \sqrt{\left(\sum w^2\right)}. \tag{8.16}$$

The parameters ϵ and their errors σ_j account for systematic uncertainties in the Monte Carlo prediction of atmospheric neutrino event rates and are described in Sec. 8.2.1.

Treatment of Systematic Uncertainties

In addition to re-weighting the Monte Carlo for neutrino oscillations, the Monte Carlo is also re-weighted to account for several sources of systematic uncertainties in the predicted zenith angle and momentum event-rate distributions. Adjusting for both neutrino oscillations and variations of Monte Carlo input parameters the weight assigned is:

$$
\begin{aligned}
w &= (1+\alpha)(E_\nu^i/E_0)^\delta(1+\eta_{s,m}\cos\Theta) \times f_{e,\mu}(\sin^2 2\theta, \Delta m^2, (1+\lambda)L/E_\nu) \\
&\times \begin{cases}
(1-\beta_s/2) & \text{sub-GeV } e\text{-like} \\
(1+\beta_s/2) & \text{sub-GeV } \mu\text{-like} \\
(1-\beta_m/2) & \text{multi-GeV } e\text{-like} \\
(1+\beta_m/2)(1-\frac{\rho}{2}\frac{N_{PC}}{N_\mu}) & \text{multi-GeV } \mu\text{-like} \\
(1+\beta_m/2)(1+\frac{\rho}{2}). & \text{PC}
\end{cases}
\end{aligned}
\tag{8.17}
$$

The meaning and estimated uncertainties of the parameters α and $\vec{\epsilon} = (\delta,\ \beta_s,\ \beta_m,\ \rho,\ \eta_s,\ \eta_m,\ \lambda)$ are described below.

Normalization and Neutrino Spectrum: α and δ

The absolute rate of atmospheric neutrino events in a given momentum bin is taken to be proportional to:

$$
N \propto (1+\alpha)\left(\frac{E_\nu}{E_0}\right)^\delta . \tag{8.18}
$$

E_ν is the average neutrino energy for charged-current events in a given momentum bin and E_0 is a reference energy arbitrarily taken to be 2 GeV. The parameters α and γ adjust the expected number of events for uncertainties in the absolute event rates and

	sub-GeV (%)	multi-GeV (%)
Event selection	$\ll 0.1$	3.0
Predicted ν_μ/ν_e ratio	5%	5%
E_ν spectral index	0.6	1.6
Particle identification	2.0	3.0
Cherenkov ring finding	3.0	6.0
Fiducial volume determination	0.6	2.4
Energy scale	1.0	4.1
Non-ν backgrounds	0.5	1.1
Cross sections	4.6	6.0
total	7.8	11.8

Table 8.2: Sources and estimates of uncertainties in the predicted $\mu-$like/$e-$like ratio for the sub-GeV and multi-GeV samples [92].

for uncertainties in the spectrum shape of atmospheric neutrinos. The uncertainty in α is estimated to be 25% combining the uncertainties in the absolute neutrino flux ($\sim$20%) with uncertainties in the total neutrino-nucleon cross-section ($\sim$15%). Due to this large uncertainty, α is fitted as a free parameter. The atmospheric neutrino spectrum is well fit by a power law $N \propto E^\gamma$ with $\gamma = -2.70 \pm 0.05$ [129]. Variations in γ are input using the parameter δ with $\sigma_\delta = 0.05$.

Flavor ratios: β_s and β_m

Several sources of systematic uncertainties in the predicted $\mu-$like/$e-$like ratios for the sub-GeV and multi-GeV samples are summarized in Table 8.2. Variations in these ratios are input using the parameters β_s and β_m for the sub-GeV and multi-GeV samples respectively. The variation in the ratio is affected by adjusting the $e-$like rates by a factor of $(1 - \beta/2)$ and the $\mu-$like rates by a factor of $(1 + \beta/2)$. This gives:

$$r'_{\mu/e} = \left(\frac{1+\beta/2}{1-\beta/2}\right)\frac{N_\mu}{N_e} \simeq (1+\beta) r_{\mu/e}. \tag{8.19}$$

Uncertainties in β_s and β_m are taken to be $\sigma_{\beta_s} = 0.08$ and $\sigma_{\beta_m} = 0.12$.

Event selection	2.5%
ν Flux	2.8%
E^{γ}	3.4%
Particle identification	0.6%
Ring counting	3.7%
Vertex resolution	1.5%
Energy calibration	1.3%
Cosmic ray μ background	1.0%
ν Cross-sections	3.0%
Hadronic simulation	1.0%
total	7.4%

Table 8.3: Contributions to the uncertainty in the relative normalization of the fully-contained multi-GeV $\mu-$like sample and the partially-contained sample.

Relative fully-contained - partially contained normalization: ρ

The multi-GeV muon sample combines both fully-contained (FC) events and partially-contained (PC) events. The average energy of the parent neutrinos for these two samples is very different; $\langle E_\nu \rangle = 3$ GeV FC and $\langle E_\nu \rangle = 15$ GeV PC. The FC and PC events have very different topologies and are selected by different reduction streams. Also, the cuts used to select events for the final sample differ; no single-ring requirement is made nor is particle identification applied to the partially-contained events. These differences introduce uncertainties in the expected relative rates of FC multi-GeV $\mu-$like events and PC $\mu-$like events. The relative normalization of the two samples is expressed as the ratio:

$$r_{FC-PC} = \frac{N_{PC}}{N_{FC} + N_{PC}}. \tag{8.20}$$

This ratio is varied during the χ^2 minimization by introducing a parameter ρ which multiplies the multi-GeV $\mu-$like rate by a factor $(1 - (\rho/2)(N_{PC}/N_\mu))$ and the PC event rate by $(1 + \rho/2)$. These adjustments approximately give $r'_{FC-PC} = (1 +$

	sub-GeV	
	$e-$like(%)	$\mu-$like(%)
0.6% Energy scale asymmetry	0.1	0.2
Flux (Honda/Bartol)	2.5	2.1
non-ν Backgrounds	<1.	<0.1
Rock over-burden	$\ll$0.1	$\ll$0.1
total	2.7	2.2
	multi-GeV	
	$e-$like (%)	$\mu-$like (%)
0.6% Energy scale asymmetry	0.9	0.7
Flux (Honda/Bartol)	1.6	1.0
non-ν Backgrounds	<0.5	<2.0
Rock over-burden	2.0	1.5
total	2.8	2.6

Table 8.4: Sources and estimates of systematic uncertainties in the prediction of U/D where U is the number of up-going events and D is the number of down-going events for the sub-GeV and multi-Gev $e-$like and $\mu-$like samples.

$\rho)r_{FC-PC}$. The uncertainty in ρ has been estimated based on several sources listed in Table 8.3. The total uncertainty is $\sigma_\rho = 7.4\%$.

Zenith angle rates: η_s and η_m

Variations in the predictions of the zenith angle rates of atmospheric neutrino events are assumed to be linear in $\cos\Theta$:

$$N' = (1 + \eta_{s,m}\cos\Theta)N. \tag{8.21}$$

The parameters η_s and η_m adjust the predicted slopes of the sub-GeV and multi-GeV samples respectively. Although these errors are small, the zenith angle rates have a very strong effect on the allowed Δm^2 range. The uncertainties on η_s and η_m are estimated from the uncertainties in the predicted ratio of the number of up-going

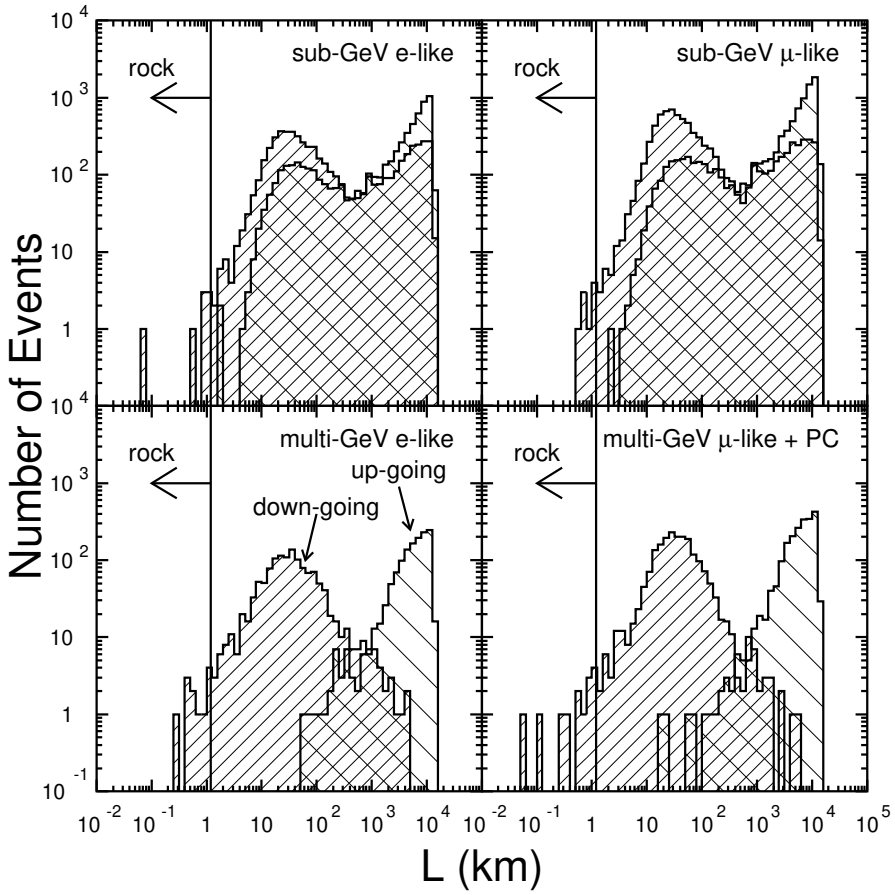

Figure 8.9: Estimates of the number of neutrinos produced in the rock over the Super–Kamiokande detector.

events to the number of down-going events for the sub-GeV and multi-GeV $e-$like and $\mu-$like samples. Sources of uncertainty in the ratio U/D include:

- Possible gain asymmetry of the Super–Kamiokande detector: the gain asymmetry has been measured using Michel electrons to be less than 0.6%.

- Flux prediction: uncertainties in the predicted U/D ratios largely result from different treatments of geo-magnetic effects. These uncertainties were estimated based on a comparison of the Honda [96] and Bartol [97] flux predictions.

- Non-neutrino background: uncertainties due to cosmic ray muon backgrounds result in an estimated 2% uncertainty in the U/D ratio for the multi-GeV $\mu-$like sample.

- Rock overburden: The neutrino flux models assume the detector is on the surface of the Earth. In fact, Super–Kamiokande is surrounded by $\sim$1.2 km of rock. Muons which stop in the rock are not likely to produce high energy neutrinos. The uncertainty in the U/D ratio this causes is estimated by removing the tail of the neutrino production height distributions that extend into the rock overburden as shown in Fig. 8.9.

Based on these estimates of the uncertainties in U/D, the uncertainties in η are taken to be 2.4% in the sub-GeV sample and 2.7% in the multi-GeV region.

Average L/E_ν: λ

The estimates of oscillation parameters depend on the physics in the Monte Carlo simulation. In this simulation, a neutrino with a given flight length L, zenith angle Θ_ν, and energy E_ν is associated with a charged lepton track traveling with zenith angle Θ and momentum p. Since the estimate of Δm^2 depends on the ratio L/E_ν, uncertainties in the average neutrino production height, average momentum transfer and average scattering angle translate directly to uncertainties in Δm^2. Uncertainties in L/E_ν due to uncertainties in the average momentum transfer are estimated to be $\simeq 2\%$; uncertainties in the average scattering angle contribute $\sim 1\%$. The predictions of neutrino production heights is estimated to be roughly 10% uncertain (see Sec. 8.1.1). Combining these errors we conservatively estimate a 15% uncertainty in the average Monte Carlo L/E_ν. Since this uncertainty is dominated by the uncertainty in the neutrino production height, this 15% estimate strictly only applies for

$\cos\Theta > 0$. However, we have assumed a 15% uncertainty for all zenith angles. The confidence intervals for Δm^2 are insensitive to the exact value of the uncertainty in λ. Variations in the average Monte Carlo L/E_ν ratio are input by replacing L/E_ν with $(1+\lambda)L/E_\nu$. The error on λ is taken to be $\sigma_\lambda = 0.15$.

8.2.2 Test of Statistical Treatment

The formulation of the statistical test used to estimate the neutrino oscillation parameters has been tested using a "toy" Monte Carlo. In the simulations fake data samples were randomly drawn from the atmospheric neutrino Monte Carlo sample with a fixed set of oscillation parameters input. The oscillation parameters were chosen to be close to those obtained when the real Super–Kamiokande data sample is fit to $\nu_\mu \leftrightarrow \nu_\tau$ oscillations; $\sin^2 2\theta = 1.0$ and $\Delta m^2 = 10^{-2.5}$ eV^2. For each trial, all systematic parameters were varied according to Gaussian distributions and the bin contents were chosen randomly from Poisson distributions. The randomly chosen "data" distributions were fit to neutrino oscillations using an identical prescription that is applied to the real Super–Kamiokande data allowing $\sin^2 2\theta$ to range into the unphysical region $\sin^2 2\theta > 1$.

The χ^2 distributions obtained from these simulations are shown in Figs. 8.10. The distribution of χ^2 evaluated at the input values of the oscillation parameters ("χ^2_{true}") (with the systematic parameters minimized) is well distributed according to the expected χ^2 behavior. When the oscillation parameters are varied to minimize χ^2 the resulting χ^2 ("χ^2_{min}") tends to slightly lower values than expected as shown in the right panel in Fig. 8.10.

To give proper coverage, the difference $\chi^2_{true} - \chi^2_{min}$ ought to be distributed as a χ^2 variable of 2 degrees of freedom; χ^2_{true} is obtained varying one free parameter (normal-

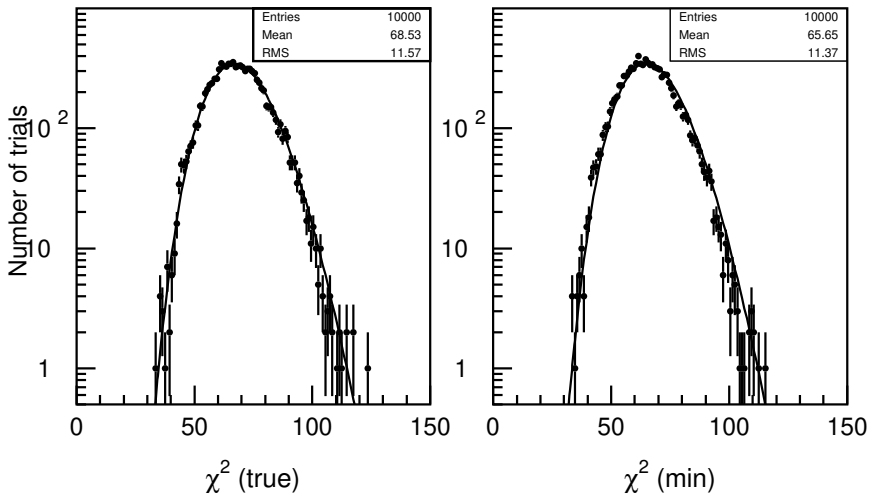

Figure 8.10: Distributions of χ^2 obtained from simulations of measurements of oscillation parameters using atmospheric neutrinos. χ^2_{true} is evaluated at the input values of the oscillation parameters; χ^2_{min} is evaluated at the value of the oscillation parameters that minimize χ^2. Each distribution is compared to the expected behavior (solid line); $\chi^2(DoF = 69)$ for χ^2_{true} and $\chi^2(DoF = 67)$ for χ^2_{min}.

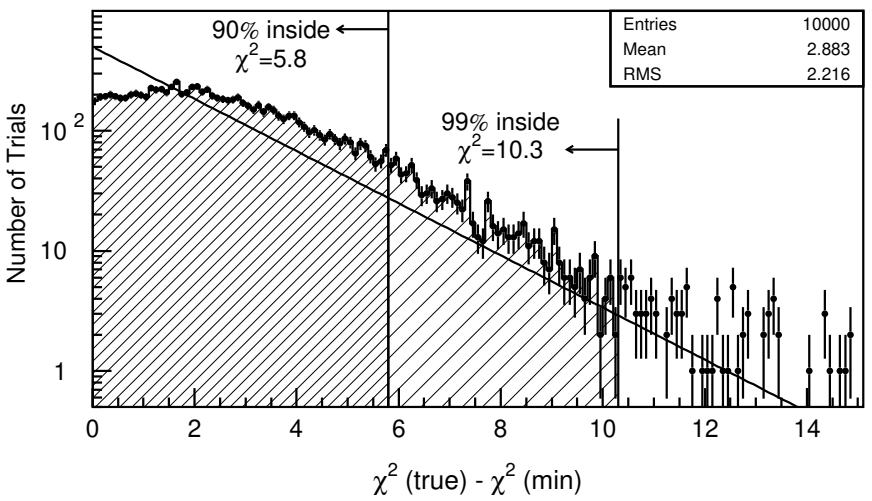

Figure 8.11: Distributions of the difference $\chi^2_{true} - \chi^2_{min}$ which is used to assign confidence levels to oscillation parameters. The expected behavior is shown by the solid line. The χ^2 differences corresponding to the 90% CL and 99%CL intervals are shown in the hatched regions.

ization), χ^2_{min} is obtained varying three free parameters (normalization, $\sin^2 2\theta$ and Δm^2), the difference is 2 degrees of freedom. The distribution of this χ^2 difference is shown in Fig. 8.11. The distribution deviates from the expected behavior due to the proximity of the physical boundary. The 90% confidence interval is at 5.8 instead of the expected 4.6, the 99% confidence interval is at 10.3 instead of the expected 9.6. These intervals agree, however, with the intervals used to draw the allowed region confidence intervals which include the effects of the physical boundary. Oscillation contours for $\nu_\mu \leftrightarrow \nu_\tau$ oscillations drawn in Fig.8.15 at $\chi^2_{min} + 5.7$ and $\chi^2_{min} + 10.3$ based on an independent estimation (see Sec.8.2.3) which this calculation confirms.

These toy Monte Carlo simulations have also been used to test for biases in the estimates of $\sin^2 2\theta$, Δm^2, or the other parameters $\vec{\epsilon}$ introduced by the fitting procedure. The distribution of the location of the χ^2 minima is shown in Fig. 8.12 with projections onto the $\sin^2 2\theta$ and Δm^2 axes. The minima are evenly distributed around the input oscillation parameters ($\sin^2 2\theta = 1.0$, $\Delta m^2 = 10^{-2.5}$ eV^2) with no significant bias. Further, the statistical procedure is very efficient at estimating the input systematic parameters. For example, the difference between the input and estimated values of the sub-GeV and multi-GeV ratio are plotted in Fig. 8.13. Again, the statistical formulation introduces no significant bias in the estimation of the $\mu-$like/$e-$like ratios.

8.2.3 Treatment of the Physical Boundary

Unitarity of the neutrino mixing matrix requires that the value of $\sin^2 2\theta$ be bounded between zero and one. Since the best fit to $\nu_\mu \leftrightarrow \nu_\tau$ oscillations (see Sec. 8.3.1) occurs at $\sin^2 2\theta = 1.05$, slightly outside the physical region, treatment of the physical boundary is important in the calculation of the confidence level for a given

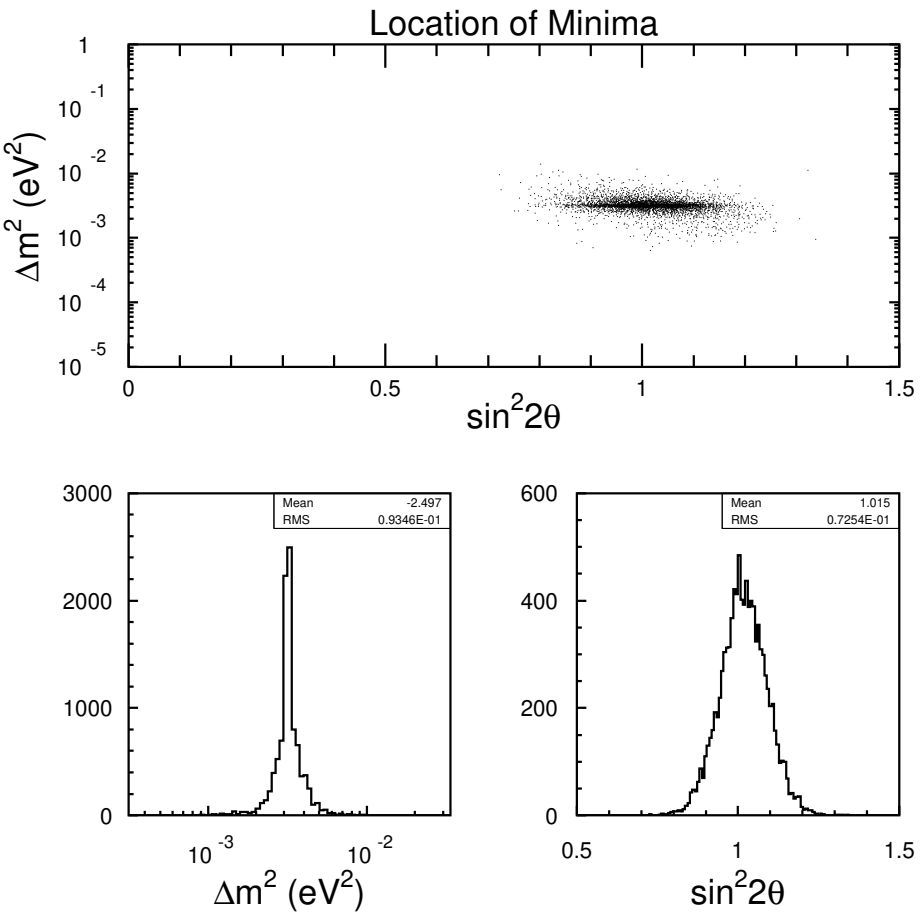

Figure 8.12: The distribution of χ^2 minima for 10,000 simulated measurements of $\sin^2 2\theta$ and Δm^2 using 736 days of atmospheric neutrinos.

$(\sin^2 2\theta, \Delta m^2)$. In this section two schemes for treating the physical boundary are discussed.

Gaussian approximation

The method used to draw the allowed region published in Ref. [47] and shown in Fig. 8.15 extends the technique recommended in Ref. [130, 131] for the one-dimensional Gaussian case to two dimensions. This method is outlined below.

If we approximate the likelihood function $\mathcal{L}(\sin^2 2\theta, \Delta m^2)$ as a two-dimensional

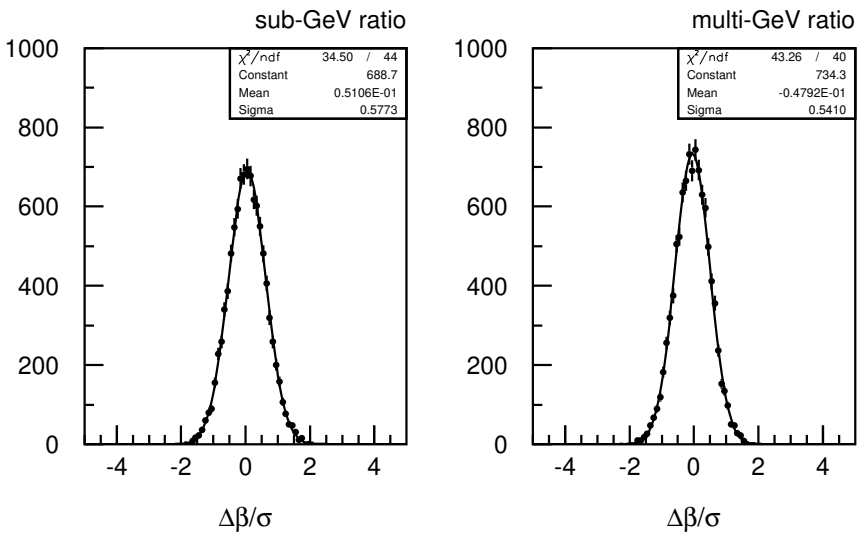

Figure 8.13: The difference between the input and estimated values of the sub-GeV and multi-GeV $\mu-$like/$e-$like ratios expressed in terms of the size of their expected errors.

Gaussian then in some suitably scaled units x and y the likelihood is given by:

$$\mathcal{L}(x,y) = Ae^{-(x^2+y^2)/2}, \tag{8.22}$$

with

$$\chi^2 = -2\ln\mathcal{L} = (x^2+y^2) + \chi^2_{min}. \tag{8.23}$$

The likelihood is normalized such that

$$\int_{-\infty}^{\infty}\int_{-\infty}^{\infty}\mathcal{L}(x,y)dxdy = 1. \tag{8.24}$$

Suppose we know, a priori, that values of x larger than a certain value b are unphysical. Then $\mathcal{L}(x>b,y)=0$ and the normalization of the likelihood becomes:

$$\alpha = \int_{-\infty}^{\infty}\int_{-\infty}^{\infty}\mathcal{L}(x,y)dxdy = \int_{-\infty}^{\infty}\int_{-\infty}^{b}\mathcal{L}(x,y)dxdy < 1. \tag{8.25}$$

At the point $(b, 0)$ we have $\chi_b^2 = b^2 + \chi_{min}^2$ which gives us the relation

$$b = (\Delta\chi^2)^{1/2}, \tag{8.26}$$

where

$$\Delta\chi^2 \equiv \chi_b^2 - \chi_{min}^2. \tag{8.27}$$

The effect of the physical boundary is completely determined by $\Delta\chi^2$, the difference between χ_{min}^2 (which may occur either inside or outside the physical region) and χ_b^2, the value of χ^2 at the boundary of the physical region. Given a measured value of $\Delta\chi^2$ we can assign a confidence level to a point (x', y') based on the χ^2 difference, $\chi^2(x', y') - \chi_{min}^2$, measured at that point:

$$C.L.(\chi^2(x', y') - \chi_{min}^2) = \frac{\int_{-\infty}^{\infty}\int_{-\infty}^{b} e^{-(x^2+y^2)/2}\Theta(\chi^2(x, y) - \chi^2(x', y'))dxdy}{\alpha}. \tag{8.28}$$

where $\Theta(u) = 0$ for $u < 0$ and $\Theta(u) = 1$ for $u \geq 1$. Figure 8.14 plots the χ^2 differences corresponding to the 68%, 90% and 99% confidence limits versus the measured value of $\Delta\chi^2$ assuming that the best fit is inside the physical region and outside the physical region. Note that as $\Delta\chi^2$ becomes large the effect of the physical region is small for best-fits inside the physical region and the χ^2 differences corresponding to the 68%, 90% and 99% confidence level contours approach their standard values of 2.3, 4.6 and 9.2 respectively.

The Method of Feldman and Cousins

A second method recently recommended by the Particle Data Group [132] is due to Feldman and Cousins [133]. These authors have proposed a method of constructing confidence intervals which handle the presence of the physical boundary by construc-

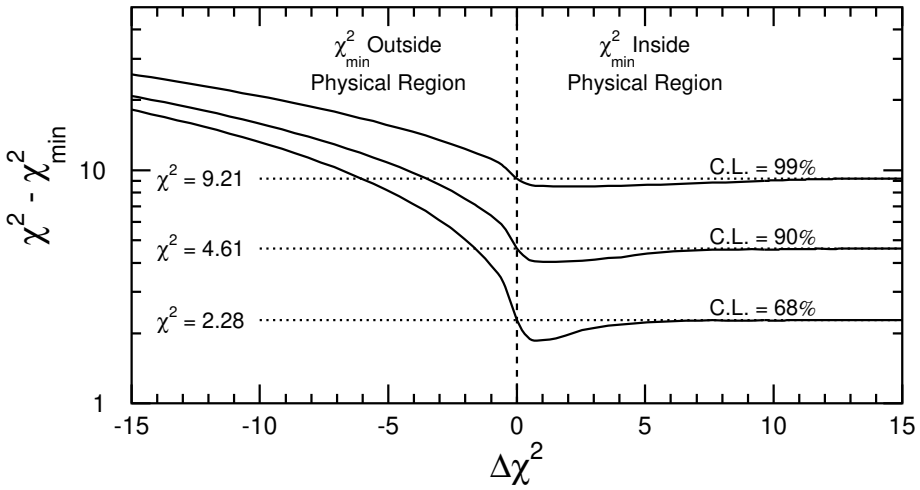

Figure 8.14: The χ^2 differences corresponding to the 68%, 90%, and 99% confidence intervals for a bounded physical region. $\Delta\chi^2$ is the difference between the value of χ^2_{min} and the value of χ^2 on the physical boundary; it is taken positive if χ^2_{min} occurs inside the physical region and negative if outside the physical region.

tion.

The application of the Feldman and Cousins method also begins by constructing a map of $\Delta\chi^2 = \chi^2(\sin^2 2\theta, \Delta m^2) - \chi^2_{min}$ differences by comparing data with expectation; however the fit for χ^2_{min} is limited to the physical region. (In practice this is easily done by minimizing with respect to 2θ instead of $\sin^2 2\theta$.) Given this map of $\Delta\chi^2(\sin^2 2\theta, \Delta m^2)$, confidence levels are assigned based on a series of Monte Carlo "experiments" as outlined below.

At a particular point in $\sin^2 2\theta$ and Δm^2 a parent distribution of the expected number of events in each analysis bin is generated based on the detector exposure using $\sin^2 2\theta$ and Δm^2 as inputs. The various systematic parameters used in the fits are also varied randomly from normal distributions based on their estimated uncertainties. From the parent distribution, a random set of "data" is generated by selecting the content of each bin according to a Poisson distributions with means

given by the parent distribution. The "data" set values of $\chi^2(\sin^2 2\theta, \Delta m^2)$ and χ^2_{min} are determined using the same procedure as is used when fitting the real data. This difference, $\chi^2(\sin^2 2\theta, \Delta m^2) - \chi^2_{min}$, is entered into a histogram and the process repeats from the beginning with the generation of the parent distribution. After a sufficient number of entries to the χ^2 difference histogram have been made, the "critical" χ^2 values for this point in $\sin^2 2\theta$ and Δm^2 can be determined: 68% of the entries in the histogram occur below χ^2_{68}, 90% below χ^2_{90} and 99% below χ^2_{99}. Similar histograms are accumulated over the entire $\sin^2 2\theta$ and Δm^2 map. The confidence level at each point in $(\sin^2 2\theta, \Delta m^2)$ is assigned by counting the number of times the simulated $\Delta\chi^2$ exceeded the value obtained from comparisons of real data with expectations.

This process is extremely CPU intensive. For example, if we desire 1000 entries into the χ^2 difference histogram, for a 30×30 grid in $\sin^2 2\theta$, Δm^2 this requires $1000 \times 30 \times 30 \times 2$ minimizations. If each minimization requires 2 seconds of CPU then the full calculation will take 3.6×10^6 seconds: over 40 CPU days. This calculation was carried out using the super-computer facilities at the Scientific and Visualization Center at Boston University. The final $\nu_\mu \leftrightarrow \nu_\tau$ allowed region shown in Fig. 8.17 is quite similar to the allowed region generated using the Gaussian approximation detailed above.

8.3 Results for Two-Flavor Neutrino Oscillations

Several two-flavor neutrino mixing schemes have been tested against the data. Oscillations of $\nu_\mu \leftrightarrow \nu_\tau$ and $\nu_\mu \leftrightarrow \nu_{sterile}$ fit the data well. Oscillations of $\nu_\mu \leftrightarrow \nu_e$ can be ruled out as a complete explanation of the observed muon neutrino deficits. Summaries of the two-flavor neutrino oscillations fit are given in Table 8.5. A fit for

Mode	χ^2_{min}/DoF	Best fit	90% Allowed ranges
$\nu_\mu \leftrightarrow \nu_\tau$	62/67, $P = 65\%$	$(1.0, 3.5 \times 10^{-3})$	$\sin^2 2\theta > 0.86$
			$1 \times 10^{-3} < \Delta m^2 < 8 \times 10^{-3}$
$\nu_\mu \leftrightarrow \nu_{sterile}$	64/67, $P = 57\%$	$(1.0, 4.5 \times 10^{-3})$	$\sin^2 2\theta > 0.87$
			$2 \times 10^{-3} < \Delta m^2 < 7 \times 10^{-3}$
$\nu_\mu \leftrightarrow \nu_e$	110/67, $P < 0.1\%$	$(0.98, 3.8 \times 10^{-3})$	-
no osc.	175/69, $P < 10^{-4}\%$	-	-

Table 8.5: Summary of two-flavor neutrino oscillation fits. Best-fit points are for $(\sin^2 2\theta, \Delta m^2 \text{ eV}^2)$.

the case of no oscillations, where only the parameters that control the systematic uncertainties in the Monte Carlo inputs are varied, is also summarized in the table. The no oscillation fit is extremely poor: $\chi^2_{min} = 175/69$ DoF, $P < 10^{-4}\%$.

Note that the parameter λ which adjusts the average Monte Carlo L/E_ν value is not included in the fits which include matter effects as it dramatically increases the number of calculations required to compute χ^2 over the entire oscillation parameter space. The effects of the L/E_ν uncertainty on the location of the confidence intervals is accounted for by convolving the confidence level map v.s. Δm^2 with a Gaussian of width equal to σ_λ. The final contours are not effected significantly by the method used to incorporate the error in λ.

8.3.1 $\nu_\mu \leftrightarrow \nu_\tau$

Oscillations of $\nu_\mu \leftrightarrow \nu_\tau$ provide the best fit to the data. The allowed ranges of oscillation parameters are shown in Fig. 8.15. The χ^2_{min} is 62.1 for 67 degrees of freedom, giving a fit probability of 65%. The best fit in the physical region occurs at $\sin^2 2\theta = 1.0$ and $\Delta m^2 = 3.5 \times 10^{-3}$ eV^2. If the mixing angle is allowed to range outside the physical region, the best fit is obtained at $\sin^2 2\theta = 1.05$ and $\Delta m^2 = 2.9 \times 10^{-3}$ eV^2. The confidence intervals for $\sin^2 2\theta$ and Δm^2 including the unphysical region, is shown in Fig. 8.16. The effects of the physical region were

	α	δ	β_s	β_m
	$\sigma = 25\%$	$\sigma = 0.05$	$\sigma = 8\%$	$\sigma = 12\%$
$\nu_\mu \leftrightarrow \nu_\tau$	8.4%	-0.004	1.5%	-12.5%
$\nu_\mu \leftrightarrow \nu_{sterile}$	10.7%	-0.018	3.5%	-14.7%
$\nu_\mu \leftrightarrow \nu_e$	-14.5%	0.023	7.2%	-8.2%
no oscillations	-9.1%	0.015%	-31.8%	-33.6%
	ρ	η_s	η_m	λ
	$\sigma = 8\%$	$\sigma = 2.4\%$	$\sigma = 2.7\%$	$\sigma = 15\%$
$\nu_\mu \leftrightarrow \nu_\tau$	-2.9%	-0.4%	-0.2%	-1.1%
$\nu_\mu \leftrightarrow \nu_{sterile}$	-3.5%	-0.7%	0.3%	-
$\nu_\mu \leftrightarrow \nu_e$	-5.1%	4.2%	5.8%	-
no oscillations	-1.9%	4.3%	5.9%	-

Table 8.6: Best fit values of the Monte Carlo input parameters for two-flavor oscillation modes.

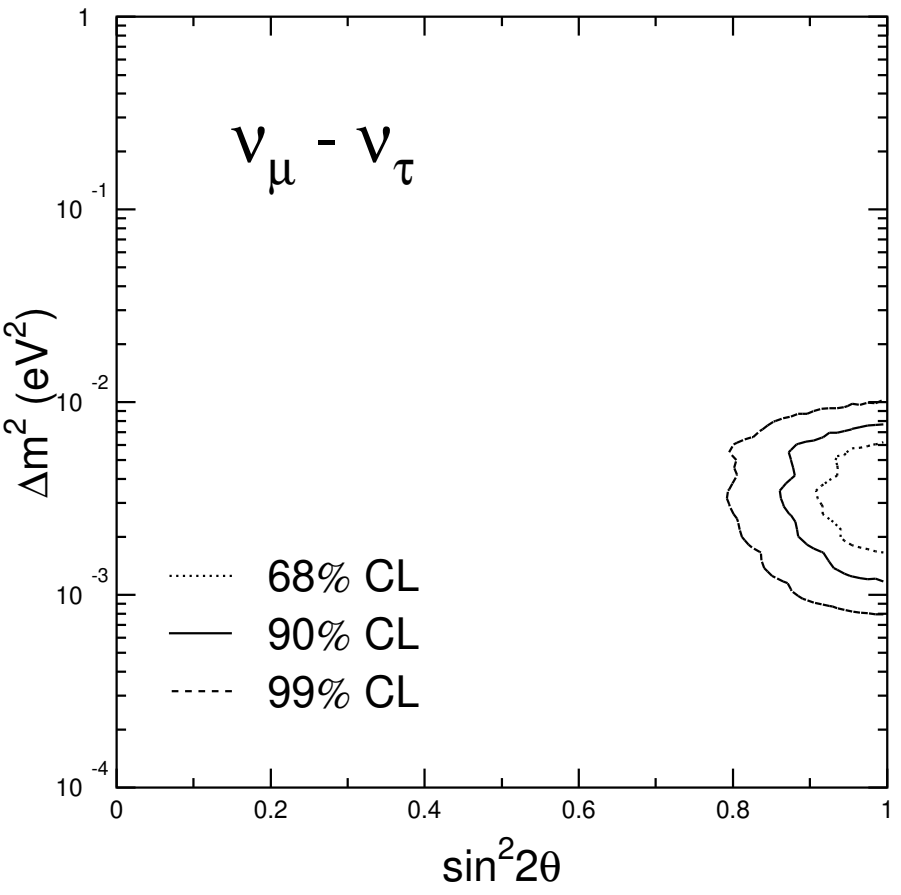

Figure 8.15: Allowed oscillation parameters for $\nu_\mu \leftrightarrow \nu_\tau$ oscillations.

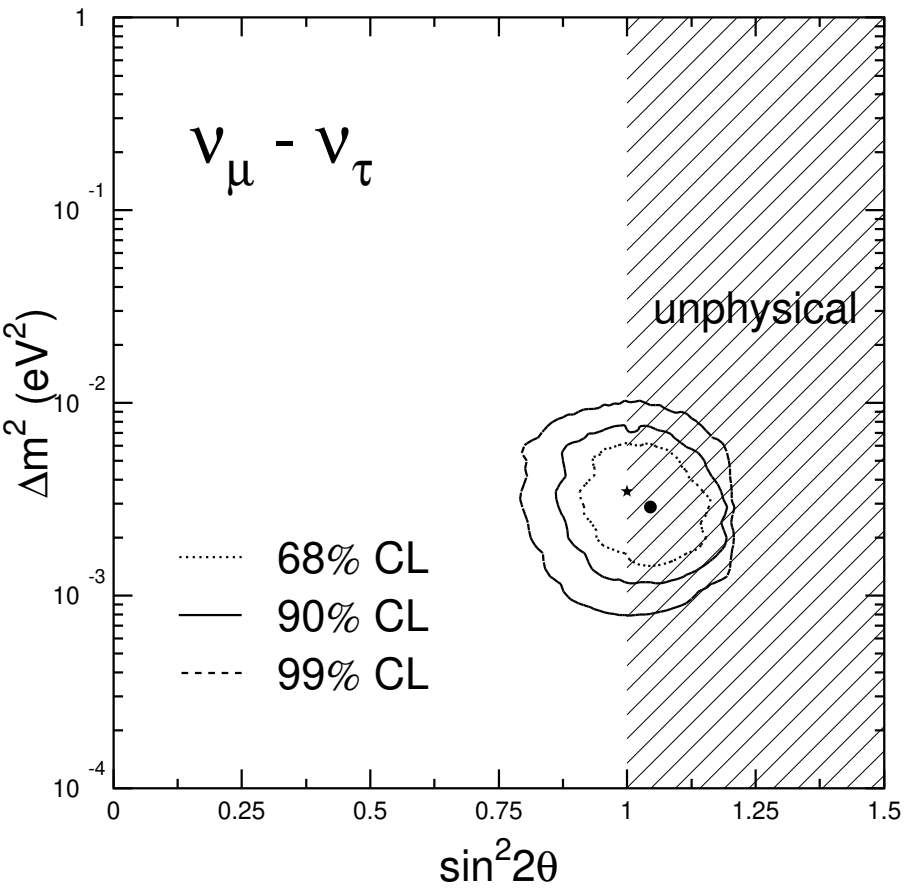

Figure 8.16: Allowed oscillation parameters for $\nu_\mu \leftrightarrow \nu_\tau$ oscillations including the unphysical region $\sin^2 2\theta > 1$.

considered using the methods described in Sec. 8.2.3. The 68% contour is located at $\chi^2 - \chi^2_{min} = 2.8$; 90% at $\chi^2 - \chi^2_{min} = 5.3$, and 99% at $\chi^2 - \chi^2_{min} = 9.9$ based on the minimum in the physical region. These intervals agree with the $\chi^2 - \chi^2_{min}$ difference distributions estimated in Sec. 8.2.2. The intervals used in Fig. 8.17 are based on the Feldman-Cousins prescription described in Sec. 8.2.3. The location of the 68% contour varies from $\chi^2 - \chi^2_{min} = 2.5$ for $\Delta m^2 \simeq 10^{-3}$ eV^2 to 4.4 near $\Delta m^2 \simeq 10^{-2}$ eV^2. The location of the 90% and 99% contours vary between 4.9 – 6.8 and 8.2 – 12.0 over the same range in Δm^2. The allowed region estimated using

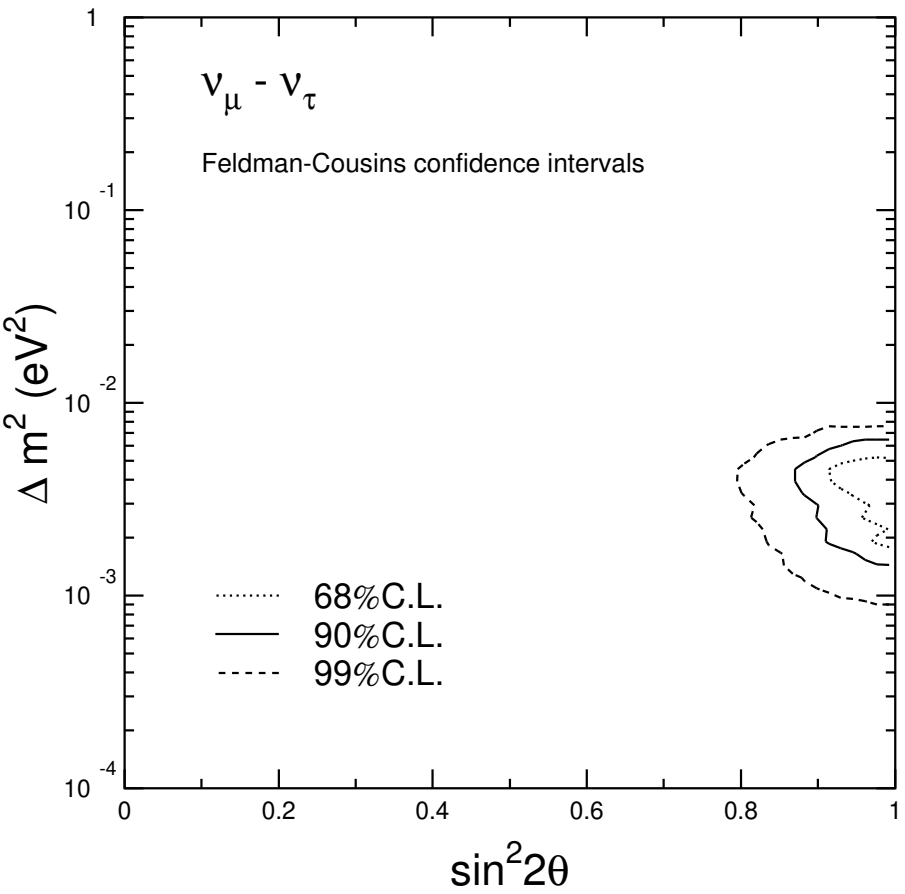

Figure 8.17: The confidence intervals for $\nu_\mu \leftrightarrow \nu_\tau$ oscillation parameters estimated using the method of Feldman and Cousins.

the Feldman-Cousins method is slightly smaller than the region estimated using the Gaussian approximation, however, the two regions are in agreement.

The best-fit residuals, $\left(N_{DATA} - N_{MC}(\sin^2 2\theta, \Delta m^2, \vec{\epsilon}\,)\right)/\sigma^2$, are plotted for each of the 70 bins used in the oscillation fit in Fig. 8.18. The fit residuals are well distributed and are consistent with a Gaussian with mean=0 and $\sigma = 1$.

The expected zenith angle rates for the sub- and multi-GeV samples is shown in Fig. 8.19 for the best-fit case of $\nu_\mu \leftrightarrow \nu_\tau$ oscillations. The $\nu_\mu \leftrightarrow \nu_\tau$ expectation fits the muon deficits well through out the entire energy range. The zenith angle

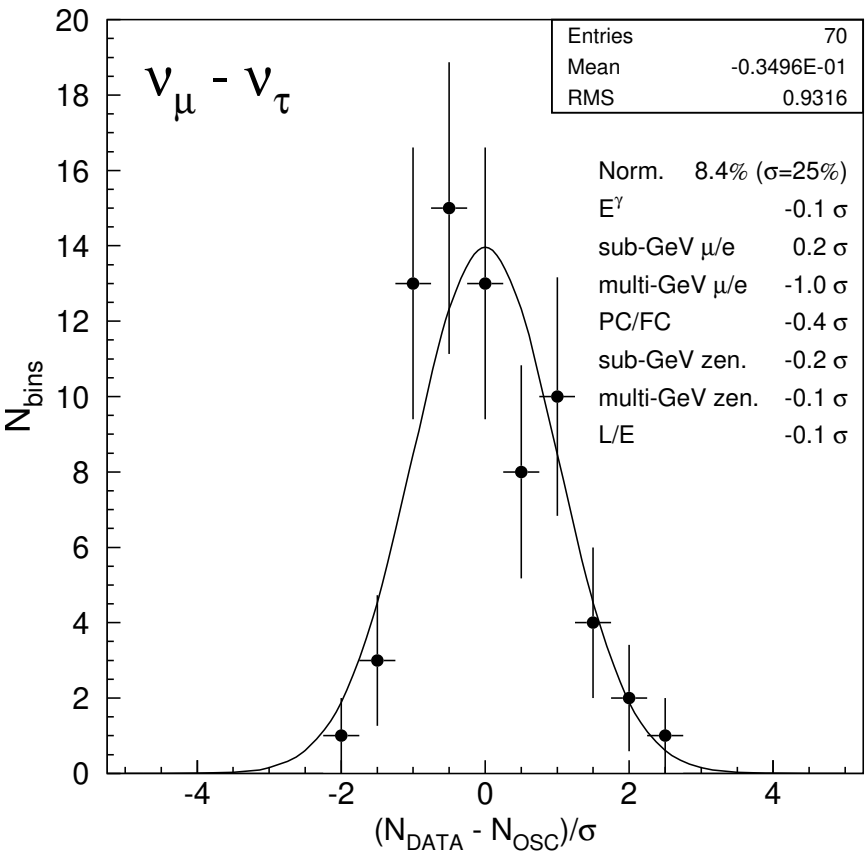

Figure 8.18: Best fit residuals for fits to $\nu_\mu \leftrightarrow \nu_\tau$ oscillations.

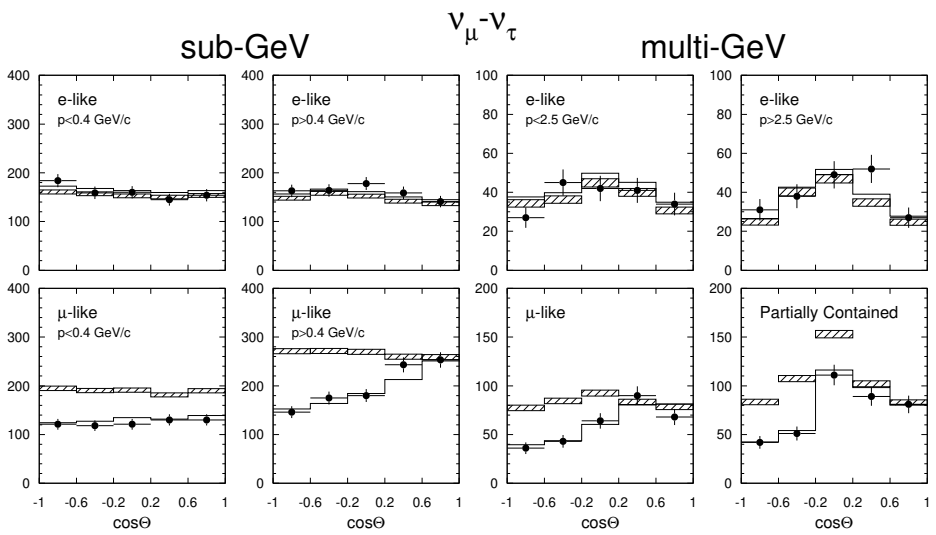

Figure 8.19: Atmospheric neutrino zenith angle event rates. Hatched region shows expectation for no oscillations with Monte Carlo statistical error, line is the best-fit expectation for $\nu_\mu \leftrightarrow \nu_\tau$ neutrino oscillations and the points are the data. The 7 momentum bins used in the fit have been combined into 4 for the purposes of the figure.

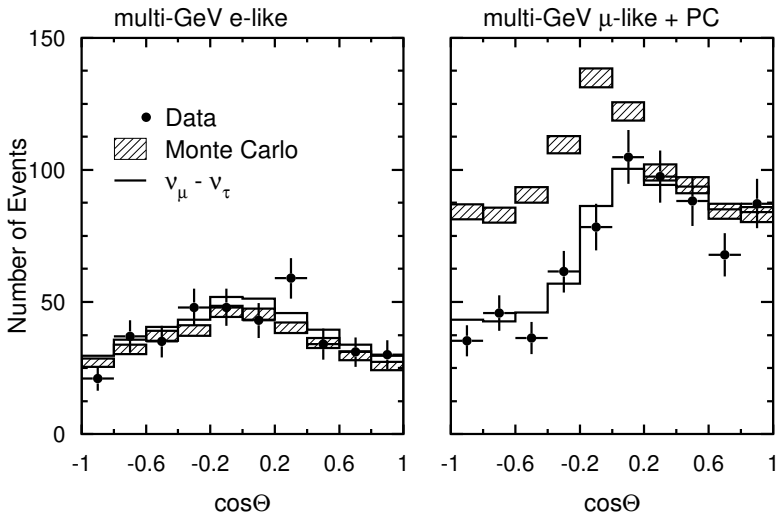

Figure 8.20: The multi-GeV $e-$like and $\mu-$like zenith angle rates in ten bins.

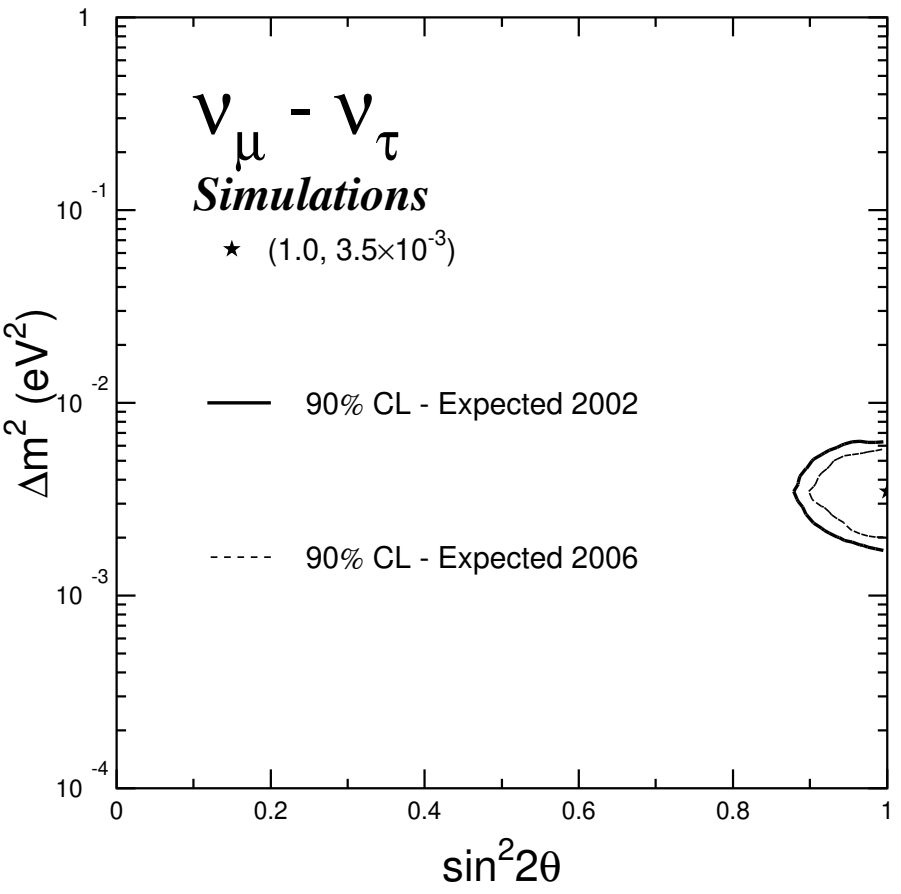

Figure 8.21: Estimated Super–Kamiokande allowed regions for the year 2002 (4.5 live-years) and 2006 (8 live-years).

distributions for the multi-GeV sample are replotted using 10 bins in $\cos\Theta$ instead of 5 bins in Fig. 8.20. With smaller bins, the rapid drop off in the data as the zenith angle approaches the horizon is very apparent. The expectation for $\nu_\mu \leftrightarrow \nu_\tau$ oscillations follows the data well through this region of rapid change.

Future Allowed Regions

The current Super–Kamiokande allowed region ranges from $1 < \Delta m^2 < 8 \times 10^{-3}$ eV^2 (90% CL) using two years of data. Based on simulations of $\nu_\mu \leftrightarrow \nu_\tau$ oscillations

using the current best-fit parameters ($\sin^2 2\theta = 1.0, \Delta m^2 = 3.5 \times 10^{-3}$ eV^2) I expect the region to shrink to $1.7 < \Delta m^2 < 6.7$ eV^2 after 4.5 years of data have been taken and $2.1 < \Delta m^2 < 5.8 \times 10^{-3}$ eV^2 after 8 years of operation. Possible Super–Kamiokande allowed regions for these two periods are shown in Fig. 8.21. These correspond to possible data sets obtained by Super–Kamiokande in the years 2001 and 2006 assuming the detector continues to collect data at the current rate of 0.8 live-days / calendar-day. Down time for a detector upgrade (2-4 months) has not been included. The estimated 90% CL region for 2006 is roughly twice as large as the region expected from the MINOS experiment.

8.3.2 $\nu_\mu \leftrightarrow \nu_{sterile}$

The $\nu_\mu \leftrightarrow \nu_{sterile}$ and $\nu_\mu \leftrightarrow \nu_\tau$ oscillation hypotheses differ in the fact that oscillations of $\nu_\mu \leftrightarrow \nu_{sterile}$ effect neutral-current interactions as well as charged-current interactions, and the presence of matter effects for $\nu_\mu \leftrightarrow \nu_{sterile}$. Figure 8.22 shows the confidence intervals for the oscillation parameters ($\sin^2 2\theta$ and Δm^2) assuming $\nu_\mu \leftrightarrow \nu_{sterile}$. The data are well fit by $\nu_\mu \leftrightarrow \nu_{sterile}$ oscillations with $\chi^2_{min} =$ 64.3/67 DoF. With the present sample, oscillations of $\nu_\mu \leftrightarrow \nu_\tau$ and $\nu_\mu \leftrightarrow \nu_{sterile}$ cannot be distinguished. However, it may be possible to distinguish the two cases based on neutral-current production of π^0's or from the suppression of oscillations due to matter effects on partially-contained neutrino interactions.

Figure 8.23 plots the expected zenith angle rates for $\nu_\mu \leftrightarrow \nu_{sterile}$ oscillations for the sub- and multi-GeV samples. Differences in the distributions from the $\nu_\mu \leftrightarrow \nu_\tau$ case are only apparent in the partially-contained sample.

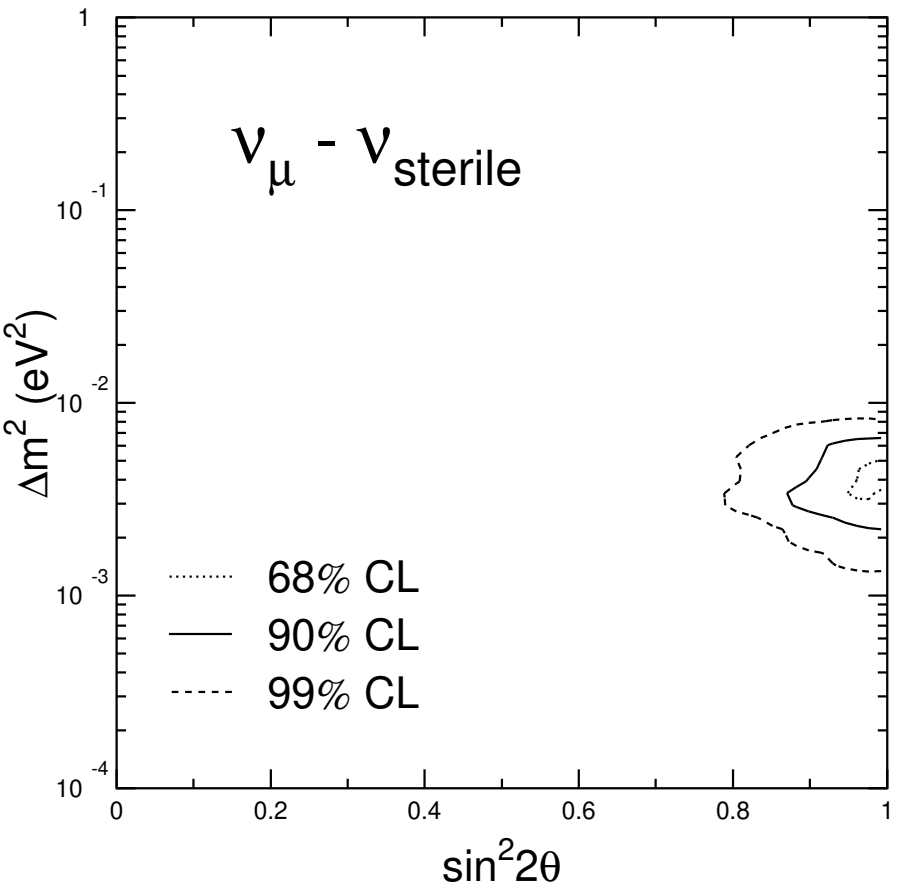

Figure 8.22: Super–Kamiokande allowed oscillations parameters for $\nu_\mu \leftrightarrow \nu_{sterile}$ oscillations.

8.3.3 $\nu_\mu \leftrightarrow \nu_e$

The $e-$like event rate and zenith angle asymmetry are in good agreement with expectations. Therefore, it is not surprising that oscillations of $\nu_\mu \leftrightarrow \nu_e$ fail to provide a complete solution to the atmospheric anomaly. Assuming two-flavor $\nu_\mu \leftrightarrow \nu_e$ oscillations the entire $\sin^2 2\theta - \Delta m^2$ parameter space is ruled out as shown in Fig. 8.24. The best-fit χ^2 is poor, 110/67, $P < 0.1\%$.

The reason for the poor fit can be understood from the zenith angle distributions plotted in Fig. 8.25. As oscillations are introduced to produce the large muon deficits

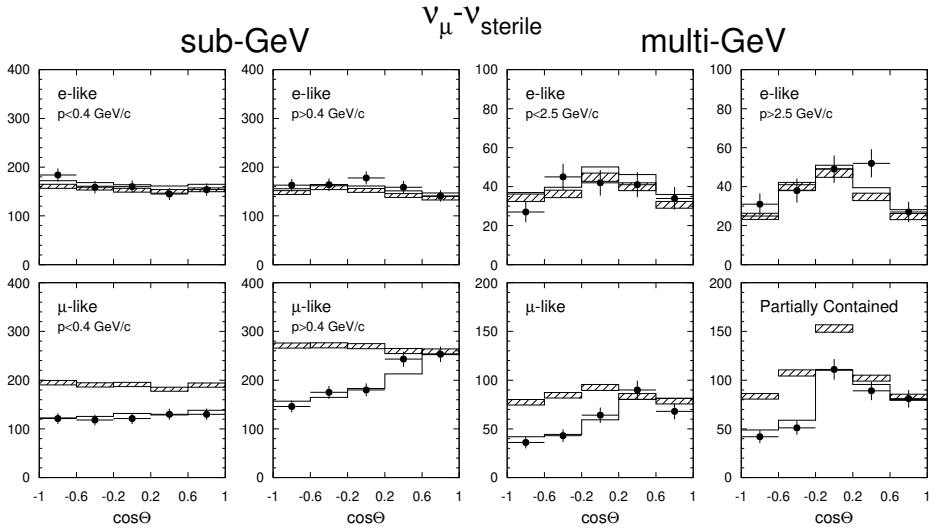

Figure 8.23: Super–Kamiokande atmospheric neutrino zenith angle event rates are plotted with the best-fit expectation for $\nu_\mu \leftrightarrow \nu_{sterile}$ oscillations. The key is same as Fig. 8.19

large excesses appear in the corresponding $e-$like distributions. These $e-$like excesses are not observed in the data.

Note that while two-flavor $\nu_\mu \leftrightarrow \nu_e$ oscillations can be ruled out as a complete solution, larger ν_μ – ν_e coupling is still allowed in a three-flavor context. Results for three-neutrinos are discussed in the next section.

8.4 Estimating L/E_ν

Ideally, neutrino oscillation experiments would like to observe the neutrino event rates as a function of the neutrino flight distance L and the neutrino energy E_ν. In this perfect world, a measurement of Δm^2 would be achieved by simply plotting the event rate as a function of the ratio L/E_ν and reading off the period of the resulting sinusoid. In the real world, however, the event-by-event reconstruction of the neutrino flight distance and energy has very large uncertainties which greatly complicate this

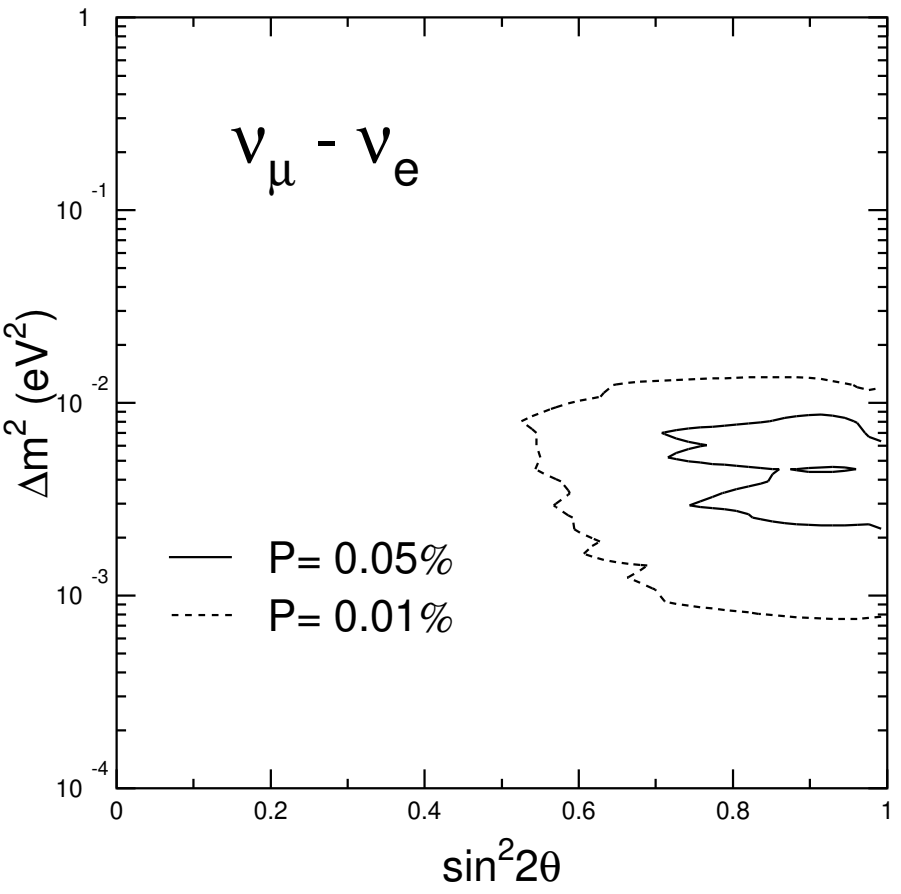

Figure 8.24: Super–Kamiokande best-fit probability for oscillations parameters assuming $\nu_\mu \leftrightarrow \nu_e$ oscillations.

simple picture. It is interesting, however, to attempt this reconstruction.

The reconstruction of L/E_ν has several sources of uncertainty. Neutrinos are observed in Super-Kamiokande via charged-current interactions of neutrinos on nuclei: $\nu + N \rightarrow l + X$. Only the final state lepton, l is observed and all the information about the original neutrino (flavor, L, and E_ν for example) must be deduced from this lepton. This lepton carries only a fraction of the incoming neutrino energy and has been scattered through some angle relative to the neutrino direction. These effects introduce large uncertainties in the estimates of both E_ν and L.

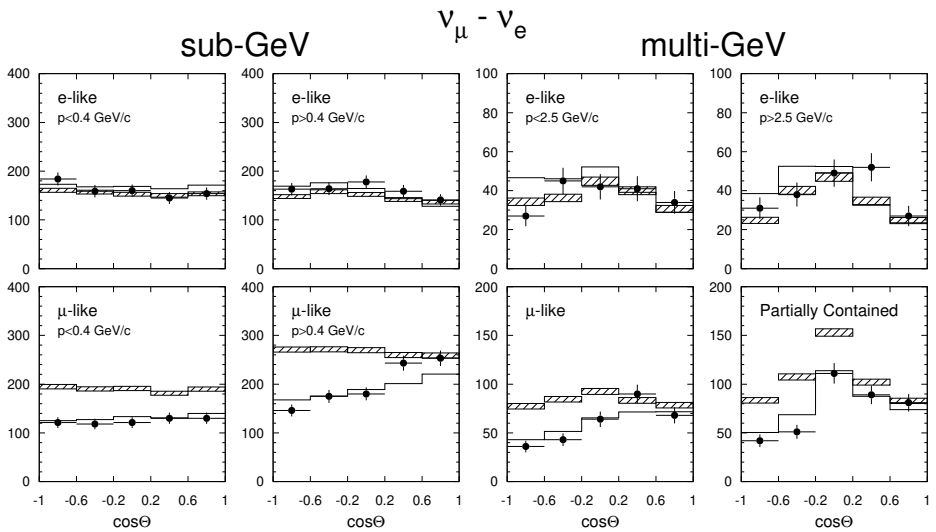

Figure 8.25: Super–Kamiokande atmospheric neutrino zenith angle event rates for the best-fit case of $\nu_\mu \leftrightarrow \nu_e$ oscillations. The key is same as Fig. 8.19.

The energy of the incoming neutrino and the energy of the final state lepton are correlated. However, some fraction of the neutrino energy is transfered to the nucleus so that the energy of the final state lepton will be smaller than that of the incoming neutrino. While it is impossible to know on an event-by-event basis how much energy is absorbed by the nucleus, this effect can be corrected for on average by applying a factor to the final state lepton momentum when estimating the parent neutrino energy:

$$E_\nu = P_l / f(P_l). \tag{8.29}$$

The factor $f(P_l)$ is estimated using a sample of atmospheric neutrino Monte Carlo neutrino interactions on nuclei. Figure 8.26 shows the ratio of P_l to E_ν as a function of P_l for ν_μ and ν_e single-ring charge-current interactions. At low momenta, the ratio is roughly 0.6 increasing to 0.85 at the highest momenta. The turn-over at the highest momenta is due to the presence of undetected particles (mostly pions) in the final state in addition to the charged lepton. Since partially-contained events deposit

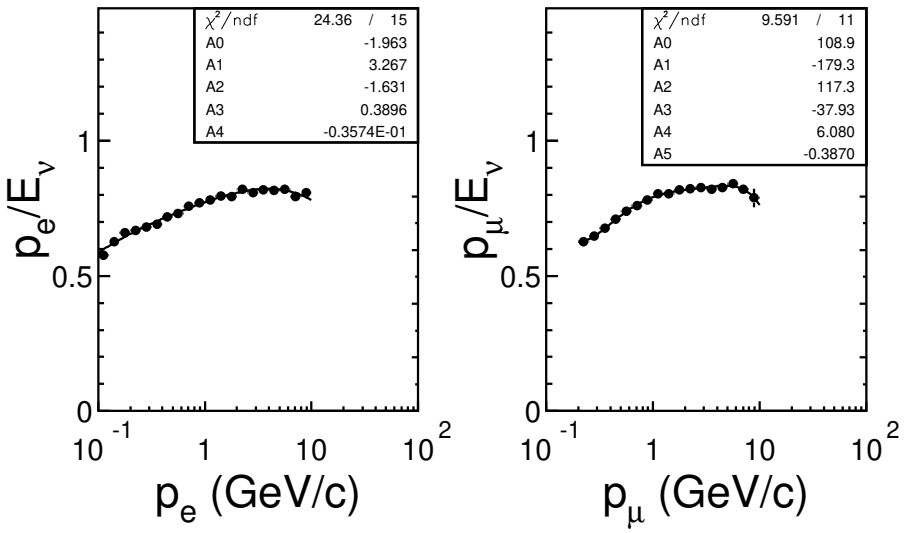

Figure 8.26: The average momentum fraction transfered to the final state lepton for single-ring charged-current neutrino interactions as a function of reconstructed lepton momentum. The distributions for e-like and μ-like events are plotted separately with fits to 4^{th} and 5^{th} order polynomials respectively.

some unknown amount of energy outside the detector, only fully-contained events are used in this analysis.

The neutrino flight distance is estimated using the reconstructed lepton zenith angle by extrapolating backwards along the lepton track direction to the altitude of neutrino production. To improve pointing, only events with $p_l > 400$ MeV/c are used in the reconstruction of L/E_ν. At $p_l = 400$ MeV/c, the average neutrino-final state lepton angle is 55°. Above the horizon, the dependence of neutrino production height on the neutrino energy is significant. For each event, the production height is estimated using the lepton zenith angle and the neutrino energy E_ν estimated in Eq. 8.29 using tables derived from Ref. [124].

The resolution of this estimate of L/E_ν is plotted versus L/E_ν in Fig.8.27. Note that the correction factors used to estimate L and E_ν were derived from the Monte

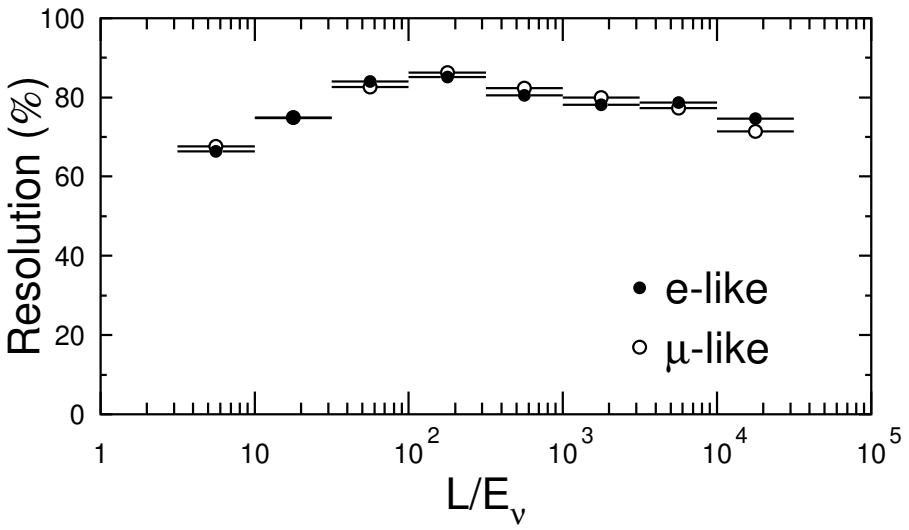

Figure 8.27: The estimated percent resolution of neutrino L/E_ν is plotted as a function of L/E_ν.

Carlo simulation used to estimate the resolution. Thus it is likely that the resolution is slightly under estimated. However, the size of this under estimate is small compared to the limit of L/E_ν resolution introduced by neutrino-nucleon scattering. The L/E_ν resolution is roughly 80% over the entire range.

Figure 8.28 plots the observed number of event for both data and Monte Carlo versus reconstructed L/E_ν. The peaks in each plot correspond to downward going events (low L/E_ν) and upward going events (large L/E_ν). The valley near $L/E_\nu \sim 10^3$ km/GeV is caused by the rapid change of L from $\sim$ 100 km to $\sim$ 1000 km at the horizon. The Monte Carlo expectation is shown for no neutrino oscillations (hatched region) and for $\nu_\mu \leftrightarrow \nu_\tau$ oscillations with the best fit parameters (dashed line). The ratio of data to Monte Carlo versus reconstructed L/E_ν is shown in Fig. 8.29. At low L/E_ν this ratio is near one for both e-like and μ-like events. The e-like ratio stays near one over the full L/E_ν range, but the μ-like ratio drops to one-half at large L/E_ν. Presumably, at large L/E_ν many oscillation cycles have been averaged

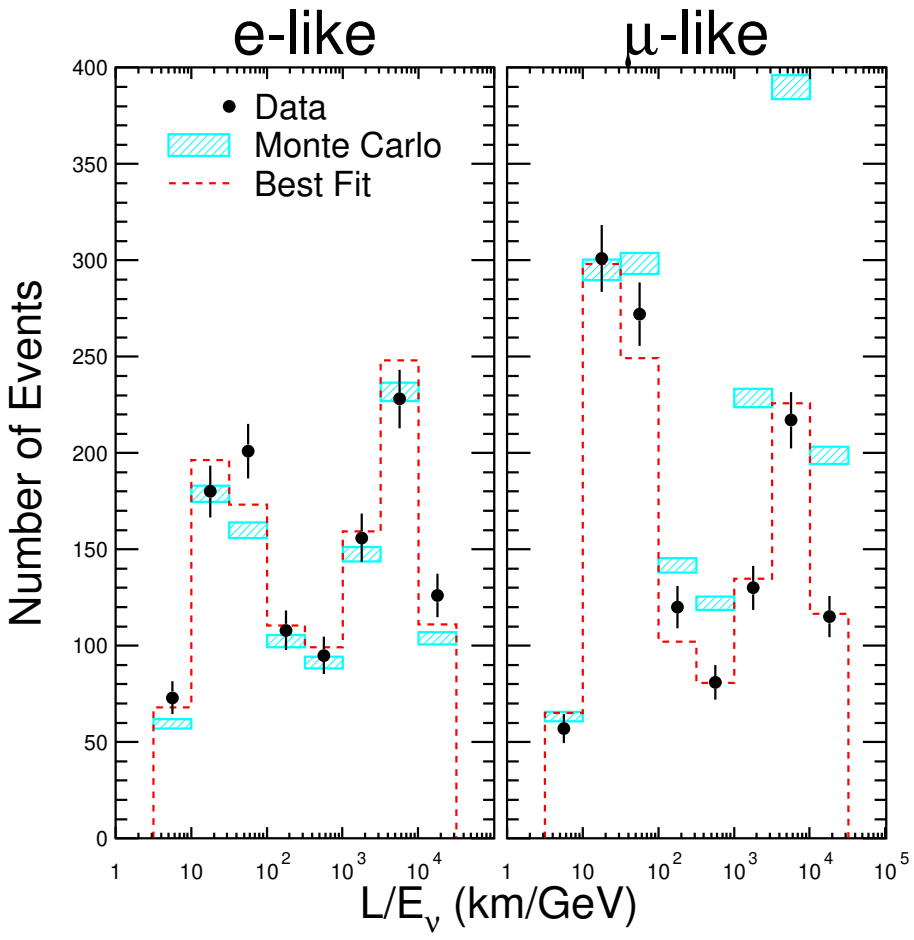

Figure 8.28: The atmospheric neutrino single-ring event rates with $p > 400$ MeV/c versus reconstructed L/E_ν are shown for a 45 kt-yr exposure of the Super-Kamiokande detector. Expected rates in the absence of neutrino oscillations are shown in the hatched regions. The dashed line is the expectation for oscillations of ν_μ to ν_τ with $\Delta m^2 = 3.5 \times 10^{-3}\text{eV}^2$ and $\sin^2 2\theta = 1.0$.

giving one-half; the expected ratio for maximal mixing.

Although it is possible to assign a value to L/E_ν on an event-by-event basis with reasonable accuracy, statistical fits to the reconstructed zenith angle and momentum distributions of atmospheric neutrinos events are preferred for several reasons to fits done in L/E_ν for estimating oscillation parameters. First, the estimates of L/E_ν have large uncertainties and in forming the ratio of L and E_ν exact information about the

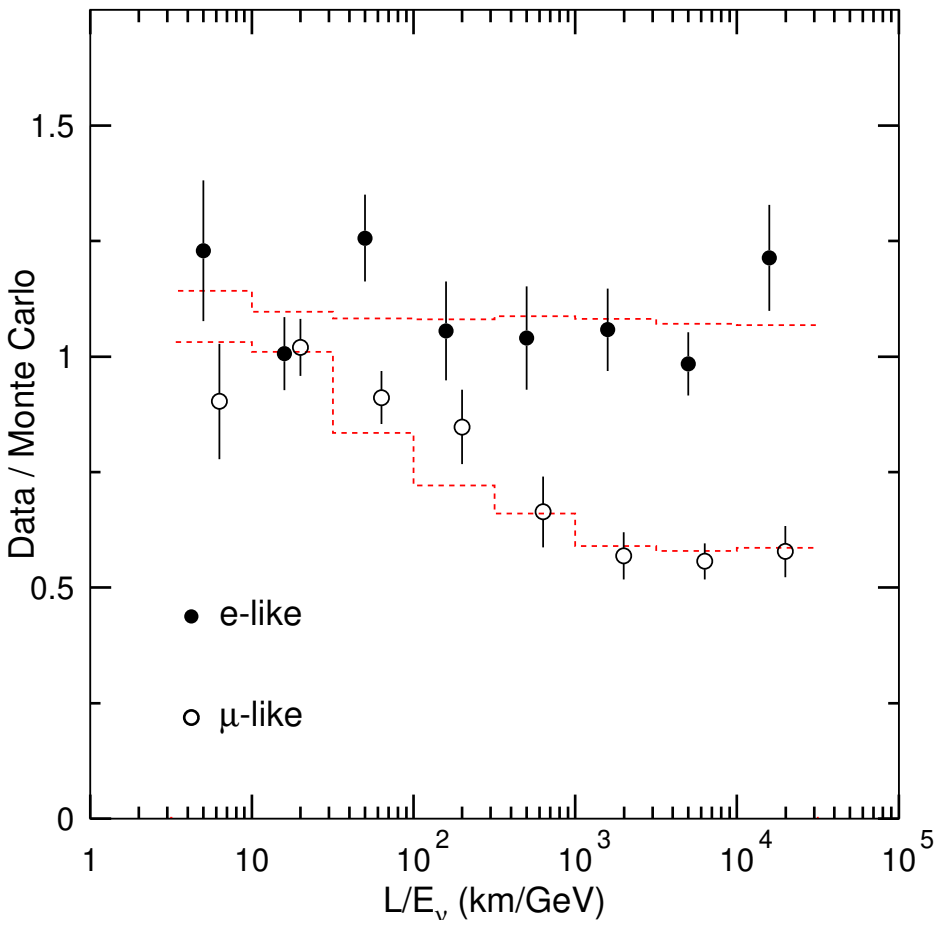

Figure 8.29: The ratio of data over Monte Carlo is plotted versus L/E_ν. The dashed line shows the expectation for oscillations of ν_μ to ν_τ with $\Delta m^2 = 3.5^{-3}\text{eV}^2$ and $\sin^2 2\theta = 1.0$. The slight dependence of the expected e-like ratio results from a roughly 2% ν_μ charged-current contamination in the e-like sample.

event zenith angle and energy is lost. Also, estimates of L/E_ν must exclude the very lowest energy events ($p < 400$ MeV/c) where the neutrino direction is very poorly measured and the highest energy events (the partially-contained events) where E_ν cannot be estimated. Finally, the oscillation probability is only a simple function of L/E_ν for the case of two-flavor oscillations in vacuum. For more general neutrino mixing schemes the oscillation probability is a complicated function of the neutrino energy, baseline and the matter density traversed.

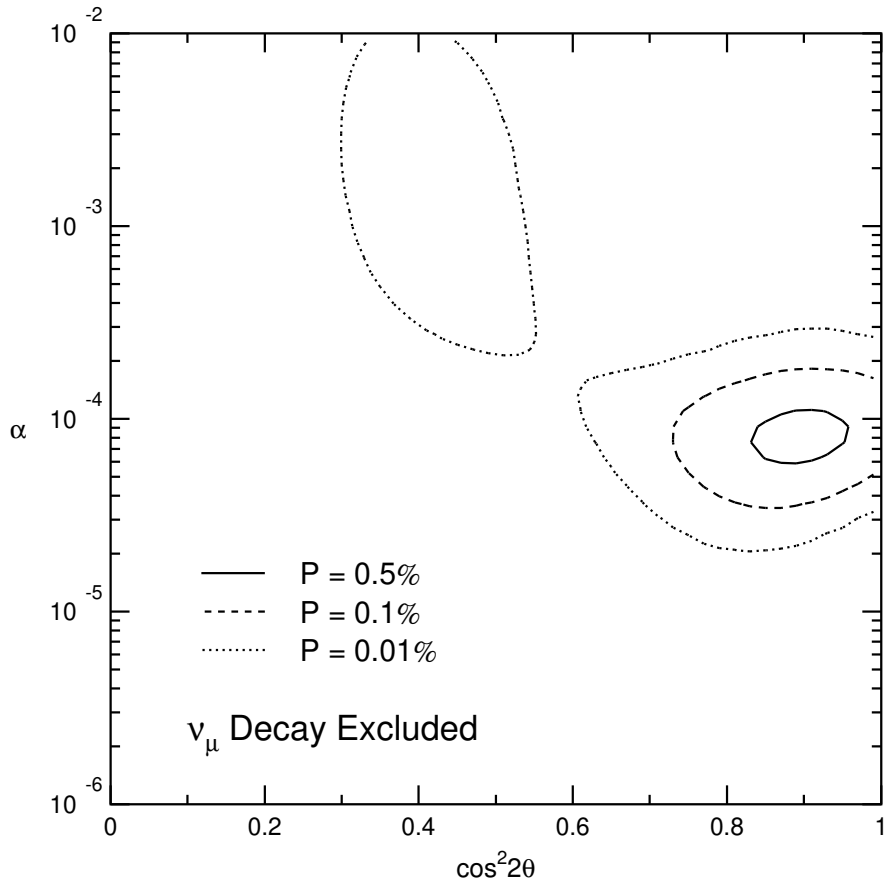

Figure 8.30: Excluded regions for the muon neutrino decay hypothesis.

8.5 Alternate Hypotheses

Other explanations for the neutrino deficits besides neutrino oscillations due to mixing of the neutrino flavor and mass eigenstates have been proposed. I have tested two of these, neutrino decay and flavor oscillations due to Lorentz non-invariance. While neutrino decay can safely be ruled out as an explanation of the observed muon-neutrino zenith angle rates, oscillations due to Lorentz non-invariance provide a fit to the FC and PC samples of comparable quality to oscillations based on mass-flavor mixing.

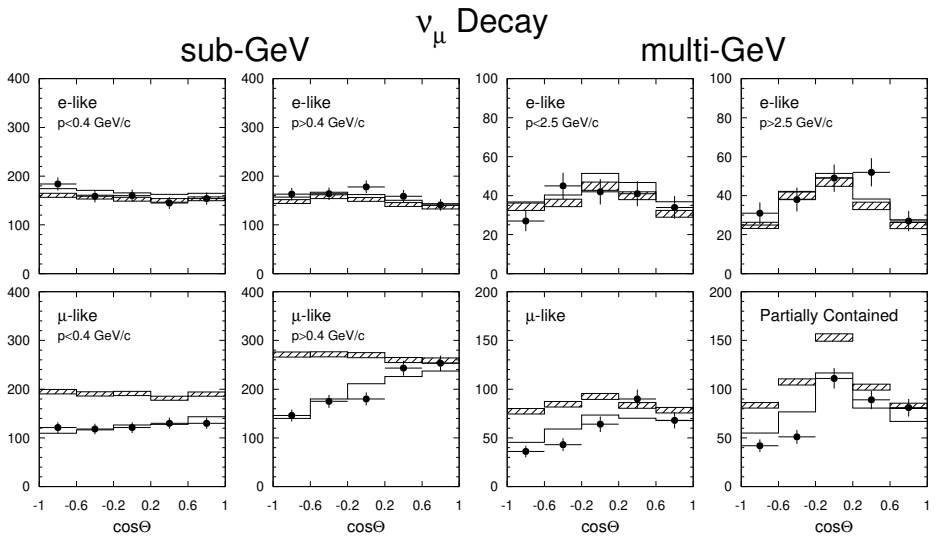

Figure 8.31: Best-fit zenith angle distributions assuming ν_μ decay (solid line). The hatched region show the expectation for no oscillations.

Muon Neutrino Decay

The possibility that the observed muon neutrino deficits could be due to muon neutrino decay was proposed by Ref. [134]. Assuming two-flavor mixing of ν_μ and ν_τ with mass eigenstates ν_1 and and unstable ν_2 with angle θ the survival probability for a muon neutrino is:

$$P_{\mu\mu} = \sin^4\theta + \cos^4\theta \exp\left(-\frac{\alpha L}{E}\right) + 2\sin^2\theta\cos^2\theta \exp\left(-\frac{\alpha L}{2E}\right)\cos\left(\frac{\Delta m^2 L}{2E}\right) \qquad (8.30)$$

Assuming Δm^2 is larger than 0.1 eV^2 the oscillatory terms average out leaving

$$P_{\mu\mu} = \sin^4\theta + \cos^4\theta \exp\left(-\alpha L/E\right). \qquad (8.31)$$

Re-weighting the neutrino flux using the survival probability in Eq. 8.31, the best-fit to the data is obtained at $\cos^2 2\theta = 0.9$, $\alpha = 8 \times 10^{-5}$. The minimum χ^2 value, however, is poor; $\chi^2_{min} = 101/67$ DoF P =0.4%. This best fit corresponds to a

τ/m of 4×10^{-11} s/eV. Neutrino decay can be ruled out as the primary source of the observed muon neutrino deficits. The exclusion contours are shown in Fig. 8.30. The best-fit zenith angle distributions are shown in Fig. 8.31. The neutrino decay hypothesis does not fit the multi-GeV and partially-contained data well.

Lorentz non-invariance

If Lorentz invariance is broken then different neutrino states may travel with slightly different velocities; ν_1 with velocity v_1 and ν_2 with velocity v_2. If these velocity states mix with the weak eigenstates then neutrino oscillations are possible [135, 136]. The oscillation probability is:

$$P = 1 - \sin^2 2\theta \sin^2 (\alpha L(\text{km}) E(\text{GeV})) \tag{8.32}$$

with

$$\alpha = 2.54 \times 10^{18} \frac{v_2 - v_1}{c}. \tag{8.33}$$

The main feature that differentiates this case from the standard oscillation formula is the dependence on the product of L and E rather than the ratio. Violation of the equivalence principle also leads to oscillations with this $L \times E$ dependence [137]. The best-fit for oscillations of this type occurs at $\sin^2 2\theta = 1.0$ and $\alpha = 4 \times 10^{-4}$. This α corresponds to $(v_2 - v_1)/c = 2 \times 10^{-22}$. This velocity difference is allowed by the limit set by Ref. [138] ($\delta v/c < 3 \times 10^{-22}$) but not by the limit obtained by Ref. [136] ($\delta v/c < 5 \times 10^{-23}$). The fit is surprisingly good; $\chi_{min} = 62.4/67$ DoF, $P = 64\%$. Figure 8.32 shows the confidence intervals for the parameters α and $\sin^2 2\theta$. The zenith angle rates are shown in Fig 8.33. The two oscillation cases (L/E and $L \times E$) are not distinguished because in the FC and PC samples the variation of L (0 - 10^4 km) is much larger than the variation of E (0.1 - 10 GeV). This situation may

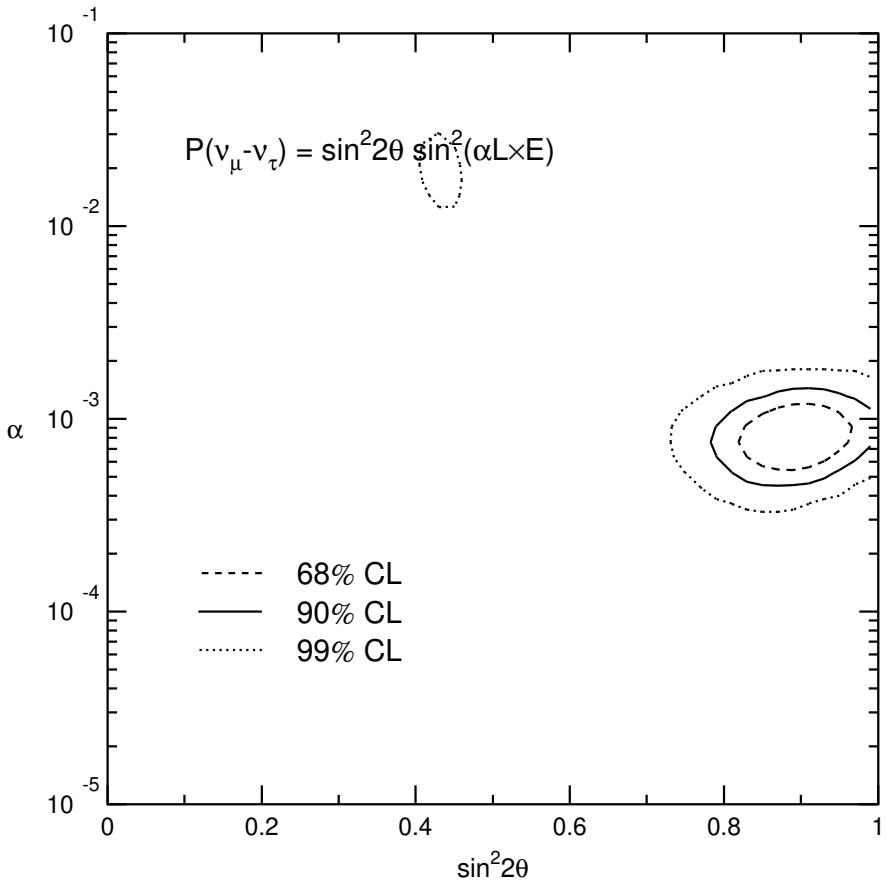

Figure 8.32: Confidence intervals for neutrino oscillations due to Lorentz non-invariance.

be improved by combining the FC, PC and neutrino-induced upward-going muon samples as this would extend the energy range to 100 GeV [139].

8.6 Results for Three-Flavor Neutrino Oscillations

Neutrino oscillations involving three neutrinos require six parameters: two Δm^2's, three angles, and one CP-violating phase. Given this large parameter space, I have chosen to examine several proposed forms of the neutrino mixing matrix for their

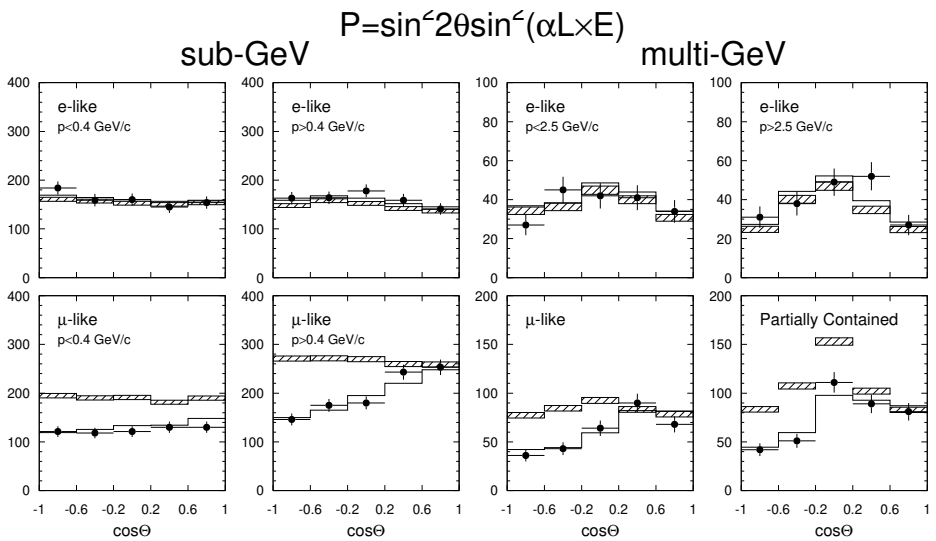

Figure 8.33: Expected zenith angle fits for best-fit oscillations assuming Lorentz non-invariance (solid line). Hatched region shows expectations for no oscillations.

consistency with the Super–Kamiokande atmospheric neutrino data. With the mixing matrix completely specified, the problem reduces to finding the allowed ranges of Δm^2_{12} and Δm^2_{23}. The mixing schemes analyzed are outlined in Table 8.7. Matter effects are important for all the mixing schemes considered and have been included using the prescription outlined in Sec. 8.1.2. The definition of χ^2 is identical to the definition used for the two-flavor oscillation modes (Eq. 8.14). The parameter λ, which controls the $\langle L/E_\nu \rangle$ uncertainty in the atmospheric neutrino Monte Carlo, is not used in the fits due to the large number of calculations required to minimize χ^2. The effects of this uncertainty on the allowed regions is applied after the confidence levels on the $(\Delta m^2_{12}, \Delta m^2_{23})$ grid have been calculated by convolving the confidence intervals with a two-dimensional Gaussian with $\sigma_x = \sigma_y = 15\%$. The final contours are insensitive to the exact method used to incorporate the uncertainty in λ.

In these studies I have chosen to express all the proposed mixing schemes in terms of their corresponding CKM angles using the form given in Eq. 2.15. The exact form of the mixing matrix given by other authors under the terms "three-fold

	θ_{12}	θ_{23}	θ_{13}	δ_{13}
Three-fold Maximal Mixing	45°	45°	35.3°	90°
Bi-maximal Mixing	45°	45°	0°	0°
Democratic Mixing	45°	54.7°	0°	0°

Table 8.7: Summary of CKM angles for 3-flavor mixing schemes.

	χ^2_{min}/67 DoF	(Δm^2_{12}, Δm^2_{23} eV^2)
Three-fold Max.	63, $P = 61\%$	$1 \times 10^{-4}, 5 \times 10^{-3}$
Bi-max.	61, $P = 68\%$	$3 \times 10^{-4}, 3 \times 10^{-3}$
Democratic	65, $P = 55\%$	$5 \times 10^{-5}, 5 \times 10^{-3}$

Table 8.8: Summary of the fit parameters for three-flavor mixing.

maximal", "bi-maximal", and "democratic" can be related to the mixing matrices given here by redefinitions of the over-all phases of the neutrino states ($|\nu_e\rangle, |\nu_\mu\rangle, |\nu_\tau\rangle$) and ($|\nu_1\rangle, |\nu_2\rangle, |\nu_3\rangle$). Results for the three mixing matrix hypotheses tests are summarized in Table 8.8.

8.6.1 Three-fold Maximal Mixing

Three-fold maximal mixing neutrino mixing has been proposed as a solution to both the atmospheric and solar neutrino problems [140, 141, 142]. Using the CKM form given in Eq. 2.15, three-fold maximal mixing is defined by $\theta_{12} = 45°$, $\theta_{23} = 45°$, $\theta_{13} = \arcsin(\sqrt{3}/3)$ and $\delta_{13} = 90°$. This gives

$$\begin{pmatrix} \nu_e \\ \nu_\mu \\ \nu_\tau \end{pmatrix} = \begin{pmatrix} \frac{\sqrt{3}}{3} & \frac{\sqrt{3}}{3} & -\frac{\sqrt{3}}{3}i \\ -\frac{1}{2} - \frac{\sqrt{3}}{6}i & \frac{1}{2} - \frac{\sqrt{3}}{6}i & \frac{\sqrt{3}}{3} \\ \frac{1}{2} - \frac{\sqrt{3}}{6}i & -\frac{1}{2} - \frac{\sqrt{3}}{6}i & \frac{\sqrt{3}}{3} \end{pmatrix} \begin{pmatrix} \nu_1 \\ \nu_2 \\ \nu_3 \end{pmatrix} \tag{8.34}$$

Under this mixing hypothesis each neutrino mass eigenstate contributes equally to each flavor state.

The best fit for three-fold maximal mixing occurs at $\Delta m^2_{12} = 1 \times 10^{-4}$, $\Delta m^2_{23} =$

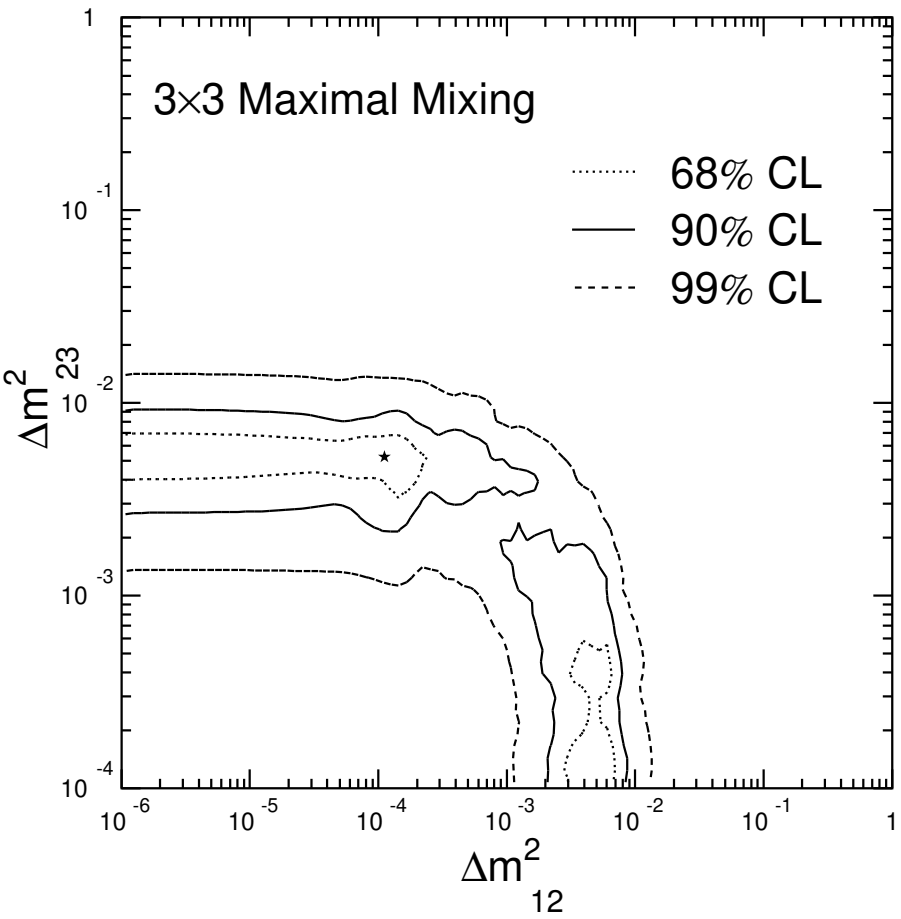

Figure 8.34: The allowed oscillation parameters assuming three-fold maximal neutrino mixing.

5×10^{-3} eV^2 with $\chi^2_{min} = 63.2/67\ DoF, P = 61\%$. The symmetry in the allowed region under the transformation $\Delta m^2_{12} \leftrightarrow \Delta m^2_{23}$ is a consequence of the symmetric nature of the mixing matrix. The symmetry is broken slightly by the matter effects in the Earth. The CP-odd terms in the matter Hamiltonian change sign under the interchange of $\Delta m^2_{23} > \Delta m^2_{12}$ and $\Delta m^2_{23} < \Delta m^2_{12}$. The effect is visible because the atmospheric neutrino flux is $\sim$10 – 20% higher than the anti-neutrino flux. The allowed region for Δm^2_{23} extends down to 10^{-3} eV^2. The CHOOZ experiment has excluded oscillations of ν_e to ν_μ or ν_τ with $\Delta m^2 > 10^{-3}$ for large mixing angle. Three-

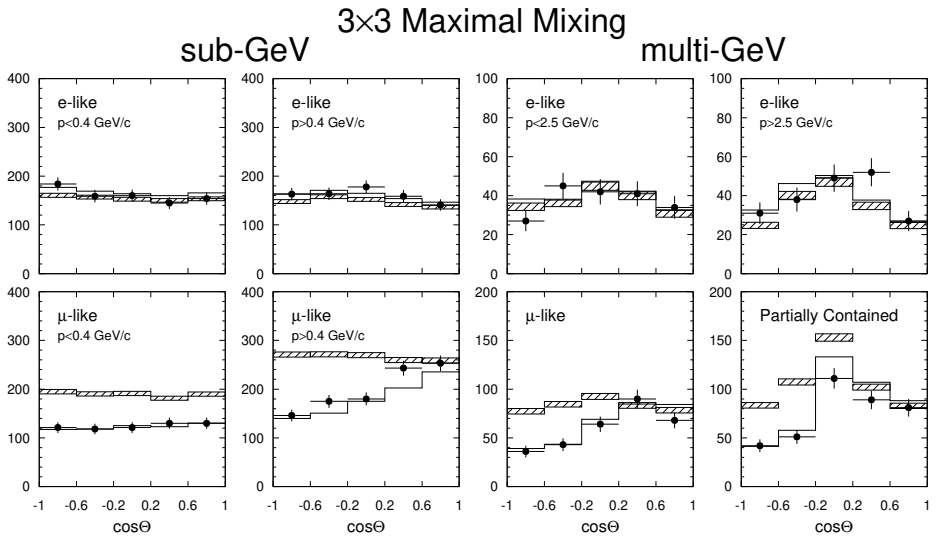

Figure 8.35: Best-fit zenith angle rates assuming three-fold maximal mixing.

fold maximal mixing is therefore only marginally consistent with the atmospheric neutrino data and the CHOOZ data taken together.

Starting from the three-fold mixing assumption, if the mixing angles are allowed to vary to minimize χ^2 then $\chi^2_{min} = 60.1/63\ DoF, P = 58\%$ is obtained at $\theta_{13} = 19°$, $\theta_{23} = 41°$, $\theta_{13} = 33°$ and $\delta_{13} = 92°$.

8.6.2 Bi-maximal Mixing

A second mixing hypothesis mixes the ν_e and ν_μ states maximally (to explain the solar neutrino data) and ν_μ and ν_τ (to explain the atmospheric data) and sets the mixing of ν_e and ν_τ to zero (in accordance with CHOOZ results). "Bi-maximal" mixing has been studied recently by many authors [143, 144, 145, 146]. The bi-maximal mixing matrix is:

$$\begin{pmatrix} \nu_e \\ \nu_\mu \\ \nu_\tau \end{pmatrix} = \begin{pmatrix} \frac{\sqrt{2}}{2} & \frac{\sqrt{2}}{2} & 0 \\ -\frac{1}{2} & \frac{1}{2} & \frac{\sqrt{2}}{2} \\ \frac{1}{2} & -\frac{1}{2} & \frac{\sqrt{2}}{2} \end{pmatrix} \begin{pmatrix} \nu_1 \\ \nu_2 \\ \nu_3 \end{pmatrix}. \tag{8.35}$$

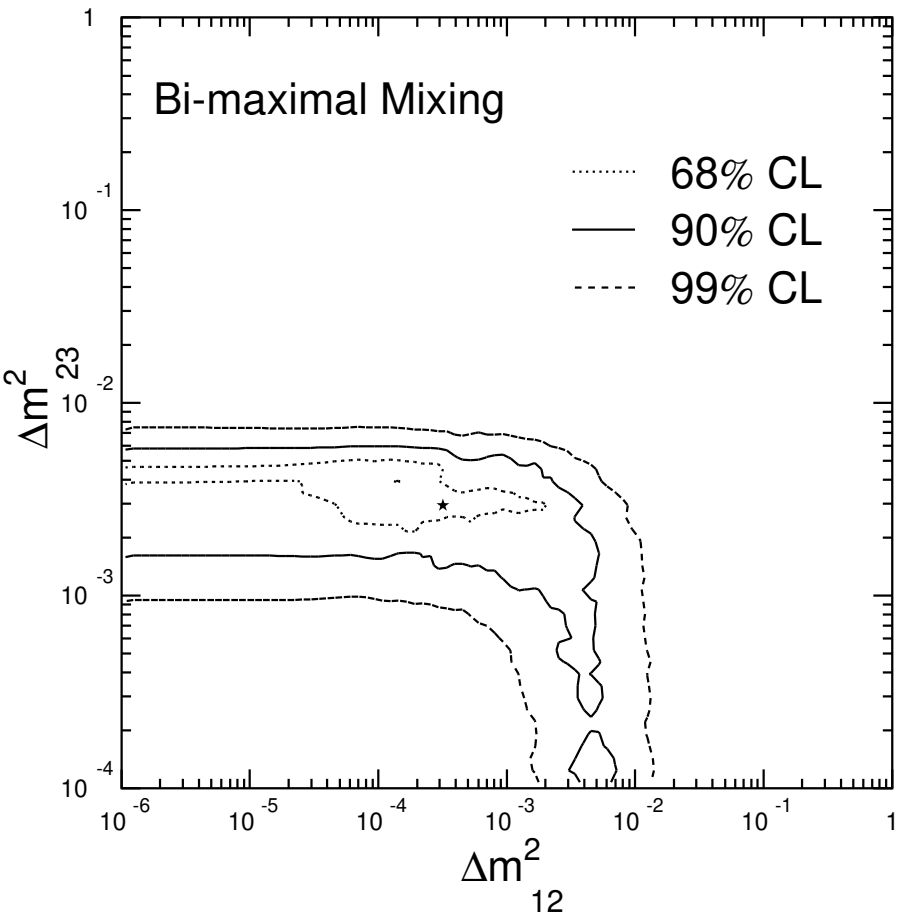

Figure 8.36: The allowed oscillation parameters assuming bi-maximal mixing.

The allowed allowed region for (Δm^2_{12}, Δm^2_{23}) is shown in Fig. 8.36. The best-fit occurs at $\Delta m^2_{12} = 3 \times 10^{-4}$ and $\Delta m^2_{23} = 3 \times 10^{-3}$ eV^2 with $\chi^2_{min} = 61.3/67$ Dof $P = 67\%$. The expected zenith angles rates are shown in Fig. 8.37.

Allowed the mixing angles to vary, the minimum χ^2 value near the bi-maximal solution, $\chi^2_{min} = 60.4/63$ DoF ($P = 57\%$), occurs at $(\Delta m^2_{12}, \Delta m^2_{23}) = (3 \times 10^{-4}, 3 \times 10^{-3}$ eV^2) with mixing angles $(\theta_{12}, \theta_{23}, \theta_{12}, \delta_{13}) = (41^\circ, 46^\circ, -6^\circ, 50^\circ)$. Although bi-maximal mixing provides the best fit to the data, the fit is only marginally better than the other mixing schemes considered.

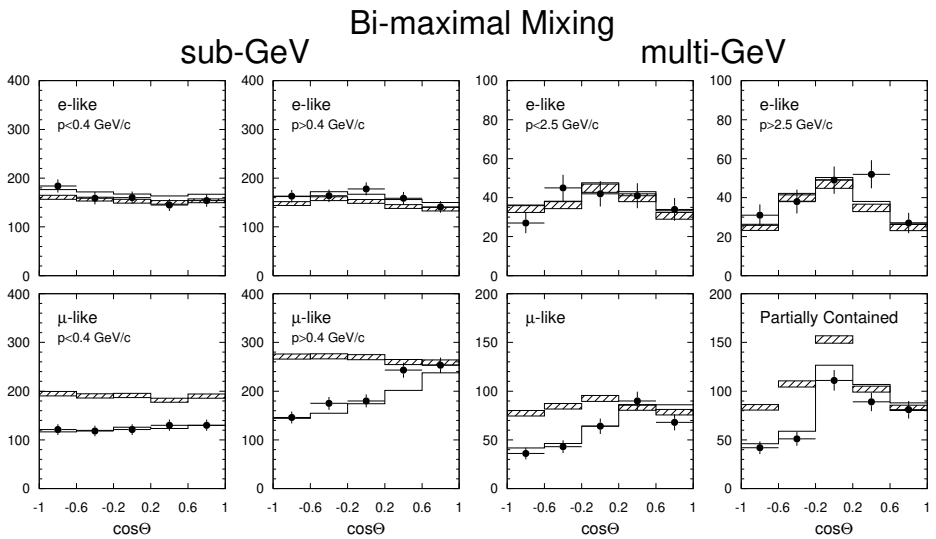

Figure 8.37: Best-fit zenith angle rates assuming bi-maximal mixing.

8.6.3 Democratic Mixing

"Democratic" mixing, (also referred to as the Fritzsch-Xing hypothesis [147]) predicts maximal mixing of ν_e – ν_μ and near maximal mixing for ν_μ – ν_τ. The mixing is specified by

$$\begin{pmatrix} \nu_e \\ \nu_\mu \\ \nu_\tau \end{pmatrix} = \begin{pmatrix} \frac{\sqrt{2}}{2} & \frac{\sqrt{2}}{2} & 0 \\ -\frac{\sqrt{6}}{6} & \frac{\sqrt{6}}{6} & \frac{\sqrt{6}}{3} \\ \frac{\sqrt{3}}{3} & -\frac{\sqrt{3}}{3} & \frac{\sqrt{3}}{3} \end{pmatrix} \begin{pmatrix} \nu_1 \\ \nu_2 \\ \nu_3 \end{pmatrix} \tag{8.36}$$

The best fit $(\Delta m^2_{12}, \Delta m^2_{23})$ for democratic mixing occurs at $(5 \times 10^{-5}, 5 \times 10^{-3})$ eV^2 with $\chi^2_{min} = 64.9/67$ Dof, $P = 55\%$. The allowed values of $(\Delta m^2_{12}, \Delta m^2_{23})$ are shown in Fig. 8.38. The expected zenith-angle distributions for the best-fit point are shown in Fig. 8.39.

The best fit allowing the mixing angles to vary near this solution is obtained at $(\Delta m^2_{12}, \Delta m^2_{23}) = (5 \times 10^{-5}, 5 \times 10^{-3})$ eV^2 and $(\theta_{12}, \theta_{23}, \theta_{13}, \delta_{13}) = (45°, 47°, 10°, -10°)$ with $\chi^2_{min} = 60.4/63$ DoF (P=57%) which essentially recovers bi-maximal mixing. The χ^2 difference is too small, however, to distinguish the two cases.

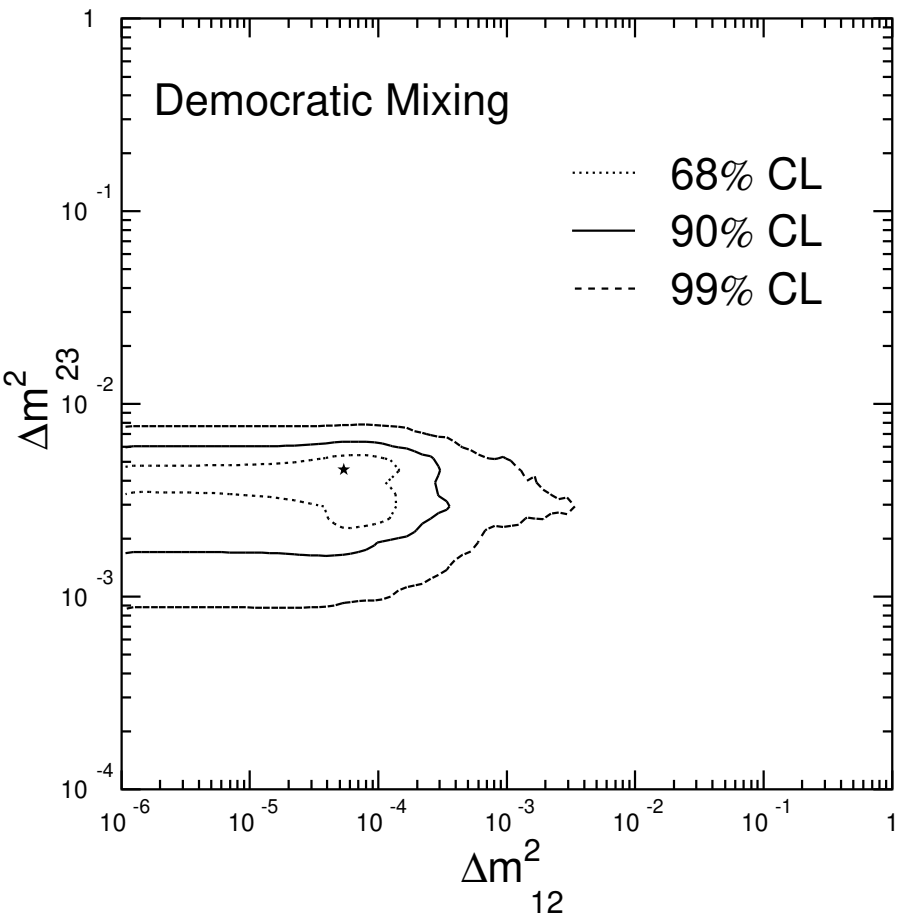

Figure 8.38: The allowed oscillation parameters assuming democratic neutrino mixing.

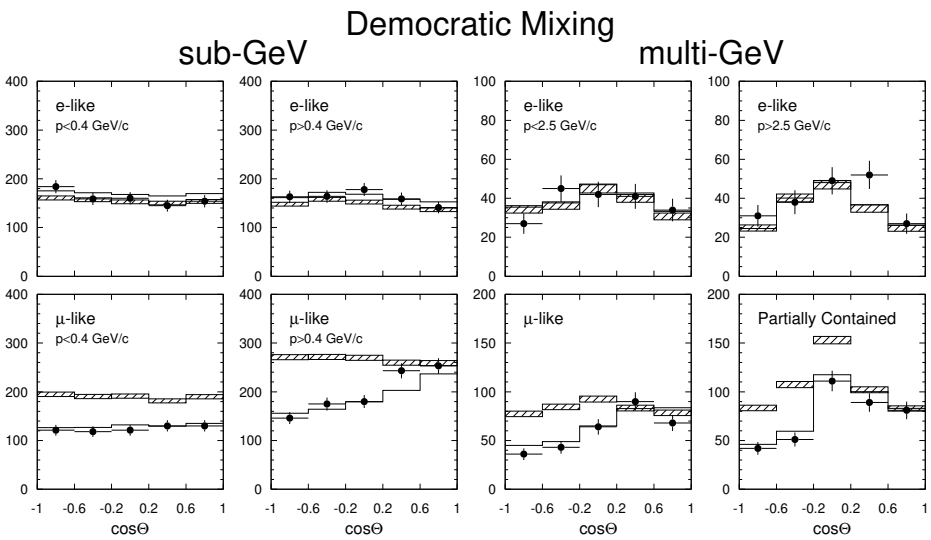

Figure 8.39: Expected zenith angle distributions for democratic neutrino mixing.

Chapter 9

Conclusions

The Super–Kamiokande detector has been operating since April 1, 1996. In its first 3 years of running, Super-K has collected over 6000 atmospheric neutrino events. These events exhibit significantly small values of the atmospheric neutrino ν_μ/ν_e ratio both above and below energies of $\sim$1 GeV due to a deficit of muon neutrinos. This deficit of muon neutrinos exhibits a significant zenith angle dependence. Both the muon neutrino deficit and zenith angle dependence are inconsistent with expectations based on calculations of the atmospheric neutrino flux. However, the data are well explained by neutrino oscillations of $\nu_\mu \leftrightarrow \nu_\tau$ with nearly maximal mixing and $1 < \Delta m^2 < 8 \times 10^{-3}$ eV^2. Confirmation of these results using man-made neutrino beams will be sought by the long-baseline neutrino experiments K2K which is currently beginning operation, and MINOS which is scheduled to begin data taking in 2002.

In this dissertation, the Super–Kamiokande data has also been compared with expectations from various three-flavor neutrino mixing hypotheses. These hypotheses seek to explain both the deficit of muons neutrinos observed by atmospheric neutrino experiments as well as the deficits observed by solar neutrino experiments. In general, these mixing hypotheses were found to be consistent with the atmospheric neutrino

data as long as they had the generic features of large $\nu_\mu - \nu_\tau$ mixing, $\Delta m^2_{12} < \Delta m^2_{23}$ and $10^{-3} < \Delta m^2_{23} < 10^{-2}$ eV^2. For Δm^2_{23} in the range indicated by the atmospheric neutrino experiments, the CHOOZ experiment has limited the magnitude of possible $\nu_e - \nu_\mu$ to roughly $\sin^2 2\theta_{13} < 0.2$. Additional constraints on Δm^2_{12} and $\sin^2 2\theta_{12}$ will come from measurements of solar neutrinos by Super–Kamiokande and soon the SNO, Borexino and KamLAND detectors.

The high τ production threshold limits the number of charged-current ν_τ interactions to an estimated 20/year and Super–Kamiokande's vertex resolution is too large to resolve τ decay. With the current data sample, oscillations of $\nu_\mu \leftrightarrow \nu_\tau$ and $\nu_\mu \leftrightarrow \nu_{sterile}$ cannot be distinguished. However, the possibility exists to resolve these two scenarios with measurements based on the suppression of neutral-current π^0 production or the suppression of $\nu_\mu \leftrightarrow \nu_{sterile}$ oscillations due to matter effects. The sensitivity to matter effects will be enhanced by combined fits of the fully-contained, partially-contained and upward-going muon samples.

Super–Kamiokande continues to collect atmospheric neutrinos at a rate of 8 per day. This data sample has already provided evidence for neutrino oscillations and placed significant constraints on the neutrino mass spectrum and mixing matrix. Future atmospheric neutrino measurements, particularly those that combine the fully-contained, partially-contained and upward-going muon samples [148], promise to improve the measurements of $\sin^2 2\theta$ and Δm^2 and determine if the observed atmospheric neutrino deficits are due to oscillations of $\nu_\mu \leftrightarrow \nu_\tau$ or $\nu_\mu \leftrightarrow \nu_{sterile}$.

Updike may not have been right, alas
When he wrote of the neutrino mass.
Neutrinos they might,
Just be very light,
Changing this one to that as they pass.

Bibliography

[1] J. Chadwick, Verhandl. Dtsch. phys. Ges. **16**, 383 (1914).

[2] W. Pauli, *Open Letter to Radioactive Ladies and Gentlemen*, (1930); (translation into English) Physics Today **31**, 27 (1978).

[3] J. Chadwick, Nature **129**, 312 (1932); Proc. Roy. Soc. **A136** 692 (1932).

[4] E. Fermi, Z. Phys. **88**, 161 (1934); Nuovo Cim. **11**, 1 (1934).

[5] B. Pontecorvo, Chalk River Laboratory Report PD-205 (1946), unpublished.

[6] F. Reines and C.L. Cowan, Phys. Rev. **92**, 830 (1953).

[7] F. Reines and C.L. Cowan, Nature **178**, 830 (1953).

[8] T.D. Lee and C.N. Yang, Phys. Rev. **104**, 254 (1956).

[9] A. Salam, Nuovo Cim. **5**, 299 (1957).

[10] C.S. Wu *et al.*, Phys. Rev. **105**, 1413 (1957).

[11] T.D. Lee and C.N. Yang, Phys. Rev. **105**, 1671 (1957).

[12] L.D. Landau, Nucl. Phys. **3**, 127 (1957); JETP, **5**, 337 (1957).

[13] M. Goldhaber, L. Grodzins, A.W. Sunyar, Phys. Rev. **109**, 1015 (1958).

[14] S.L. Glashow, Nucl. Phys. **22**, 579 (1961).

[15] A. Salam and J.C. Ward, Phys. Lett. **13**, 168 (1964).

[16] S. Weinberg, Phys. Rev. Lett. **19**, 1264 (1967).

[17] B. Pontecorvo, JETP **10**, 1236 (1960).

[18] G.T. Danby *et al.*, Phys. Rev. Lett. **9**, 36 (1962).

[19] R. Davis, Harmer and K.C. Hoffman, Phys. Rev. Lett. **21**, 1205 (1968).

[20] M.L. Perl *et al.*, Phys. Rev. Lett. **35**, 1489 (1975); Phys. Lett. **B63**, 466 (1976); Phys. Lett. **B70**, 487 (1977).

[21] Aachen-Brussels-CERN-Paris-Milan-Orsay-London Collaboration, J. Blietschau *et al.*, Nucl. Phys. **b114**, 189 (1976).

[22] H. Faissner *et al.*, Phys. Rev. Lett. **41**, 213 (1978); Phys. Rev. Lett. **41**, 1083, (1978).

[23] The UA1 Collaboration, G. Arnison *et al.*, Phys. Lett. **B122**, 103, (1983); Phys. Lett. **B126**, 398 (1983).

[24] The UA2 Collaboration, M. Banner *et al.*, Phy. Lett. **B122**, 476 (1983); Phy. Lett. **B129**, 130 (1983).

[25] K. Hirata *et al.*, Phys. Rev. Lett. **58**, 1490 (1987).

[26] R.M. Bionta *et al.*, Phys. Rev. Lett. **58**, 1494 (1987).

[27] The MARK-II Collaboration, G.S. Abrams *et al.*, Phys. Rev. Lett. **63**, 2173 (1989).

[28] The L3 Collaboration, B. Adeva *et al.*, Z. Phys. **C51**,179 (1991).

[29] The OPAL Collaboration, G. Alexander *et al.*, Z. Phys. **C42** 175, (1991).

[30] The DELPHI Collaboration, P. Abreu *et al.*, Nucl. Phys. **B367**, 511 (1991).

[31] The ALEPH Collaboration, D. Decamp *et al.*, Z. Phys. **C53**, 1, (1992).

[32] The ALEPH, LEP, DELPHI, LE, and OPAL Collaborations, D. Decamo *et al.*, Phys. Lett. **276B**, 247 (1991).

[33] Belesev *et al.*, Phys. Lett. **B350**, 263 (1995).

[34] Stoefll and Decman, Phys. Rev. Lett. **75**, 3237 (1995).

[35] Assamagan, *et al.*, Phys. Rev. **D53**, 6065 (1996).

[36] The ALEPH Collaboration, R. Barate *et al.*, Euro. Phys. J., **C2**, 395 (1998).

[37] L. Baudis *et al.*, Phys. Lett. **B407**, 219 (1995).

[38] Bernatow *et al.*, Phys. Rev. Lett. **69**, 2341 (1992).

[39] B. Pontecorvo, JETP **33**, 549 (1957); JETP **34**, 247 (1958); Zh. Eksp. Teor. Fiz. **53**, 1717 (1967).

[40] D. Casper *et al.*, Phys. Rev. Lett. **66**, 2561 (1991); R. Becker-Szendy *et al.*, Phys. Rev. **D46**, 3720 (1992).

[41] K.S. Hirata *et al.*, Phys. Lett. **B205**, 416 (1988); Phys. Lett. **B280**, 146 (1992).

[42] K. Daum *et al.*, Z. Phys. **C66**, 417 (1995).

[43] M. Aglietta *et al.*, Europhys. Lett. **8**, 611 (1989).

[44] Y. Fukuda *et al.*, Phys. Lett. **B335**, 237 (1994).

[45] Super–Kamiokande Collaboration, Y. Fukuda *et al.*, Phys. Lett. **B433**, 9 (1998).

[46] Super–Kamiokande Collaboration, Y. Fukuda *et al.*, Phys. Lett. **B436**, 33 (1998).

[47] Super–Kamiokande Collaboration, Y. Fukuda *et al.*, Phys. Rev. Lett. **81** 1562 (1998).

[48] F. Boehm and P. Vogel, *Physics of Massive Neutrinos*, Cambridge University Press, New York (1992).

[49] L. Wolfenstein, Phys. Rev. **D17**, 2369 (1978).

[50] S. P. Mikheyev and A. Y. Smirnov, Sov. J. Nucl. Phys. **42**, 1441 (1985); S. P. Mikheyev and A. Y. Smirnov, Nuovo Cim. **9C**, 17 (1986); S. P. Mikheyev and A. Y. Smirnov, Sov. Phys. Usp. **30**, 759 (1987).

[51] V. Barger *et al.*, Phys. Rev. **D22** 2718, (1980).

[52] P. Lipari and M. Lusignoli, Phys. Rev. **D58** 073005 (1998).

[53] J.N. Bachall, Astrophys. J. **467**, 475 (1996).

[54] J.N. Bahcall, S. Basu, and M.H. Pinsonneault, Rev. Mod. Phys. **64**, 885 (1998).

[55] B.T. Cleveland *et al.*, Astrophys. J. **496**, 505 (1998).

[56] The SAGE Collaboration, A.I. Abazov *et al.*, Phys. Rev. Lett. **67**, 3332 (1991).

[57] The SAGE Collaboration, D.N. Abdurashitov, Phys. Rev. Lett. **77**, 4708 (1996).

[58] The GALLEX Collaboration, P. Anselmann *et al.*, Phys. Lett. **B285**, 376 (1992).

[59] The GALLEX Collaboration, W. Hampel *et al.*, Phys. Lett. **B388**, 384 (1996).

[60] K.S. Hirata *et al.*, Phys. Rev. Lett. **65**, 1297 (1990); Phys. Rev. **D44**, 2241 (1991), **D45**, 2170E (1992).

[61] Kamiokande Collaboration, Y. Fukuda *et al.*, Phys. Rev. Lett. **77**, 1683 (1996).

[62] Super–Kamiokande Collaboration, Y. Fukuda *et al.*, Phys. Rev. Lett. **81**, 1158 (1998); Erratum-ibid. **81**, 4279 (1998).

[63] Super–Kamiokande Collaboration, Y. Fukuda *et al.*, Phys. Rev. Lett. **82**, 1810 (1999).

[64] J.N. Bahcall, S. Basu, M.H. Pinsonneault, Phys. Lett. **B433**, 1 (1998); J.N. Bahcall, M.H. Pinsonneault, S. Basu, and J. Christensen-Dalsgaard, Phys. Rev. Lett. **78**, 171 (1997).

[65] N. Hata and P. Langacker, Phys. Rev. **D56**, 6107 (1997).

[66] J.N. Bahcall, P.I. Krastev and A.Y. Smirnov, Phys. Rev. **D58** 096016 (1998).

[67] G. Zacek *et al.*, Phys. Rev. **D34**, 2621 (1986).

[68] B. Achkar *et al.*, Nucl. Phys. **B434**, 503 (1995).

[69] M. Apollonio *et al.*, Phys. Lett. **B420** 397 (1998)

[70] L. Borodovsky *et al.*, Phys. Rev. Lett. **68**, 274 (1992).

[71] N. Ushida *et al.*, Phys. Rev. Lett. **57**, 2897 (1986).

[72] G. N. Taylor *et al.*, Phys. Rev. **D28**, 2705 (1983).

[73] E. B. Brucker *et al.*, Phys. Rev. **D34**, 2183 (1986).

[74] F. Dydak *et al.*, Phys. Lett. **B134**, 281 (1984).

[75] F. Bergsma *et al.*, Phys. Lett. **142**, 103 (1984).

[76] The CHORUS Collaboration, proceedings of the XXIX International Conference on High Energy Physics, July 23–28, 1996, Vancouver, BC, Canada.

[77] J. Altegoer *et al.*, CERN-EP/98-57, submitted to Phys. Lett. B.

[78] C. Athanassopoulos *et al.*, Phys. Rev. **C54**, 2685 (1996); Phys. Rev. Lett. **77**, 3082 (1996); Phys. Rev. Lett. **81** 1774 (1998);

[79] The KARMEN Collaboration, B. Armbruster *et al.*, Proc. of the XXXIIIrd Rencontres de Moriond: '98 Electroweak Interactions and Unified Theories, to be published in Editions Frontiéres (1998), available from http://www-ik1.fzk.de/www/karmen; Phys. Rev. **C57**, 3414 (1998); K. Eitel and B. Zeitnitz, proceedings of the XVIIth International Conference on Neutrino Physics and Astrophysics, Takayama, Japan, June 1998 (hep-ex/9809007);

[80] W.W.M. Allison *et al.*, Phys. Lett. **B391**, 491 (1997); T. Kafka, proceedings of 5th Int. Workshop on Topics in Astroparticle and Underground Physics, Gran Sasso, Italy, Sep. 1997. W.W.M. Allison *et al.*, to be published in Phys. Lett. B (hep-ex/9901024).

[81] R. Becker-Szendy *et al.*, Phys. Rev. Lett. **69**, (1992) 1010;

[82] S. Mikheyev *et al.*, Baksan Collaboration, Proceedings of TAUP'97, Nucl. Phys. **B70** (Proc. Supp.), 371 (1999).

[83] The Kamiokande Collaboration, S. Hatakeyama *et al.*, Phys. Rev. Lett. **81**, 2016 (1998).

[84] The MACRO Collaboration, M. Ambrosio *et al.*, Phys. Lett. **B434**, 451 (1998).

[85] The Super–Kamiokande Collaboration, Y. Fukuda *et al.*, submitted to Phys. Rev. Lett. (hep-ex/9812014).

[86] P. Lipari, M. Lusignoli, and F. Sartogo, Phys. Rev. Let. **74**, 4384 (1995).

[87] Super-Kamiokande Collaboration: Y. Takeuchi *et al.*, to be published in Phys. Lett. **B**, (hep-ex/9903006).

[88] H. Kume *et al.*, Nucl. Instrum. Meth. **205**, 443 (1983); Nucl. Instrum. Meth. **A329**, 299 (1993).

[89] T. Tanimori *et al.*, IEEE Trans. Nucl. Sci. **36**, 497 (1989).

[90] R. Claus *et al.*, Nucl. Instrum. Meth. Phys. Res. **A261**, 540 (1987);

[91] J.S. George, *Experimental Study of the Atmospheric ν_μ/ν_e Ratio in the Multi-GeV Energy Range*, Ph.D. Thesis, U. Washington, Jun. 1998.

[92] S. Kasuga, *Observation of a Small ν_μ/ν_e Ratio of Atmospheric Neutrinos in Super-Kamiokande by the Method of Particle Identification*, Ph.D. Thesis, U. Tokyo, Jan. 1998

[93] M. Shiozawa, talk presented at RICH 98, Ein-Gedi, Dead-Sea, Israel, November 15-20, 1998 (available at http://www-sk.icrr.u-tokyo.ac.jp/doc/sk/pub).

[94] S. Kasuga *et al.*, Phys. Lett. **B374**, 238 (1996).

[95] The Super–Kamiokande Collaboration, M. Nakahata *et al.*, Nucl. Instrum. Meth. **A421**, 113 (1999).

[96] M. Honda *et al.*, Phys. Lett. **B248**, 193 (1990); M. Honda *et al.*, Phys. Lett. **D52**, 4985 (1995).

[97] G. Barr *et al.*, Phys. Rev. **D39**, 3532 (1989); V. Agrawal *et al.*, Phys. Rev. **D53**, 1313 (1996); T. K. Gaisser and T. Stanev, Proc. 24th Int. Cosmic Ray Conf. (Rome) Vol. 1 694 (1995).

[98] L.V. Volkova, Sov. J. Nucl. Phys. **37**, 784 (1980).

[99] K. Mitsui, Y. Minorikawa, and H. Komori, Nuovo Cim. **C9**, 995 (1986).

[100] A.V. Butkevich, L.G. Dedenko, and I.M. Zhelsnyhk, Sov J. Nucl. Phys. **50**, 90 (1989).

[101] P. Lipari, Astropart. Phys. **1**, 195 (1993).

[102] E.V. Bugaev and V.A. Naumov, **B105**, 884 (1989).

[103] H. Lee and Y. Koh, Nuovo Cim. **B105**, 884 (1990).

[104] D.H. Perkins, Astropart. Phys **2**, 249 (1994).

[105] Data compiled by the NOAA, ftp://ftp.ngdc.noaa.gov/STP/SOLAR_DATA/SUNSPOT_NUMBERS/YEARLY.

[106] D.R. Barraclough *et al.*(IAGA Division I Working Group 1), J. Geomagn. Geoelectr. **37**, 1157 (1985).

[107] Super–Kamiokande Collaboration, T. Futagami *et al.*, submitted to Phys. Rev. Lett. (astro-ph/9901139).

[108] K. Hanssget and J. Ranft, Comput. Phys. **39**, 37 (1986); Nucl. Sci. Eng. **88**, 537 and 551 (1984).

[109] B. Nilsson-Almquist and E. Stenlund, Comput. Commun. **43**, 387 (1987).

[110] T. Sjostrand and M. Bengtsson, Comput. Commun. **43**, 367 (1987).

[111] K. Kasahara and S. Torii, Comput. Phys. Commun. **64**, 109 (1991); K. Kasahara, S Torii, and T. Yuda, in *Proceedings of the Sixteenth International Cosmic Ray Conference, Kyoto 1979* (University of Tokyo, Tokyo, Japan), Vol. 13, p 70.

[112] S.E. Forsythe, *Smithsonian Physical Tables*, Smithsonian Institution Press, Washington DC (1969).

[113] M. Nakahata *et al.*, J. Phys. Soc. Jpn. **55**, 3786 (1986).

[114] C.H. Llewellyn Smith, Phys. Rep. **3**, 261 (1972).

[115] S. Hiramatsu *et al.*, Proceedings of the Int. Conf. on Nucl. Structure Studies Using Electron Scattering and Photoreaction, Sedai, 429 (1972).

[116] D. Rein and L.M. Seghal, Ann. of Phys. **133**, 79 (1981); Z. Phys. **C35**, 43 (1987). Nucl. Phys. **B223**, 29 (1983).

[117] M. Gluck, E. Reya, and A. Vogt, Z. Phys. **C67**, 433 (1995).

[118] S.J. Barigh *et al.*, Phys. Rev. **D17**, 1 (1978).

[119] H. Sarikko, proceedings of the International Conference on Neutrino Physics and Astrophysics, 1979.

[120] P. Musset and J.P. Vialle, Phys. Rep. **C39**, 1 (1978).

[121] J.E. Kim *et al.*, Rev. Mod. Phys. **53**, 211 (1981).

[122] *GEANT Detector Description and Simulation Tool*, CERN Program Library, W5013 (1994).

[123] T.A. Gabriel *et al.*, IEEE Trans. Nucl. Sci. **36**, 41 (1989).

[124] T. K. Gaisser and T. Stanev, Phys. Rev. **D57**, 1977 (1998).

[125] J.N. Bahcall and P.I. Krastev, Phys. Rev. **C56**, 2839 (1997).

[126] A.M. Dziewonski and D.L. Anderson, Phys. Earth Plan. Int. **25**, 297 1981.

[127] F.D. Stacey, *Physics of the Earth* (Wiley, New York, 1969).

[128] G. D'Agostini, Nucl. Instrum. Meth. **A346**, 306 (1994).

[129] T.K. Gaisser, *Cosmic Rays and Particle Physics*, Cambridge University Press, New York (1991).

[130] Particle Data Group, Review of Particle Physics, R.M. Barnett *et al.*, Phys. Rev. **D54**, 375 (1996).

[131] F.T. Solmitz, Ann. Rev. Nucl. Sci. **14**, 375 (1964).

[132] C. Caso *et al.*, Euro. Phys. J. **C3**, 1 (1998).

[133] G.J. Feldman and R.D. Cousins, Phys. Rev. **D57**, 3873 (1998)

[134] V. Barger *et al.*, submitted to Phys. Rev. Lett, astro-ph/9810121.

[135] S.L. Glashow *et al.*, Phys. Rev. **D56** 2433 (1997);

[136] S.C. Coleman and S.L. Glashow, Phys.Lett. B405 (1997) 249-252

[137] M. Gasperini, Phys. Rev. **D38**, 2635 (1988); A. Halprin and C.N. Leung, Phys. Rev. Lett. **67**, 1833 (1991).

[138] S.K. Lamoreaux *et al.*, Phys. Rev. Lett. **57**, 2135 (1986).

[139] P. Lipari, M. Lusignoli, hep-ph/9901350.

[140] P. F. Harrison, D. H. Perkins, and W. G. Scott, Phys. Lett. **B333**, 471 (1994); Phys. Lett. **B349**, 137 (1995); Phys. Lett. **B374**, 111 (1996); Phys. Lett. **B396**, 186 (1997).

[141] C. Giunti, C. W. Kim and J. D. Kim, Phys. Lett. **B352**, 357 (1995).

[142] S. M. Bilenky, C. Giunti and C. W. Kim, Phys. Lett. **B380**, 331 (1996)

[143] V. Barger, S. Pakvasa, T. J. Weiler, and K. Whisnant, Phys. Lett. **B437**, 107 (1998).

[144] S. Davidson, S.F. King, Phys. Lett. **B445**, 191, (1998).

[145] Y. Nomura and T. Yanagida, Phys. Rev. **D59**, 017303 (1999).

[146] C. Giunti, Phys. Rev. **D59**, 077301 (1999).

[147] H. Fritzsch, Z. Xing, Phys. Lett. **B372**, 265 (1996); Phys. Lett. **B440**, 313 (1998); hep-ph/9807234.

[148] A.H. Habig, talk presented at American Physical Society, Division of Particles and Fields Conference (DPF'99), Jan 5-9, 1999.